A 4-Volume Set

# BIOMECHANICAL SYSTEMS TECHNOLOGY

## Muscular Skeletal Systems

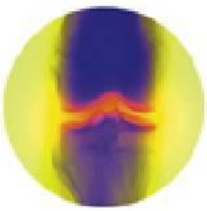

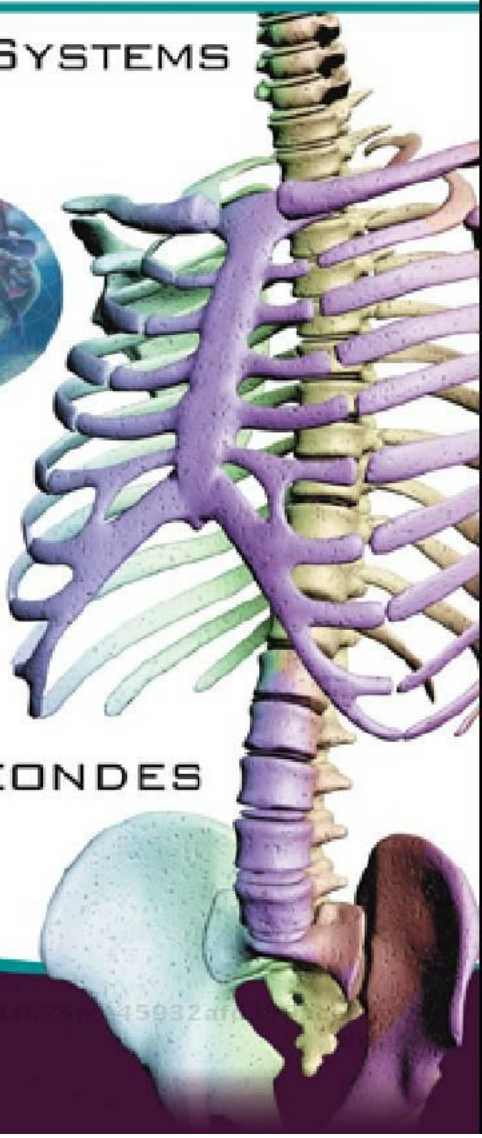

Cornelius T Leondes
Editor

World Scientific

# BIOMECHANICAL SYSTEMS TECHNOLOGY

## Muscular Skeletal Systems

**BIOMECHANICAL SYSTEMS TECHNOLOGY**
**A 4-Volume Set**
**Editor:** Cornelius T Leondes *(University of California, Los Angeles, USA)*

---

Computational Methods
ISBN-13 978-981-270-981-3
ISBN-10 981-270-981-9

Cardiovascular Systems
ISBN-13 978-981-270-982-0
ISBN-10 981-270-982-7

Muscular Skeletal Systems
ISBN-13 978-981-270-983-7
ISBN-10 981-270-983-5

General Anatomy
ISBN-13 978-981-270-984-4
ISBN-10 981-270-984-3

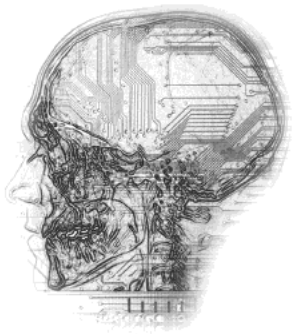

A 4-Volume Set

# BIOMECHANICAL SYSTEMS TECHNOLOGY

## Muscular Skeletal Systems

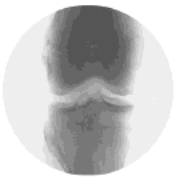

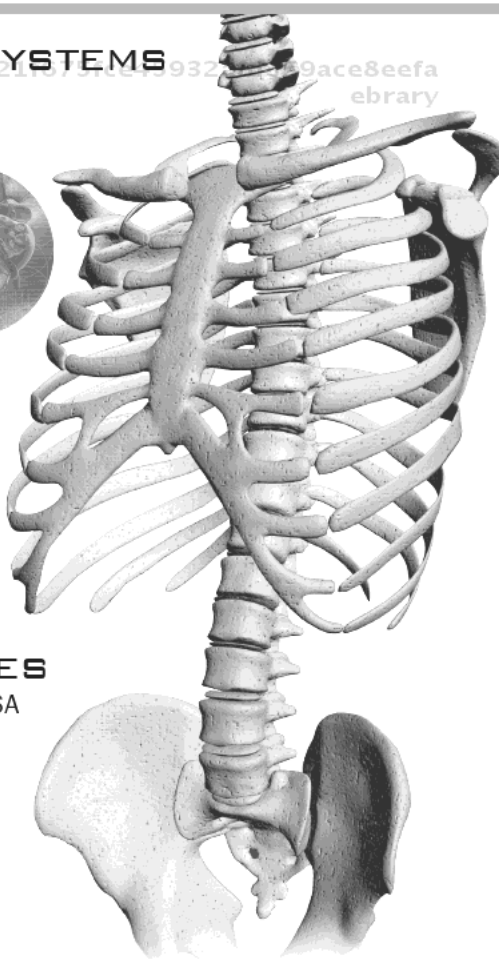



Editor

**Cornelius T Leondes**

University of California, Los Angeles, USA

World Scientific

NEW JERSEY • LONDON • SINGAPORE • BEIJING • SHANGHAI • HONG KONG • TAIPEI • CHENNAI

*Published by*

World Scientific Publishing Co. Pte. Ltd.

5 Toh Tuck Link, Singapore 596224

*USA office:* 27 Warren Street, Suite 401-402, Hackensack, NJ 07601

*UK office:* 57 Shelton Street, Covent Garden, London WC2H 9HE

**British Library Cataloguing-in-Publication Data**

A catalogue record for this book is available from the British Library.



**Biomechanical Systems Technology**
**A 4-Volume Set**
**Muscular Skeletal Systems**



ISBN-13 978-981-270-798-7 (Set)
ISBN-10 981-270-798-0 (Set)

ISBN-13 978-981-270-983-7
ISBN-10 981-270-983-5

Printed in Singapore.

# PREFACE

Because of rapid developments in computer technology and computational techniques, advances in a wide spectrum of technologies, and other advances coupled with cross-disciplinary pursuits between technology and its applications to human body processes, the field of biomechanics continues to evolve. Many areas of significant progress can be noted. These include dynamics of musculosketal systems, mechanics of hard and soft tissues, mechanics of bone remodeling, mechanics of implant-tissue interfaces, cardiovascular and respiratory biomechanics, mechanics of blood and air flow, flow-prosthesis interfaces, mechanics of impact, dynamics of man-machine interaction, and many more. This is the third of a set of four volumes and it treats the area of Muscular Skeletal Systems in biomechanics.

The four volumes constitute an integrated set. The titles for each of the volumes are:

- Biomechanical Systems Technology: Computational Methods
- Biomechanical Systems Technology: Cardiovascular Systems
- Biomechanical Systems Technology: Muscular Skeletal Systems
- Biomechanical Systems Technology: General Anatomy

Collectively they constitute an MRW (Major Reference Work). An MRW is a comprehensive treatment of a subject area requiring multiple authors and a number of distinctly titled and well integrated volumes. Each volume treats a specific but broad subject area of fundamental importance to biomechanical systems technology.



Each volume is self-contained and stands alone for those interested in a specific volume. However, collectively, this 4-volume set evidently constitutes the first comprehensive major reference work dedicated to the multi-discipline area of biomechanical systems technology.

There are over 120 coauthors from 18 countries of this notable MRW. The chapters are clearly written, self contained, readable and comprehensive with helpful guides including introduction, summary, extensive figures and examples with comprehensive reference lists. Perhaps the most valuable feature of this work is the breadth and depth of the topics covered by leading contributors on the international scene.

The contributors of this volume clearly reveal the effectiveness of the techniques available and the essential role that they will play in the future. I hope that practitioners, research workers, computer scientists, and students will find this set of volumes to be a unique and significant reference source for years to come.

This page intentionally left blank

# CONTENTS

# CHAPTER 1

# ARTICULAR CARTILAGE BIOMECHANICS, MECHANOBIOLOGY, AND TISSUE ENGINEERING

EUGENE KOAY and KYRIACOS ATHANASIOU*
*Department of Bioengineering, Rice University*
*PO Box 1892, MS 142 Houston, TX 77251-1892*
**athanasiou@rice.edu*



Tissue engineering is a promising solution to address articular cartilage pathology. The creation of strategies for functional replacement of diseased cartilage relies heavily on the knowledge of the physiology and development of articular cartilage, especially in terms of the influence of biomechanical forces on the tissue. This review will present the current knowledge of biomechanical structure–function relationships of native articular cartilage, and synthesize this knowledge with strategies to engineer the tissue *in vitro*.

*Keywords*: Articular cartilage; mechanobiology; mechanotransduction; tissue engineering.

## 1. Introduction

The potential of biotechnology has been highly touted for many years. The field of tissue engineering, in particular, has captured the imagination of many. Being able to replace virtually any body part would have profound implications for the treatment of chronic diseases, such as diabetes and osteoarthritis, and may have a great impact on human longevity. Strategies for functional replacement of tissues vary greatly, but even with the widely disparate approaches to tissue engineering, it is clear that a successful strategy will require a multidisciplinary approach and sound understanding of the native tissue. Previously distinct fields of research are being redefined and melded together throughout academia and industry to address many pathophysiology problems. This approach to research is aptly illustrated in the case of articular cartilage.



Articular cartilage is a specialized form of hyaline cartilage that covers the articulating ends of bones and serves as a lubricated, wear resistant, friction-reducing surface that evenly distributes forces. To perform these functions, the tissue has an elegantly simple structure. Unfortunately, this structure is not conducive to repair, as the tissue is deficient of blood vessels and lymphatics, and has low cellularity. The loss of this tissue due to disease (i.e., osteoarthritis) or trauma can result in significant patient morbidity because the tissue is unable to restore itself naturally to a functional state. Currently, most treatments for joint disease are

palliative, not curative. The burden of cartilage pathology on society encompasses not only patient pain and suffering but also a great economic cost. There are various methods to address this significant problem by assisting the healing process in articular cartilage. Tissue engineering has great potential for this purpose.

The idea of treating diseases related to structural tissues like articular cartilage and metabolic tissues such as the liver by engineering each tissue *in vitro* has been a tantalizing prospect ever since seminal papers were published on the use of bioabsorbable materials with the appropriate cells from the body.[1,2] The original idea was to place these cells, such as chondrocytes, onto a biocompatible scaffold. These scaffolds were made of biomaterials that would degrade as the cells built a neotissue, with the scaffold serving as a structural foundation and a biological stimulus (in some cases) for the cells to adhere and deposit their matrix molecules. The field quickly blossomed, growing into a major area of study covering a wide range of topics that span virtually every field of science and engineering. Today, teams of scientists and engineers work together in an integrated manner to address the challenges to articular cartilage tissue engineering.



Although the full potential of tissue engineering has not been realized yet, the field has made great strides toward the ultimate goal of treating major clinical problems such as osteoarthritis. As with any fertile field of study, even with major advances, there are always challenges and questions, new and old, to address. This review will examine some of the major challenges of articular cartilage tissue engineering. The objective is to provide a broad view of this field of study, emphasizing major tenets and identifying particular areas that require attention. Specifically, this chapter is divided into two major areas related to articular cartilage: (1) native structure–function relationships and (2) tissue engineering (Fig. 1).

Reflecting on the past two decades of tissue engineering research, much emphasis has been placed on the restoration of function to damaged tissues. In order to do this, particular focus has been placed on understanding the normal, healthy tissue. For articular cartilage, it is clear that the tissue serves a biomechanical function. The tissue's structure facilitates this function very well, and biomechanical forces play a major role in determining the tissue's architecture, maintaining the tissue's health, and causing the tissue's failure. Thus, the first section of this paper describes the native biomechanical structure–function relationships of articular cartilage, where these roles of biomechanics will be described in detail.



The second part of this chapter pertains to efforts attempting to engineer functional articular cartilage tissue *in vitro*. Organizing the chapter in this manner emphasizes a well-accepted idea that understanding the native tissue will provide insight and design parameters for the engineering of tissue in the laboratory. During the discussion of the major results in the field, an effort will be made to identify certain challenges and future directions. Overall, this review should serve to provide a foundation for understanding native articular cartilage and the pursuits related to its tissue engineering.

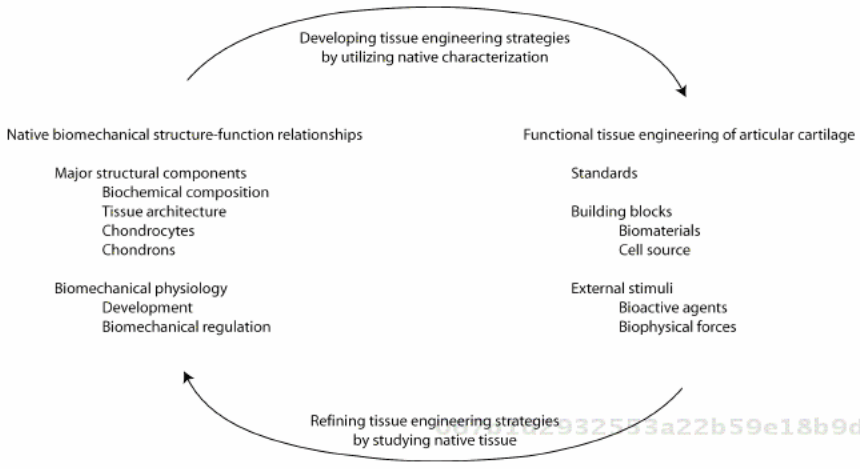


Fig. 1. Articular cartilage is a biomechanical tissue. This description entails many aspects, including the tissue's structure and function and physiology, in both health and disease. In each of these aspects, researchers have gleaned information that has helped to focus efforts to tissue engineer articular cartilage *in vitro*. Without a thorough characterization of the native tissue's composition and structure as well as a firm grasp of the native tissue's physiology and disease, choosing design variables and planning articular cartilage tissue-engineering studies would be an insurmountable task. Thus, these biomechanical aspects of the native tissue are critical to developing and refining tissue-engineering strategies that may be able to treat cartilage diseases. Because biomechanics play such a central role in so many ways of understanding articular cartilage, this biomechanical system has spawned a wide array of studies. In this review, these studies will be synthesized to provide a comprehensive view of the native tissue, providing a framework for understanding the approaches and challenges of articular cartilage regeneration.

## 2. Native Biomechanical Structure–Function Relationships

The structure and biomechanical function of articular cartilage are intimately related. In this section, these structure–function relationships will be analyzed at different levels, from the tissue composition and architecture down to the single chondrocyte (Fig. 2). Additionally, the changes in articular cartilage structure with disease will be analyzed to help explain how the tissue's function becomes compromised. Basic studies of native articular cartilage have set benchmarks and design criteria for tissue engineers, vital pieces of information for any successful engineering project.

### 2.1. *Structural components of native articular cartilage*

#### 2.1.1. *Composition*

Much effort in tissue engineering has been placed on the characterization of native cartilage, with the hope of setting benchmarks for the engineering of functional tissue. Grossly, normal articular cartilage is a white, smooth, and glistening tissue. The tissue is composed mostly of water (60%–85%), and the remaining tissue is

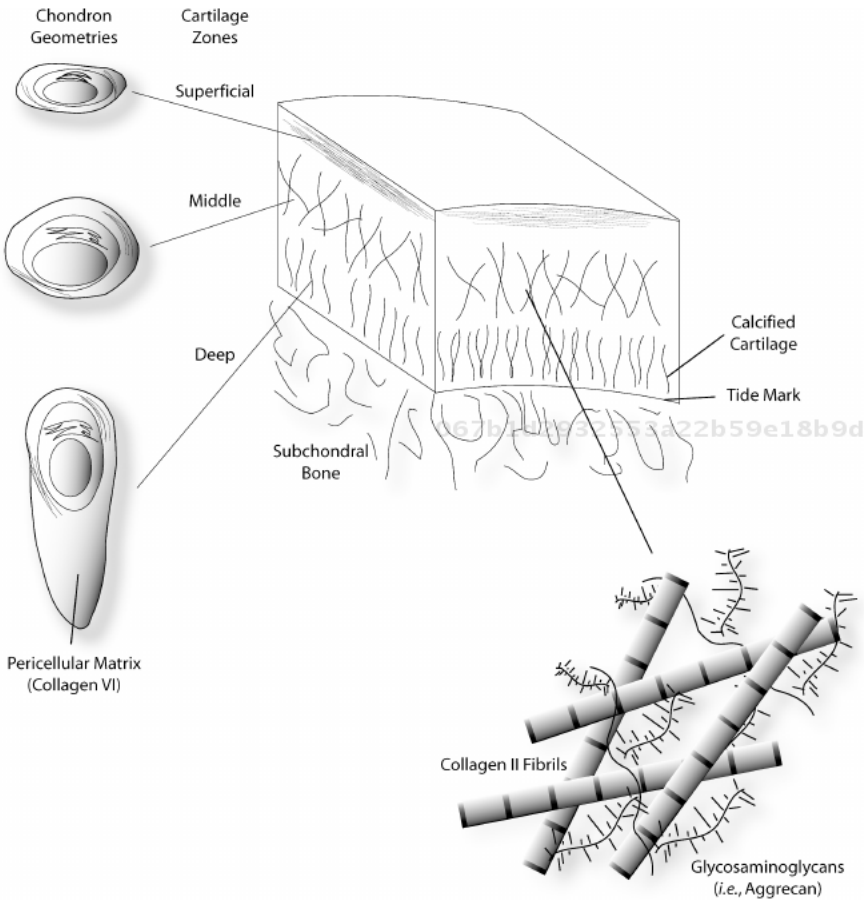


Fig. 2. Native articular cartilage exhibits a structure that accommodates its biomechanical functions of protecting the ends of long bones, distributing loads, and near-frictionless movement. This can be seen from the bulk tissue level, the single cell level, and the protein level.

extracellular matrix (ECM) composed of cross-linked collagen II (15%–22% by wet weight and 80%–85% of the total collagen), proteoglycans (4%–7% by wet weight), and lesser amounts of other collagen types, such as collagens IX and XI,[3] and proteins, such as decorin, biglycan, and fibromodulin.[4–7] The structure of selected molecules is shown in Fig. 2.

Collagen II is one of the most abundant proteins found in the animal kingdom, and it is a defining component of articular cartilage structure and function. Like other common collagens such as I and III, it forms a fibril structure, consisting of three coiled subunits. In the particular case of collagen II, it is composed of three $\alpha 1$(II) chains, a homotrimer. Collagen molecules are approximately 300 nm long and form striated fibrils due to lateral alignment between the molecules, which are staggered by 67 nm (D bands).[8] Concerning the bulk tissue properties, collagen II contributes to the tensile strength of the tissue.[9] This tensile strength depends on

the fibril diameter and on the crosslinks between collagen molecules within the triple helix that form the collagen fibril.[10] The crosslinks are mostly based on pyridinoline and occur at a higher rate than other tissues such as tendon.[11] These crosslinks are necessary for the formation of a collagen network that is under constant tension due to the swelling pressure created by the surrounding proteoglycan and water gel.[12]

Proteoglycans are a special class of glycoproteins with long, unbranched, and highly charged glycosaminoglycan (GAG) chains.[13] The major type of proteoglycan found in cartilage is aggrecan, which provides the tissue's compressive strength.[14] The highly charged GAG chains in cartilage attract cations, and this creates a positive osmotic pressure that causes cartilage to swell.[15,16] During a compressive load, the interstitial water supports much of the initial load,[17] and friction between the water and matrix helps dissipate the applied force, eventually reaching equilibrium when the osmotic pressure equals the load.[18] Removal of the load allows fluid back into the GAG network.



This fluid movement is essential for the transport of nutrients to chondrocytes, which are the cells that produce and maintain articular cartilage. These cells are adapted to a relatively low nutrient, low oxygen-tension environment, which is a result of the avascular nature of cartilage. Chondrocytes are metabolically active, primarily using glycolysis to fuel the constant remodeling of the matrix around them.[19] While collagens have a low turnover rate, proteoglycans have a half-life of a couple of weeks.

In osteoarthritis, the degradation of these matrix components exceeds the ability of chondrocytes to replace them, resulting in functional failure of the tissue.[20] Macroscopically, osteoarthritic cartilage is yellowish or brownish, in stark contrast to its normal white appearance. The tissue progresses through stages of degradation, showing surface roughening initially and noticeable fibrillation and matrix loss later. These changes in the tissue appear to result from both biochemical (i.e., degradative enzymes and proinflammatory mediators) and biomechanical influences, leading to degradation of molecular components and supramolecular structures.[20]



During this process of degradation and change, the biomechanics of the tissue alter. While collagen content remains relatively steady throughout the disease process, the collagen network transforms drastically.[21,22] Intimately linked to this change is the loss of fixed charges in articular cartilage. In fact, an early sign of osteoarthritis is a loss of aggrecan.[21] While it is understood that a loose collagen network leads to aggrecan loss and vice versa, it is not clear which event occurs first. Even with the loss of the majority of the fixed charges in the tissue, which normally hold water in, the failure of the collagen network results in the diseased tissue's swollen, hyperhydrated appearance. This may be explained by the failure of the collagen network to provide tensile resistance to the swelling pressure in the tissue. As the tissue's internal structure and, subsequently, biomechanics change, the bulk tissue begins to experience an altered biomechanical environment during activity in the joint. A vicious cycle emerges where a loose collagen network leads to loss of aggrecan, and this proteoglycan loss results in mechanical overloading,

further loosening the collagen network.[12] A number of other changes occur in osteoarthritic tissue, especially the expression of proteins not found in normal cartilage.[23–25] Additionally, there are changes that occur in specific aspects of the tissue's architecture, disrupting what is commonly referred to as the zones of articular cartilage. The structure and function of these zones in articular cartilage health and disease will be described in detail in the next section.

### 2.1.2. *Tissue architecture*

The zonal structure of articular cartilage is closely related to the tissue's biomechanical function. Articular cartilage covers the subchondral bone of diarthrodial joints, and can be divided into different zones, corresponding to depth from the cartilage surface down to the bone. These zones are named superficial, middle, deep, and calcified. They are characterized by their depth in the tissue, cellular morphology, collagen orientation, and GAG content, among other characteristics (Fig. 2).

At the surface is the superficial zone, comprising about 10%–20% of the thickness of the tissue.[26] The superficial zone ECM is composed primarily of collagen and a small amount of proteoglycans.[27,28] This zone has a high water content and densely packed collagen fibers aligned tangential to the tissue surface, imparting a high tensile strength and stiffness to this zone.[29] Superficial chondrocytes appear flat and elongated, and they have been shown to be distinct from chondrocytes in the other zones of cartilage in terms of their metabolic activity and protein production.[30,31] In particular, these cells do not produce very much matrix and secrete a protein called superficial zone protein (SZP). SZP, like aggrecan, is a proteoglycan. Unlike aggrecan, it is not found throughout articular cartilage, but instead, it is synthesized by superficial zone chondrocytes. SZP has long been believed to play a role in lubricating the cartilage surface,[32] helping to provide for the tissue's biomechanical function of reducing friction between joint surfaces, although recent work has challenged this notion.[33]

Below the superficial zone, collagen fibers are more randomly aligned, and the chondrocytes appear larger and are rounded. These morphological characteristics define the middle zone of cartilage. The general trend that occurs from superficial to deep zones is that chondrocytes become sparser and more metabolically active. Middle zone chondrocytes fit into this trend. The middle zone takes up to 60% of the thickness. These cells synthesize more ECM containing a higher amount of proteoglycans than superficial cells.[27,28,34–37] They have also been shown to express more collagen II mRNA than superficial cells.[38]

Farther down into the tissue is the deep zone of cartilage, where the cells appear ellipsoid in shape. These cells have proliferative ability and produce the largest amount of matrix.[31,39] The chondrocytes and collagen fibers in the deep zone align perpendicular to the subchondral bone (Fig. 2). While collagen II is the predominant form, other collagens (VI, IX, X, and XI) are dispersed throughout the tissue.[8]

A transitional calcified zone is below the deep zone, leading to the subchondral bone. The deep and calcified zones are separated by the tidemark, a narrow band of aggregates of mineral associated with matrix vesicles. These vesicles seem to be secreted by the chondrocytes in this area, playing a role in mineralization of the cartilage matrix.[40]

The layered structure of articular cartilage develops after birth as an adaptation to increased physical activity (see Sec. 2.2.1, Biomechanical development). The establishment of the mature stratified structure of articular cartilage is necessary for a normal joint to withstand physiological forces. Each zone of cartilage is specifically adapted to perform a role in carrying out the tissue's primary functions of load distribution, joint protection, and low friction movement. As described previously, the collagen network and GAGs also play a vital part in the normal functions of articular cartilage. It is the specific arrangement of these components that truly defines the mature tissue. The thin collagen fibrils of the superficial zone form a sheath parallel to the surface[40] and, during physical activity, this zone acts partly as a seal at the joint surface, experiencing high fluid flow across the surface, fluid pressure and tension, large compressive strains that result in consolidation of the surface, and tensile surface strains.[41] The superficial zone constrains the middle zone of cartilage from above, while adjacent tissue and the subchondral bone restrict the middle zone from the sides and from below, respectively. These restraints result in low fluid flow and high fluid pressurization in the middle zone, and this hydrostatic pressure supports the bulk of the load.



Corresponding to these different mechanical environments between zones, the heterogeneous, zonal structure of mature articular cartilage is also manifest in differing mechanical properties between zones.[42,43] Studies of the deformation behavior of full thickness articular cartilage have demonstrated that the strain fields in the tissue vary according to depth, in agreement with the varying mechanical properties between zones and their corresponding biomechanical functions.[44] In subsequent sections, the implications of these biomechanical structure–function relationships will be analyzed in terms of the tissue's physiology and tissue engineering.



The importance of the zonal structure of articular cartilage to normal function is perhaps best demonstrated by describing how alterations to this structure affect the tissue, namely in diseases like osteoarthritis. Effectively, erosion or degradation of the zonal architecture will result in a loss of tissue function. Degradative processes seem to be especially prominent in the superficial zone during osteoarthritis and experimental models of osteoarthritis.[22,45,46] In this zone, it appears that biochemical changes mirror those of the rest of the tissue, including an increase in water content, decrease in fixed-charge density, and loosening of the collagen network (possibly by a decrease in hydroxypyridinium cross-links). However, these changes are more pronounced in the superficial zone than the rest of the tissue.[22] With these compositional changes come structural changes that impair the tissue's biomechanical function, resulting in progressive degradation of the tissue. Part of

the reason for this failure is the ineffective response of chondrocytes to these disease processes.

### 2.1.3. *Chondrocytes*

In mature articular cartilage, chondrocytes are believed to be the single population of cells and occupy 10% of the volume. In immature, growing articular cartilage, there is evidence that a precursor cell exists that may aid in appositional growth.[47] As the evidence for the presence of cell types other than chondrocytes in articular cartilage is limited, the remaining discussion will pertain only to mature, differentiated chondrocytes. These cells have limited capacity for replication and migration within the tissue, and they secrete ECM molecules such as collagen II and aggrecan.[19,48] While matrix production is sufficient for tissue maintenance from normal activities and ECM turnover, there is a limited increase in matrix synthesis in response to injury or inflammation, as occurs in osteoarthritis.[20] The factors that control chondrocyte proliferation, migration, and matrix synthesis are of great interest for regenerative therapies, including *in vitro* tissue engineering strategies.



There are few sites in the body available for articular chondrocyte harvest, making the use of primary cells in a tissue engineering strategy difficult.[49] Expansion of these cells is possible, but many studies have shown that the expanded cells lose their phenotype with each passage.[38,50,51] Compounding this issue is the fact that chondrocytes seem to lose their main functions, and thus effectiveness, over time. For example, it is well accepted that the matrix produced by older chondrocytes is different compared to that produced by younger cells.[52,53] Another age-related change in chondrocytes includes senescence, which would affect their ability to proliferate, synthesize matrix, and respond to normal physiological cues.[54–56] This loss of efficacy is true for many systems in the body. For articular cartilage cell-based therapies, this is especially problematic since the afflicted population is characteristically older. Beyond age-related changes, there are many biochemical and biomechanical factors that affect the functions of articular chondrocytes. Growth factors, ion concentrations, and nutrient supplies all dictate the metabolism of these cells. Understanding the influences of each has been the subject of intense study due to their potential for regenerative therapies. Biomechanical factors have been shown to have a profound influence on chondrocytes, causing changes in gene transcription and metabolism.[57–59] This phenomenon of mechanotransduction has been studied in a number of different manners, which will be examined further in subsequent sections.



Pertaining strictly to the chondrocyte's biomechanical experience, a growing body of work is demonstrating that understanding the phenomenon of mechanotransduction begins at the single cell level. A theoretical model of articular cartilage demonstrated that to obtain a full picture of how mechanical forces acted on cartilage, it was necessary to quantify the local stress and strain fields around chondrocytes.[60] This study, along with several other theoretical studies, has

demonstrated that the mechanical environment around the cell is nonuniform and dependent on the intrinsic material properties of the cells and their pericellular matrix. Thus, there was an impetus to measure these properties, which required the development of methods to mechanically test samples at the single cell level. Several methods had been developed at that point — and others have since been developed — to study cellular mechanics, including cytodetachment,[61,62] cytoindentation,[63,64] cytocompression,[65–67] micropipette aspiration,[68–72] magnetic bead rheometry,[73] laser tweezers,[74] and atomic force microscopy.[75] Each of these methods has contributed significantly to the study of single cell mechanics, but only cytodetachment, cytoindentation, cytocompression, and micropipette aspiration have been used to study single chondrocyte biomechanics.

While cytodetachment has been used to characterize the adhesion of chondrocytes,[61,62] cytoindentation,[63,64] cytocompression,[65–67] and micropipette aspiration[69,72] have been used to obtain the mechanical properties of single chondrocytes. This work has revealed that the chondrocyte experiences stresses and strains that are vastly different than those of the surrounding ECM. Particularly, these cells have a stiffness modulus that is about three orders of magnitude less than the bulk tissue.[63–66,69,72] The chondrocyte also appears to change its mechanical properties with osteoarthritis.[69,72] Just as the stress–strain environment changes between zones of cartilage due to changes in the zonal mechanical properties, the local stress–strain field of each chondrocyte differs from the surrounding tissue. These single cell studies have demonstrated that obtaining a full picture of how mechanical forces are transmitted from the tissue down to the cell in both health and disease will require understanding the mechanical nature of single chondrocytes. These techniques can also be used to study chondrocyte mechanobiology, as will be described in Sec. 4.



#### 2.1.4. *Chondrons*



Each chondrocyte is surrounded by a pericellular matrix (PCM), with the combined structure of cell and PCM making the functional unit of cartilage called the chondron.[76] The PCM has been studied for years, and significant progress has been made to understand its roles. In particular, it was shown that the PCM regulates the osmolarity of the cell[77] and organizes and constructs collagen fibrils.[78] Considering the PCM's role in organizing collagen fibrils, its possible role in tissue engineering efforts has been analyzed, demonstrating cells that retain their native PCM produce more ECM and create stiffer engineered constructs.[79] Structurally, the chondron has been shown to contain collagens II, VI, and IX, the aggrecan components chondroitin 4-sulfate, chondroitin 6-sulphate, keratin sulphate, core protein, and hyaluronan binding region, and the glycoprotein fibronectin.[80–84]

Biomechanically, it was hypothesized that the PCM acted as a buffer of mechanical stress, with recent studies of the single chondron supporting this idea.[85,86] In particular, it was shown that the PCM stiffness was significantly higher

than that of the chondrocyte but generally lower than the surrounding extracellular matrix (ECM). This finding suggested that the PCM plays an important role in modulating the local stress–strain environment of the cell.[85,86] More recently, confocal analysis of the chondron by collagen VI fluorescence immunolabeling has demonstrated zonal variations in chondron shape and orientation, consistent with the previous observations of zonal chondrocyte shapes. The structural changes in chondrons with depth in articular cartilage appear to reflect the collagen architecture in each zone.[87] Considering the role of the PCM in modulating the biomechanical environment of the chondrocyte as well as coordinating cell–matrix interactions, understanding the morphology, biochemical content, and biomechanical properties of the chondron will be important in understanding articular cartilage mechanobiology. This may be especially true in elucidating the role of biomechanics in the pathogenesis of osteoarthritis. Several investigations have described changes in the PCM in disease, including an increase in size,[88] an increased proteoglycan concentration,[89] and the disruption of collagen fibrils.[84,90,91] These changes result in a softer PCM, which may indicate that its biomechanical function is compromised in the disease.[85,86]



## 2.2. *Biomechanical physiology of articular cartilage*

The preceding discussion has revolved around the biomechanical structure and functions of articular cartilage. In analyzing how these aspects are intertwined, it is clear that biomechanical forces play a central role in defining the tissue. In the following discussion, the role of biomechanical forces on the development, maintenance, and disease of articular cartilage will be scrutinized. These biomechanical studies have been fruitful areas of research, inspiring promising tissue engineering strategies that utilize the beneficial effects of mechanical stimulation to produce more robust engineered tissue. Similarly, these studies have shed light on biomechanical etiologies of cartilage diseases, such as osteoarthritis.



### 2.2.1. *Biomechanical development*

The formation of cartilage, or chondrogenesis, is a complex event that can be described in four stages: (1) progenitor cell migration to the site of chondrogenesis, (2) epithelial–mesenchymal interactions, resulting in (3) condensation formation, and (4) overt differentiation of chondroblasts. Condensation formation is a critical stage of mesenchymal development where a previously dispersed cell population gathers to differentiate into a particular mesenchymal tissue, such as cartilage, bone, or muscle. During this time, the shape, size, position, and number of skeletal elements are established.[92] Toward articular cartilage formation, active cell movement results in an increase in the number of cells per unit volume, and both *in vivo* and *in vitro* work suggests that there is a high cell density requirement for chondrogenesis to occur.[93] The major molecular events during

these stages of chondrogenesis and skeletogenesis, in general, have been well characterized, though it is still not clear what triggers the final transition to overt differentiation.[94]

These developmental processes occur as a series of events that begin during fetal life and extend until skeletal maturation occurs. Toward the later stages of fetal development, the shafts of the long bones have ossified, though the bone ends, which are the sites of bone growth and articulation, are still cartilaginous. For humans, bone growth occurs at secondary ossification centers within the cartilaginous epiphysis present in most long bones. At these ossific nuclei, the growth plate cartilage and articular cartilage are progressively defined over time.[41]

The multitude of factors and agents acting on cartilage results in a dynamic tissue that changes over the course of a lifetime. Throughout these developmental stages, biochemical factors and biomechanical forces are working to direct the differentiation of progenitor cells and stem cells, as well as helping to shape the geometry of the tissue.[95] As articular cartilage matures under these influences, the morphological, biochemical, and biomechanical properties of the tissue are defined. Marked changes have been observed in equine articular cartilage within a short period of time after birth. From birth to 5 months of age, cartilage changed from uniformity to heterogeneity in terms of biochemical and biomechanical parameters, likely as a functional adaptation to weight bearing.[96,97] In fact, different levels of exercise resulted in differences in biochemical parameters, with heterogeneity (and hence maturity) of cartilage being delayed in those deprived of exercise.[98]

The zonal architecture is a result of the developmental history and biomechanical milieu of the tissue.[41] The distinguishing characteristics of the different zones can be understood in terms of the local biomechanical environment of each. In the superficial zone, cells are subjected to fluid flow, hydrostatic pressure, and compression, giving them a flattened shape and requiring that they maintain a higher proportion of collagen relative to proteoglycans. In the middle and deep zones, the primary loading is hydrostatic pressure with little strain or fluid flow.[41] As a result, the cells in these regions are rounded and synthesize high amounts of GAGs and collagen II, as previously described (Sec. 2.1.2). The effects of growth factors, cell–matrix interactions, cellular signaling, and nutrients, among other factors, play significant roles in the development and maintenance of the tissue as well.[57,92,99]

While these patterns can be generalized for articular cartilage of any joint, it is important to note that different joints can experience markedly different biomechanical environments. One way to assess these differences is by mechanically testing articular cartilage to derive intrinsic biomechanical properties of the tissue. This has been demonstrated by experiments in the ankle,[100] hip,[101] knee,[102] and first metatarsophalangeal joints,[103] where the anatomical location of the articular cartilage resulted in different biomechanical properties. Even within a joint,

high- and low-weight bearing areas exist, and this results in different biomechanical properties.[100–103]

### 2.2.2. *Biomechanical regulation*

Beyond the goal of understanding the fundamental processes involved in mechanotransduction, studying native articular cartilage responses to mechanical stimuli can have utility for cartilage tissue engineering. With a grasp of native responses, researchers have been guided to enhance engineered constructs, with the goal of making them suitable for possible cartilage therapies. Particularly, these native tissue studies have demonstrated that cartilage has certain physiological thresholds within which it can adapt functionally.

While these thresholds remain poorly defined, it is clear that articular cartilage can withstand a wide range of stress magnitudes. Contact pressures in the hip and patellofemoral joints have been measured between 3 to 18 MPa.[104–106] The predominant stresses experienced by the tissue include, compression, hydrostatic pressure, fluid shear, and tension (Fig. 3). Understanding how mechanical forces influence native cartilage began with animal experiments where the effects of joint loading were studied. These studies demonstrated that the tissue's morphology, biochemistry, and biomechanics altered in response to a change in joint loading. The nature of the response depended on whether the load was increased or decreased as well as the degree of change. In several animal models, including dogs, rabbits, and horses, "physiological" exercise caused changes in articular cartilage thickness, proteoglycan content, and mechanical stiffness.[107–111] A measurable change in the overall tissue mass as a functional adaptation to exercise does not appear to occur in humans, though some efforts suggest that GAG content may increase with exercise.[112]

In contrast to normal exercise, "strenuous" exercise was shown to result in gross cartilage lesions due to alterations in the collagen network.[113] A severe decrease in joint loading such as immobilization led to healthy tissue thinning and softening.[114–116] Interestingly, there appears to be a level of tissue recovery that can be achieved, if the joint is mobilized back into the physiological range.[117–119] The most widely studied methods of altering joint biomechanics include ligament transection and meniscectomy. These methods have proved particularly useful in studying the progression of joint degeneration and are well accepted as experimental models of osteoarthritis.

The use of ligament transection as a model of osteoarthritis was partly based on the idea that biomechanical forces play a crucial role in the initiation and progression of osteoarthritis.[120,121] In fact, clinical evidence demonstrates that human knee degeneration occurs when joint instability follows cruciate ligament rupture.[122] Osteoarthritis has been characterized in a number of ways, with changes demonstrated in the structure, composition, and cells of articular cartilage and surrounding tissues. The sequence of events that lead to the observed

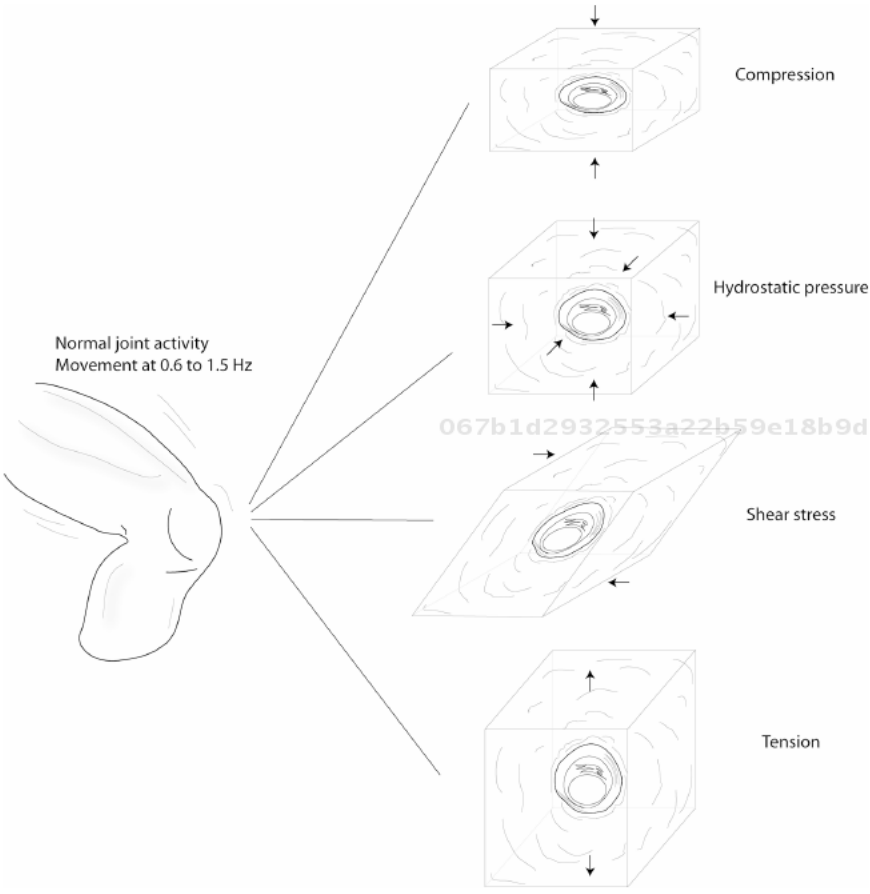


Fig. 3. The predimonant stresses in articular cartilage can be described in terms of compression, hydrostatic pressure, shear, and tension. These biomechanical factors play a role in tissue development, remodeling, and regulation. Bioreactors have been designed to apply such stresses to articular cartilage explants and tissue-engineered cartilage, in order to isolate and understand the differential effects of each of these stresses. Normal physiological limits, such as human cadence (0.6 to 1.5 Hz), have helped to direct these studies, since a number of design variables can be manipulated (Sec. 4.3.2).

changes is still unclear, however. In particular, it is not known whether the biomechanical changes in the tissue precede or are the result of the disease. Ligament transection and meniscectomy have been demonstrated to exhibit osteoarthritic changes in many animal models, and are performed to help elucidate these open questions.

These *in vivo* studies inspired *in vitro* work on cartilage explants, tissue-engineered constructs, and individual chondrocytes with the major goals of isolating the negative and positive effects of the predominant forces experienced in the tissue and enhancing tissue-engineered cartilage. These studies will be examined in more detail in Sec. 4.3.2.

## 3. Future Directions for Native Biomechanical Structure–Function Investigations

The work on native articular cartilage has helped guide the engineering of the tissue *in vitro*. One important contribution of this basic work is the understanding that while biomechanical forces dictate many normal processes of articular cartilage, they can also lead to its detriment. As this structure–function work progresses in conjunction with engineering efforts, it will be important to elucidate the specific control mechanisms that push native and engineered cartilage to synthetic or degenerative states. Additionally, understanding the remodeling of the tissue may be important in developing ways to control these processes through bioreactors or bioprocesses. Finally, a better characterization of the tissue biomechanics (i.e., failure and sub-failure properties) will help establish better design parameters for the engineering of the tissue.[123]



## 4. Tissue Engineering of Articular Cartilage

This review has covered some key areas involved in articular cartilage research. In any tissue-engineering endeavor, it is important to identify specific design criteria for functional replacement of diseased tissue. Therefore, articular cartilage tissue engineering has focused heavily on understanding structure–function relationships in the native tissue, such as tissue composition and architecture, as well as its normal developmental processes and physiology, particularly as these bioprocesses relate to biomechanical influences. The previous sections discussed evidence that biomechanical forces strongly dictate the morphogenesis, health, and disease of articular cartilage. This understanding of the tissue's structure–function relationships and physiology has been critical to the development of innovative tissue-engineering strategies.



In this section, the state-of-the-art in articular cartilage regeneration efforts will be presented and synthesized with the major points of the previous topics. The major aims are to identify challenges for this field of research and propose possible solutions. This section will be divided into research areas related to articular cartilage tissue engineering. The possible building materials for neocartilage will be presented, focusing on biomaterials and cell sources for articular cartilage. Also, the use of exogenous stimuli, such as growth factors and bioreactors, will be examined for their potential to enhance regeneration efforts. First and foremost, however, we will evaluate the field as a whole, especially pertaining to the establishment of standard success criteria for articular cartilage tissue-engineering endeavors.

### 4.1. *Standards for tissue engineering studies*

The field of articular cartilage tissue engineering is progressing toward a long-term treatment for articular cartilage diseases. While many researchers share the same

goal, they approach the problem using a wide array of methods. The areas of biomaterials, stem cells, bioactive agents, and mechanical stimulation are fueling innovation and making the ultimate goal tenable. The field, as a whole, is a fertile ground for research. As it grows and matures, however, the need for standardization is becoming readily apparent.

To demonstrate, a sample of cartilage tissue-engineering studies was randomly selected from a Pubmed search to analyze how engineered constructs were evaluated, dating from 1992 to 2006 (Table 1). For this analysis, only studies that used mature native articular chondrocytes were included, since any stem cell, fibrochondrocyte, or purely computational study would likely skew the results. Functional assays were categorized into one of seven general groups: morphology, histology, gene expression, biochemistry, biomechanics, metabolism, and *in vivo* implantation. Simple tabulation of the assays in this way revealed a wide disparity in assessment practices. Morphology at any scale (gross pictures, light microscopy, SEM, etc.) was described in 65% of the studies. A large number (85%) provided histological analysis. Biochemical content was quantified in 68% of the sampled studies, while less than 24% assessed construct biomechanics. Gene expression (26%), metabolic assays (11%), and *in vivo* testing of constructs (10%) were also used infrequently. While this survey of tissue-engineering studies has limitations, it shows that the



Table 1. Various types of assessments used in articular cartilage tissue-engineering.

| | |
|---|---|
| Morphology | $65\% \pm 9.9\%$ |
| Histology | $85\% \pm 7.4\%$ |
| Gene expression | $26\% \pm 9.2\%$ |
| Biochemistry | $68\% \pm 9.7\%$ |
| Biomechanics | $24\% \pm 8.9\%$ |
| Metabolism | $11\% \pm 6.6\%$ |
| *In vivo* testing | $10\% \pm 6.3\%$ |



Generally, these can be categorized as morphological, histological, genetic expression, biochemical, biomechanical, metabolic, or *in vivo* testing. Morphological assessments include gross pictures and measurements (i.e., thickness, width), SEM pictures, and use of other microscopy. Histology includes both standard stains (i.e., Alcian blue, picrosirius red) and immunohistochemistry. Gene expression could be either qualitative or quantitative. Biochemistry encompasses assays such as picogreen, DMMB, hydroxyproline, and ELISAs for specific collagens. Biomechanics includes any biomechanical test (i.e., tensile, compressive, indentation, etc.). Metabolic tests are primarily the radiolabeling assays for $^{3}H$ and $^{35}S$ incorporation. Finally, *in vivo* testing would involve engineering tissue *in vitro*, then implanting and assessing tissue performance in one of the previously mentioned ways. A Pubmed search was conducted for all articular cartilage tissue-engineering studies performed from 1992 to 2006. After eliminating studies that did not use native articular chondrocytes for *in vitro* engineering (i.e., any stem cell, computational, or fibrocartilage-related study), a total of 428 primary manuscripts were found, of which 88 randomly selected studies were analyzed by tabulating how constructs were assessed. In doing so, quantitative measures (95% confidence intervals) were obtained concerning how successful engineering of articular cartilage has been defined. Results indicate that biomechanical evaluations of constructs, which are arguably the most useful functional data for *in vitro* studies, are used much less than qualitative data, such as morphology and histology. Defining successful engineering in a consistent manner is a major challenge that the field must address.

field has no consensus regarding how to characterize cartilage constructs (one would expect the percentages to approach 100%, if consensus existed for a particular type of assessment).

This lack of standardization in the field makes it difficult to compare results across studies. In addition to comparing different types of data (histology versus gene expression, for example), researchers may be comparing different animal species and joints, which can have a profound impact on results. The results of the survey also reveal that definitions of successful cartilage tissue engineering are not always consistent with the native structure and function of articular cartilage. The survey suggests a tendency in the field to concentrate on qualitative information (morphology and histology) and protein production by cells (biochemistry), while largely ignoring the biomechanical function and *in vivo* performance of the constructs. In essence, the seven groupings of assays represent a functional spectrum for engineered cartilage, with the qualitative data complementing the quantitative data. Within each general grouping of assays, it is apparent that another degree of variability in the field exists. For example, there are a number of ways to characterize the biomechanics of constructs, including compressive, tensile, and shear properties. Also, there are a number of ways to evaluate the presence of specific cartilage markers. The point is that the tools available for a specific genre of assays require standardization, just as the field needs to standardize which genres to use in defining successful engineering. These different levels of uniformity need to be adopted eventually, but it is more realistic, and perhaps more pressing, that the field adopt a consistent and sufficiently general definition of success to accommodate the variability within each group of assays.



Achieving this level of order will logically depend on the functional information that a group of assays provides. Concerning functionality, long-term evaluation *in vivo* is the best indicator of successful regeneration, but this is not always feasible. For strategies that are not ready for *in vivo* evaluation, the biomechanical properties of the construct are arguably the best means of demonstrating functionality. Again, there are various manners to evaluate the biomechanics of a construct, and a major question for the field will be how to prioritize the various mechanical properties of the tissue.[123] Among these include the compressive, tensile, shear, and frictional properties. Characterizing all of these properties would be very difficult to set as a standard, which is why ranking these properties will be of utmost importance. The key consideration in doing so must be the functional replacement of articular cartilage. Given the closely intertwined form and function of the tissue, the best complement of assays for *in vitro* work is one that allows analysis of the biomechanics of engineered constructs in terms of biochemical content, morphological assessment, and histological structure. Although an exact replication of native articular cartilage may not be possible, functional replacement may be achieved if an understanding of native tissue is fully utilized to guide the design and engineering of *in vitro* generated cartilage. A standardized definition of successful articular cartilage tissue engineering will greatly facilitate these efforts.

## 4.2. *Building blocks for engineering articular cartilage*

### 4.2.1. *Biomaterials*

Beyond defining criteria for successful articular cartilage tissue engineering, the field faces key questions regarding the basic components of a regeneration strategy. One of these key questions is what biomaterial to use. Subsequent to this question is how to use the biomaterial to promote or direct regeneration. There are many studies that have demonstrated the use of biomaterials as scaffoldings or cell carriers for chondrocytes and various other cell sources with chondrogenic potential to produce articular cartilage matrix. More recently, biomaterials like agarose have been used as moldings to direct tissue formation. A number of different variables can be taken into account when analyzing the data for the following discussion. These include the animal model, joint location of cells, age of the animal, and the media components, among many others. Although these are important considerations, they will not be emphasized here, as the discussion is aimed at demonstrating general trends in the field and major principles by using select examples.

Among the most intensely studied biomaterials include substances such as collagen,[124–126] fibrin,[127–129] hyaluronic acid,[130] chitosan,[131] and agarose.[132,133] Synthetic polymers that have received a great amount of attention due to their approval for clinical use in the United States include poly(lactic acid) (PLA), poly(glycolic acid) (PGA), and their copolymers poly(lactic-co-glycolic acid) (PLGA).[134–145] Each substance has distinct characteristics that researchers have sought to take advantage of in their engineering schemes. Generally speaking, some of the most important characteristics for a biomaterial include the biocompatibility/toxicity of the material and its degradation products, the kinetics of the biomaterial's degradation, and the ability of chondrocytes or chondrogenic cells to attach to the substrate and maintain their phenotype. In each of these respects, the aforementioned biomaterials demonstrate a spectrum of properties. A number of strategies have been employed to modify each characteristic so that the properties of the biomaterial can be optimized for articular cartilage regeneration. Among these strategies are crosslinking the polymers to alter degradation profiles and scaffold properties,[146] modifying the material with adhesive peptides,[147] and incorporating growth factors to stimulate cellular proliferation and synthesis of ECM molecules.[148] Another popular strategy involves the combination of biomaterials to make hybrid structures.[149,150] The basic premise of hybrid biomaterials is that the advantages of the individual components can be harnessed. These hybrids take many forms, using many different combinations of biomaterials. For example, recent advances in biomaterials research have aimed at engineering a zonal architecture by varying material properties and architecture of the scaffold.[151]

These biomaterial studies and strategies represent a vast body of work with one common denominator: using the biomaterial as a scaffold or cell carrier. While some of these studies have shown certain degrees of efficacy, many have encountered various drawbacks. These include contraction of the construct, excessive cellular

stresses (possibly leading to inflammatory responses) due to crosslinking processes or toxic degradation products, loss of the chondrocytic phenotype, inhibition of cell migration, lack of cell to cell communications, stress shielding of cells from mechanical stimuli, obstruction of cell growth, and prevention of ECM remodeling. Many of the biomaterial modifications previously mentioned were designed specifically to address some of these issues, but a robust engineered tissue has remained elusive using these approaches.

While the promise of tissue engineering through the use of biomaterials as scaffolds or cell carriers has not been completely fulfilled, many valuable lessons have been learned. For example, various biomaterials have demonstrated their ability to maintain the chondrocytic phenotype. Though it does not form strong adhesive interactions with chondrocytes, agarose has been shown to encourage the retention of the characteristic spherical shape of chondrocytes and hence their definitive ECM production.[133] Also, studies of articular chondrocytes seeded onto biomaterials consistently demonstrated that a high density of cells resulted in better ECM production and hence mechanical properties.[152] This result was echoed by studies using aggregate culture.[153,154] and pellet culture.[79] In each of these strategies, chondrocytes are in direct contact with each other upon initial seeding and appear to receive the necessary cues to produce articular cartilage matrix components.



Considering these results, a recently developed scaffoldless approach, termed self-assembly, harnessed a high-density culture of primary chondrocytes to produce articular cartilage constructs with morphological, biochemical, and biomechanical properties approaching native tissue values after 12 weeks of culture.[155] A relatively simple, but pivotal innovation in this strategy was the use of agarose as a mold, rather than a cell carrier or scaffold. One of the considerations in using agarose in this manner was that chondrocytes do not adhere to the agarose and retain their characteristic shape and phenotype. Thus, creating a cylindrical well coated with agarose and allowing primary chondrocytes to sediment inside the well established a high-density culture that encouraged cell-to-cell contacts and communication and articular cartilage protein production.



The advantages of this approach over traditional scaffold-based approaches pertain mainly to the disadvantages of the methods mentioned previously. Since agarose is a hydrogel without toxicity to chondrocytes and no scaffold is utilized, there is no concern about degradation products, stress shielding from mechanical stimuli, contraction or loss of construct shape. The constructs produced in this manner demonstrate ECM remodeling and appear to follow a maturation path similar to native articular cartilage.[155] On a wet weight basis, the collagen content of self-assembled constructs showed similar results to PGA cultures (~1.5% ww), though they were lower compared to the constructs cultured within agarose. It is likely that specific media containing chondrogenic agents, such as ascorbic acid, dexamethasone, and growth factors like TGF-$\beta$3, can increase the ECM content of self-assembled constructs. Another exciting prospect for this scaffoldless approach

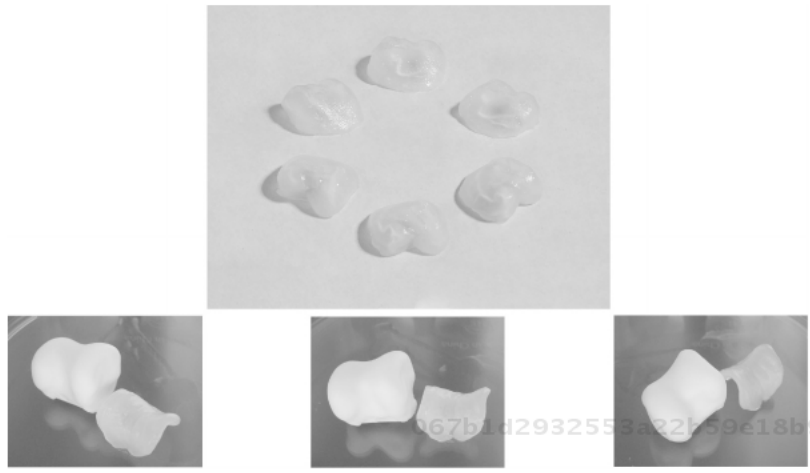

Fig. 4. Self-assembly of articular chondrocytes is a scalable and moldable process, meaning that the process can control the size, shape, and anisotropic biomechanical properties of engineered cartilage. These constructs were made using primary bovine chondrocytes and positive and negative molds of a rabbit femur.

is the ability to control the shape of the cartilage produced (Fig. 4). Thus, tissue engineers can conceive replacing more than just focal defects.

While the field of articular cartilage tissue engineering has seen major advances recently, it remains to be seen whether the strategies of self-assembly, scaffold-based, or cell carrier approaches can produce viable tissue-engineered products for clinical use. Several challenges need to be addressed. One particularly vexing problem is the issue of a cell source. The major drawback to both scaffoldless and scaffold-based strategies is that many cells are required to produce the constructs. Initially, sub-culturing procedures were used to expand chondrocytes to fulfill the cellular requirements of these strategies. As previously mentioned in Sec. 2.1.3, monolayer culture of these cells results in a loss of phenotype. Efforts to rescue this phenotype after expansion may hold some promise.[156–158] Another strategy involves the use of precursor and stem cells. These cells have been investigated for their chondrogenic potential and have gained popularity in all aspects of tissue engineering. The plethora of sources for these cells and their chondrogenic potential will be analyzed next.

### 4.2.2. *Cell source*

The use of primary native chondrocytes for an *in vitro* tissue-engineering strategy is not currently a practical solution for patient therapies.[49] There are simply too few chondrocytes in the body (donor tissue scarcity) that can be reasonably harvested to support the generation of tissue constructs for effective treatment of clinically relevant articular cartilage pathology. Although expansion of these cells is possible, the expanded cells lose their phenotype with each passage.[38,50,51] Stem cells and

other adult cell sources, such as dermis cells with chondrogenic potential,[159] have emerged as a possible solution. Particularly attractive in using these cells is the characteristic that they can be expanded *in vitro* to the desired number of cells and subsequently differentiated to express a particular phenotype. Stem cells can be found in many parts of the body and at many stages of development. Pertaining to cartilage, a vast amount of work has focused on mesenchymal stem cells (MSCs), adult stem cells that can be found in the bone marrow. Other stem cells have also been investigated for their chondrogenic potential, such as adipose derived stem cells,[160] embryonic stem (ES) cells,[161–166] embryonic germ cells,[167] progenitor cells from the placenta,[168] and umbilical cord blood stem cells.[169]

When considering which class of stem cells to use for therapeutic applications, it is important to understand their basic differences. The first major difference is the differentiation capacity of each. Embryonic stem cells are termed pluripotent, as they hold the ability to become any of the three germ layers. This has been demonstrated with each of the NIH-approved human embryonic stem cell (hESC) lines, such as H9[170] and BG01V.[171,172] Efforts into the directed differentiation of each of these cell lines into cells or tissues with therapeutic potential have been pursued for musculoskeletal.[173] and neural tissues,[172] among others. The pluripotency of these stem cells largely embodies the excitement and danger of using these cells as a therapy. While they can theoretically differentiate into any cell in the body, they can also form tumors called teratomas. Other stem cells, such as MSCs, adipose-derived stem cells, embryonic germ cells, and umbilical cord blood stem cells do not form tumors, but also do not have the differentiation potential of ES cells. Each of these classes of stem cells has been shown to have the capacity to differentiate into cells that produce cartilaginous matrix.[160,167,169] In contrast to other stem cells, it appears that ES cells are immortal, meaning that they theoretically can be expanded without losing phenotype. However, the culture of hESCs remains an issue because of the use of feeder layers, such as mouse embryonic fibroblasts (MEFs). These feeders or media conditioned by the feeder cells have been generally used for the culture of hESCs in an undifferentiated state. This co-culture system involving human and animal cells presents practical problems for future therapies since animal products or pathogens can be transmitted. Efforts are underway to address this,[174–177] although no alternative to MEFs has been adopted universally. As indicated in their nomenclature, the source of the stem cells is also a major difference, and the successful isolation of each type of stem cell varies. For example, MSCs constitute a low proportion of bone marrow stromal cells and may contain genetic abnormalities, caused by exposure to metabolic toxins and errors in DNA replication accumulated during the course of the lifetime.[49] ES cells, on the other hand, have been shown to be relatively homogenous and genetically stable in culture.

Regarding the chondrogenic differentiation of stem cells, most information gathered centers around MSCs. In addition to cartilage, these are the progenitors of multiple other lineages, including bone, muscle, and fat. The multipotent properties

of MSCs have been elegantly exploited in the design of composite structures such as the articular condyle.[178–180] There have been many different strategies to induce chondrogenic differentiation. One of the most common is the use of differentiation factors, such as TGF-$\beta$1, BMP-2, and IGF-I.[181–184] These factors have been applied directly, in the form of soluble agents added to growth media, or cells have been modified to produce the factors. For example, genetic manipulation has been used to induce MSCs to produce growth factors.[182] Another strategy that involves genetic manipulation is a modification of cells to express key signaling and transcription factors of cartilage.[185,186] Despite this progress, it remains to be seen whether pursuits with MSCs will demonstrate the generation of tissue that has the biomechanical wherewithal of native cartilage, or that MSC-derived cartilage can provide long-term solutions to cartilage pathology.[187]

The evidence remains scarce regarding the use of ES cells for cartilage tissue engineering strategies. Much of the evidence supporting the use of ES cells for cartilage tissue engineering comes from work with mouse ES cells.[188] The chondrogenic differentiation of these cells has been demonstrated *in vitro* using BMP-2 (2 ng/ml; 10 ng/ml), and BMP-4 (10 ng/ml).[164] Their phenotypic stability in a differentiated state has also been investigated.[164,166] Others have also been able to differentiate ES cells into a chondrogenic lineage with the use of special culture conditions with growth factors,[161,163] without growth factors,[165] and in co-culture with limb bud progenitor cells.[162] Hwang and associates[189] have investigated the use of hydrogels with mouse ES cells that were chondrogenically differentiated with TGF-$\beta$1 or BMP-2. Recently, hESCs were differentiated into mesenchymal precursors, which could be subsequently chondrogenically differentiated with TGF-$\beta$3 (10 ng/ml).[173] Nakayama and associates[161] have also induced a mesodermal lineage from mouse ES cells. They used TGF-$\beta$3 (10 ng/ml) and formed hyaline-like cartilage in pellet culture. This study was particularly notable since the differentiation was performed in serum-free conditions. The musculoskeletal differentiation of human embryonic germ cells has also been achieved with a chemically defined chondrogenic differentiation medium with 1% serum and with one of two differentiation factors, BMP-2 and TGF-$\beta$3.[167]

In critically analyzing the use of stem cells for cartilage tissue-engineering therapies, the issue of animal products or cells is an important consideration. For clinical applications of stem cells, it is important that protocols exclude the use of animal or human products, like MEFs or serum, that may carry pathogens or potentially increase the antigenicity of the transplanted cells.[49] This problem has been recognized for some time and attempts to eliminate the use of murine feeder cells in the media are underway.[174–177] The introduction of serum for *in vitro* applications also increases the variability of components in the culture media. However, culturing stem cells under serum-free conditions may result in a lower mitotic index for cells, apoptosis, and poor adhesion.[190,191] Additionally, there are many interactions between individual growth factors and serum components that cannot be ignored. Due to the interrelated mechanisms of growth factor action,

in order to study the effect of differentiation factors, it may be necessary for serum (which includes several types of growth factors) to be present. Chondrogenic effects of individual growth factors were demonstrated with levels as high as 20% serum.[164,166] One has to be cognizant, however, that when serum is used, there is a risk of saturating the experiment with growth factors, yielding results that suggest the growth factor of interest has had no effect compared to controls. This limitation can be addressed by using a minimal amount of serum.[192]

Another major challenge in stem cell research is in defining success criteria for differentiation. Part of the problem in characterizing or defining differentiation is the fact that the pathways of differentiation are poorly understood. A better grasp of how differentiation occurs and what defines a particular cell lineage will be challenges for stem cell research, in general. Typically, cells can be identified by a distinct set of cell surface markers or the expression of key genes. These approaches have been applied to MSCs and ESCs alike. For *in vitro* and *in vivo* work with stem cells, investigations into their ability to chondrogenically differentiate is commonly defined as a process that results in cells with the ability to produce both collagen II and GAGs.[161,164,188,193] In pursuits related to articular cartilage, there is a growing recognition that the presence of collagen I is also an important consideration, as native tissue does not contain any of this protein.[194–196] However, the presence or absence of these proteins should not be the only end points of stem cell based tissue-engineering studies. The goal remains functional tissue replacement, which should entail the same set of standards that have been laid out previously regarding structure–function relationships.



### 4.3. *External stimuli*

Regardless of which biomaterial or cell source is used in a particular tissue-engineering strategy, many researchers have attempted to enhance engineered tissue through the use of exogenous stimuli, especially bioactive agents (i.e., growth factors) and mechanical stimulation. Considering the role of these factors in normal articular cartilage development and maintenance, it should not be surprising that their *in vitro* effects are potent, and, as some have shown, their combined effects are synergistic.

#### 4.3.1. *Bioactive agents*

In studying the effects of growth factors, several experimental variables can be considered. Among these variables include the concentration of the growth factor, the dosage frequency, the presence of serum, and the combination of growth factors. The multitude of experimental groups that these variables can generate is overwhelming. A generalized approach to tackling this problem has not emerged, and research has relied mainly on the knowledge of physiological levels of particular growth factors and their empirically studied effects.

There are numerous growth factors that have been studied for articular cartilage regeneration. In addition to controlling ECM synthesis, many of these growth factors play roles in the proliferation of precursor cells and differentiation of chondrocytes, as mentioned in the previous section. The transforming growth factor (TGF) family has received particular attention. At least 10 ng/ml TGF-$\beta$1 was shown to promote the synthesis of collagen II[197] and sulfated GAGs.[198–200] and to increase chondrocyte proliferation.[198,201] TGF-$\beta$1 was employed in a goat model to show that it can promote neocartilage formation.[142] TGF-$\beta$3 has high homology to TGF-$\beta$1, and produces similar effects on cells. However, it has been shown to have a different potency than TGF-$\beta$1.[202] Various concentrations and dosage regimens of TGF-$\beta$1, ranging from 100 ng/ml for 30 min to 10 ng/ml continuously, showed enhancement of cartilage formation.[203] Treatment of chondrocytes with TGF-$\beta$3 was shown to inhibit physeal chondrocyte hypertrophy,[204] as well as to stimulate cartilage-specific proteoglycan production.[205] It is believed that TGF-$\beta$3 may enhance cartilage formation.[206] through mechanisms such as induction of chondrogenesis in pre-chondrocytes and enhancement of chondrogenesis by chondrocytes.[207] Other isoforms of TGF have also been studied.[208,209] The TGF family also includes bone morphogenetic proteins (BMPs). BMP-2 at 100 ng/ml was shown to maintain the articular chondrocyte phenotype in long-term culture by way of mRNA expression for collagen II.[210] An *in vivo* study.[211] in murine knees found that BMP-2 (single dose of 200 ng) induced an earlier stimulation of proteoglycan synthesis than TGF-$\beta$1 (same single dose), but this lasted only 3–4 days, while the TGF-$\beta$1 effect lasted up to 21 days.

Some of the most promising results in articular cartilage regeneration have been seen when using IGF-I.[212] The interaction of TGF-$\beta$1 (1 ng/ml) and IGF-I (25 ng/ml) resulted in a synergistic effect, as shown by increased DNA synthesis of chondrocytes in monolayer and the expression of aggrecan mRNA.[213] Synergy was also seen when TGF-$\beta$1 (10 ng/ml) and IGF-I (300 ng/ml) were combined with dynamic loading, as demonstrated in biochemical and biomechanical properties.[214] One application of IGF-I (300 ng/ml) exhibited an additive effect when used in conjunction with direct compression, resulting in major increases in ECM synthesis in explants.[215] Another benefit of using IGF-I is the autoinductive autocrine/paracrine response that occurs *in vivo*.[216]

Other growth factors that have been studied include PDGF, HGF, and bFGF. PDGF has an effect on proliferation,[217,218] but its effects on synthesis and differentiation have not been recorded extensively. HGF is another growth factor that may promote cartilage and bone regeneration[219–221] bFGF has been shown to increase proliferation and synthesis in articular cartilage,[222–224] but primarily in fibrocartilages.[225–227]

In most of the studies mentioned above, continuous application of growth factors was employed. Recent studies have investigated intermittent dosing regimens of exogenous growth factors as a means to maintain phenotype and enhance ECM production.[228,229] Intermittent regimens, which include treatment once per week as

opposed to traditional continuous treatment, aided in phenotype maintenance as well as matrix production.

These data demonstrate the potential of these agents to modulate cellular activity. There are several challenges that these studies present. First, while the individual effects of growth factors may be apparent, there are complex interactions between different growth factors and serum components that are poorly understood. Explicating these interactions through basic science and engineering will significantly boost efforts to engineer articular cartilage. Apropos to understanding these mechanisms, the optimal conditions for growth factor application may be revealed. Particularly, it will be important to understand how frequently and at what concentration these growth factors should be applied. Finally, it will be of interest to expand the study of interactions between biochemical and biophysical stimuli, as performed with IGF-I already, to enhance *in vitro* generated articular cartilage. Similar to other pursuits related to articular cartilage, native tissue provides an excellent starting point to understanding these interactions.



#### 4.3.2. *Biophysical forces*

Toward functional replacement of articular cartilage, physical stimuli are increasingly receiving attention. As discussed in Sec. 2.2, these stimuli are responsible for modulating matrix synthesis by chondrocytes as well as matrix remodeling during development. Various bioreactor and instrument designs have emerged to apply specific types of loads at various scales *in vitro*. Tissue explants or tissue-engineered constructs have received most attention, being exposed to forces such as hydrostatic pressure, fluid shear, and direct compression. The effects of shear have also been studied using isolated cells of cartilage. Recently, a method has been developed to study the effects of direct compression on individual cells. Studies with these systems have yielded a wealth of information regarding the physical and biochemical responses of cartilage to these biomechanical conditions. Particularly, these studies have demonstrated that the responses of articular cartilage explants, engineered cartilage, or isolated chondrocytes depend on a number of variables, including the type of load applied, the magnitude of the load, and the load frequency.



Selecting loading regimens for articular cartilage tissue engineering has utilized observations of normal loading conditions. Normal adult cadence corresponds to 0.6 to 1.1 Hz loading per leg,[230] which can increase to >1.5 Hz during running.[231] The patellofemoral and hip joints can experience contact pressures between 3–18 MPa.[232–234] It is believed that physiological levels of deformation in femoral head articular cartilage range between 2%–10%.[235] Stresses and strains in these ranges have guided efforts with an assortment of bioreactors and experimental apparatuses to understand how native tissue and engineered tissue respond to mechanical stimuli.

Shear forces have been investigated by culturing cells in turbulent flow spinner flasks and laminar flow rotating bioreactors,[236] as well as a cone viscometer.[237] The basic design of the reactor involves a rotating piece that causes fluid flow. One of the simplest designs is the mechanically stirred bioreactor, which uses an impeller (spinner flask) or an orbital shaker to mix fluid and nutrients. While the fluid dynamics of these bioreactors have been characterized,[238–240] there are problems using these devices for tissue engineering, including nonuniform mass transfer rates, shear gradients, and biochemical gradients. The cone viscometer can overcome some of these limitations. It can achieve uniform shear distribution by using a cone that rotates above a flat surface. A cell monolayer seeded onto the surface can experience shear stresses from $10^{-3}$ to 10 Pa.[241] Stimulation in this manner caused the release of the pro-inflammatory mediator, nitric oxide, decreased aggrecan and collagen II gene expression, and caused changes associated with apoptosis.[58,59]



Direct perfusion bioreactors and low-shear, high diffusion bioreactors have demonstrated more positive results toward engineering articular cartilage. Direct perfusion causes medium to flow through cell-seeded scaffolds. Various designs have emerged, showing increases in ECM molecules, such as GAG and collagen II.[242,243] Common to these designs is a unidirectional bulk flow, resulting in nonuniform mechanical stress as well as an uneven distribution of nutrients and other biochemical factors. The low-shear rotating-wall bioreactor attempted to address this problem by using fluid flow and gravity to exert a low level of shear on cells.[244] The typical stresses applied with these systems have been calculated to be on the order of 0.1 Pa. This design demonstrated impressive results for bovine chondrocytes seeded onto PGA in terms of GAG and collagen II production.[245]

The configurations of hydrostatic pressure bioreactors are less diverse than bioreactors that apply shear forces. While some designs can handle batch processes,[246] others have been equipped to handle semicontinuous processes.[247] Typically, a piston causes small displacements of fluid within a pressure vessel, quickly increasing the hydrostatic pressure inside. With these apparatuses, the major experimental variables are the amount of pressure applied, the duration of load application, the duration of unloading, and the frequency. A physiological range (3–15 MPa) of hydrostatic pressure applied for just 20 s was shown to increase metabolic activity, unlike pressures above the physiological range.[248,249] Application of 5 MPa to either articular cartilage explants, or primary chondrocyte cultures at various frequencies (0.0167 to 0.5 Hz for explants, and 0.0082 and 0.0034 Hz for primary chondrocyte cultures) demonstrated that ECM interactions with chondrocytes are involved in regulation of proteoglycan synthesis and that the duration of loading influences metabolism, possibly due to the time necessary for pre- and post-translational effects to take place.[250] With monolayer cultures of articular chondrocytes, increases in mRNA expression for aggrecan and collagen II have been demonstrated using 10 MPa at 1 Hz for both 4 h and 4 days of stimulation, using constant or intermittent application.[246,251] Self-assembled constructs have also received similar loading regimens for a longer culture period

(8 weeks), demonstrating increases in collagen production and prevention of GAG loss.[252]

Direct compression has been studied in a similar fashion as hydrostatic pressure, where different loading regimens are examined. The typical control variable, in contrast to hydrostatic pressure experiments, is strain, not stress. Typical deformations of the femoral head cartilage usually range between 2%–10%.[253] Beneficial effects (i.e., higher GAG content or increased $^{35}S$ and $^{3}H$ incorporation) have been observed for strains of 1%–30% and frequencies of 0.5–2 Hz for 1–4 h per day.[254–257] In explants, an increase of 20%–40% for both $^{35}S$-sulfate and $^{3}H$-proline incorporation was shown at 0.01–1 Hz and ~1%–5% strain.[258] Possible synergy was observed for explant protein and proteoglycan synthesis when IGF-I was used in conjunction with direct compression.[57] These dynamic loading regimens have generally shown beneficial effects, whereas static loading of constructs has been shown to be detrimental, for the most part.[57,259,260] While many studies use explants to understand how direct compression affects chondrocyte synthesis, dynamic stimulation (10% strain, at 1 Hz intermittently for 4 weeks) has been utilized to improve the biomechanical properties of cell-seeded agarose disks, causing a six-fold increase in the equilibrium aggregate modulus over free swelling controls.[261]



It is also notable that many of the methods described here have been applied to various populations of stem cells, for several tissue systems. It will be of tremendous interest to use mechanical stimuli to enhance cartilage constructs, as has been performed with native chondrocyte systems. Additionally, the influence of mechanical forces on cartilage development (Sec. 2.2.1) may have important consequences for the tissue-engineering field. This topic has been reviewed in depth elsewhere, analyzing the effects of mechanical stimuli on stem cells using many loading regimens, including shear stress, hydrostatic pressure, and compressive stress.[262]



The studies summarized in this section so far have concentrated on the bulk effects of mechanical stimulation in native tissue, tissue constructs, or populations of cells. The characterization of stress and strain fields found in each of these stimulation modes has been investigated thoroughly. However, there are inevitably going to be local variations in stress and strains due to inhomogeneity in the system of study. This inspired a single cell approach to studying mechanical stimuli. These studies have also demonstrated that the quantitative gene expression response of chondrocytes may not follow a normal distribution, but rather a log normal distribution, suggesting that quantifying the gene expression of a population of cells may not be representative of the majority.[263] Additionally, differential effects on the gene expression profile of single chondrocytes have been shown with dynamic compression of single cells.[263] Studies of this nature may help direct tissue-engineering efforts by identifying biomechanical factors most critical to stimulating regenerative processes. Additionally, they may help elucidate biomechanical etiologies of osteoarthritis.

## 5. Future Directions for Articular Cartilage Tissue Engineering

There are many exciting avenues to explore in the realm of articular cartilage research. The elegant interplay between tissue structure and biomechanical function strongly influences the approaches of scientists and engineers in designing strategies for tissue regeneration. While this review has provided a wide overview of the field, there are still other issues that were not covered that are receiving a great deal of attention and will likely be the focus of future endeavors. Among these are immunological concerns. For any *in vitro* work, the possibility of an adverse immune response from the recipient must be a consideration, since this issue can dictate success or failure. Another concern for the strategies discussed here is the integration of tissue into the defect site. This is crucial for an engineered tissue product to serve its purpose. Articular cartilage is naturally an anti-adhesive surface partly due to the presence of GAGs, and technologies need to be developed to address this problem. While these issues are being addressed, researchers in the field must make a concerted effort to standardize definitions of successful articular cartilage regeneration, as discussed in Sec. 4.1. We propose a functional approach to this, combining quantitative biomechanical and biochemical evaluations with qualitative information such as morphological descriptions and histology. This approach to studying engineered constructs may not only facilitate understanding by a wider audience, but it may also reveal structure–function relationships in engineered tissue, leading to improvements in the technology.



Relating to the core strategies to engineering articular cartilage, a better fundamental understanding of the processes that control chondrocyte function will be of great benefit. It is becoming apparent that growth factors and biomechanical forces share certain molecular pathways, which may explain the observed synergistic effects that some have reported between these stimuli. Elucidating the effects of these same stimuli on the differentiation of stem cells will also be a major research thrust. Basic science approaches should be balanced with "engineering" approaches that empirically test the effects of these stimuli in these different systems. This combination of approaches can reveal a great deal of information to guide regeneration efforts. Strong collaborations between basic scientists and engineers will prove fruitful in this endeavor.



## 6. Conclusions

An *in vitro* articular cartilage tissue engineering strategy is an exciting prospect for regenerative medicine. There are many hurdles to overcome before these strategies can become successful therapies. The major theme that this review has attempted to convey is that the native tissue offers many lessons for functional replacement of diseased articular cartilage. Engineering principles and strategies have developed from these lessons, which occur at all levels of the tissue. Even with the advent of

new innovations, native articular cartilage will continue to serve as a benchmark and should be incorporated as an integral part of defining success for tissue-engineering endeavors.

## Acknowledgments

We gratefully acknowledge support from the NIH and an NSF IGERT traineeship for Eugene Koay. We would also like to thank Zaven Sargsyan for his help with the survey of tissue-engineering studies.

## References

1. J. P. Vacanti, M. A. Morse, W. M. Saltzman, A. J. Domb, A. Perez-Atayde and R. Langer, *J. Pediatr. Surg.* **23** (1988) 3–9.
2. R. Langer, L. G. Cima, J. A. Tamada and E. Wintermantel, *Biomaterials* **11** (1990) 738–745.
3. P. Bruckner and M. van der Rest, *Microsci. Res. Tech.* **28** (1994) 378–384.
4. D. Heinegard and A. Oldberg, *FASEBJ* **3** (1989) 2042–2051.
5. E. Hedbom and D. Heinegard, *J. Biol. Chem.* **268** (1993) 27307–27312.
6. J. E. Scott, *Biochemistry* **35** (1996) 8795–8799.
7. Y. Yamaguchi, D. M. Mann and E. Ruoslathi, *Nature* **346** (1990) 281–284.
8. M. van der Rest and R. Garrone, *FASEB J.* **5** (1991) 2814–2823.
9. E. M. Hasler, W. Herzog, J. Z. Wu, W. Muller and U. Wyss, *Crit. Rev. Biomed. Eng.* **27** (1999) 415–488.
10. D. R. Eyre, J. J. Wu and P. Woods, *Articular Cartilage and Osteoarthritis*, eds. K. Kuettner, R. Schleyrenbach, J. G. Peyron and V. Hascall (Raven Press, New York, 1992), pp. 119–131.
11. D. R. Eyre, I. R. Dickson and K. Van Ness, *Biochem. J.* **252** (1988) 495–500.
12. A. Maroudas, *Nature* **260** (1976) 808–809.
13. A. J. Fosang and T. E. Hardingham, *Extracellular Matrix*, ed. W. D. Comper (Harwood Academic Publishers, The Netherlands, 1996), pp. 200–229.
14. G. E. Kempson, *Adult Articular Cartilage*, ed. M. Freeman (Pitman Medical, London, 1979), pp. 333–414.
15. W. M. Lai, V. C. Mow and W. Zhu, *J. Biomech. Eng.* **115** (1993) 474–480.
16. A. Maroudas and G. Grushko, *Methods in Cartilage Research*, eds. A. Maroudas and K. Kuettner (Academic Press, San Diego, 1990), pp. 298–301.
17. M. A. Soltz and G. A. Ateshian, *J. Biomech.* **31** (1998) 927–934.
18. G. A. Ateshian, W. H. Warden, J. J. Kim, R. P. Grelsamer and V. C. Mow, *J. Biomech.* **30** (1997) 1157–1164.
19. C. W. Archer and P. Francis-West, *Int. J. Biochem. Cell Biol.* **35** (2003) 401–404.
20. T. Aigner and L. McKenna, *Cell. Mol. Life Sci.* **59** (2002) 5–18.
21. H. J. Mankin and L. Lippiello, *J. Bone. Joint Surg.* **52A** (1970) 424–434.
22. F. Guilak, A. Ratcliffe, N. Lane, M. P. Rosenwasser and V. C. Mow, *J. Orthop. Res.* **12** (1994) 474–484.
23. T. Aigner, W. Bertling, H. Stoss, G. Weseloh and K. von der Mark, *J. Clin. Invest.* **91** (1993) 829–837.
24. T. Aigner, Y. Zhu, H. Chanksi, F. A. Matsen, W. J. Maloney and L. J. Sandell, *Arthritis Rheum.* **42** (1999) 1443–1450.

25. D. M. Salter, *Br. J. Rheumatol.* **32** (1993) 780–786.
26. J. C. Hu and K. A. Athanasiou, *Functional Tissue Engineering*, eds. F. Guilak, D. L. Butler and D. Mooney (Springer Verlag, New York, 2003), pp. 227–243.
27. N. P. Comacho, P. West, P. A. Torzilli and R. Mendelsohn, *Biopolymers (Biospectroscopy)* **62** (2001) 1–8.
28. H. Muir, P. Bullough and A. Maroudas, *J. Bone Joint Surg. Br.* **50** (1970) 554–563.
29. J. A. Buckwalter and H. J. Mankin, *Instr. Course Lect.* **47** (1998) 477–486.
30. C. W. Archer, J. McDowell, M. T. Bayliss, M. D. Stephens and G. Bently, *J. Cell Sci.* **97** (1990) 361–370.
31. M. B. Aydelotte and K. E. Kuettner, *Conn. Tiss. Res.* **18** (1988) 205–222.
32. C. R. Flannery, C. E. Hughes, B. L. Schumacher, D. Tudor, M. B. Aydelotte, K. Kuettner and B. Caterson, *Biochem. Biophys. Res. Comm.* **254** (1999) 535–541.
33. R. Krishnan, M. Caligaris, R. L. Mauck, C. T. Hung, K. D. Costa and G. A. Ateshian, *Osteoarthritis Cartil.* **12** (2004) 947–955.
34. M. B. Aydelotte, R. R. Greenhill and K. E. Kuettner, *Conn. Tiss. Res.* **18** (1988) 223–234.
35. R. K. Jacoby and M. I. V. Jayson, *J. Rheumatol.* **2** (1975) 280–286.
36. G. H. V. Korver, R. J. Van de Stadt, G. P. J. Van Kampen and J. K. Van der Korst, *Matrix* **10** (1990) 394–401.
37. P. J. Marles, J. A. Hoyland, R. Parkinson and A. J. Freemont, *Int. J. Exp. Path.* **72** (1991) 171–182.
38. E. M. Darling and K. A. Athanasiou, *J. Orthop. Res.* **23** (2005) 425–432.
39. M. Wong, P. Wuethrich, P. Eggli and E. Hunziker, *J. Orthop. Res.* **14** (1996) 424–432.
40. R. K. Schenk, P. Eggli and E. Hunziker, *Articular Cartilage Biochemistry*, eds. K. Kuettner, R. Schleyer and V. Hascall (Raven Press, New York, 1986), pp. 3–22.
41. M. Wong and D. R. Carter, *Bone* **33** (2003) 1–13.
42. S. Tomkoria, R. V. Patel and J. J. Mao, *Med. Eng. Phys.* **26** (2004) 815–822.
43. R. M. Schinagl, D. Gurskis, A. C. Chen and R. L. Sah, *J. Orthop. Res.* **15** (1997) 499–506.
44. A. L. Clark, L. D. Barclay, J. R. Matyas and W. Herzog, *J. Biomech.* **36** (2003) 553–568.
45. R. A. Bank, M. Krikken, B. Beekman, R. Stoop, A. Maroudas, F. P. Lafeber and J. M. Tekoppele, *Matrix Biol.* **16** (1997) 233–243.
46. G. R. Dodge and A. R. Poole, *J. Clin. Invest.* **83** (1989) 647–661.
47. G. P. Douthwaite, J. C. Bishop, S. N. Redman, I. M. Khan, P. Rooney, D. Evans, L. Haughton, Z. Bayram, S. Boyer, B. Thomson, M. S. Wolfe and C. W. Archer, *J. Cell Sci.* **117** (2004) 889–897.
48. K. Kuettner, M. B. Aydelotte and E. J. Thonar, *J. Rheumatol. Suppl.* **27** (1991) 46–48.
49. B. C. Heng, T. Cao and E. H. Lee, *Stem Cells* **22** (2004) 1152–1167.
50. J. Glowacki, E. Trepman and J. Folkman, *Proc. Soc. Exp. Biol. Med.* **172** (1983) 93–98.
51. K. von der Mark, V. Gauss, H. von der Mark and P. Muller, *Nature* **267** (1977) 531–532.
52. T. Wells, M. Davidson, M. Morgelin, J. L. Bird, M. T. Bayliss and J. Dudhia, *Biochem. J.* **370** (2003) 69–79.
53. J. L. Carrington, *Biochem. Biophys. Res. Comm.* **328** (2005) 700–708.
54. A. Barbero, S. Grogan, D. Schafer, M. Heberer, P. Mainil-Varlet and I. Martin, *Osteoarthritis Cartil.* **12** (2004) 476–484.

55. N. Verzijl, J. DeGroot, S. R. Thorpe, R. A. Bank, J. N. Shaw, T. J. Lyons, J. W. Bijlsma, F. P. Lafeber, J. W. Baynes and J. M. Tekoppele, *J. Biol. Chem.* **275** (2000) 39027–39031.
56. J. A. Martin and J. A. Buckwalter, *J. Bone Joint Surg. Am.* **85-A** (2003) 106–110.
57. L. J. Bonassar, A. Grodzinsky, E. H. Frank, S. G. Davila, N. R. Bhaktav and S. B. Trippel, *J. Orthop. Res.* **19** (2001) 11–17.
58. R. L. Smith, D. R. Carter and D. J. Schurman, *Clin. Orthop. Relat. Res.* **427S** (2004) S89–S95.
59. R. L. Smith, B. S. Donlon, M. K. Gupta, M. Mohtai, P. Das, D. R. Carter, J. Cooke, G. Gibbons, N. Hutchinson and D. J. Schurman, *J. Orthop. Res.* **13** (1995) 824–831.
60. F. Guilak and V. C. Mow, *J. Biomech.* **33** (2000) 1663–1673.
61. K. A. Athanasiou, B. S. Thoma, D. R. Lanctot, D. Shin, C. M. Agrawal and R. G. LeBaron, *Biomaterials* **20** (1999) 2405–2415.
62. G. Hoben, W. Huang, B. S. Thoma, R. G. LeBaron and K. A. Athanasiou, *Ann. Biomed. Eng.* **30** (2002) 703–712.
63. E. J. Koay, A. C. Shieh and K. A. Athanasiou, *J. Biomech. Eng.* **125** (2003) 334–341.
64. D. Shin and K. A. Athanasiou, *J. Orthop. Res.* **17** (1999) 880–890.
65. N. D. Leipzig and K. A. Athanasiou, *J. Biomech.* **38** (2005) 77–85.
66. A. C. Shieh and K. A. Athanasiou, *J. Biomech.* **39** (2005) 1595–1602.
67. A. C. Shieh, E. J. Koay and K. A. Athanasiou, *Biomech. Model Mechanobiol.* **5** (2006) 172–179.
68. F. Guilak, J. R. Tedrow and R. Burgkart, *Biochem. Biophys. Res. Comm.* **269** (2000) 781–786.
69. W. R. Jones, H. P. Ting-Beall, G. M. Lee, S. S. Kelley, R. M. Hochmuth and F. Guilak, *J. Biomech.* **32** (1999) 119–127.
70. M. Sato, M. J. Levesque and R. M. Nerem, *J. Biomech. Eng.* **109** (1987) 27–34.
71. M. Sato, M. J. Levesque and R. M. Nerem, *Arteriosclerosis* **7** (1987) 276–286.
72. W. R. Trickey, G. M. Lee and F. Guilak, *J. Orthop. Res.* **18** (2000) 891–898.
73. A. R. Bausch, F. Ziemann, A. A. Boulbitch, E. Jacobson and E. Sackmann, *Biophys. J.* **75** (1998) 2038–2049.
74. O. Thoumine, P. Kocian, A. Kottelat and J. J. Meister, *Eur. Biophys. J.* **29** (2000) 398–408.
75. G. Binnig, C. F. Quate and C. Gerber, *Phys. Rev. Lett.* **56** (1986) 930–933.
76. F. Guilak, L. G. Alexopolous, M. L. Upton, I. Youn, J. B. Choi, L. Cao, L. A. Setton and M. A. Haider, *Ann. NY. Acad. Sci.* **1068** (2006) 498–512.
77. W. A. Hing, A. F. Sherwin, J. M. Ross and C. A. Poole, *Osteoarthritis Cartil.* **10** (2002) 297–307.
78. C. A. Poole, *J. Anat.* **191** (1997) 1–13.
79. R. D. Graff, S. S. Kelley and G. M. Lee, *Biotechnol. Bioeng.* **82** (2003) 457–464.
80. C. A. Poole, S. Ayad and R. T. Gilbert, *J. Cell Sci.* **103** (1992) 1101–1110.
81. C. A. Poole, S. Ayad and J. R. Schofield, *J. Cell Sci.* **90** (1988) 635–643.
82. C. A. Poole, M. H. Flint and B. W. Beaumont, *J. Orthop. Res.* **6** (1988) 408–419.
83. C. A. Poole, T. T. Glant and J. R. Schofield, *J. Histochem. Cytochem.* **39** (1991) 1175–1187.
84. C. A. Poole, A. Matsuoka and J. R. Schofield, *Arthritis Rheum.* **34** (1991) 22–35.
85. L. G. Alexopolous, M. A. Haider, T. P. Vail and F. Guilak, *J. Biomech. Eng.* **125** (2003) 323–333.
86. L. G. Alexopolous, G. M. Williams, M. L. Upton, L. A. Setton and F. Guilak, *J. Biomech.* **38** (2005) 509–517.
87. I. Youn, J. B. Choi, L. Cao, L. A. Setton and F. Guilak, *Osteoarthritis Cartil.* **14** (2006) 889–897.

88. G. M. Lee, T. A. Paul, M. Slabaugh and S. S. Kelley, *Osteoarthritis Cartil.* **8** (2000) 44–52.
89. N. Mitchell and N. Shepard, *Arthritis Rheum.* **24** (1981) 958–964.
90. L. Hambach, D. Neureiter, G. Zeiler, T. Kirchner and T. Aigner, *Arthritis Rheum.* **41** (1998) 986–997.
91. W. S. Hwang, B. Li, L. H. Jin, K. Ngo, N. S. Schachar and G. N. F. Hughes, *J. Pathol.* **167** (1992) 425–433.
92. R. S. Tuan, *Clin. Orthop. Relat. Res.* **427S** (2004) S105–S117.
93. P. B. Ahrens, M. Solursh and R. S. Reiter, *Dev. Biol.* **60** (1977) 69–82.
94. B. K. Hall and T. Miyake, *BioEssays* **22** (2000) 138–147.
95. J. H. Heegaard, G. S. Beaupre and D. R. Carter, *J. Orthop. Res.* **17** (1999) 509–517.
96. P. A. Brama, J. M. Tekoppele, R. A. Bank, A. Barneveld and P. R. Van Weeren, *Equine Vet. J.* **32** (2000) 217–221.
97. H. Brommer, P. A. Brama, M. S. Laasanen, H. J. Helminen, P. R. Van Weeren and J. Jurvelin, *Equine Vet. J.* **37** (2005) 148–154.
98. P. A. Brama, J. M. Tekoppele, R. A. Bank, A. Barneveld and P. R. van Weeren, *Equine Vet. J.* **34** (2002) 265–269.
99. L. J. Bonassar, A. Grodzinsky, A. Srinivasan, S. G. Davila and S. B. Trippel, *Arch. Biochem. Biophys.* **379** (2000) 57–63.
100. K. A. Athanasiou, G. G. Niederauer and R. C. Schenck, *Ann. Biomed. Eng.* **23** (1995) 697–704.
101. K. A. Athanasiou, A. Agarwal, A. Muffoletto, F. J. Dzida, G. Constantinides and M. Clem, *Clin. Orthop. Relat. Res.* **316** (1995) 254–266.
102. K. A. Athanasiou, A. Agarwal and F. J. Dzida, *J. Orthop. Res.* **12** (1994) 340–349.
103. K. A. Athanasiou, G. T. Liu, L. A. Lavery, D. R. Lanctot and R. C. Schenck, *Clin. Orthop. Relat. Res.* **348** (1998) 269–281.
104. N. Y. Afoke, P. D. Byers and W. C. Hutton, *J. Bone Joint Surg. Br.* **69** (1987) 536–541.
105. W. A. Hodge, K. L. Carlson, R. S. Fijan, R. G. Burgess, P. O. Riley, W. H. Harris and R. W. Mann, *J. Bone Joint Surg. Am.* **71** (1989) 1378–1386.
106. H. H. Huberti and W. C. Hayes, *J. Bone Joint Surg. Am.* **66** (1984) 715–724.
107. J. Jurvelin, I. Kiviranta, M. Tammi and H. J. Helminen, *Int. J. Sports Med.* **7** (1986) 106–110.
108. I. Kiviranta, M. Tammi, J. Jurvelin, A. M. Saamanen and H. J. Helminen, *J. Orthop. Res.* **6** (1988) 188–195.
109. A. M. Saamanen, M. Tammi, I. Kiviranta and H. J. Helminen, *Int. J. Sports Med.* **9** (1988) 127–132.
110. J. H. Plochocki, C. J. Riscigno and M. Garcia, *Anat. Rec. A Discov. Mol. Cell Evol. Biol.* **288** (2006) 776–781.
111. E. C. Firth, *J. Anat.* **208** (2006) 513–526.
112. F. Eckstein, M. Hudelmaier and R. Putz, *J. Anat.* **208** (2006) 491–512.
113. P. A. Brama, J. M. Tekoppele, R. A. Bank, A. Barneveld, E. C. Firth and P. R. van Weeren, *Equine Vet. J.* **32** (2000) 551–554.
114. J. Jurvelin, I. Kiviranta, M. Tammi and H. J. Helminen, *Clin. Orthop. Relat. Res.* **207** (1986) 246–252.
115. H. J. Helminen, A. M. Saamanen, J. Jurvelin, I. Kiviranta, J. J. Parkkinen, M. J. Lammi and M. Tammi, *Duodecim.* **108** (1992) 1097–1107.
116. M. J. Palmoski, R. A. Colyer and K. D. Brandt, *Arthritis Rheum.* **23** (1980) 325–334.
117. J. Haapala, J. Arokoski, J. Pirttimaki, T. Lyyra, J. Jurvelin, M. Tammi, H. J. Helminen and I. Kiviranta, *Int. J. Sports Med.* **21** (2000) 76–81.

118. J. Haapala, J. P. Arokoski, M. M. Hyttinen, M. J. Lammi, M. Tammi, V. Kovanen, H. J. Helminen and I. Kiviranta, *Clin. Orthop. Relat. Res.* **362** (1999) 218–229.
119. J. Jurvelin, I. Kiviranta, A. M. Saamanen, M. Tammi and H. J. Helminen, *J. Orthop. Res.* **7** (1989) 352–358.
120. D. S. Howell, B. V. Treadwell and S. B. Trippel, *Osteoarthritis: Diagnosis and Medical/Surgical Management*, eds. R. W. Moskowitz, D. S. Howell, V. M. Goldberg and H. J. Mankin (W.B. Saunders, Philadelphia, 1992), pp. 233–252.
121. R. W. Moskowitz, *Osteoarthritis: Diagnosis and Medical/Surgical Management*, eds. R. W. Moskowitz, D. S. Howell, V. M. Goldberg and H. J. Mankin (W.B. Saunders, Philadelphia, 1992), pp. 213–232.
122. F. Conteduca, A. Ferretti, P. P. Mariani, G. Puddu and L. Perugia, *Am. J. Sports Med.* **19** (1991) 119–123.
123. F. Guilak, D. L. Butler and S. A. Goldstein, *Clin. Orthop. Relat. Res.* **391S** (2001) S295–S305.
124. S. Nehrer, H. A. Breinan, A. Ramappa, H. P. Hsu, T. Minas, S. Shortkroff, C. B. Sledge, I. V. Yannas and M. Spector, *Biomaterials* **19** (1998) 2313–2328.
125. S. Nehrer, H. A. Breinan, A. Ramappa, S. Shortkroff, G. Young, T. Minas, C. B. Sledge, I. V. Yannas and M. Spector, *J. Biomed. Mater. Res.* **38** (1997) 95–104.
126. L. Schuman, P. Buma, B. Versleyen, B. de Man, P. M. van der Kraan, W. B. van den Berg and G. N. Homminga, *Biomaterials* **16** (1995) 809–814.
127. R. P. Silverman, D. Passaretti, W. Huang, M. A. Randolph and M. J. Yaremchuck, *Plast. Reconstr. Surg.* **103** (1999) 1809–1818.
128. V. Ting, C. D. Sims, L. E. Brecht, J. G. McCarthy, A. K. Kasabian, P. R. Connelly, J. Elisseeff, G. K. Gittes and M. T. Longaker, *Ann. Plast. Surg.* **40** (1998) 413–420.
129. J. L. van Susante, P. Buma, L. Schuman, G. N. Homminga, W. B. Van den Berg and R. P. Veth, *Biomaterials* **20** (1999) 1167–1175.
130. L. A. Solchaga, J. E. Dennis, V. M. Goldberg and A. I. Caplan, *J. Orthop. Res.* **17** (1999) 205–213.
131. M. Mattioli-Belmonte, A. Gigante, R. A. Muzzarelli, R. Politano, A. De Benedittis, N. Specchia, A. Buffa, G. Biagini and F. Greco, *Med. Biol. Eng. Comput.* **37** (1999) 130–134.
132. P. D. Benya and J. D. Shaffer, *Cell* **30** (1982) 215–224.
133. H. J. Hauselmann, R. J. Fernandes, S. S. Mok, T. M. Schmid, J. A. Block, M. B. Aydelotte, K. Kuettner and E. J. Thonar, *J. Cell Sci.* **107** (1994) 17–27.
134. C. R. Chu, R. D. Coutts, M. Yoshioka, F. L. Harwood, A. Z. Monosov and D. Amiel, *J. Biomed. Mat. Res.* **29** (1995) 1147–1154.
135. C. R. Chu, A. Z. Monosov and D. Amiel, *Biomaterials* **16** (1995) 1381–1384.
136. L. E. Freed, D. A. Grande, Z. Lingbin, J. Emmanual, J. C. Marquis and R. Langer, *J. Biomed. Mat. Res.* **28** (1994) 891–899.
137. L. E. Freed, J. C. Marquis, A. Nohria, J. Emmanual, A. G. Mikos and R. Langer, *J. Biomed. Mat. Res.* **27** (1993) 11–23.
138. M. Sittinger, D. Reitzel, M. Dauner, H. Hierlemann, C. Hammer, E. Kastenbauer, H. Planck, G. R. Burmester and J. Bujia, *J. Biomed. Mat. Res.* **33** (1996) 57–63.
139. C. M. Agrawal and K. A. Athanasiou, *J. Biomed. Mat. Res.* **38** (1997) 105–114.
140. C. M. Agrawal, D. Huang, J. P. Schmitz and K. A. Athanasiou, *Tissue Eng.* **3** (1997) 345–352.
141. K. A. Athanasiou, C. M. Agrawal, F. A. Barber and S. S. Burkhart, *Arthroscopy* **14** (1998) 726–737.
142. K. A. Athanasiou, D. Korvick and R. C. Schenck, *Tissue Eng.* **3** (1997) 363–373.
143. K. A. Athanasiou, G. G. Niederauer and C. M. Agrawal, *Biomaterials* **17** (1996) 93–102.

144. K. A. Athanasiou, A. R. Singhal, C. M. Agrawal and B. D. Boyan, *Clin. Orthop. Relat. Res.* **315** (1995) 272–281.
145. D. Thompson, C. M. Agrawal and K. A. Athanasiou, *Tissue Eng.* **2** (1996) 61–74.
146. S. M. Vickers, L. S. Squitieri and M. Spector, *Tissue Eng.* **12** (2006) 1–11.
147. S. Hsu, S. Chang, H. Yen, S. W. Whu, C. Tsai and D. C. Chen, *Artif. Organs* **30** (2006) 42–55.
148. A. Yasuda, K. Kojima, K. W. Tinsley, H. Yoshioka, Y. Mori and C. A. Vacanti, *Tissue Eng.* **12** (2006) 1237–1245.
149. G. Chen, S. Takashi, U. Takashi, N. Ochiai and T. Tateishi, *Tissue Eng.* **10** (2004) 323–330.
150. C. R. Lee, S. Grad, K. Gorna, S. Gogolewski, A. Goessi and M. Alini, *Tissue Eng.* **11** (2005) 1562–1573.
151. T. B. Woodfield, C. A. Van Blitterswijk, J. De Wijn, T. J. Sims, A. P. Hollander and J. Riesle, *Tissue Eng.* **11** (2005) 1297–1311.
152. L. E. Freed, J. C. Marquis, G. Vunjak-Novakovic, J. Emmanual and R. Langer, *Biotechnol. Bioeng.* **43** (1994) 605–614.
153. K. S. Furukawa, H. Suenaga, K. Toita, A. Numata, J. Tamaka, T. Ushida, Y. Sakai and T. Tateishi, *Cell Transplant* **12** (2003) 475–479.
154. C. Tacchetti, R. Quarto, L. Nitsch, D. J. Hartmann and R. Cancedda, *J. Cell Biol.* **105** (1987) 999–1006.
155. J. C. Hu and K. A. Athanasiou, *Tissue Eng.* **12** (2006) 969–979.
156. E. M. Darling and K. A. Athanasiou, *Tissue Eng.* **11** (2005) 395–403.
157. K. G. Yang, D. B. Saris, R. E. Geuze, Y. J. Helm, M. H. Rijen, A. J. Verbout, W. J. Dhert and L. B. Creemers, *Tissue Eng.* **12** (2006) 2435–2447.
158. M. Kino-Oka, S. Yashiki, Y. Ota, Y. Mushiaki, K. Sugawara, T. Yamamoto, T. Takezawa and M. Taya, *Tissue Eng.* **11** (2005) 597–608.
159. Y. Deng, J. C. Hu and K. A. Athanasiou, *Arthritis Rheum.* **56** (2006) 168–176.
160. H. Betre, S. R. Ong, F. Guilak, A. Chilkoti, B. Fermor and L. A. Setton, *Biomaterials* **27** (2006) 91–99.
161. N. Nakayama, D. Duryea, R. Manoukian, G. Chow and C. Y. Han, *J. Cell Sci.* **116** (2003) 2015–2028.
162. Y. Sui, T. Clarke and J. S. Khillan, *Differentiation* **71** (2003) 578–585.
163. N. I. zur Nieden, G. Kempka, D. E. Rancourt and H. J. Ahr, *BMC Dev. Biol.* **5** (2005) 1.
164. J. Kramer, C. Hegert, K. Guan, A. M. Wobus, P. K. Muller and J. Rohwedel, *Mech. Dev.* **92** (2000) 193–205.
165. H. Tanaka, C. L. Murphy, C. Murphy, M. Kimura, S. Kawai and J. M. Polak, *J. Cell Biochem.* **93** (2004) 454–462.
166. C. Hegert, J. Kramer, G. Hargus, J. Muller, K. Guan, A. M. Wobus, P. K. Muller and J. Rohwedel, *J. Cell Sci.* **115** (2002) 4617–4628.
167. M. S. Kim, N. S. Hwang, J. Lee, T. K. Kim, K. Leong, M. J. Shamblott, J. Gearhart and J. Elisseeff, *Stem Cells* **23** (2005) 113–123.
168. G. G. Wulf, V. Viereck, B. Hemmerlein, D. Haase, K. Vehmeyer, T. Pukrop, B. Glass, G. Emons and L. Trumper, *Tissue Eng.* **10** (2004) 1136–1147.
169. J. R. Fuchs, D. Hannouche, S. Terada, S. Zand, J. P. Vacanti and D. O. Fauza, *Stem Cells* **23** (2005) 958–964.
170. J. A. Thomson, J. Itskovitz-Eldor, S. S. Shapiro, M. A. Waknitz, J. J. Swiergiel, V. S. Marshall and J. M. Jones, *Science* **282** (1998) 1145–1147.
171. T. W. Plaia, R. Josephson, Y. Liu, X. Zeng, C. Ording, A. Toumadje, S. N. Brimble, E. S. Sherrer, E. W. Uhl, W. J. Freed, T. C. Schulz, A. Maitra, M. S. Rao and J. M. Auerbach, *Stem Cells* **24** (2006) 531–546.

172. X. Zeng, J. Chen, Y. Liu, Y. Luo, T. C. Schulz, A. J. Robins, M. S. Rao and W. J. Freed, *Restor. Neurol. Neurosci.* **22** (2004) 421–428.
173. T. Barberi, L. M. Willis, N. D. Socci and L. Studer, *PLoS Med.* **2** (2005) e161.
174. M. Amit, C. Shariki, V. Margulets and J. Itskovitz-Eldor, *Biol. Reprod.* **70** (2004) 837–845.
175. Y. Li, S. Powell, E. Brunette, J. Lebkowski and R. Mandalam, *Biotechnol. Bioeng.* **91** (2005) 688–698.
176. M. Amit, V. Margulets, H. Segev, C. Shariki, I. Laevsky, R. Coleman and J. Itskovitz-Eldor, *Biol. Reprod.* **68** (2003) 2150–2156.
177. I. Klimanskaya, Y. Chung, L. Meisner, J. Johnson, M. D. West and R. Lanza, *Lancet* **365** (2005) 1631–1641.
178. A. Alhadlaq, J. Elisseeff, L. Hong, C. G. Williams, A. I. Caplan, B. Sharma, R. A. Kopher, S. Tomkoria, D. P. Lennon, A. Lopez and J. J. Mao, *Ann. Biomed. Eng.* **32** (2004) 911–923.
179. A. Alhadlaq and J. J. Mao, *J. Bone Joint Surg. Am.* **87** (2005) 936–944.
180. J. J. Mao, *Biol. Cell* **97** (2005) 289–301.
181. D. Bosnakovski, M. Mizuno, G. Kim, T. Ishiguro, M. Okumura, T. Iwanaga, T. Kadosawa and T. Fujinaga, *Exp. Hematol.* **32** (2004) 502–509.
182. K. Gelse, K. Von der Mark, T. Aigner, J. Park and H. Schneider, *Arthritis Rheum.* **48** (2003) 430–441.
183. D. Noel, D. Gazit, C. Bouquet, F. Apparailly, C. Bony, P. Plence, V. Millet, G. Turgeman, M. Perricaudet, J. Sany and C. Jorgensen, *Stem Cells* **22** (2004) 74–85.
184. H. M. van Beuningen, H. L. Glansbeek, P. M. Van der Kraan and W. B. Van den Berg, *Osteoarthritis Cartil.* **6** (1998) 306–317.
185. D. A. Grande, J. Mason, E. Light and D. Dines, *J. Bone Joint Surg. Am.* **85-A** (2003) 111–116.
186. H. Tsuchiya, H. Kitoh, F. Sugiura and N. Ishiguro, *Biochem. Biophys. Res. Commun.* **301** (2003) 338–343.
187. C. Jorgensen, J. Gordeladze and D. Noel, *Curr. Opin. Biotechnol.* **15** (2004) 406–410.
188. J. Kramer, C. Hegert and J. Rohwedel, *Meth. Enzymol.* **365** (2003) 251–268.
189. N. S. Hwang, M. S. Kim, S. Sampattavanich, J. H. Baek, Z. Zhang and J. Elisseeff, *Stem Cells* **24** (2005) 284–291.
190. D. P. Lennon, S. E. Haynesworth, R. G. Young, J. E. Dennis and A. I. Caplan, *Exp. Cell. Res.* **219** (1995) 211–222.
191. M. Wong and R. S. Tuan, *In Vitro Cell Dev. Biol. Anim.* **29A** (1993) 917–922.
192. C. C. Schmidt, H. I. Georgescu, C. K. Kwoh, G. L. Blomstrom, C. P. Engle, L. A. Larkin, C. H. Evans and S. L. Woo, *J. Orthop. Res.* **13** (1995) 184–190.
193. D. Bosnakovski, M. Mizuno, G. Kim, T. Ishiguro, M. Okumura, T. Iwanaga, T. Kadosawa and T. Fujinaga, *Exp. Hematol.* **32** (2004) 502–509.
194. G. Lisignoli, S. Cristino, A. Piacentini, N. Zini, D. Noel, C. Jorgensen and A. Facchini, *J. Biomed. Mater. Res. Part A* **77** (2005) 497–506.
195. P. J. Emans, D. Surtel, E. J. Frings, S. K. Bulstra and R. Kuijer, *Tissue Eng.* **11** (2005) 369–377.
196. G. Chen, D. Liu, M. Tadokoro, R. Hirochika, H. Ohgushi, J. Tanaka and T. Tateishi, *Biochem. Biophys. Res. Comm.* **322** (2004) 50–55.
197. M. B. Sporn, A. B. Roberts, L. M. Wakefield and R. K. Assoian, *Science* **233** (1986) 532–534.
198. P. van der Kraan, E. Vitters and W. van den Berg, *J. Rheumatol.* **19** (1992) 140–145.
199. D. M. Rosen, S. A. Stempien, A. Y. Thompson and S. M. Seyedin, *J. Cell Physiol.* **134** (1988) 337–346.

200. P. Galera, D. Vivien, S. Pronost, J. Bonaventure, F. Redini, G. Loyau and J. P. Pujol, *J. Cell Physiol.* **153** (1992) 596–606.
201. M. de Haart, W. J. Marijnissen, G. J. van Osch and J. A. Verhaar, *Acta Orthop. Scand.* **70** (1999) 55–61.
202. J. L. Graycar, D. A. Miller, B. A. Arrick, R. M. Lyons, H. L. Moses and R. Derynck, *Mol. Endocrinol.* **3** (1989) 1977–1986.
203. Y. Miura, J. Parvizi, J. S. Fitzsimmons and S. W. O'Driscoll, *J. Bone Joint Surg. Am.* **84-A** (2002) 793–799.
204. R. Ballock, A. Heydemann and L. M. Wakefield, *Develop. Biol.* (1993) 414–442.
205. J. U. Yoo, T. S. Barthel, K. Nishimura, L. Solchaga, A. I. Caplan, V. M. Goldberg and B. Johnstone, *J. Bone Joint Surg. Am.* **80** (1998) 1745–1757.
206. E. F. Roark and K. Greer, *Dev. Dyn.* **200** (1994) 103–116.
207. J. I. Ahn, S. T. Canale, S. D. Butler and K. A. Hasty, *J. Orthop. Res.* **22** (2004) 1215–1221.
208. S. M. Kunisaki, R. W. Jennings and D. O. Fauza, *Stem Cells Dev.* **15** (2006) 245–253.
209. G. J. van Osch, S. W. van der Veen, E. H. Burger and H. L. Verwoerd-Verhoef, *Tissue Eng.* **6** (2000) 321–330.
210. L. Z. Sailor, R. M. Hewick and E. A. Morris, *J. Orthop. Res.* **14** (1996) 937–945.
211. H. M. van Beuningen, H. L. Glansbeek, P. M. van der Kraan and W. B. van den Berg, *Osteoarthritis Cartil.* **6** (1998) 306–317.
212. A. J. Nixon, L. A. Fortier, J. Williams and H. Mohammed, *J. Orthop. Res.* **17** (1999) 475–487.
213. T. Tsukazaki, T. Usa, T. Matsumoto, H. Enomoto, A. Ohtsuru, H. Namba, K. Iwasaki and S. Yamashita, *Exp. Cell Res.* **215** (1994) 9–16.
214. R. L. Mauck, S. B. Nicoll, S. L. Seyhan, G. A. Ateshian and C. T. Hung, *Tissue Eng.* **9** (2003) 597–611.
215. L. J. Bonassar, A. J. Grodzinsky, E. H. Frank, S. G. Davila, N. R. Bhaktav and S. B. Trippel, *J. Orthop. Res.* **19** (2001) 11–17.
216. A. J. Nixon, R. A. Saxer and B. D. Brower-Toland, *J. Orthop. Res.* **19** (2001) 26–32.
217. K. Kieswetter, Z. Schwartz, M. Alderete, D. D. Dean and B. D. Boyan, *Endocrine* **6** (1997) 257–264.
218. L. Weiser, M. Bhargava, E. Attia and P. A. Torzilli, *Tissue Eng.* **5** (1999) 533–544.
219. O. Amano, U. Koshimizu, T. Nakamura and S. Iseki, *Arch. Oral Biol.* **44** (1999) 935–946.
220. T. Takebayashi *et al.*, *J. Cell Biol.* **129** (1995) 1411–1419.
221. R. M. Grumbles, D. S. Howell, L. Wenger, R. D. Altman, G. A. Howard and B. A. Roos, *Bone* **19** (1996) 255–261.
222. C. A. Arevalo-Silva, Y. Cao, Y. Weng, M. Vacanti, A. Rodriguez, C. A. Vacanti and R. D. Eavey, *Tissue Eng.* **7** (2001) 81–88.
223. E. Fujimoto, M. Ochi, Y. Kato, Y. Mochizuki, Y. Sumen and Y. Ikuta, *Arch. Orthop. Trauma Surg.* **119** (1999) 139–145.
224. B. C. Toolan, S. R. Frenkel, J. M. Pachence, L. Yalowitz and H. Alexander, *J. Biomed. Mater. Res.* **31** (1996) 273–280.
225. M. S. Detamore and K. A. Athanasiou, *Arch. Oral Biol.* **49** (2004) 577–583.
226. M. A. Sweigart, A. C. Aufderheide and K. A. Athanasiou, *Topics in Tissue Engineering 2003*, ed. A. Ferretti (2003), p. 19.
227. R. J. Webber, M. G. Harris and A. J. Hough, *J. Orthop. Res.* **3** (1985) 36–42.
228. E. Lieb, S. Milz, T. Vogel, M. Hacker, M. Dauner and M. B. Schulz, *Tissue Eng.* **10** (2004) 1399–1413.
229. E. Lieb, T. Vogel, S. Milz, M. Dauner and M. B. Schulz, *Tissue Eng.* **10** (2004) 1414–1425.

230. R. L. Waters, B. R. Lunsford, J. Perry and R. Byrd, *J. Orthop. Res.* **6** (1988) 215–222.
231. G. H. Schwab, D. R. Moynes, F. W. Jobe and J. Perry, *Clin. Orthop.* **176** (1983) 166–170.
232. N. Y. Afoke, P. D. Byers and W. C. Hutton, *J. Bone Joint Surg. Br.* **69** (1987) 536–541.
233. W. A. Hodge, K. L. Carlson, R. S. Fijan, R. G. Burgess, P. O. Riley, W. H. Harris and R. W. Mann, *J. Bone Joint Surg. Am.* **71** (1989) 1378–1386.
234. H. H. Huberti and W. C. Hayes, *J. Bone Joint Surg. Am.* **66** (1984) 715–724.
235. C. G. Armstrong, A. S. Bahrani and D. L. Gardner, *J. Bone Joint Surg. Am.* **61** (1979) 744–755.
236. G. Vunjak-Novakovic, I. Martin, B. Obradovic, S. Treppo, A. J. Grodzinsky, R. Langer and L. E. Freed, *J. Orthop. Res.* **17** (1999) 130–138.
237. R. L. Smith, B. S. Donlon, M. K. Gupta, M. Mohtai, P. Das, D. R. Carter, J. Cooke, G. Gibbons, N. Hutchinson and D. J. Schurman, *J. Orthop. Res.* **13** (1995) 824–831.
238. M. S. Croughan, J. F. Hamel and D. I. Wang, *Biotechnol. Bioeng.* **67** (2000) 841–852.
239. R. S. Cherry and T. Papoutsakis, *Biotechnol. Bioeng.* **32** (1988) 1001–1014.
240. K. J. Gooch, J. H. Kwon, T. Blunk, R. Langer, L. E. Freed and G. Vunjak-Novakovic, *Biotechnol. Bioeng.* **72** (2001) 402–407.
241. S. Bussolari, C. Dewey and M. Gimbrone, *Rev. Sci. Instrum.* **53** (1982) 1851–1854.
242. N. S. Dunkelman, M. P. Zimber, R. G. LeBaron, R. Pavelec, M. Kwan and A. F. Purchio, *Biotechnol. Bioeng.* **46** (1995) 299–305.
243. D. Pazzano, K. A. Mercier, J. M. Moran, S. S. Fong, D. D. DiBiasio, J. X. Rulfs, S. S. Kohles and L. J. Bonassar, *Biotechnol. Prog.* **16** (2000) 893–896.
244. C. M. Begley and S. J. Kleis, *Biotechnol. Bioeng.* **70** (2000) 32–40.
245. L. E. Freed, A. P. Hollander, I. Martin, J. R. Barry, R. Langer and G. Vunjak-Novakovic, *Exp. Cell Res.* **240** (1998) 58–65.
246. R. L. Smith, S. F. Rusk, B. E. Ellison, P. Wessells, K. Tsuchiya, D. R. Carter, W. E. Caler, L. J. Sandell and D. J. Schurman, *J. Orthop. Res.* **14** (1996) 53–60.
247. S. E. Carver and C. A. Heath, *Tissue Eng.* **5** (1999) 1–11.
248. A. C. Hall, J. P. Urban and K. A. Gehl, *J. Orthop. Res.* **9** (1991) 1–10.
249. J. J. Parkkinen, M. J. Lammi, A. Pelttari, H. J. Helminen, M. Tammi and I. Virtanen, *Ann. Rheum. Dis.* **52** (1993) 192–198.
250. J. J. Parkkinen, J. Ikonen, M. J. Lammi, J. Laakkonen, M. Tammi and H. J. Helminen, *Arch. Biochem. Biophys.* **300** (1993) 458–465.
251. R. L. Smith, J. Lin, M. C. Trindade, J. Shida, G. Kajiyama, T. Vu, A. R. Hoffman, M. C. van der Meulen, S. B. Goodman, D. J. Schurman and D. R. Carter, *J. Rehabil. Res. Dev.* **37** (2000) 153–161.
252. J. C. Hu and K. A. Athanasiou, *Tissue Eng.* **12** (2006) 1–8.
253. C. G. Armstrong, A. S. Bahrani and D. L. Gardner, *J. Bone Joint Surg. Am.* **61** (1979) 744–755.
254. R. L. Mauck, M. A. Soltz, C. C. Wang, D. D. Wong, P. H. Chao, W. B. Valhmu, C. T. Hung and G. A. Ateshian, *J. Biomech. Eng.* **122** (2000) 252–260.
255. D. A. Lee, T. Noguchi, S. P. Frean, P. Lees and D. L. Bader, *Biorheology* **37** (2000) 149–161.
256. S. H. Elder, S. A. Goldstein, J. H. Kimura, L. J. Soslowsky and D. M. Spengler, *Ann. Biomed. Eng.* **29** (2001) 476–482.
257. M. D. Buschmann, Y. A. Gluzband, A. J. Grodzinsky and E. B. Hunziker, *J. Cell Sci.* **108** (1995) 1497–1508.
258. R. L. Sah, Y. J. Kim, J. Y. Doong and A. Grodzinsky, *J. Orthop. Res.* **7** (1989) 619–636.

259. Y. J. Kim, R. L. Sah, A. Grodzinsky, A. H. Plaas and J. D. Sandy, *Arch. Biochem. Biophys.* **311** (1994) 1–12.
260. P. A. Torzilli, R. Grigiene, C. Huang, S. M. Friedman, S. B. Doty, A. L. Boskey and G. Lust, *J. Biomech.* **30** (1997) 1–9.
261. R. L. Mauck, M. A. Soltz, C. C. Wang, D. D. Wong, D. D. Chao, W. B. Valhmu, C. T. Hung and G. A. Ateshian, *J. Biomech. Eng.* **122** (2000) 252–260.
262. B. T. Estes, J. M. Gimble and F. Guilak, *Curr. Topics Develop. Biol.* **60** (2004) 91–126.
263. A. C. Shieh and K. A. Athanasiou, *Osteoarthritis Cartil.* **15** (2006) 328–334.

This page intentionally left blank

# CHAPTER 2

# TECHNIQUES IN MODERN GAIT ANALYSIS AND THEIR APPLICATION TO THE STUDY OF KNEE OSTEOARTHRITIS

J. L. ASTEPHEN and K. J. DELUZIO
*Dalhousie University, Canada*



Modern gait analysis results in large quantities of correlated data. A current challenge in the field is the development of appropriate data analysis techniques for the representation and interpretation of these data. Knee osteoarthritis is a common debilitating disease of the musculoskeletal system that has been the focus of many gait studies in recent years. Various data analysis techniques have been used to extract pathological information from gait data in these studies. The following review discusses the successes and limitations of many of these analysis techniques in the attempt to understand the biomechanics of knee osteoarthritis.

*Keywords*: Gait analysis; data analysis; techniques; knee osteoarthritis; biomechanics.

## 1. Introduction

Gait analysis, the systematic study of human locomotion, has evolved from simple descriptive studies of motion, to the use of photographic recordings, and more recently to sophisticated computer models. Improvements in gait quantification methods over the years have correspondingly increased our ability to measure large quantities of data in a single gait study. The current challenge in modern gait analysis is the development of appropriate data analysis techniques for the representation and interpretation of these data.



The most commonly used gait data analysis techniques are parameter-based methods that use univariate statistical tests on discrete gait measures (dgm) and parameters extracted from gait waveforms. Although simplistic in nature, these techniques have allowed researchers to detect important biomechanical characteristics of osteoarthritic gait. Waveform-based analyses, which have been used less extensively than parameter-based analyses, are well-suited to capturing the temporal variation in biomechanical variables as an individual walks. These analyses have allowed researchers to localize biomechanical differences to specific phases and events that occur during walking. Multivariate analysis techniques have also been used to identify relationships between gait variables and to develop an understanding of how the interrelationships between the variables during gait may contribute to observed differences in gait patterns.

Osteoarthritis (OA) is a common age-related impairment that causes pain and disability, and most commonly affects the knee joint.[39] The disease produces great social and economic cost to society, and contributes to substantial disability associated with activities of daily living.[86] The recent view of the disease is that it is a metabolically active, dynamic process that includes both destruction and repair mechanisms that may be triggered by both biochemical and mechanical insults.[38] The pathomechanics of the disease are not well understood, nor are the causes for its progression, but many links to mechanical factors have been suggested. Gait analysis, therefore, has the potential to provide: (i) insight into the destructive process of knee OA, and (ii) the basis for the design of interventions for the treatment of knee OA.

In the past few decades, gait analysis has been used extensively to study differences in the biomechanics of individuals with knee OA, in an attempt to understand the mechanical factors of the disease. Various gait data analysis techniques have been used in knee OA gait studies to extract pathological information from the data, and a great deal of information about the mechanics of the disease has been acquired. The purpose of this review is to discuss the results of many knee OA gait studies in terms of the data analysis techniques used, and to suggest direction in the development of new analysis technique designs that may address the limitations in our current knowledge of the pathomechanics of the disease.



## 2. Measurement of Gait

Gait analysis is the systematic study of human walking, a discipline that dates back in time to the Renaissance with early visual descriptive studies. The historical development of modern gait analysis is an interesting story that has been documented by a number of authors.[15,16,20,25,63,84,100–102] The study of gait has become more automated and quantitative in nature. Quantitative gait analysis can involve a number of different measurements, but arguably the three core data acquisition systems include: (i) motion capture, (ii) ground reaction force measurement, (iii) electromyographic measurement. Gait is a cyclic activity, that is, the movements associated with walking are repeated over and over. A complete description of this activity can be restricted to one complete gait cycle which is the time interval between two consecutive foot contacts with the ground with a single foot. There are two distinct phases of the gait cycle: stance phase when the foot is in contact with the ground, and swing phase when the foot leaves the ground to prepare for ground contact again. Stance phase generally comprises the first 60% of the gait cycle, and swing phase the final 40%.

Of particular interest in most gait studies are the kinematics and kinetics of the lower limb joints during gait, as well as stride characteristics such as

velocity, cadence, and stride length. Different motion capture systems for gait quantification do exist, but most systems used today involve the use of positional information from surface markers that are placed on limb segments and particular anatomical landmarks on a subject to describe gait kinematics, the relative motion and orientation between limb segments. The motion between two connected limb segments is defined about a joint coordinate system, an example of which is described in more detail by Grood and Suntay.[44] Three anatomical axes at each joint define a joint coordinate system, depicted in Fig. 1 for the knee joint. In the coordinate system described by Grood and Suntay, flexion/extension motion at the knee is described about a bone-embedded axis that runs in a medial–lateral (ML) direction between the two femoral condyles. The internal/external rotation axis is another bone-embedded axis that is directed in the anterior–posterior (AP) direction from the center of the tibial plateau to the midpoint between the malleoli of the ankle. The ab/adduction axis is a floating axis that is mutually orthogonal to the two other axes and is directed in the proximal–distal (PD) direction.

Additional information from force platforms embedded in the walking surface and limb inertial properties allow us to calculate joint kinetics (i.e., the resultant forces and moments) using an inverse dynamics procedure.[11] In the inverse dynamics

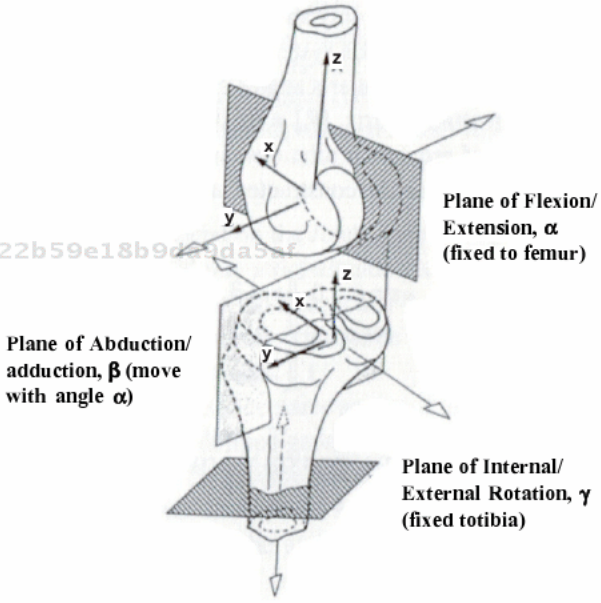


Fig. 1. The joint coordinate system shown above is often used to describe the motion of the knee joint. The flexion/extension axis is used to describe motion in the sagittal plane, the ad/abduction axis describes motion in the frontal plane, and the internal/external rotation axis describes motion in the transverse plane. (An and Chao, 1991.)

procedure, net external joint moments can be calculated directly from the dynamic equations of motion, given the ground reaction force, and limb segment kinematics, and anthropometric data. These moments are equal and opposite to the net internal moment at the joint, which is generated by muscle forces, soft tissue forces, and contact forces between the limb segments. Calculation of the contact forces within the joint is more complex, and generally involves simplifying assumptions. The literature contains a large range in joint contact forces determined from a variety of modeling techniques, and there is a need for further development and validation of these techniques.[59] The net external joint moments provide meaningful measures of joint function because they relate to muscular function and joint loading. In particular, the net external knee moment in the frontal plane (the knee adduction moment) has been shown to relate to joint loading.[95]

In a complete gait analysis of the lower extremity, kinematics, and kinetics of the hip, knee, and ankle joints are calculated, along with a number of stride characteristics. Table 1 summarizes the gait variables that are usually measured in a typical gait analysis study of the lower extremity. Depending on the application and the research question posed, different subsets of the variables included in this table are reported.

Table 1. Common gait variables measured in a three-dimensional gait analysis trial.

| Stride characteristics | Kinematics | Kinetics | |
|---|---|---|---|
| | | Moments | Forces |
| Speed | Hip flexion/extension angle | Hip flexion/extension moment | AP hip force |
| Stride length | Hip ad/abduction angle | Hip ad/abduction moment | ML hip force |
| Cadence | Hip internal/external rotation angle | Hip internal/external rotation moment | PD hip force |
| Stride time | Knee flexion/extension angle | Knee flexion/extension moment | AP knee force |
| Stance time | Knee ad/abduction angle | Knee ad/abduction moment | ML knee force |
| Stance % | Knee internal/external rotation angle | Knee internal/external rotation moment | PD knee force |
| Swing % | Ankle flexion/ extension angle | Ankle flexion/extension moment | AP ankle force |
| | Ankle ad/abduction angle | Ankle ad/abduction moment | ML ankle force |
| | Ankle internal/external rotation angle | Ankle internal/external rotation moment | PD ankle force |
| | | | AP ground reaction force |
| | | | ML ground reaction force |
| | | | PD ground reaction force |

*Notes*: AP represents the anterior–posterior anatomical direction; ML is the medial–lateral direction; PD is the proximal–distal direction.

## 3. The Nature of Gait Data

Gait data are voluminous and complex. In a typical gait study, multiple interrelated gait measures are calculated continuously in time during gait for a number of subjects (Table 1). The resulting data are therefore time-dependent, multivariate, correlated, and highly variable, particularly in the study of persons with pathologies such as knee OA. The recognition of the dimensionality and the level and type of variation within the data are important considerations before selecting an appropriate analysis technique for use.

### 3.1. *Variability*

Gait data are highly variable and the variability comes from a number of sources. There is natural variation in the biological system being characterized, and there is inherent variation in the collection and synthesis of gait data that arises from both the instrumentation and the assumptions that are made in the mathematical modeling of the system. There is also variability between subjects, some that can be explained by the natural variation in the biological system, and some that represents adaptations and differences that may be related to pathology. The goal of many gait analyses is to isolate and interpret the variability that characterizes biomechanical differences between groups of subjects. In the study of knee OA, we are interested in the biomechanical differences that are due to the physical disorder. Therefore, we refer to this as pathological variability.

The continuous measurement of gait variables (i.e., joint angles and moments) during gait results in a series of data that can be represented graphically as waveforms. Most commonly, these data are time normalized to represent one complete stride, defined with equidistant data points that represent percentages of the gait cycle. This normalization allows for easier comparison of gait waveforms between subjects with different stride times. Figure 2 shows the knee

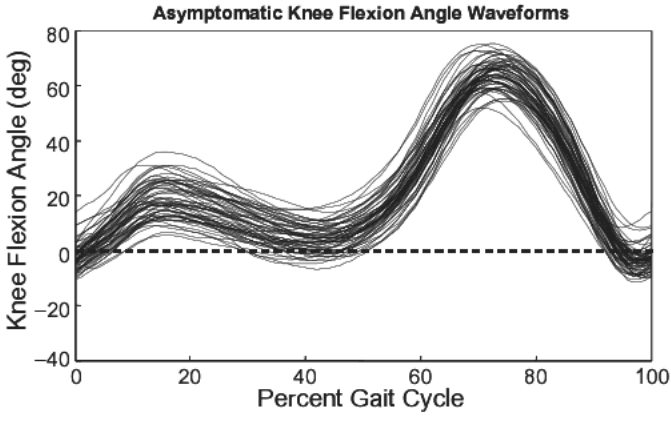


Fig. 2. Knee flexion angle waveforms for 63 asymptomatic subjects.[26]

flexion/extension angle waveforms for a group of 63 asymptomatic adults that were recently studied by the authors.[26] The waveform for each subject is the average of five gait trials, and the data is time normalized to represent one stride. In this example, the waveform is defined with 101 data points, one for each percentage of the gait cycle from 0% to 100%. Each waveform varies temporally because the value of the knee flexion/extension angle changes continuously as the individual progresses through the gait cycle. Most of the waveforms begin at foot contact with the knee in a slightly extended position (negative) and move through a range of approximately 40° in stance and 70° in swing. The waveforms also vary in amplitude. The magnitude of flexion/extension reached at each percentage of the gait cycle varies from subject to subject. Although differences in the amplitude and timing of the knee flexion/extension angles for this group of asymptomatic subjects are evident, the subjects appear to follow a similar pattern of motion. The variability between these waveforms is a natural level of variability that describes subtle differences between the walking styles of individuals.



In comparison, Fig. 3 shows the knee flexion angle waveforms for a group of 50 adults with severe knee OA that were also studied by the authors.[26] The variability in this group appears to be more complex than the variability in the asymptomatic waveforms. The natural level of variability still exists within this group of subjects, but there is also variability in the *pattern* of motion. Some osteoarthritic waveforms do follow a similar pattern to the asymptomatic waveforms, but many follow a pattern that involves a flatter knee flexion/extension profile during stance, with a less distinct peak flexion and extension angles. This variability in the pattern of the waveforms is the pathological variation that we seek to characterize in gait analysis studies for knee OA.

Pathological variation is also evident in the knee adduction moment. Figure 4 shows the mean knee adduction moment waveforms for the same groups of



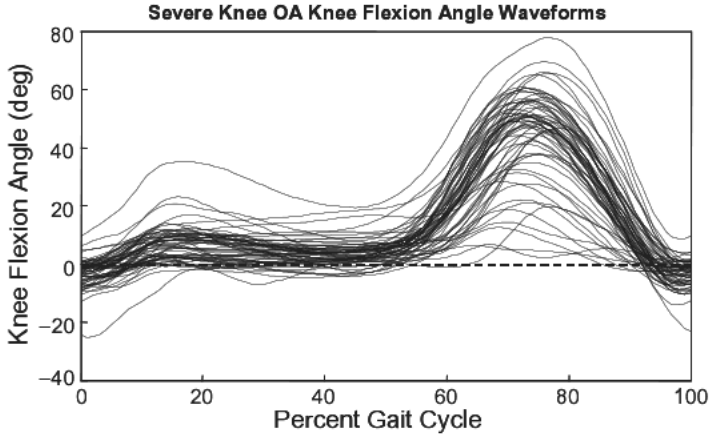


Fig. 3. Knee flexion angle waveforms for 50 individuals with end stage knee osteoarthritis.[26]

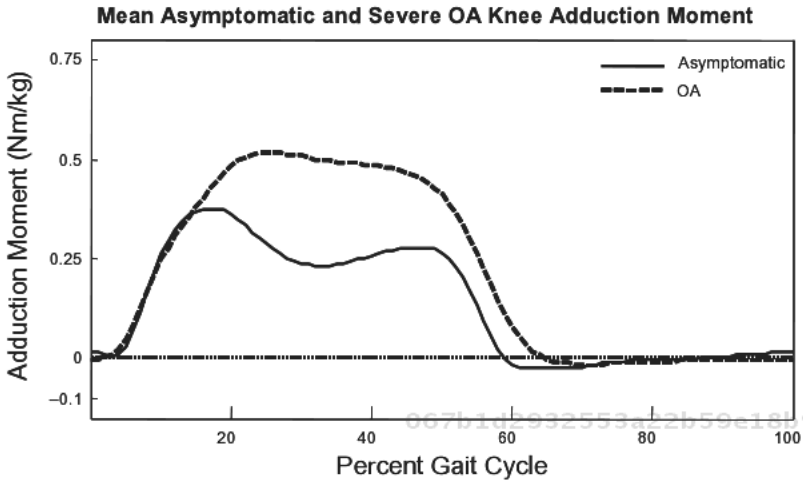


Fig. 4. Knee adduction moment mean waveforms for a group of 63 asymptomatic adults (solid curve) and for a group of 50 persons with severe knee osteoarthritis (dashed curve).[26]

63 asymptomatic adults and 50 persons with severe knee OA that are included in Figs. 2 and 3.[26] The amplitudes of the group mean waveforms appear to differ, and so do the temporal patterns, or the shapes of the waveforms. The knee adduction moment of the asymptomatic group peaks in early stance, reduces during the weight acceptance phase of stance and then increases a small amount again toward the end of stance. The OA mean waveform increases slowly during stance, plateaus at a higher level than the asymptomatic mean, and remains high until the end of stance. Both the peak magnitude of the knee adduction moment and the temporal pattern of the adduction moment have been identified in the literature as pathological variation relating to knee OA.[7,26,51,61,97]



### 3.2. *Dimensionality*

The data that results from a gait study is multidimensional (Table 1). In a gait study, three dimensions of joint kinematics and kinetics during gait are often measured for multiple joints and for multiple subjects or subject groups. For example, if three-dimensional angles and moments at the knee, hip, and ankle joints are measured and represented by a different data point at each percentage of the gait cycle, there would be three (number of anatomical planes) × three (number of joints) × two (angles and moments) × 101 (percentages of the gait cycle) = 1818 variables measured for each limb of each subject to represent their gait pattern.

The harmonious nature of gait suggests a high level of correlation between the variables measured during gait, and therefore a much smaller fundamental dimension of gait than the large number of variables that are measured. Data

reduction is therefore a common, important first goal in any gait data analysis technique.

In the study of knee OA gait patterns, the goal is to not only reduce the dimensionality of the data, but to do it in such a way that only information related to the pathology is retained in the analyses. Referring back to the discussion on variability in the preceding section, some gait variables may contain a level of natural variability that exists even within an asymptomatic population. It is the pathological variability that describes *differences* between an asymptomatic population and an osteoarthritic population that is sought.

## 4. Gait Data Analysis in the Study of Knee Osteoarthritis



Analysis techniques for gait data have evolved from simple visual descriptions of the data to complex computerized models. Quantitative analysis of gait data has been defined as any mathematical operation that is performed on a set of data to present them in another form or to combine the data with other data to produce a variable that is not directly measurable.[111] Most gait data analyses that are used in the study of knee OA fall into two categories: parameter-based analyses and waveform-based analyses. These analyses are used to capture the discriminatory variability within the data set that describes differences in gait measures in a group of persons with knee OA, usually compared to an asymptomatic group. To address the dimensionality of the data, multivariate analyses are sometimes used in combination with a parameter or waveform-based analysis.

### 4.1. *Parameter-based analyses*



Parameter-based analysis techniques have probably been the most commonly used analysis techniques for gait data because of their simplicity. They include analyses of time–distance gait measures such as average walking velocity, or of discrete parameters extracted with simple computational algorithms from gait waveforms such as peak values, means or ranges.

Figure 5 shows some example parameters highlighted on two asymptomatic knee flexion angle waveforms. The figure shows peak stance phase flexion angle, peak swing phase flexion angle, and peak extension angle. One of the biggest limitations of using parameter-based analyses is the loss of temporal pattern information when only extracted parameters are analyzed. For example, the timing of the peak extension angles for these two subjects in Fig. 5 is different. One subject reaches maximum extension in late stance phase and the other reaches a maximum extension in late swing phase just before foot contact with the ground. These two parameters represent angle values at very different events, and their comparison would not capture the temporal difference.

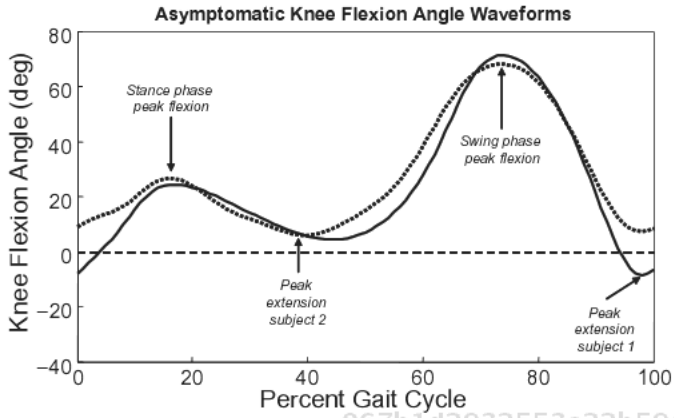




Fig. 5. Knee flexion angle waveforms for two asymptomatic adults labeled with parameters stance peak flexion, swing peak flexion, and peak extension. Peak extension occurs in late stance for one of the subjects (subject 2) and in late swing phase for the other subject (subject 1).

Statistical analysis of gait parameters commonly involves the use of a Student's $t$-test to compare the mean values of a parameter for two groups of subjects, or analysis of variance methods (ANOVA) to compare the mean values of several groups of subjects. It is important to consider the correlation between parameters when using these statistical techniques on a number of parameters. Correlation between multiple parameters increases the probability of a Type I statistical error, which is finding a statistically significant difference when the populations are actually the same. Another difficulty in the analysis of multiple gait parameters is the simultaneous interpretation of the differences found. It can be difficult to assimilate the findings into a clinically meaningful story. For example, Kaufman *et al.*[56] performed a large study on the knee joint kinetics and kinematics associated with knee OA. For level walking, nine parameters extracted from the knee joint angle and moment waveforms were analyzed with Student's $t$-tests. Subjects with OA were found to have reduced peak knee flexion angles, reduced peak extension moments, and increased peak adduction moments. While this study successfully documented gait adaptations used by patients with knee OA, no attempt was made to understand any mechanistic relationships between the gait measures that may be contributing the pathology.



The definition of parameters can also be problematic, particularly in the study of pathological gait such as knee OA. It can be difficult to define and extract parameters from pathological waveforms that are easily distinguishable on asymptomatic waveforms. Figure 4 showed the mean knee adduction waveforms for a group of severe knee OA subjects (dashed line) and a group of asymptomatic subjects (solid line). The mid-stance knee adduction moment has been identified as effective in differentiating between OA and asymptomatic gait.[109] While there is a definite mid-stance minimum of the knee adduction moment in the asymptomatic

mean waveform in Fig. 4, there is not a definite mid-stance minimum in the OA mean waveform. An extracted parameter analysis to capture this important difference between the two subject groups would therefore be difficult. Hurwitz *et al.*[51] also had difficulty extracting a second peak value from the knee adduction moment waveforms of 29% of their asymptomatic subjects and 52% of their osteoarthritic subjects. They attempted to deal with this problem by using the value of the knee adduction moment at the time of the peak internal rotation moment since these values tended to be coincident for those individuals with distinct second peaks to the knee adduction moment.

### 4.2. *Waveform-based analyses*



Waveform-based analysis techniques for gait data are those techniques that retain or exploit the temporal information within the data. These techniques are inherently more complex than parameter-based analysis techniques because it is more difficult to compare a set of curves than a set of discrete values. There is yet no generally agreed upon distance definition for gait curves,[18] so these techniques have not been as readily applied to gait data as parameter-based analysis techniques.

Waveform-based analysis techniques treat the gait data that is collected over the gait cycle either analytically as a curve, or more commonly as a continuum of data points. As described above, gait measures are often time normalized to represent one complete stride, and defined with 101 data points, one for each percentage of the gait cycle, from 0% to 100%. In this sense, the gait measure is a 101-dimensional vector, $\vec{\text{gm}}$.

$$\vec{\text{gm}} = [\text{gm}_1 \quad \cdots \quad \text{gm}_{101}]$$



Waveform-based analysis techniques that have been applied to gait data include multivariate statistical techniques such as principal component analysis (PCA), factor analysis and correspondence analysis, as well as other techniques such as fuzzy analysis, fractal analysis, wavelet transforms, and neural networks. A summary of gait applications of these techniques was recently produced in a two-part review article by Chau.[18,19]

#### 4.2.1. *Principal component analysis*

PCA is the only waveform-based analysis technique that has seen continued use in the study of knee OA gait.[5,6,26–28,61,70,94] PCA is foremost a data reduction technique that is designed to reduce a number of variables to a smaller number of indices called principal components (PCs), which are uncorrelated linear combinations of the original variables. Geometrically, the PCs are objectively defined as directions of maximal variability, providing a simpler description of the covariance structure in the original data.

Mathematically, PCA is an orthogonal transformation that converts $p$ correlated variables into $p$ new uncorrelated PCs, $\vec{z}_i$. In the case of the gait waveform data, suppose that the data for one gait waveform measure (gm) for $n$ subjects was contained in the matrix GM, where each vector $\vec{\text{gm}}_i$ is $n$-dimensional.

$$\text{GM} = [\vec{\text{gm}}_1 \quad \cdots \quad \vec{\text{gm}}_{101}] .$$

The PC model transforms the data matrix GM to a matrix of PC scores, $Z$, with a second matrix of loading vectors, $U$.

$$Z = U^T GM ,$$

where

$$U = [\vec{u}_1 \quad \cdots \quad \vec{u}_{101}] , \quad \text{and} \quad Z^T = [\vec{z}_1 \quad \cdots \quad \vec{z}_{101}] .$$



The columns of $U$, $\vec{u}_i$, are called the PC loading vectors, and are the eigenvectors of the covariance matrix of $GM$ arranged in decreasing order of their corresponding eigenvalues. The rows of $Z$, $\vec{z}_i$, are the PC scores that represent the vector of the projections of subject waveforms onto each respective PC loading vectors. The $\vec{z}_i$ are mutually uncorrelated in the sample and are arranged in decreasing order of their sample variances. The majority of the important variability information within the data is generally contained within the first few PCs, and so the original data can be more compactly described in terms of a few PCs rather than the original 101 variables that define the waveform. Criteria for selecting the number of PCs to retain in an analysis are based on the portion of explained variance, such as a 90% trace criteria.[55] For more information on the mathematical details of PCA, see Ref. 55.

PCA is also a tool for the *interpretation* of difference between gait waveforms. PCs extracted from gait waveform data are 101-dimensional curves that represent patterns of variation within the data. Differences in PC scores therefore reflect differences in the shapes of gait waveforms, capturing the temporal information that is lost in common parameter-based analysis techniques. The PC scores can be used in statistical hypothesis tests (i.e., student's $t$-tests, and analysis of variance) to determine differences in waveform shape. Some more recent studies have used discriminant analysis to detect more multidimensional differences between groups.[6,26] Once differences are identified with these techniques, the PC's that describe discriminatory information between the groups are interpreted in terms of waveform pattern difference they are describing. Detailed examples of this interpretation phase can be found in a recent paper by Deluzio and Astephen.[26]



#### 4.2.2. *Other waveform-based analysis techniques for gait data*

PCA is the waveform-based analysis technique that has been used most extensively in the study of knee osteoarthritic gait patterns. However, there are a number of other waveform-based analysis techniques that have potential power for particular investigations.

Factor analysis is a multivariate statistical analysis technique that is very similar in theory to PCA because it attempts to account for the variation in a number of variables by using a smaller number of index variables or factors.[70] The difference of the technique from PCA is that factors need not be PCs and may be rotated for better interpretation. Factor analysis has been used in gait analysis primarily as a tool to unveil interactions among multiple electromyographic patterns.[24,75,88]

Fuzzy analysis is a generalized clustering technique that attempts to account for nonstatistical uncertainties in the data and finds natural groupings within the data. The use of fuzzy analysis for gait data has been limited because aspects of the technique are very subjective and they cannot deal with multiple gait measures at the same time.[18] The techniques have been used to find compensatory strategies of persons with cerebral palsy[85] and with Parkinson's disease.[103]



Fractal analysis is a technique that can be used to explore self-similarity properties of gait signals over a significant period of time. These techniques are best used to examine long time-series of gait data to examine long-range correlations in the data. This type of analysis can shed light on the physiological mechanisms involved in the movement, but lack the practicality for common use in gait analysis studies. They have been used to attempt to explain the seemingly complex changes in gait cycle duration from stride to stride for an individual and to find long-range correlations in stride interval variations.[47]

Wavelet transforms is a technique that has proven to be a potentially powerful tool in gait analysis because the technique provides both time and frequency information contained within a signal. Different than other waveform-based analysis technique, wavelets provide local information so that dynamic gait changes can be easily detected.[19] Wavelets are therefore a desirable technique when localized information in the gait waveform is sought. They have not been used yet in the study of knee osteoarthritic gait, but have been used in gait analysis to reduce the noise content in kinematic data.[54,106] The down side to the technique is that there is no best method for selecting appropriate wavelet basis functions.



Neural networks are another nonstatistical analysis technique that has the potential to provide insight into complicated relationships between gait variables because they allow nonlinear modeling, are robust to errors and can handle vast amounts of data. However, they unfortunately do not automatically provide information into the relationships that are modeled and require a rather judicious selection of input variables. In gait analysis, neural networks have been used to categorize gait pathology based on measurements of ground reaction forces,[49] to reconstruct electromyographic data based on kinematic data,[48] to recognize gait changes with aging[10] and to diagnose gait disorders.[9] Based on their previous applications, neural networks are a potentially very useful analysis technique in the study of knee OA gait patterns.

### 4.3. *Multivariate analyses*

Knee OA involves multiple interacting factors, some of which are measured in gait analysis studies (Table 1). There is correlation between these gait variables that is lost when individual analyses are used. There is, however, a complexity trade-off in the decision to use multivariate analyses in gait analysis studies. In some applications, single variable analyses are sufficient in answering the research question. In these cases, the added complexity of a multivariate analysis is not justified. However, some analyses seek to understand the interaction of gait variables in their contribution to osteoarthritic gait patterns. The interrelationships between the measures during gait may describe mechanisms that contribute to either the compensation strategies associated with the disease or to disease progression.

The most commonly used and simplistic multivariate analysis techniques for gait data are correlation and regression analyses. Correlation analysis is used to quantify the linear association between two or more gait variables. The correlation coefficient, $r$, which ranges in value from negative one to positive one, is the statistic that is defined to represent the relative association. For two continuous gait variables, $x$ and $y$, it would be calculated as follows:

$$r = \frac{\sigma_{xy}}{\sigma_x \sigma_y},$$

where $\sigma_{xy}$ is the covariance between $x$ and $y$, $\sigma_x$ is the variance of the gait variable, $x$, and $\sigma_y$ is the variance of the gait variable $y$.

A perfect linear relationship between two variables would result in a correlation coefficient of plus one; a perfect negative relationship would result in a value of negative one. When correlation analysis is used for gait data, the variables $x$ and $y$ often represent time–distance characteristics or parameters extracted from gait waveform data, described in the parameter-based analysis techniques section above.

Regression analysis, as an extension of correlation analysis, attempts to define the relationships between gait variables. Simple linear regression is used to define a linear relationship between one gait variable and a second variable, referred to as the covariate. Multiple linear regression would include more than one covariate. If, for example, it is desired to define a linear relationship between one gait variable, $x$, and two covarying gait variables, $y$ and $z$, the following regression equation would be used:

$$x = \beta_0 + \beta_1 y + \beta_2 z\,.$$

The coefficients, $\beta_0$, $\beta_1$, and $\beta_2$ are usually estimated with a least-squares method, which minimizes the sum of squared differences between the observed $x$

values and those predicted with the modeled linear relationship defined above. The regression sum of squares value, $R^2$, which is also calculated in a regression analysis and often reported in the results of such analyses, is the proportion of variability in the gait variable $x$ that is accounted for by the regression model. If the variable $x$ can be perfectly predicted by the variables $y$ and $z$ in the example above, an $R^2$ value of one would result.

Knee OA researchers have used correlation and regression analyses to correlate gait variables or to relate gait variables to other factors that may be important to the disease process. Hurwitz *et al.*[51] used a regression analysis to relate the peak knee adduction moment to several factors including the mechanical axis of the leg, radiographic measures of OA severity, toe out angle, and clinical assessments of pain, stiffness, and function.

PCA, a multivariate statistical technique described in the waveform-based analysis technique section above, has also been used as a multivariate analysis technique in gait studies. It has been applied to multiple gait parameters to determine interrelationships between the measures in a knee OA gait study.[79] In this case, PCA allowed the investigators to cluster groups of interrelated gait variables, simplifying the interpretation of multiple differences in gait measures.

As an extension of PCA applied to gm, the technique was recently used as a multivariate waveform-based analysis technique by Astephen *et al.* to simultaneously analyze multiple gm to determine interrelationships between the measures that may be important in differentiating between osteoarthritic and asymptomatic gait patterns.[5,6] PCA was applied to all 101 time instants of the gait cycle for nine gm and eight dgm, which included stride characteristics and anthropometric measures such as body mass index (BMI). In the waveform-based PCA technique described above, the GM matrix now contained nine gait gm, each containing 101 data points for each percentage of the gait cycle, and well as eight dgm. The vector $\mathrm{gm}\vec{j}_i$ is an $n$-dimensional vector containing observations of the $j$th gait measure at $i$ percent of the gait cycle for $n$ subjects. The vector $\mathrm{dgm}\vec{j}$ is an $n$-dimensional vector containing the $n$ subject observations of the $j$th dgm.

$$\mathrm{GM} = [\mathrm{g}\vec{\mathrm{m}}1_1 \quad \cdots \quad \mathrm{g}\vec{\mathrm{m}}1_{101} \quad \cdots \quad \mathrm{g}\vec{\mathrm{m}}9_1 \quad \cdots \quad \mathrm{g}\vec{\mathrm{m}}9_{101} \quad \mathrm{dg}\vec{\mathrm{m}}1 \quad \cdots \quad \mathrm{dg}\vec{\mathrm{m}}8]$$

Correspondence analysis is another multivariate statistical technique that has been used in gait analyses, although it has yet to be applied to the study of knee OA gait. It is used to find interdependencies among a group of categorical variables by constructing axes to simultaneously plot a gait variable of interest along with the characteristics that are used to describe the variable. This technique has been used to simultaneously examine hip, knee, and ankle excursions in the sagittal plane and ground reaction forces for asymptomatic subjects.[67] The greatest limitation of the technique is the amount of expertise required to interpret the results.[18]

## 5. Biomechanical Factors of Knee Osteoarthritis

The structural, functional and even neurological changes that occur with knee OA compromise an individual's ability to accomplish the fluid locomotion that is often exhibited by asymptomatic individuals. Efficient gait requires a level of strength, balance, stability, and mobility that may not be achievable for a person with knee OA. These changes may be the result of the joint damage and the other physiological changes that occur throughout the disease process. However, there is accumulating evidence that some gait differences with knee OA contribute to the progressive deterioration of the knee joint, and are therefore important to the pathomechanics of the disease. In an effort to avoid pain and accomplish the tasks of locomotion, knee OA patients often employ consistently abnormal body movements during gait that manifest themselves as quantitative differences in joint dynamics.[89]



The goal of many earlier knee OA gait studies was to characterize the biomechanical changes associated with the disease, without regard to the question of causation versus symptomatic changes. These studies generally employed simple analysis techniques such as parameter-based Student's *t*-tests to develop a general level of understanding of the joint dynamic changes that change in an individual with knee OA. In more recent years, some studies have begun using more waveform-based analysis techniques and even multivariate analyses for more comprehensive evaluation of knee OA gait patterns. There has been a recent shift in the application of gait analysis for studying knee OA toward trying to understand some of the mechanical factors that may be contributing to disease progression. The following sub-sections present some of the kinematic and kinetic gait changes that have been identified in the literature to be associated with knee OA.

### 5.1. *Kinematics*



#### 5.1.1. *Stride characteristics*

Stride characteristics are the most commonly assessed gait measures because they are direct measures of gait performance, simple to measure, and easy to comprehend. They have been often used as objective measures to quantify loss of function associated with knee OA and the improvement in gait following surgical intervention (Table 2).[2,96] These studies of knee OA subjects at later stages of the disease process have found that knee OA gait is characterized by slower walking velocities, reduced cadence during walking, smaller stride lengths, increased time in the stance phase of the gait cycle and increased percentage of time in stance. Stride characteristics are considered crude indicators of knee joint function,[22,110] and walking speed in particular has been shown to reflect the severity of knee OA.[12,56,99] It should be noted, however, that gait speed may not be affected early in the disease process. Two recent studies have reported no differences in gait speed for subjects with moderate knee OA.[61,83]

Table 2. Literature summary of changes in stride characteristics that are associated with knee osteoarthritis.

| References | Parameter analyzed | Analysis technique | Findings |
|---|---|---|---|
| 1, 3, 43, 56, 72, 104 | Average gait velocity | Student's $t$-test | OA < control |
| 3, 43, 104 | Cadence | Student's $t$-test | OA < control |
| 1, 8, 43 | Stride length | Student's $t$-test | OA < control |
| 1, 3, 41, 43, 104 | Stance time and percentage of time in stance | Student's $t$-test | OA > control |
| 83 | Stride characteristics | Student's $t$-test | OA = control (moderate) |

### 5.1.2. *Joint angles*



Dynamic joint angles that are measured continuously in a gait analysis study provide us with quantitative information on the kinematic limitations associated with knee OA. These angular measures give more time-localized indicators of dysfunction than stride characteristic data, and tell more about dynamic functional ability than any static clinical measures such as alignment or passive range of motion.

Table 3 summarizes some of the joint angular changes associated with knee OA that have been identified in previous gait studies. Most gait studies have analyzed joint angle measures using statistical analyses (i.e., student's $t$-tests) of peak and range values extracted from dynamic joint angle waveforms. These studies have indicated that persons with knee OA walk with a limited range of knee motion in the sagittal plane,[2,12,79,99] and reduced peak knee flexion angles during the stance phase of the gait cycle,[1,21,43,56] and reduced swing phase knee flexion angles.[43]

Similar knee flexion angle results were identified in a recent waveform-based PCA.[26] The authors found a discriminatory PC that represented the range of the knee flexion angle over the stance phase of the gait cycle, and OA scores of this feature were smaller than asymptomatic scores, indicating that the OA group walked with smaller overall ranges of knee flexion angles during stance. In a multivariate discriminant analysis that included several PCs from the knee flexion angle, the knee flexion moment, the knee adduction moment, and the knee internal rotation



Table 3. Literature summary of kinematic factors that are associated with knee osteoarthritis.

| References | Parameter analyzed | Analysis technique | Findings |
|---|---|---|---|
| 2, 12, 79, 99 | Knee flexion angle range | Student's $t$-test | OA < control |
| 1, 21, 43, 56 | Peak stance phase knee flexion angle | Student's $t$-test | OA < control |
| 43 | Peak swing phase knee flexion angle | Student's $t$-test | OA < control |
| 26 | Range of knee flexion angle in stance | Waveform PCA | OA < control |
| 1 | Hip flexion angle range | Student's $t$-test | OA < control |
| 1 | Ankle flexion angle range | Student's $t$-test | OA < control |

moment, this feature of gait was one of the most important in the multivariate differentiation between the two groups.

Kinematic gait studies for knee OA have paid little attention to changes at the other joints of the lower extremity. One study associated knee OA with smaller ranges of hip and ankle angles in the sagittal plane.[1] The synergistic changes between all joints of the lower limb may be important to knee OA and should be investigated in future gait analyses for knee OA.

### 5.2. *Kinetics*

There was an early recognition that joint loading may be an important part of the degenerative process of knee OA.[91] Changes in the dynamic kinetics associated with knee OA have therefore been thoroughly investigated in gait analysis studies. Early gait studies primarily characterized changes in ground reaction forces associated with knee OA, as well as changes in sagittal plane moments and attempts at quantifying joint loads. The findings of many of these studies are summarized in Table 4. In more recent decades, researchers developed an awareness of the importance of frontal plane kinetics to knee OA, and so many later knee OA gait studies have focused on the dynamic knee adduction moment during gait. Most of

Table 4. Literature summary of kinetic factors that are associated with knee osteoarthritis.

| References | Parameter analyzed | Analysis technique | Findings |
|---|---|---|---|
| 43, 45, 99 | Peak vertical ground reaction force | Student's *t*-test | OA < control |
| 23, 79, 93 | Peak vertical ground reaction force | Student's *t*-test | OA > control |
| 104 | Peak bone-on-bone forces in the frontal plane | Student's *t*-test | OA > control |
| 8, 43, 74 | Peak knee flexion moment | Student's *t*-test | OA < control |
| 8, 43, 74 | Peak knee extension moment | Student's *t*-test | OA < control |
| 61 | Knee flexion moment in early stance | Waveform PCA | OA < control |
| 26 | Overall magnitude of knee flexion moment in stance early stance knee | Waveform PCA | OA < control |
| 26 | Flexion moment and late stance extension moment | Waveform PCA | OA < control |
| 43 | Peak knee internal rotation moment | Student's *t*-test | OA > control |
| 61 | Knee internal rotation moment in early stance | Waveform PCA | OA < control |
| 82 | Peak hip flexion moment in terminal stance | Student's *t*-test | OA > control |
| 82 | Peak ankle inversion moment in terminal stance | Student's *t*-test | OA < control |

Table 5. Literature summary of knee adduction moment findings associated with knee osteoarthritis.

| References | Parameter analyzed | Analysis technique | Findings |
|---|---|---|---|
| 8, 43, 109 | Peak | Student's $t$-test | OA > control |
| 51 | First peak | Student's $t$-test | OA > control |
| 51 | Second peak | Student's $t$-test | OA > control |
| 65 | Peak | ANCOVA with speed as covariate | OA > control |
| 82 | Peak | ANOVA | More severe > less severe |
| 82 | First peak | ANOVA | More severe > less severe<br>More severe > control |
| 82 | Second peak | ANOVA | More severe > less severe<br>Control > less severe |
| 97 | Peak | Student's $t$-test | More severe > less severe |
| 109 | Mid-stance value | Student's $t$-test | OA > control |
| 56, 61 | Peak | Student's $t$-test | OA = control |
| 26 | Overall knee adduction moment in stance | Waveform PCA | OA > control |
| 26 | First peak | Waveform PCA | OA < control |
| 29 | Overall knee adduction moment in stance | Waveform PCA and ANCOVA with speed and BMI as covariates | More severe > less severe<br>More severe > control |

the knee adduction moment findings from gait analysis studies are summarized in Table 5.

There have been conflicting results from studies of peak values extracted from ground reaction forces profiles. Some have found reduced peak vertical ground reaction forces associated with knee OA.[45,99] Others have found increased peak vertical ground reaction forces.[23,79,93] These discrepancies may be attributed to differences in the population studied, differences in footwear, or in the analysis of ground reaction force data. A limitation in the measurement of ground reaction forces is that they do not accurately reflect the loading at the joint surface.[111]

Joint contact forces can be several times larger than the ground reaction forces[60,81] due to the contribution of muscle forces surrounding the joint. Unfortunately, the internal contact forces cannot be measured, and estimating them is still a major challenge.[59] Using a simplistic knee model, Teixeira and Olney[104] attempted to calculate bone-on-bone forces at the knee joint during gait and found that individuals with knee OA exhibited larger peak bone-on-bone forces in the frontal plane (directed in the ML direction). These forces are determined primarily from the dynamic knee adduction moment in the frontal plane, and so these results support the commonly reported finding of larger knee adduction moments with knee OA.[8,43,51]

In the sagittal plane, parameter-based analyses have been used to associate knee OA with reduced peak knee flexion moments and extension moments during

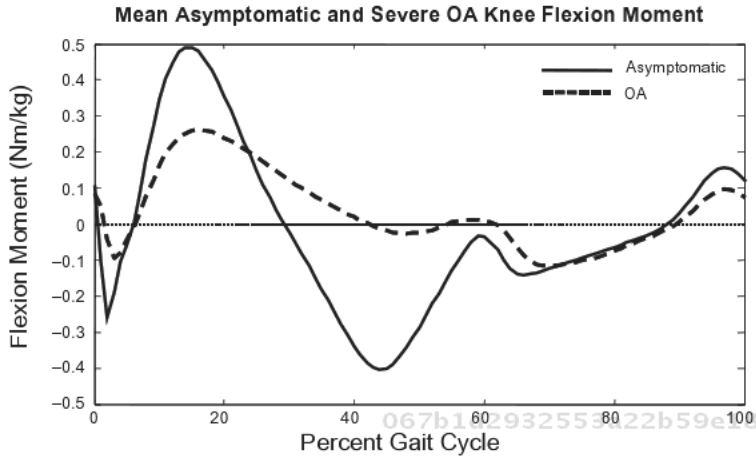


Fig. 6. Knee flexion moment mean waveforms for a group of 63 asymptomatic adults (solid curve) and for a group of 50 persons with severe knee osteoarthritis (dashed curve).[26]

gait.[8,43,73] The results of a recent waveform-based PCA of knee flexion moment waveforms supported the results of these parameter-based studies.[26] The authors found that OA walked with smaller overall knee flexion moments during stance, as well as smaller early stance flexion moments and smaller late stance extension moments (Fig. 6). Some researchers have attributed these sagittal plane moment difference to quadriceps weakness,[73] as decreased quadriceps activation and force production has been associated with knee OA.[50,79] However, it is important to recognize that the flexion moment measured through inverse dynamics is not directly related to muscle function because it represents the *net* contribution of both the flexors and extensors at the knee.

Other researchers have attributed changes in sagittal plane moments to an effort to lessen the painful joint compressive stresses that are associated with knee OA,[99] or to the limited dynamic range of motion and activity with knee OA.[43,79] However, changes in flexion moments have also been reported in OA populations of more moderate severity,[61] suggesting that the changes cannot be explained entirely by the effect of pain or structural changes that are associated with end stages of the disease.

There have been few studies to report differences in the transverse plane moments with knee OA, but some differences have been found. In a parameter-based analysis, Gok *et al.*[43] found greater peak internal rotation moments at the knee with knee OA. Contrary to these results, Landry *et al.*[61] used a waveform-based PCA and found that early stance phase internal rotation moments at the knee were smaller in an osteoarthritic population. The discrepancy in these results may be due to differences in the analyses techniques used, or to differences in the patient populations under study. Landry *et al.* studied a group with moderate knee OA and Gok *et al.* looked at a small group of individuals with early OA.

Few studies have characterized kinetic gait differences at the other joints of the lower extremity. Mundermann *et al.*[82] were one of the few groups to characterize moments at the hip and ankle joints. Using a parameter-based analysis, they found increases in peak hip flexion moments and decreases in peak ankle inversion moments in terminal stance with knee OA. These results suggest that altered joint mechanics from knee OA affects the dynamics of the other connected joints, and these differences should also be considered in gait analyses for a more complete understanding of compensation mechanisms associated with the disease.

### 5.2.1. *The knee adduction moment*

Much more attention has been focused on frontal plane kinetics than the other planes in knee OA gait studies because of speculations on the possible role of frontal plane dynamics in the mechanical progression of the disease. The peak external knee adduction moment in the frontal plane, the torque that tends to adduct the knee during gait, is the gait parameter that has most often been related to knee OA.[8,43,51,65,82,97,109] The peak knee adduction moment has been shown to correspond to increased loads on the medial compartment of the knee,[95,96] and with the medial to lateral bone distribution of the proximal tibia,[53] suggesting the role of the knee adduction moment in disease progression.

Some authors have reported no differences in the peak knee adduction moment with knee OA.[56,61] Both of these studies that did not find differences in peak adduction values analyzed a population of OA subjects of more moderate severity, suggesting that the peak value of the adduction moment waveform may not be the most important parameter to the pathomechanics. The knee adduction moment waveform profile during gait for most asymptomatic persons follows a double-peak pattern like the asymptomatic mean knee adduction moment waveform in Fig. 4. The waveform is characterized by two peaks during stance, with a distinctive dip mid-stance during the weight-acceptance phase of the gait cycle. It has been suggested that the mid-stance value of the knee adduction moment waveform may be more important for differentiating osteoarthritic gait patterns than the peak value.[109] This suggestion was substantiated by some recent waveform-based PCA.[26,29,61] In these studies, a discriminatory PC that described the overall magnitude of the knee adduction moment during stance was identified. The knee OA subjects walked with more sustained knee adduction moments during stance, and this shape difference between their waveform patterns was more discriminatory than peak adduction moment values.

Recognizing the double-peak profile of the knee adduction moment, some researchers have chosen to analyze the first and second peaks of the waveform using parameter-based analyses.[51,82] Hurwitz *et al.*[51] found higher first and second peak knee adduction moments with knee OA. Mundermann *et al.*,[82] comparing a moderate OA and a severe OA group to a control group, found that the more severe

OA group had higher first peak knee adduction moments than the moderate and control groups, and that the moderate group had smaller second peak moments than the other two groups. These results would suggest that persons with moderate OA do not walk with higher than normal knee adduction moments. Analyzing the gait of a similar moderate OA population, Landry *et al.*[61] used a waveform-based PCA and found differences in the shape of the knee adduction moment waveforms of the moderate OA group. The authors found higher overall levels of knee adduction moment during stance, which took into account the magnitude of the moment throughout the entire stance phase. They also found higher mid-stance knee adduction moments in the moderate OA population, a difference that was not detected analyzing only first and second peak knee adduction moment parameters. The parameter-based analysis used by Mundermann *et al.* was unable to detect the knee adduction moment profile differences with the moderate OA group that were detected by Landry *et al.* using a waveform-based PCA.



## 6. Challenges in the Analyses of Knee Osteoarthritis

### 6.1. *Gait disease severity*

Knee OA is a progressive joint disorder that is characterized by clinical, biomechanical, and radiographic symptoms that are constantly changing. The consideration of OA a single disease entity has led to contradictory results in gait studies, and may be the reason why OA research has gone in circles for so many years.[90] It has been suggested that OA is a group of disorders with a similar pathological endpoint that may have differing risk factors depending on the particular pathway to the endpoint, and depending on the stage of advancement of the disease.[31] Most gait analysis studies have focused on single OA subject groups, usually persons with more severely advanced OA.[1,12,26,45,99] More recently, some researchers have turned their attention to more moderate severity OA populations or patients with a spectrum of disease severity in an attempt to understand some of the mechanisms of disease progression.[17,61,83] It has been suggested that the initiation and progression of cartilage damage are very distinct phenomena,[92] and so comparing and interpreting the results of gait analyses should be made in light of the severity level of the disease being presented.



Gait analyses of patient groups with end-stage knee OA can be used to present information about the mechanical condition of the diseased joint, but it should be kept in mind that the changes found are likely secondary to other changes in the diseased joint, and may be influenced by levels of pain, dysfunction, and compensation mechanisms that often characterize the later phases of the disease process. For example, increases in pain levels have been shown to relate to decreased peak external knee adduction moments,[96] so the increased peak knee adduction moments commonly associated with knee OA may not be observed in persons

experiencing great levels of pain during gait trials. Decreases in pain levels have also been related to increases in joint loading,[52] suggested that there is a load-avoidance association with pain. The effect of confounding variables in knee OA studies is of particular importance when studying end-stage populations because there are a number of other changes associated with the later stages of the disease process that may affect joint mechanics, such as slower walking velocities,[56,104] or increased levels of obesity.[78,98]

Individuals with moderate knee OA walk tend to walk with stride characteristics similar to those of an asymptomatic population,[83] so there tend to be no visual mechanical cues of the disease. However, kinematics and kinetic analyses of the gait patterns suggest that there are definite gait differences in moderate OA persons from asymptomatics, and recent literature has suggested that the gait patterns of persons with more moderate knee OA severity levels differ from those with severe levels of the disease. Increased peak knee adduction moments and increased first peaks of the knee adduction moment are commonly reported factors of knee OA for patient groups in more advanced stages of the disease process.[7,51]

Studies of more moderate OA populations have found no differences in peak knee adduction moments compared to a control group,[61,82] and smaller peak and first peak adduction moments compared to a more severe population.[82,97] While this parameter-based results might suggest that changes in the knee adduction moment are an end-stage phenomena of the disease, using a waveform-based PCA study, Landry *et al.*,[61] were able to identify knee adduction moment differences in a moderate OA group. While there were no differences in peak values of the waveforms, the overall magnitude of the knee adduction moments for the moderate OA group were higher than the controls during stance, and the shape of their adduction moment waveforms differed. The moderate OA group exhibited a more sustained knee adduction moment during stance, whereas the control group exhibited the common double-peak adduction moment profile. The major difference was therefore the mid-stance knee adduction moment magnitude, being higher for the moderate OA group than for the control group.

Different biomechanics in the hip joint with differing knee OA severity levels have also been reported. Comparing gait patterns of a less severe and more severe knee OA populations, Mundermann *et al.*[82] found that the more severe population had reduced hip adduction moments compared to the less severe group and a control group. The authors suggested that the difference in the severe group could be explained by a lack of hip abductor muscle strength, whereas as the more moderate group had sufficient strength to maintain an altered trunk position that they were also observing in all OA patients. This hip adduction mechanism may be important in protecting the knee joint against further progression of the disease. Chang *et al.*[17] associated increased hip adduction moments with decreased likelihood of progression of knee OA, with an odds ratio of 0.52.

The knee adduction moment example above suggests that while parameter-based studies may be sufficient for detecting some of the gait changes associated

with knee OA, perhaps more sophisticated techniques, and particularly waveform-based analyses, are required to detect the subtle biomechanical changes that are associated with earlier phases of the disease process. The hip adduction moment example emphasizes the need for further biomechanical studies that include dynamic measures from all lower extremity joints, and perhaps simultaneous information on muscle strength and activation levels.

Another issue in the discussion of severity is the difference between radiographic and symptomatic or clinical knee OA. In an advanced disease state, both conditions are likely present, but distinction should be made between the mechanical and the inflammatory processes of the disease when studying more moderate levels. The radiographic disease reflects changes to joint structure, and the symptomatic disease reflects the illness that is expressed as joint pain and disability. While structural joint change generally leads to the onset of pain, the relationships between structural disease severity and symptoms has been reported as poor.[46] Radiographic changes are only a weak risk factor for symptomatic knee OA.[30] There are many people who have severe structural changes to their joints who are asymptomatic,[33,62] and there are those who experience symptomatic worsening the disease without radiographic progression.[57]



In conclusion, it is imperative that the knee OA researcher is aware of the level of radiographic and clinical severity of the patient population being studied so that no misleading conclusions are drawn and that comparisons between studies are accurate. In the future, it is the hope that more reliable and validated clinical diagnostic tools for knee OA will help to better define the true level of disease in an individual so that progression studies can be carried out more effectively.

### 6.2. *Confounding variables*



Knee OA is a disease process that involves multiple interacting factors, some of which are biomechanical in nature, some that are not. In gait analyses research of knee OA, the goal is often to describe the biomechanics of knee OA gait, or to identify changes in the biomechanics that may be related to the progression of the disease. In the analysis of these biomechanical variables, it is important to realize that it is impossible to completely isolate the biomechanical system. Even within a relatively homogenous study population, every individual included in a study will have a unique combination of biomechanical, physiological, anatomical, neurological, and even emotional factors that combine to define the state of disease on the day of testing, and that result in the observed kinematic and kinetic data that are collected. Factors that may contribute to the quantitative differences that are observed in the data are called confounding variables. These can include biomechanical factors such as walking velocity, or other factors such as body mass, age, and sex. In a review of knee OA gait studies, Messier[76] remarked that it is difficult to discern the effect of OA on gait on the studies that had been conducted

to date at that time because of the population differences between the OA groups and the normal groups that were not being accounted for in the analyses, such as age, weight, height, and walking speed.

### 6.2.1. *Speed*

There was an early recognition in gait analysis of the speed dependence of some gait measures.[2,3] Other stride characteristics have been related to speed. Cadence and step length tend to vary linearly with speed; time of support and time of swing are inversely proportional to speed.[3]

In the sagittal plane, peak knee flexion angles and peak knee flexion moments have been shown to be strongly related to speed.[52,58,64,77] Parameters other than peak values, however, have not been as linked to speed. Brinkmann and Perry[12] calculated correlation coefficients to determine relationships between velocity and the rate of knee flexion/extension and range of motion in arthritic subjects. Positive correlations for osteoarthritic subjects were only found post-total knee replacement surgery, indicating that pre-operative reduced rates and ranges of flexion/extension could not be attributed to reduced walking velocities with knee OA. In a waveform-based analysis, Landry *et al.*[61] found a speed effect in the overall magnitude of the knee flexion angle during the entire gait cycle, using a two-factor repeated measure ANOVA. They also found that the early stance flexion moment and the overall magnitude of the flexion moment during stance were both positively related to walking speed.

The knee adduction moment in the frontal plane has not been as related to speed as the sagittal plane measures. Although the problem of comparing peak knee adduction moments without controlling for walking speed has been raised,[76,83] Kirtley *et al.*[58] found that the peak knee adduction moment is virtually independent of speed. Speed effects on the adduction moment were found however in the waveform-based PCA used by Landry *et al.*[61] The overall magnitude of the knee adduction moment in stance did not relate to speed, but the shape of the waveform did relate to speed. Faster speeds related to larger first peaks of the knee adduction moment relative to a smaller mid-stance adduction moment value. In a similar study, Diamond *et al.*[29] used analysis of covariance techniques combined with PCA to study knee adduction moment differences with OA, with speed as a covariate. Again, differences in the overall magnitude of the adduction moment during the stance phase of the gait cycle were not confounded by speed, but differences in the first peak of the adduction moment and the shape of the adduction moment profile were due entirely to the effect of speed.

Consideration of speed effects may also help to explain discrepancies in the results of different studies. Kaufman *et al.*[56] and Weidenhielm *et al.*,[109] two groups that did *not* report a significant difference in the peak knee adduction moments of knee OA subjects, suggested that the lack of difference may be a result of slower walking speeds or the BMI of the subjects that they studied. In studying a similar

patient group but selecting gait trials at approximately the same speed, Baliunas *et al.*[7] reported greater peak knee adduction moments in the OA population than the controls.

The effect of speed in gait analyses is a particularly important consideration in knee OA studies because persons with diseased joints often walk slower than their normal counterparts.[3,72,87] In interpreting the results of a gait analysis, it is therefore very important to consider whether or not the osteoarthritic population walked with a slower average walking velocity than the asymptomatic population. If this is the case, results should be interpreted in light of the speed effects described in the literature. Many OA gait studies, particularly those on populations of severe knee OA individuals, showed speed differences between the OA group and the asymptomatic group.[26,43,56] The biomechanical differences reported in these studies should be interpreted in consideration of the speed differences between the groups. However, the results, however, are still valid because, regardless of any speed effects, they characterize the true mechanical state of the joint during the walking trial. The results of such studies are arguably more valid than those of a study design where speed is controlled. Some researchers have selected gait trials at a speed closest to a pre-determined velocity.[7,51,80,97] However, the moment measured at this pre-selected speed may not reflect the mechanical loads that occur normally during gait, and this method does not capture a subject's natural mechanics.



### 6.2.2. *Obesity*

Obesity is probably the most well-established risk factor for knee OA.[40–42,69] Obesity encourages immobility, which can inadvertently lead to gait changes that may not be related to disease-associated impairments in gait. The disability associated with knee OA can also pre-dispose persons with the disease to obesity. The interaction of obesity with the disease process of knee OA appears to be both systemic in nature,[105] and also mechanical in terms of increases in joint loading.[4] It has been shown in one investigation that every pound of excess weight is multiplied threefold to sixfold in terms of its effect on loading.[36]



BMI, a relative obesity measure that is calculated as body mass divided by height squared, is the most commonly reported obesity measure in gait analysis that has been shown to relate to some gait variables. Messier *et al.*[78] found BMI to be positively correlated with peak knee extension angles, the peak magnitude of the vertical ground reaction force, vertical impulse and the rate of loading in a large group of elderly knee OA patients. Kaufman *et al.*[56] found a significant relationship between BMI and the external knee flexion moment. They suggested that subjects with increased BMI protected their knees by decreasing the knee extensor moment. In a multivariate waveform-based analysis using PCA, Astephen and Deluzio[6] identified a very discriminatory gait feature that was localized to the loading response phase of the gait cycle (i.e., approximately the first 12%), and had the greatest contribution from BMI. This finding suggested that the effects of BMI

on gait dynamics for persons with knee OA are great during the initial phase of the gait cycle.

Joint malalignment in the frontal plane, which is common in individuals with knee OA,[66,71,98,108] is thought to play a large role in the relationship between obesity and OA in terms of joint mechanics.[37,98] Obese persons with malalignment of the knee will have especially high levels of focal loading within the joint.

The effect of obesity on joint dynamics is yet unclear, but previous results point to relationships between obesity measures and gait variables. It is therefore important in a gait analysis to either account for an obesity measure in the analysis as a confounding variable, or to at least consider the effects of obesity on the results obtained, if the populations under study are not matched in terms of obesity.

#### 6.2.3. *Age*



Age has been shown to be a substantial risk factor for radiographic and symptomatic OA at all sites, including the knee joint, and increasing age is associated with increasing prevalence.[32,35] Aging is associated with decreased strength, increased muscle atrophy and frailty,[34] as well as a decreased quantity of muscle fibers and a decreased number of motor units.[14] These factors lead to the potential for differences in gait mechanics that can be attributed to age. Some studies have studied osteoarthritic populations with substantially higher mean ages than the control groups to which they were compared.[12,45] Every effort should be made in the design of gait analysis studies to use age-matched groups to remove any confounding effects with aging.

#### 6.2.4. *Sex*



Gender is another important consideration in gait studies. Knee OA is two to three times more prevalent in females than in males.[13] The effect of sex on OA and biomechanics, however, remains unclear. Several authors have documented gait changes in females with OA that are different then their male counterparts,[74,56,107,109] but few have explored any causative effect it may have on the disease. Some studies have indicated that males exhibit gait patterns more consistent with OA gait than females[56,109]; however, results concerning differences in the adduction moment have been conflicting.[107,109]

One of the most comprehensive studies on sex differences in the biomechanical effects of knee OA subject was recently performed.[74] In this investigation, significant sex effects were found in the internal rotation angle, the adduction moment and flexion moment at the hip and the internal rotation moment at the knee. Females walked with significantly less hip internal rotation, smaller hip flexion moments, larger hip adduction moments, and smaller internal/external rotation moments at the knee than their male counterparts. It is also important to note that none of the biomechanical differences reported could be attributed to differences in anthropometrics, stride characteristics, strength, pain, stiffness, function or

radiographic disease severity between the sexes. Thus, the sex association of gait measures is one that should be considered in spite of any other differences between the populations. Similar to age, sex should be considered in the study design of gait analyses, or treated as a possible confounding variable in the analyses.

## 7. Future Directions in Gait Analysis for Knee Osteoarthritis: Multivariate, Multidisciplinary, Multi-Center Analyses

Our understanding of the biomechanics of knee OA has increased steadily over the past few decades through numerous gait analysis studies, many of which were included in the discussions of the preceding sections. Many of the biomechanical changes that are characteristic of the disease are now well-established. Gait analysis research for knee OA is now beginning to change its focus, with the global purpose of the research now aimed at developing an understanding of the biomechanical pathways of the disease. OA is now conceived as the endpoint of a complex series of events, rooted in factors that have been recognized as associated with OA for many years.[68] This new focus will help in developing more early diagnosis strategies and early treatment options that may precede and remove the need for the common invasive total knee replacement, still the number one treatment of the disease.

The quest for understanding pathological pathways of knee OA with gait analysis research will require studies designed to capture very comprehensive data sets that include not only complete joint dynamics of the lower extremity, but also neuromuscular information from electromyographic data, as well as complete subject demographic information so that all possible confounding variables can be accounted for in the analysis. Analyses of these data should be multivariate in nature, such that they preserve the interactions between these variables during gait. Few multidimensional gait data analyses have been used in the past for the study of knee OA,[5,6] and none have comprehensively included multiple gait and electromyographic measures. To understand the mechanisms of either compensation due to the disease or of progression of the disease, an understanding of how neuromuscular strategies relate to observed joint dynamics is required.

Knee OA involves not only mechanical factors, but biological, chemical and even psychological factors as well. It is important to understand how the various risk factors and characteristics of knee OA interact to understand the pathways of disease and to develop appropriate treatment strategies. Teams of researchers of various disciplines will be needed to develop studies that are designed to capture the multiple factors of the disease.

It is the hope that multi-center research will become more common-place in the future. As a global research community, we must define our methods, share our data and map out the biomechanical course of the disease using appropriately sophisticated analysis tools. Discrepancies between analysis results due to lack of information about study populations, data collection methods, and data analysis

techniques inhibit our learning of the disease and prevent the quick translation of biomechanical findings into clinical practice. With the current state of the art in motion capture there is a great deal of information that has already been collected for knee OA. It is the assimilation and extraction of meaningful information from the data that has delayed our knowledge.

Longitudinal studies, although time-consuming to perform, will likely become an important part of gait analysis research for knee OA in the future. Longitudinal studies can provide information on biomechanical changes that happen throughout the course of the disease, and can be used to better understand which factors may be causative in nature. In the more immediate future, more cross-sectional studies on populations of varying knee OA severity will likely be used as a more time-efficient alternative to longitudinal studies.

Finally, biomechanical modeling, we believe, will begin to play a larger role in gait analysis studies for knee OA. Information gained from dynamic simulations has the potential to provide information on causal relationships between many of the knee OA factors. It has been suggested that to understand how muscles coordinate walking in humans, and how the system changes in individuals with impairments, the causal relationship between EMG patterns and gait kinetics and kinematics has to be ascertained.[112] As well, dynamic simulations are a very cost-effective and ethical way to investigate the influence of changes to the human musculoskeletal system, which can be difficult to treat experimentally. These simulations will become more important as knee OA research turns to developing less-invasive, early treatment options for the disease.



## References

1. K. S. Al Zahrani and A. M. Bakheit, A study of the gait characteristics of patients with chronic osteoarthritis of the knee, *Disabil. Rehabil.* **24** (2002) 275–280.
2. T. P. Andriacchi, J. O. Galante and R. W. Fermier, The influence of total knee-replacement design on walking and stair-climbing, *J. Bone Joint. Surg. [Am]* **64A** (1982) 1328–1335.
3. T. P. Andriacchi, J. A. Ogle and J. O. Galante, Walking speed as a basis for normal and abnormal gait measurements, *J. Biomech.* **10** (1977) 261–268.
4. J. P. Arokoski, J. S. Jurvelin, U. Vaatainen and H. J. Helminen, Normal and pathological adaptations of articular cartilage to joint loading, *Scand. J. Med. Sci. Sports* **10** (2000) 186–198.
5. J. L. Astephen and K. J. Deluzio, A multivariate gait data analysis technique: Application to knee osteoarthritis, *Proc. Inst. Mech. Eng. [H]* **218** (2004) 271–279.
6. J. L. Astephen and K. J. Deluzio, Changes in frontal plane dynamics and the loading response phase of the gait cycle are characteristic of severe knee osteoarthritis application of a multidimensional analysis technique, *Clin. Biomech. (Bristol., Avon.)* **20** (2005) 209–217.
7. A. J. Baliunas, D. E. Hurwitz, A. B. Ryals, A. Karrar, J. P. Case, J. A. Block and T. P. Andriacchi, Increased knee joint loads during walking are present in subjects with knee osteoarthritis, *Osteoarthr. Cartil.* **10** (2002) 573–579.

8. A. J. Baliunas, A. R. Ryals, D. E. Hurwitz, A. Karrar and T. P. Andriacchi, Gait adaptations associated with early radiographic tibiofemoral knee osteoarthritis (Orthopaedic Research Society, Orlando, Florida, 2000), p. 260.
9. J. G. Barton and A. Lees, An application of neural networks for distinguishing gait patterns on the basis of hip-knee joint angle diagrams, *Gait Posture* **5** (1997) 28–33.
10. R. Begg and J. Kamruzzaman, A machine learning approach for automated recognition of movement patterns using basic, kinetic and kinematic gait data, *J. Biomech.* **38** (2005) 401–408.
11. W. Braune and O. Fischer, *The Human Gait* (Springer-Verlag, Berlin, 1987) (Orig. Published 1895–1904).
12. J. R. Brinkmann and J. Perry, Rate and range of knee motion during ambulation in healthy and arthritic subjects, *Phys. Ther.* **65** (1985) 1055–1060.
13. J. A. Buckwalter and D. R. Lappin, The disproportionate impact of chronic arthralgia and arthritis among women, *Clin. Orthop. Relat. Res.* (2000) 159–168.
14. M. J. Campbell, A. J. McComas and F. Petito, Physiological changes in ageing muscles, *J Neurol. Neurosurg. Psychiatry* **36** (1973) 174–182.
15. A. Cappozzo, U. Della, A. Leardini and L. Chiari, Human movement analysis using stereophotogrammetry. Part 1: Theoretical background, *Gait Posture* **21** (2005) 186–196.
16. P. R. Cavanagh and J. D. Henley, The computer era in gait analysis, *Podiatr. Med. Surg.* **10** (1993) 471–484.
17. A. Chang, K. Hayes, D. Dunlop, J. Song, D. Hurwitz, S. Cahue and L. Sharma, Hip abduction moment and protection against medial tibiofemoral osteoarthritis progression, *Arthritis Rheum.* **52** (2005) 3515–3519.
18. T. Chau, A review of analytical techniques for gait data. Part 1: Fuzzy, statistical and fractal methods, *Gait Posture* **13** (2001) 49–66.
19. T. Chau, A review of analytical techniques for gait data. Part 2: Neural network and wavelet methods, *Gait Posture* **13** (2001) 102–120.
20. L. Chiari, Croce U. Della, A. Leardini and A. Cappozzo, Human movement analysis using stereophotogrammetry. Part 2: Instrumental errors, *Gait Posture* **21** (2005) 197–211.
21. J. D. Childs, P. J. Sparto, G. K. Fitzgerald, M. Bizzini and J. J. Irrgang, Alterations in lower extremity movement and muscle activation patterns in individuals with knee osteoarthritis, *Clin. Biomech. (Bristol., Avon.)* **19** (2004) 44–49.
22. M. C. Collopy, M. P. Murray, G. M. Gardner, R. A. DiUlio and D. R. Gore, Kinesiologic measurements of functional performance before and after geometric total knee replacement: One-year follow-up of twenty cases, *Clin. Orthop. Relat. Res.* (1977) 196–202.
23. D. Cooke, A. Scudamore, J. Li, U. P. Wyss, J. T. Bryant and P. Costigan, Axial lower-limb alignment: Comparison of knee geometry in normal volunteers and osteoarthritis patients, *Osteoarthritis Cartil.* **5** (1997) 39–47.
24. B. L. Davis and C. L. Vaughan, Phasic behavior of emg signals during gait — Use of multivariate-statistics, *J. Electromyogr. Kinesiol.* **3** (1993) 51–60.
25. Croce U. Della, A. Leardini, L. Chiari and A. Cappozzo, Human movement analysis using stereophotogrammetry. Part 4: Assessment of anatomical landmark misplacement and its effects on joint kinematics, *Gait Posture* **21** (2005) 226–237.
26. K. J. Deluzio and J. L. Astephen, Biomechanical Features of gait waveform data associated with knee osteoarthritis an application of principal component analysis, *Gait Posture* (2006).

27. K. J. Deluzio, U. P. Wyss, P. Costigan, C. Sorbie and B. Zee, Gait assessment in unicompartmental knee arthroplasty patients: Principal component modelling of gait waveforms and clinical status, *Hum. Movement Sci.* **18** (1999) 701–711.
28. K. J. Deluzio, U. P. Wyss, B. Zee, P. A. Costigan and C. Sorbie, Principal component models of knee kinematics and kinetics: Normal versus pathological gait patterns, *J. Hum. Movement Sci.* **16** (1997) 201–217.
29. L. E. Diamond, K. J. Deluzio, C. L. Hubley-Kozey, J. Kozey and W. D. Stanish, *Adduction Moment and Neuromuscular Patterns During Gait in Knee Osteoarthritis Patients* (Dalhousie University, 2005).
30. P. A. Dieppe, Relationship between symptoms and structural change in osteoarthritis: What are the important targets for therapy? *J. Rheumatol.* **32** (2005) 1147–1149.
31. P. A. Dieppe and L. S. Lohmander, Pathogenesis and management of pain in osteoarthritis, *Lancet* **365** (2005) 965–973.
32. M. Dougados, A. Gueguen, M. Nguyen, A. Thiesce, V. Listrat, L. Jacob, J. P. Nakache, K. R. Gabriel, M. Lequesne and B. Amor, Longitudinal radiologic evaluation of osteoarthritis of the knee, *J. Rheumatol.* **19** (1992) 378–384.
33. M. Englund and L. S. Lohmander, Risk factors for symptomatic knee osteoarthritis fifteen to twenty-two years after meniscectomy, *Arthritis Rheum.* **50** (2004) 2811–2819.
34. J. A. Faulkner, S. V. Brooks and E. Zerba, Skeletal muscle weakness and fatigue in old age: Underlying mechanisms, *Annu. Rev. Gerontol. Geriatr.* **10** (1990) 147–166.
35. D. T. Felson, The epidemiology of knee osteoarthritis: Results from the framingham osteoarthritis study, *Semin. Arthritis Rheum.* **20** (1990) 42–50.
36. D. T. Felson and C. E. Chaisson, Understanding the Relationship between body weight and osteoarthritis, *Baillieres Clin. Rheumatol.* **11** (1997) 671–681.
37. D. T. Felson, D. R. Gale, Gale M. Elon, J. Niu, D. J. Hunter, J. Goggins and M. P. Lavalley, Osteophytes and progression of knee osteoarthritis, *Rheumatol. (Oxford)* **44** (2005) 100–104.
38. D. T. Felson, R. C. Lawrence, P. A. Dieppe, R. Hirsch, C. G. Helmick, J. M. Jordan, R. S. Kington, N. E. Lane, M. C. Nevitt, Y. Zhang, M. Sowers, T. McAlindon, T. D. Spector, A. R. Poole, S. Z. Yanovski, G. Ateshian, L. Sharma, J. A. Buckwalter, K. D. Brandt and J. F. Fries, Osteoarthritis: New insights. Part 1: The disease and its risk factors, *Ann. Intern. Med.* **133** (2000) 635–646.
39. D. T. Felson, A. Naimark, J. Anderson, L. Kazis, W. Castelli and R. F. Meenan, The prevalence of knee osteoarthritis in the elderly: The framingham osteoarthritis study, *Arthritis Rheum.* **30** (1987) 914–918.
40. D. T. Felson, Y. Zhang, M. T. Hannan, A. Naimark, B. Weissman, P. Aliabadi and D. Levy, Risk factors for incident radiographic knee osteoarthritis in the elderly: The framingham study, *Arthritis Rheum.* **40** (1997) 728–733.
41. N. M. Fisher and D. R. Pendergast, Reduced muscle function in patients with osteoarthritis, *Scand. J. Rehab. Med.* **29** (1997) 213–221.
42. A. C. Gelber, M. C. Hochberg, L. A. Mead, N. Y. Wang, F. M. Wigley and M. J. Klag, Body mass index in young men and the risk of subsequent knee and hip osteoarthritis, *Am. J. Med.* **107** (1999) 542–548.
43. H. Gok, S. Ergin and G. Yavuzer, Kinetic and kinematic characteristics of gait in patients with medial knee Arthrosis, *Acta Orthop. Scand.* **73** (2002) 647–652.
44. E. S. Grood and W. J. Suntay, A joint coordinate system for the clinical description of three-dimensional motions: Application to the knee, *J. Biomech. Eng.* **105** (1983) 136–144.

45. A. N. Gyory, E. Y. Chao and R. N. Stauffer, Functional evaluation of normal and pathologic knees during gait, *Arch. Phys. Med. Rehabil.* **57** (1976) 571–577.
46. M. T. Hannan, D. T. Felson and T. Pincus, Analysis of the discordance between radiographic changes and knee pain in osteoarthritis of the knee, *J. Rheumatol.* **27** (2000) 1513–1517.
47. J. M. Hausdorff, Y. Ashkenazy, C. K. Peng, P. C. Ivanov, H. E. Stanley and A. L. Goldberger, When human walking becomes random walking: Fractal analysis and modeling of gait rhythm fluctuations, *Physica A* **302** (2001) 138–147.
48. B. W. Heller, P. H. Veltink, N. J. M. Rijkhoff, W. L. C. Rutten and B. J. Andrews, Reconstructing muscle activation during normal walking — A comparison of symbolic and connectionist machine learning techniques, *Biol. Cybern.* **69** (1993) 327–335.
49. S. H. Holzreiter and M. E. Kohle, Assessment of gait patterns using neural networks, *J. Biomech.* **26** (1993) 645–651.
50. M. V. Hurley, D. L. Scott, J. Rees and D. J. Newham, Sensorimotor changes and functional performance in patients with knee osteoarthritis, *Ann. Rheum. Dis.* **56** (1997) 641–648.
51. D. E. Hurwitz, A. B. Ryals, J. P. Case, J. A. Block and T. P. Andriacchi, The knee adduction moment during gait in subjects with knee osteoarthritis is more closely correlated with static alignment than radiographic disease severity, toe out angle and pain, *J. Orthop. Res.* **20** (2002) 101–107.
52. D. E. Hurwitz, A. R. Ryals, J. A. Block, L. Sharma, T. J. Schnitzer and T. P. Andriacchi, Knee pain and joint loading in subjects with osteoarthritis of the knee, *J. Orthop. Res.* **18** (2000) 572–579.
53. D. E. Hurwitz, D. R. Sumner, T. P. Andriacchi and D. A. Sugar, Dynamic knee loads during gait predict proximal tibial bone distribution, *J. Biomech.* **31** (1998) 423–430.
54. A. R. Ismail and S. S. Asfour, Discrete wavelet transform: A tool in smoothing kinematic data, *J. Biomech.* **32** (1999) 317–321.
55. J. E. Jackson, *A User's Guide to Principal Components* (John Wiley & Sons, New York, 1991).
56. K. R. Kaufman, C. Hughes, B. F. Morrey, M. Morrey and K. N. An, Gait characteristics of patients with knee osteoarthritis, *J. Biomech.* **34** (2001) 907–915.
57. W. Y. Kim, J. Richards, R. K. Jones and A. Hegab, A new biomechanical model for the functional assessment of knee osteoarthritis, *Knee* **11** (2004) 225–231.
58. C. Kirtley, M. W. Whittle and R. J. Jefferson, Influence of walking speed on gait parameters, *J. Biomed. Eng.* **7** (1985) 282–288.
59. R. D. Komistek, T. R. Kane, M. Mahfouz, J. A. Ochoa and D. A. Dennis, Knee mechanics: A review of past and present techniques to determine *in vivo* loads, *J. Biomech.* **38** (2005) 215–228.
60. M. S. Kuster, G. A. Wood, G. W. Stachowiak and A. Gachter, Joint load considerations in total knee replacement, *J. Bone and Joint Surgery (B)* **79(B)** (1997) 109–113.
61. S. C. Landry, K. A. Mckean, C. L. Hubley-Kozey, W. D. Stanish and K. J. Dleuzio, Knee biomechanics of moderate OA patients measured during gait at a self-selected and fast walking speed, *J. Biomech.* (2006).
62. J. S. Lawrence, J. M. Bremner and F. Bier, Osteo-arthrosis: Prevalence in the population and relationship between symptoms and X-ray changes, *Ann. Rheum. Dis.* **25** (1966) 1–24.

63. A. Leardini, L. Chiari, Croce U. Della and A. Cappozzo, Human movement analysis using stereophotogrammetry. Part 3. Soft tissue artifact assessment and compensation, *Gait Posture* **21** (2005) 212–225.
64. J. L. Lelas, G. J. Merriman, P. O. Riley and D. C. Kerrigan, Predicting peak kinematic and kinetic parameters from gait speed, *Gait Posture* **17** (2003) 106–112.
65. M. D. Lewek, K. S. Rudolph and L. Snyder-Mackler, Control of frontal plane knee laxity during gait in patients with medial compartment knee osteoarthritis, *Osteoarthritis Cartil.* **12** (2004) 745–751.
66. L. S. Lohmander and D. Felson, Can we identify a 'high risk' patient profile to determine who will experience rapid progression of osteoarthritis? *Osteoarthritis Cartil.* **12** (2004) S49–S52.
67. P. Loslever, E. M. Laassel and J. C. Angue, Combined statistical study of joint angles and ground reaction forces using component and multiple correspondence analysis, *IEEE Trans. Biomed. Eng.* **41** (1994) 1160–1167.
68. B. Mandelbaum and D. Waddell, Etiology and pathophysiology of osteoarthriti, *Orthoped.* **28** (2005) s207–s214.
69. N. J. Manek, D. Hart, T. D. Spector and A. J. MacGregor, The association of body mass index and osteoarthritis of the knee joint: An examination of genetic and environmental influences, *Arthritis Rheum.* **48** (2003) 1024–1029.
70. B. F. J. Manley, *Multivariate Statistical Methods: A Primer*, Vol. 2 (Chapman & Hall, London, New York, 1997).
71. P. G. Maquet, A. J. Van de Berg and J. C. Simonet, Femorotibial weight-bearing areas. experimental determination, *J. Bone Joint Surg. Am.* **57** (1975) 766–771.
72. E. Mattsson, L. A. Brostrom and D. Linnarsson, Changes in walking ability after knee replacement, *Int. Orthop.* **14** (1990) 277–280.
73. T. E. McAlindon, C. Cooper, J. R. Kirwan and P. A. Dieppe, Determinants of disability in osteoarthritis of the knee, *Ann. Rheum. Dis.* **52** (1993) 258–262.
74. K. A. Mckean, C. S. N. Landry, C. L. Hubley-Kozey, M. J. Dunbar, W. D. Stanish and K. J. Deluzio, Gender differences exist in osteoarthritic gait, *Clin. Biomech.* (2006).
75. L. A. Merkle, C. S. Layne, J. J. Bloomberg and J. J. Zhang, Using factor analysis to identify neuromuscular synergies during treadmill walking, *J. Neurosci. Meth.* **82** (1998) 207–214.
76. S. P. Messier, Osteoarthritis of the knee and associated factors of age and obesity: Effects on gait, *Med. Sci. Sports Exer.* **26** (1994) 1446–1452.
77. S. P. Messier, P. DeVita, R. E. Cowan, J. Seay, H. C. Young and A. P. Marsh, Do older adults with knee osteoarthritis place greater loads on the knee during gait? A preliminary study, *Arch. Phys. Med. Rehabil.* **86** (2005) 703–709.
78. S. P. Messier, W. H. Ettinger, T. E. Doyle, T. Morgan, M. K. James, M. L. O'Toole and R. Burns, Obesity: Effects on gait in a osteoarthritic population, *J. Appl. Biomech.* **12** (1996) 161–172.
79. S. P. Messier, R. F. Loeser, J. L. Hoover, E. L. Semble and C. M. Wise, Osteoarthritis of the knee: Effects on gait, strength and flexibility [published erratum appears in *Arch. Phys. Med. Rehabil.* **73** (1992) 252]. *Arch. Phys. Med. Rehabil.* **73** (1992) 29–36.
80. T. Miyazaki, M. Wada, H. Kawahara, M. Sato, H. Baba and S. Shimada, Dynamic load at baseline can predict radiographic disease progression in medial compartment knee osteoarthritis, *Ann. Rheum. Dis.* **61** (2002) 617–622.
81. J. B. Morrison, Bioengineering analysis of forces actions transmitted by the knee joint, *Biomed. Eng.* **4** (1968) 164–170.

82. A. Mundermann, C. O. Dyrby and T. P. Andriacchi, Secondary gait changes in patients with medial compartment knee osteoarthritis: Increased load at the ankle, knee and hip during walking, *Arthritis Rheum.* **52** (2005) 2835–2844.
83. A. Mundermann, C. O. Dyrby, D. E. Hurwitz, L. Sharma and T. P. Andriacchi, Potential strategies to reduce medial compartment loading in patients with knee osteoarthritis of varying severity: Reduced walking speed, *Arthritis Rheum.* **50** (2004) 1172–1178.
84. B. M. Nigg and W. Herzog, *Biomechanics of the Musculoskeletal System* (John Wiley & Sons, Chichester, 1999).
85. M. J. O'Malley, M. F. Abel, D. L. Damiano and C. L. Vaughan, Fuzzy clustering of children with cerebral palsy based on temporal-distance gait parameters, *IEEE Trans. Rehabil. Eng.* **5** (1997) 300–309.
86. S. C. O'Reilly, A. Jones, K. R. Muir and M. Doherty, Quadriceps weakness in knee osteoarthritis: The effect on pain and disability, *Ann. Rheum. Dis.* **57** (1998) 588–594.
87. S. J. Olney, M. P. Griffin and I. D. McBride, Temporal, kinematic, and kinetic variables related to gait speed in subjects with hemiplegia: A regression approach, *Phys. Ther.* **74** (1994) 872–885.
88. K. S. Olree and C. L. Vaughan, Fundamental patterns of bilateral muscle-activity in human locomotion, *Biol. Cybern.* **73** (1995) 409–414.
89. J. Perry, *Gait Analysis Normal and Pathological Function* (McGraw-Hill Ryerson Limited, Whitby, Ontario, 1992).
90. E. L. Radin, Who gets osteoarthritis and why? An update, *J. Rheumatol.* **32** (2005) 1136–1138.
91. E. L. Radin and I. L. Paul, Role of mechanical factors in pathogenesis of primary osteoarthritis, *The Lancet* (1972) 519–522.
92. E. L. Radin and R. M. Rose, Role of subchondral bone in the initiation and progression of cartilage damage, *Clin. Orthop. Relat. Res.* (1986) 34–40.
93. E. L. Radin, K. H. Yang, C. Riegger, V. L. Kish and J. J. O'Connor, Relationship between lower limb dynamics and knee joint pain, *J. Orthop. Res.* **9** (1991) 398–405.
94. H. Sadeghi, F. Prince, S. Sadeghi and H. Labelle, Principal component analysis of the power developed in the flexion/extension muscles of the hip in able-bodied gait, *Med. Eng. Phys.* **22** (2000) 703–710.
95. O. D. Schipplein and T. P. Andriacchi, Interaction between active and passive knee stabilizers during level walking, *J. Orthop. Res.* **9** (1991) 113–119.
96. T. J. Schnitzer, J. M. Popovich, G. B. Andersson and T. P. Andriacchi, Effect of piroxicam on gait in patients with osteoarthritis of the knee, *Arthritis Rheum.* **36** (1993) 1207–1213.
97. L. Sharma, D. E. Hurwitz, E. J. Thonar, J. A. Sum, M. E. Lenz, D. D. Dunlop, T. J. Schnitzer, G. Kirwan-Mellis and T. P. Andriacchi, Knee adduction moment, serum hyaluronan level and disease severity in medial tibiofemoral osteoarthritis, *Arthritis Rheum.* **41** (1998) 1233–1240.
98. L. Sharma, C. Lou, S. Cahue and D. Dunlop, *The Mechanism of the Effect of Obesity in Patients with Knee OA: The Mediating Role of Malalignment*, Vol. 261 (Orthopaedic Research Society, Orlando, Florida, 2000).
99. R. N. Stauffer, E. Y. Chao and A. N. Gyory, Biomechanical gait analysis of the diseased knee joint, *Clin. Orthop. Relat. Res.* (1977) 246–255.
100. D. H. Sutherland, The evolution of clinical gait analysis. Part I: Kinesiological EMG, *Gait Posture* **14** (2001) 61–70.
101. D. H. Sutherland, The evolution of clinical gait analysis. Part II: Kinematics, *Gait Posture* **16** (2002) 159–179.

102. D. H. Sutherland, The evolution of clinical gait analysis. Part III: Kinetics and energy assessment, *Gait Posture* **21** (2005) 447–461.
103. T. Tan, L. Guan and J. Burne, A real-time image analysis system for computer-assisted diagnosis of neurological disorders, *Real-Time Imag.* **5** (1999) 253–269.
104. L. F. Teixeira and S. J. Olney, Relationship between alignment and kinematic and kinetic measures of the knee of osteoarthritic elderly subjects in level walking, *Clin. Biomech. (Bristol., Avon.)* **11** (1996) 126–134.
105. J. L. van Saase, J. P. Vandenbroucke, L. K. van Romunde and H. A. Valkenburg, Osteoarthritis and obesity in the general population. A relationship calling for an explanation, *J. Rheumatol.* **15** (1988) 1152–1158.
106. M. P. Wachowiak, G. S. Rash, P. M. Quesada and A. H. Desoky, Wavelet-based noise removal for biomechanical signals: A comparative study, *IEEE Trans. Biomed. Eng.* **47** (2000) 360–368.
107. M. Wada, Y. Maezawa, H. Baba, S. Shimada, S. Sasaki and Y. Nose, Relationships among bone mineral densities, static alignment and dynamic load in patients with medial compartment knee osteoarthritis, *Rheumatol. (Oxford)* **40** (2001) 499–505.
108. H. Wang and S. J. Olney, Relationships between alignment, kinematic and kinetic measures of the knee of normal elderly subjects in level walking, *Clin. Biomech.* **9** (1994) 245–252.
109. L. Weidenhielm, O. K. Svensson, L. A. Brostrom and E. Mattsson, Adduction moment of the knee compared to radiological and clinical parameters in moderate medical osteoarthrosis of the knee, *Ann. Chir. Gynaecol.* **83** (1994) 236–242.
110. M. W. Whittle and R. J. Jefferson, Functional biomechanical assessment of the oxford meniscal knee, *J. Arthroplasty* **4** (1989) 231–243.
111. D. A. Winter, *Biomechanics of Human Movement* (John Wiley & Sons, New York, 1979)
112. F. E. Zajac, R. R. Neptune and S. A. Kautz, Biomechanics and muscle coordination of human walking: Part II: Lessons from dynamical simulations and clinical implications, *Gait Posture* **17** (2003) 1–17.

# CHAPTER 3

# FINITE ELEMENT MODELING OF THE MICROARCHITECTURE OF CANCELLOUS BONE: TECHNIQUES AND APPLICATIONS

AMIT GEFEN
*Department of Biomedical Engineering*
*Tel Aviv University, Tel Aviv 69978, Israel*
*gefen@eng.tau.ac.il*



Cancellous bone is a complex structure with mechanical behavior that is affected by bone tissue-level mechanical properties as well as by the shape of trabeculae, their spatial arrangement, and their level of connectivity. The increasing public health threat of osteoporosis motivates investigations of the mechanical behavior of cancellous bone with particular emphasis on characterizing its stiffness and strength as function of its tissue-level properties and microarchitectural structure. The small scale at which mechanical phenomena occur in cancellous bone (100–1000 $\mu$m) limits experimental work. Thus, finite element modeling became a superior tool for studying load-bearing phenomena at the trabecular scale. This chapter describes modeling techniques and provides examples for finite element simulations of load-bearing conditions in cancellous bone microarchitecture. After discussing some general considerations in modeling the geometry and mechanical properties of cancellous bone, the two dominant modeling approaches, micro-imaging-based modeling and generic lattice modeling, are reviewed. The single-trabecula building-block, a standard (generic) model component for large-scale finite element models of cancellous bone, is employed here to study several load-bearing phenomena in normal and osteoporotic cancellous bone, including studies of the apparent compression behavior of cancellous bone, the strain inhomogeneity in individual trabeculae, and buckling behavior of trabeculae.



*Keywords*: Tissue mechanical properties; trabecular bone mechanics; spongy bone; osteoporosis; trabeculae.

## Nomenclature

| | |
|---|---|
| 2D: | two-dimensional |
| 3D: | three-dimensional |
| $A_{\mathrm{Tb}}(z)$: | cross-sectional area of a trabecula along its longitudinal axis $z$ |
| BMD: | bone mineral density (at the tissue-level) |
| CT: | computed tomography |
| $E_{\mathrm{cb}}$: | apparent elastic modulus of cancellous bone |
| $E_{\mathrm{t}}$: | tissue-level elastic modulus of cancellous bone |

$F_c$: compression force through a trabecular column
$F_{c(critical)}$: critical force through a trabecular column that leads to buckling
FE: finite element
$I_t$: moment of inertia of a trabecula
$L$: length of a trabecula
$L_{cb}$: face length of a cubic trabecular lattice
MRI: magnetic resonance imaging
QCT: quantitative computed tomography
$r(z)$: local radius of a trabecula along its longitudinal axis $z$
Tb.Th: trabecular thickness
Tb.Sp: trabecular separation
$t_{max}$: maximal thickness at the edge of a trabecula
$t_{min}$: minimal thickness at the center of a trabecula
$r_{min}$: minimal radius of a trabecula (at its center)
$V_f$: volume fraction of cancellous bone (% bone per whole specimen volume)
$V_{Tb}$: volume of an individual trabecula
$\alpha, \beta, \gamma, \lambda, \eta$: shape constants of a trabecula
$\delta_{Tb}$: axial deformation of a trabecula in compression
$\Delta\varepsilon$: difference between maximal strain $\varepsilon_{max}$ and minimal strain $\varepsilon_{min}$ along a trabecula
$\varepsilon_{cb}$: apparent compression strain in a trabecular lattice
$\nu_t$: tissue-level Poisson's ratio of cancellous bone
$\rho_{cb}$: apparent density of a trabecular lattice
$\rho_t$: tissue-level density of a trabecula
$\sigma_{cb}$: apparent compression stress in a trabecular lattice



## 1. Introduction

Cancellous bone is an extremely complex living structure made of delicate plates and struts of mineralized tissue — trabeculae — that split and interconnect, and together shape a sponge-like three-dimensional (3D) lattice. Cancellous bone support mechanical stress and reacts to mechanical stress by adopting its microarchitecture. The basic load-bearing elements in cancellous bone are individual trabeculae, which function mechanically as rods and beams subjected to compression and bending. Culman, von Meyer, Wolff, and others hypothesized at the end of the 19th century that the spatial arrangement of trabeculae is regulated by the history of mechanical stresses to which the whole bone was subjected. With several reservations and improvements, this fundamental theory was widely adopted by the scientific community and evolved to the modern field of studying mechanobiology of cancellous bone remodeling and adaptation. The theory of cancellous bone adaptation, which was tested in numerous experimental and computational models, ultimately postulates that the 3D microarchitecture of

cancellous bone aligns with the principal load-transfer pathways in whole bone under physiological loading, and that this allows efficient distribution of concentrated loads in skeletal joints.

The load distribution capacity, and particularly, the optimal stiffness and strength per cancellous bone mass are constituted by two main factors, the mechanical properties of the solid bone that compose trabeculae (tissue-level properties), and the microarchitectural structure of trabeculae. The microarchitectural structure of cancellous bone is characterized by many morphological parameters including the apparent (macroscopic) bone density, the trabecular thickness and separation, the spatial arrangement of individual trabeculae, the intertrabecular connectivity, etc. Owing to the complexity of microarchitecture and the small scale at which the details of cancellous bone structure exist (typical order of dimensions for human trabeculae are of length 1000 $\mu$m and diameter of 100 $\mu$m), very little is known about the load-bearing behavior of individual trabeculae. The small scale, particularly, limits direct measurements of strains and stresses in individual trabeculae, as attachment of finite-size sensors to cancellous bone tissue is very difficult technically and may influence the measurements. Fortunately, with today's computer power, numerical methods such as finite element (FE) modeling can serve as a substitute for actual measurements and can be employed to investigate the mechanical function of the microarchitecture of cancellous bone.

Investigations of the mechanical behavior of cancellous bone at the microarchitectural level are not merely a topic for research work in basic science; they are strongly motivated by the increasing public health treat of osteoporosis (Fig. 1). Presently, osteoporosis affects an estimated 44 million aging Americans, and has been determined to be responsible for about 300,000 hip fractures per year in the United States.[1,2] Ten million individuals are estimated to already have osteoporosis and additional 34 million have a degree of low bone mass — osteopenia — which indicates a probable risk for ultimate osteoporosis.[2] One in two women and one in four men over the age of 50 are at risk of sustaining osteoporosis-related fracture in their lifetime. The consequences of an osteoporotic fracture can be tragic. Of the individuals who fracture a hip, approximately one-half will be permanently disabled, and almost 20% will require long-term home nursing care. Up to a 24% excess mortality rate within one year after hip fracture has been reported.[1] Women who are 65 years and older, and had suffered osteoporotic fractures, were shown to have an increased mortality rate of up to twice that of non-osteoporotic women.[3] The costs for treating osteoporotic fractures are greater than those for treating either congestive heart failure or asthma, and are estimated to exceed US$17 billion per year.[2]

The vast impact of osteoporosis on patient suffering, quality of life, and health costs prompts understanding of the relationships between osteoporotic-related changes in cancellous bone microarchitecture and its mechanical function, particularly in terms of stiffness and strength. In osteoporosis, cancellous bone loss typically precedes loss of cortical bone thickness. Cancellous bone loss also occurs faster than cortical bone loss. Accordingly, loss of cancellous bone is more dominant

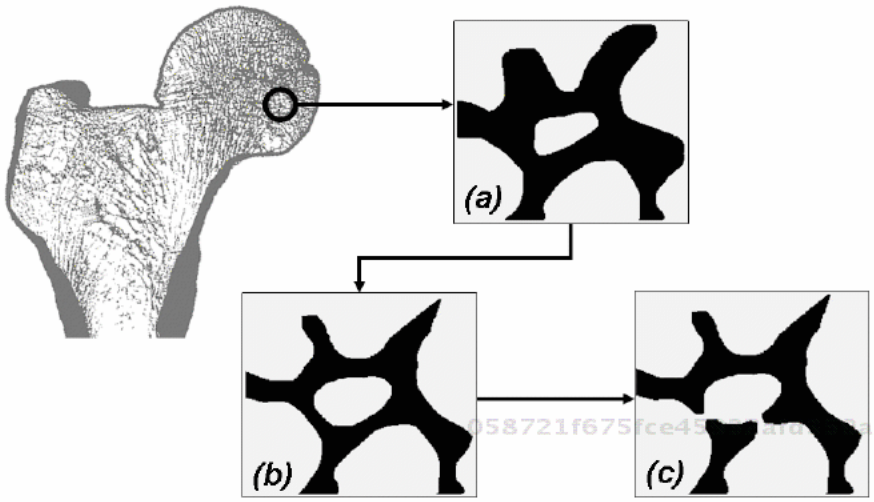


Fig. 1. Schematic illustration of the deterioration in the microarchitecture of cancellous bone with osteopenia, from a condition of thick, interconnected trabeculae in a healthy bone (a), through thinning of trabeculae (b), and, finally, occurrence of breaks in trabeculae which disconnect pathways of mechanical load transfer, and thus, overload the remaining, abnormally thinned trabeculae (c).

than loss of cortical bone in osteoporotic patients. For example, in postmenopausal osteopenic American women, bone loss in the proximal femur consists of ~50% of trabecular epiphyseal tissue and ~35% of cortical thickness.[4–6] The bone loss in osteoporosis is of both collagenous bone matrix and mineral. Two of the most highly influenced sites are the vertebrae and the proximal femur, which contain mainly cancellous bone. In vertebrae, horizontal "connecting struts" perforate and resorb. Once completely disconnected, no load is transferred through such struts, and the disconnected edges of the trabeculae are gradually resorbed by osteoclastic activity. With progressive reduction in the number of horizontal trabecular struts, the cancellous bone lattice changes to a structure that contains longer, thinner vertical rods. These longer and thinner rods are subjected to larger strains, particularly at their center which is thinner than the edges. The slender osteoporotic trabeculae also buckle more easily under compression forces borne by vertebrae, with respect to the shorter, healthy vertical trabeculae that are reinforced by horizontal struts. If buckling occurs locally, vertical trabeculae may fail in bending, and thus, the cancellous bone structure gradually weakens, and loads on the cortical shell increase. Eventually, in lack of the structural support provided by the trabecular "truss," the cortical shells fail and collapse inwards, damaging additional cancellous bone. This a-traumatic vertebral fracture is typical in osteoporosis and is called a vertebral compression fracture. Vertebral compression fractures affect approximately 25% of all postmenopausal women in the United States.[7] In the proximal femur, a similar process of thinning, disconnection, and further resorption at disconnected

trabeculae occurs (Fig. 1), and this ultimately leads to reduction of the overall strength of the proximal femur.[8] As trabeculae in the femur support bending-related compression and tension,[9] loss of cancellous bone at the compressive and tensile bands decreases the bending strength of the femoral neck in particular. Thus, in advanced osteopenia, even a minor fall which induces bending stresses in the femoral neck may cause a hip fracture. Overall, the progressive loss of trabeculae in both spinal and femoral cancellous bone is likely to be a result of two coupled mechanisms, biological resorption by osteoclastic activity and mechanical failure at the trabecula-level. Biological resorption may, in some cases, be the direct cause for disconnection if a trabecula is already so thin that osteoclastic resorption cuts through it (Fig. 1).[10]

Osteoporosis is a condition generally considered to describe loss of bone mass per unit volume (density) without a reduction of the ratio of mineral to organic phase of bone. The question whether osteoporotic bone is less stiff and less strong due to loss of morphology as a sole factor, or also due to degradation in tissue-level elastic modulus, has been an issue for a debate in recent years. However, most investigators agree today that at the tissue level, mechanical properties of osteoporotic cancellous bone are similar to those of normal bone.[11] Since bone loss is global and does not appear to include demineralization of remaining bone (i.e., bone mass is lost but what remains appears to be normal), morphological parameters of cancellous bone alone can be used to determine the severity of osteoporosis. Many morphological parameters were suggested to characterize the microarchitecture of normal and osteoporotic cancellous bone. Typically, such parameters are measured from histological slices through cancellous bone or from high-resolution cancellous bone images. Important morphological parameters are the volume fraction of cancellous bone tissue per specimen volume, $V_f$, the mean thickness of trabeculae, Tb.Th, the mean separation between trabeculae, Tb.Sp, and the level of connectivity of trabeculae. The Tb.Th can be measured directly from 3D reconstructions of cancellous bone or be evaluated from two-dimensional (2D) images based on a ratio between bone tissue area and perimeter of trabeculae. Likewise, the Tb.Sp can be measured directly or be evaluated from mean lengths of line segments that intersect marrow space. Connectivity is a quantitative measure of interconnectedness between trabeculae, which is evaluated in multiple ways (e.g., in terms of shape of an ellipse, tensor, or scalar number). Characteristic values of tissue-level elastic modulus, $V_f$, Tb.Th, and Tb.Sp, in humans are given in Table 1.

Morphological parameters of cancellous bone are age-dependent in both females and males. In thoraco-lumbar vertebral cancellous bone, males show a statistically significant decreased Tb.Th in rod-like trabeculae with increasing age (Tb.Th $[\mu\text{m}] = -0.15 \times \text{Age}\ [\text{years}] + 38$).[15] Likewise, females show a statistically significant increased trabecular length $L$ with increased age ($L\ [\mu\text{m}] = 2.22 \times \text{Age}\ [\text{years}] + 427$).[15] In postmenopausal women, a 5%/year decrease in $V_f$, a $-20\,\mu$m/year decrease in Tb.Th, and a $+80\,\mu$m/year increase in Tb.Sp were observed in the iliac crest.[16] Studies which examined the occurrence of osteoporotic fractures as

Table 1. Mechanical and morphological parameters of normal human cancellous bone.

| Morphological parameter | Mean ± standard deviation | |
|---|---|---|
| | Vertebral bodies | Femoral neck |
| Tissue-level elastic modulus ($E_t$) [GPa][12,13] | $13 \pm 2$ | $11 \pm 6$ |
| Cancellous bone volume fraction ($V_f$) [%][14] | $17 \pm 8$ | $27 \pm 15$ |
| Trabecular thickness (Tb.Th) [$\mu$m][14] | $170 \pm 20$ | $190 \pm 40$ |
| Trabecular separation (Tb.Sp) [$\mu$m][14] | $1110 \pm 700$ | $650 \pm 320$ |

*Sources*: References 12–14.

function of cancellous bone morphology found that in osteopenic males, compression fractures in vertebrae appeared when $V_f$ dropped below 12% and Tb.Sp increased ~1.3-fold.[16] No statistically significant difference was found between Tb.Th of osteoporotic patients who suffered a vertebral compression fracture and osteopenic subjects who did not suffer a fracture[17]; however, as explained above, gradual loss of Tb.Th ultimately causes local failures which, effectively, increase Tb.Sp. Hence, Tb.Th and Tb.Sp in cancellous bone should be considered as interrelated.

Analysis of the relationships between tissue-level constitutive parameters (e.g., tissue elastic modulus, Poisson's ratio), morphological parameters such as $V_f$, Tb.Th, and Tb.Sp, and the apparent stiffness and strength of normal and osteoporotic cancellous bone requires direct experimentation and computational work (Fig. 2). Experimental testing of isolated cancellous bone specimens in compression, tension, shear or torsion was conducted by many investigators, and empirical relationships between the above parameters were obtained with reasonable statistical power.[18–21]

Nevertheless, experiments with no computational support are rather limited, owing to several reasons: (i) specimens for mechanical testing are extracted from a limited number of bones/animals/cadavers, and so, generalization of the results over large populations is problematic; (ii) specimens of limited geometrical size can be obtained, and often, the small size of specimens contributes to measurement errors, e.g., as free-edge trabeculae buckle during compression and thus strain is overestimated; (iii) if specimens are damaged during preparation for testing (e.g., when sawing, polishing, etc.), results are biased; (iv) uniaxial loading requires perfect surface parallelism between the specimen's surface and loading jigs (Fig. 2). Even if efforts are made to achieve surface parallelism (Figs. 2(a) and 2(b)), uniform transfer of loads is problematic; and (v) the information obtained during experiments is usually limited and insufficient for characterizing the full constitutive behavior of cancellous bone. While it is relatively straightforward from a technical aspect to determine the compression or tension longitudinal moduli in the orthogonal directions (Fig. 2), it is more difficult to obtain apparent Poisson's ratios or shear moduli.[22]

Fortunately, it is possible to overcome most of these limitations using computational modeling of the microarchitecture of cancellous bone. In particular, an FE model which characterizes some given cancellous bone tissue-level mechanical

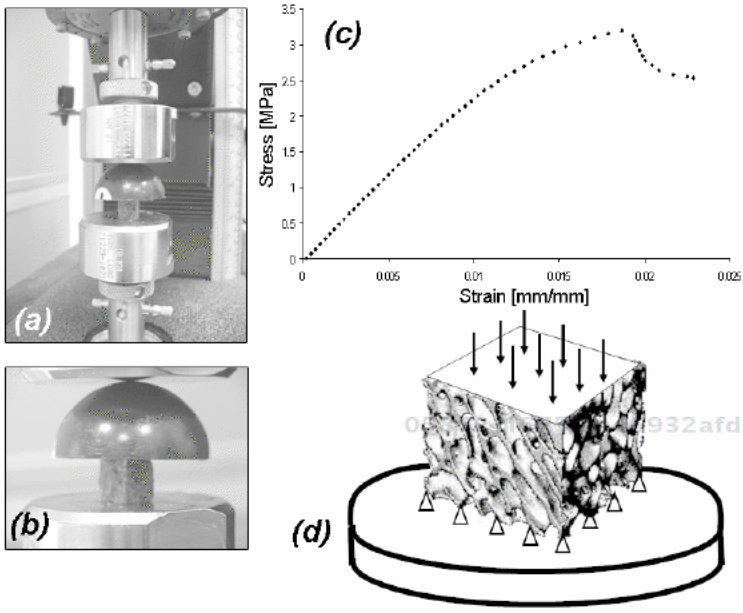


Fig. 2. Studies of cancellous bone stiffness under compression: A cubic cancellous bone specimen (face length ∼9 mm) is compressed in an Instron material testing machine, which applies force on its superior surface through a half-sphere that ensures surface parallelism (a). The inferior surface is free to slip on the pre-lubricated rigid support, as shown in the magnification (b). The axial displacement of the loading machine's arm is recorded with the force applied on the specimen, to produce a stress–strain curve for this specimen (c). This experiment can be represented computationally, where the cancellous bone specimen is loaded via its superior surface and is free to slide laterally at its inferior surface ("slip"), but vertical downward displacements of the inferior surface are prevented (d).

properties and a specific microarchitecture can be subjected to different loading modes for complete characterization of the constitutive behavior at the apparent level. The microarchitectural FE model also provides additional information over that provided in experiments: the distribution of microscopic strains and stresses in individual trabeculae. The following sections discuss the assumptions, considerations, and techniques in FE modeling of cancellous bone, and the effects of osteoporotic changes. The model applications analyzed herein were selected to describe important load-bearing phenomena which lead to the mechanical dysfunction of osteoporotic cancellous bone, including local failures of trabeculae due to inhomogeneous strain distributions and buckling, and loss of stiffness and strength at the apparent level.

## 2. General Considerations and Finite Element Techniques in Models of Normal and Osteoporotic Cancellous Bone

Modeling the microarchitecture of cancellous bone always requires data on (i) geometry, (ii) constitutive properties of the bone at the tissue-level, and

(iii) the loading mode and constraints. Considerations regarding the geometry and constitutive properties of cancellous bone are common to many applications, and accordingly, they are discussed in detail in the next sections. The loading mode and constraints depend on the specific objective of the study and may represent a physiological condition or some experimental conditions. Cancellous bone is physiologically loaded in compression (e.g., femoral condyles), tension (e.g., upper femoral neck), less often in shear (e.g., in the anterior–posterior direction of thoracic and lumbar vertebrae during bending), and in real-world situations may be subjected to compound loading. Determining a loading mode that represents physiological loading on cancellous bone is a difficult task, which typically requires prior stress/strain analysis of the whole bone, considering joint, ligament, and muscle system loading, to isolate a loading mode on the region of interest containing cancellous bone. This approach is called hierarchical modeling, and is reviewed in detail elsewhere.[9] In other cases, it may be desired to simulate laboratory experiments with cancellous bone specimens, i.e., to virtually load a computational model of a cubic cancellous bone specimen in uniaxial compression (confined or unconfined), uniaxial tension, simple shear, or torsion (Fig. 2). In such cases, the experimental conditions can be reproduced in the computational model, e.g., a uniaxial compression test can be simulated by applying pressure on a free surface of a reconstructed geometry from a cancellous bone specimen, after constraining the opposite specimen surface for vertical displacements only ("slip" boundary condition) or for all displacements ("no slip"). Shear loading may also be applied in such modeling configuration. Simulated loads can be applied directly on the free trabecular edges, or on a rigid computational surface that is fixed to the free trabeculae, to reduce St. Venant's boundary effects (Fig. 2). The stress/strain relationship under a given loading mode — a typical outcome of the modeling process — depends on the microarchitectural properties of the specimen that was simulated, namely on the shape of individual trabeculae and trabecular structures, and on the tissue-level mechanical properties. These issues are discussed next.



### 2.1. *Microarchitectural properties of cancellous bone*

Microarchitectural geometry of cancellous bone can be characterized by first studying the geometrical properties of individual trabeculae, and then studying the intertrabecular connectivity and the spatial structures formed by trabeculae.

#### 2.1.1. *Shape of individual trabeculae*

Sheep and dogs are common orthopaedic models as their size permits prosthetic implantation and also allows collection of substantial blood and urine samples as well as multiple bone biopsies (e.g., from the iliac crest), where needed.[23,24] Sheep in particular are well suited for the study of osteoporosis for the following reasons: (i) similarly to postmenopausal osteoporosis in women, bone loss associated with

estrogen deficiency in sheep has been documented; (ii) the ovine hormone profiles are temporally and quantitatively similar to those of women; and (iii) the osteoblast product, osteocalcin, has been clearly defined in sheep.[24] Accordingly, we studied the geometrical properties of individual trabeculae in cancellous bone of sheep and dogs, and developed a single-trabecula geometrical model based on statistical analysis of dimensions of 1114 rod-like trabeculae from the core of 36 dog vertebrae (L1 and C7) and 200 rod-like trabeculae from the epiphyseal parts of six ovine femora.

Six specimens were transversally cut from the upper-third of the epiphysis of each ovine femur, and one specimen was cut from each dog vertebra, using an electrically powered saw, after drying the bones at 85°C for 4.5 h. The dried samples were kept at −18°C, and defrosted to room temperature before measurements of trabecular dimensions. Under digital optical microscopy (Axiolab A, ZEISS Co., magnification ×30) we measured the length ($L$), base thickness ($t_{\max}$ at the trabecular junctions), and minimal thickness ($t_{\min}$ at the center of the strut) of each trabecula (Fig. 3) from a transverse view using designated software for microscopic measurements (MGI photosuite 3.0SE). The base thickness ($t_{\max}$) at each edge of a trabecula was determined by containing the respective trabecular junction within a circle and measuring the distance between points common to the profiles of the trabecula and the junction circle, as demonstrated in Fig. 3. This uniquely defines the base thickness ($t_{\max}$) values for each trabecula (Fig. 3). The value of $t_{\min}$ was measured at the center of the trabecula, halfway between the two locations of its

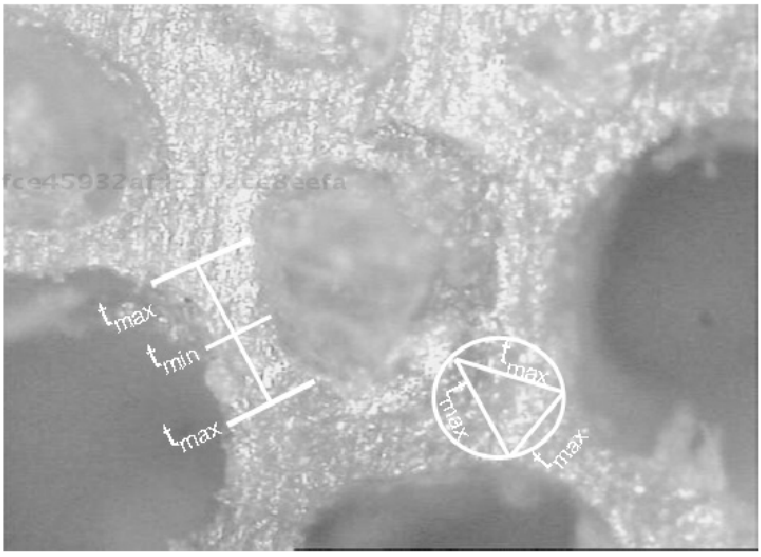


Fig. 3. Basic geometrical dimensions of a trabecula marked on a microscopic image of cancellous bone from a dog vertebra (×30). Measurements of base thickness, $t_{\max}$, and thickness at the center, $t_{\min}$, are marked on the left part of the frame. On the right side, the method of determination of the base thickness is demonstrated. A circle is first marked to contain the trabecular junction. The points common to the profile of trabeculae and the junction circle define the base thickness $t_{\max}$ of each trabecula at the junction.

$t_{max}$ boundaries (Fig. 3). We found significant linear correlation ($R^2 \sim 0.7, p < 0.05$) between the base and minimal thickness dimensions of individual trabeculae at both sheep femora and dog vertebrae ($t_{max} = \alpha t_{min} + \beta$, where $\alpha = 1$ and $\beta = 60\,\mu$m in dog vertebrae, and $\alpha = 1.37$ and $\beta = 41\,\mu$m in sheep femora). Dimensions of trabeculae are provided in Fig. 4. The thickness and the length of both canine and ovine trabeculae are right-skewed (log-normal distributions), demonstrating a large range of intraspecimen and interspecimen variations in shape and size (Fig. 4). The right-skewed distribution is not surprising, considering that many other biological parameters are distributed according to log-normal frequency curves instead of normal ones.[25] It also agrees with previous measurements of Tb.Th intraspecimen variation in two human vertebrae that showed a right-skewed distribution.[26]



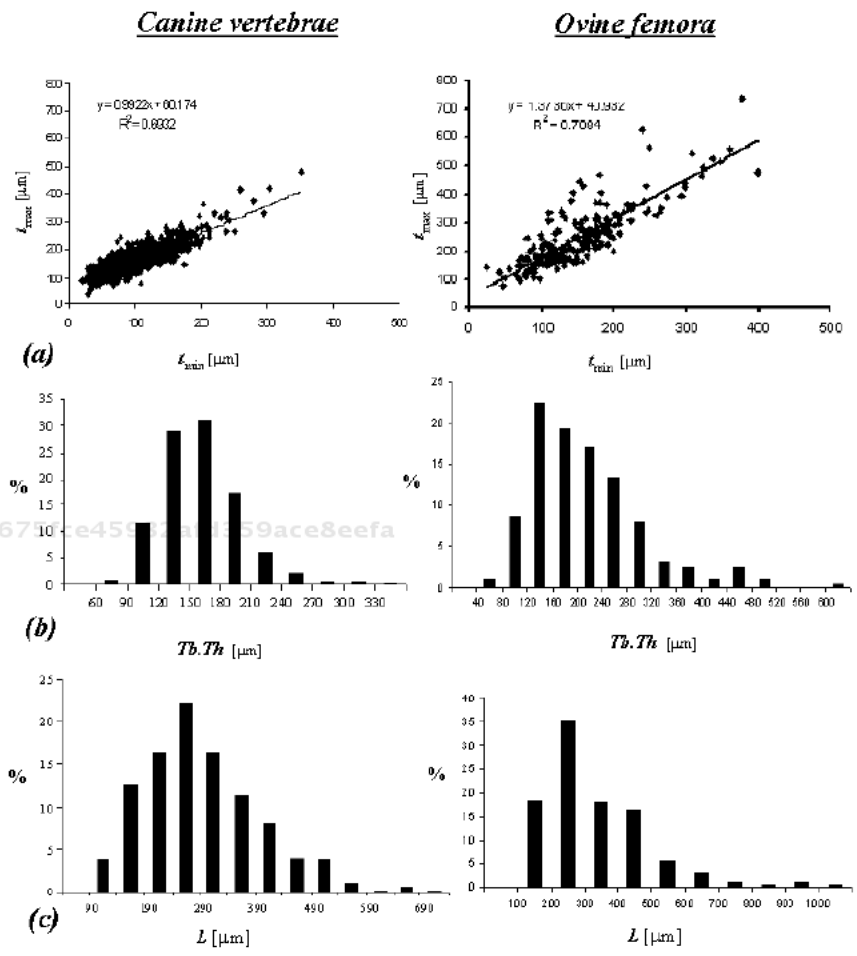


Fig. 4. Dimensions of trabeculae in canine vertebrae (left column) and ovine proximal femora (right column): (a) Base thickness, $t_{max}$, and minimum thickness at the center, $t_{min}$, were found to be linearly correlated ($p < 0.05$, $R^2 \sim 0.7$), (b) histogram of mean thickness of trabeculae Tb.Th, and (c) histogram of length of trabeculae, $L$.

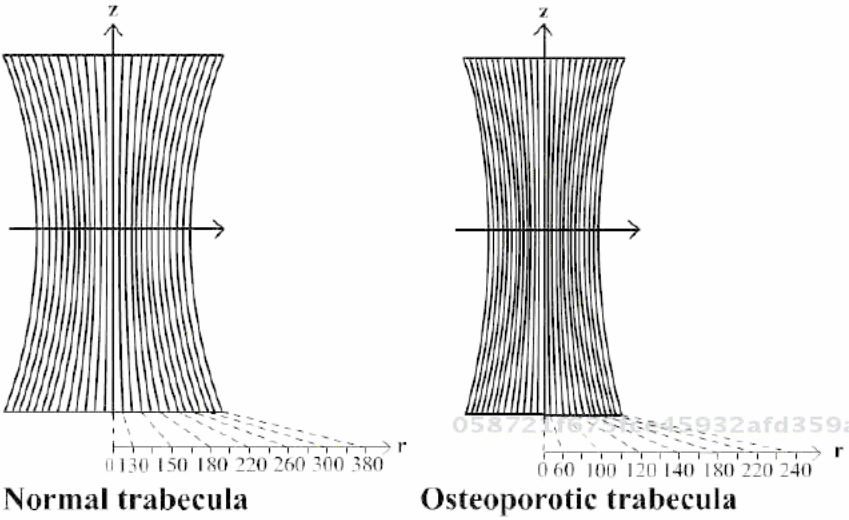


Fig. 5. Potential surface profiles of rod-like trabeculae in vertebral cancellous bone of humans, predicted from Eq. (2) after setting the average trabecular thickness Tb.Th as 180 $\mu$m for normal trabeculae (left), and as 120 $\mu$m for osteoporotic trabeculae (right). Length $L$ was set as 1200 $\mu$m in both cases.

By means of cross-correlation of digitized trabecular profiles, we also found high degrees of symmetry of the curvature of individual trabeculae around their longitudinal ($z$) and radial ($r$) axes ($R^2 = 0.97 - 0.99$), which made it possible to fit cosinusoidal curves to the upper and lower trabecular profiles (Fig. 5):

$$\frac{r}{t_{\min}} = \pm\left\{\cos\left(\frac{2z}{L}\cos^{-1}\left(\frac{1}{2}\left(3-\alpha-\frac{\beta}{t_{\min}}\right)\right)\right)-\frac{3}{2}\right\}. \quad (1)$$

Considering that $t_{\min}$ and $t_{\max}$ are linearly related (Fig. 4a), Eq. (1) can also be formulated in terms of $t_{\max}$. It is also possible to write both $t_{\min}$ and $t_{\max}$ as functions of the average thickness of a trabecula Tb.Th (where $\text{Tb.Th} = (t_{\min} + t_{\max})/2$) and of the constants $\alpha$, $\beta$. This allowed to simplify the representation of trabecular profiles in Eq. (1) so that only two parameters — the characteristic length of the trabecula ($L$) and the average trabecular thickness Tb.Th — are incorporated:

$$r(z) = \pm\frac{2\cdot\text{Tb.Th}-\beta}{1+\alpha} \times\left\{\cos\left(\frac{2z}{L}\cos^{-1}\left(\frac{1}{2}\left(3-\alpha-\frac{\beta\cdot(1+\alpha)}{2\cdot\text{Tb.Th}-\beta}\right)\right)\right)-\frac{3}{2}\right\}. \quad (2)$$

Our microscopy measurements yielded that the range of thickness of trabeculae Tb.Th was between ~0.3-fold and ~threefold the mean thickness, in both dog vertebrae and ovine femora (mean Tb.Th was 130 $\mu$m in dog vertebrae and 215 $\mu$m in sheep femora, Fig. 4). Considering this range around the mean Tb.Th, Eq. (2)

allows representation of the complete spectrum of potential trabecular profiles in canine or ovine cancellous bone.

The volume bounded within the surface of revolution derived from Eq. (2) (i.e., the surface generated by rotating the positive curve of Eq. (2) 360° about the $z$-axis) provides an estimate for the volume $V_{\mathrm{Tb}}$ of a trabecula with given nominal thickness Tb.Th and length $L$:

$$V_{\mathrm{Tb}} = \pi \cdot \mathrm{Tb.Sp} \cdot \frac{(\beta - 2 \cdot \mathrm{Tb.Th})^2}{4\gamma(1+\alpha)^2} \cdot (11\gamma + \sin 2\gamma - 12 \sin \gamma)\,, \tag{3}$$

where

$$\gamma = \cos^{-1}\left[\frac{1}{2}\left(3 - \alpha - \frac{\beta\,(1+\alpha)}{2\mathrm{Tb.Th} - \beta}\right)\right],$$



where $\mathrm{Tb.Th} > 0$ and $L > 0$. Equation (3) thus approximates the distribution of volumes of trabeculae in ovine femoral and canine vertebral cancellous bone.

Bone morphology studies across species suggest that the shape of individual trabeculae is common to all mammals, although dimensions of trabeculae and their structural arrangement do differ between species.[27] Accordingly, to represent a single, normal rod-type trabecula in a human vertebra with mean dimensions, we scaled the parameters of Eqs. (2) and (3) so that $L = 1200\,\mu$m and $\mathrm{Tb.Th} = 180\,\mu$m.[14] To further represent the spectrum of potential trabecular profiles in a normal cancellous bone from human vertebrae we assumed that the extent of biological variation in trabecular thickness found in normal sheep and dogs (Fig. 4) applies to normal humans, i.e., the ratios of maximal-to-mean and minimal-to-mean thickness are similar in normal ovine/canine and normal human cancellous bone. This assumption allowed plotting of the spectrum of potential geometrical profiles of human spinal trabeculae (Fig. 5). The 3D reconstruction of a rod-type human trabecula using Eq. (2) yields the single-trabecula building-block,[28] which is applied in Fig. 6 to represent vertebral cancellous bone as an orthogonal lattice model.



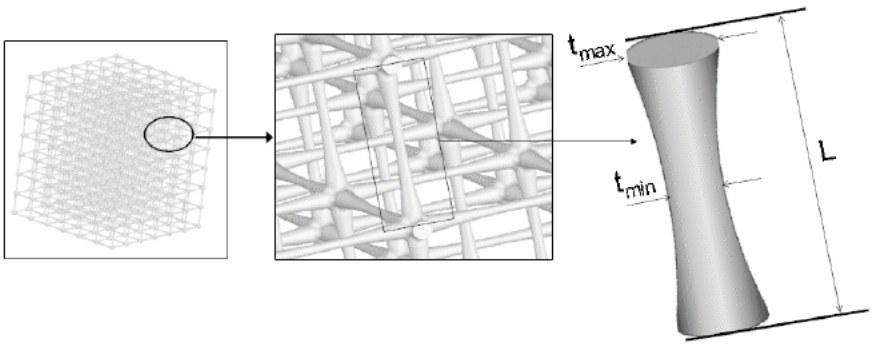


Fig. 6. Orthogonal trabecular lattice representing human vertebral cancellous bone. Details of the lattice are magnified (left to right) to show the generic single-trabecula building-block (right frame): the volume of revolution representing the idealized geometry of a single trabecula.[25]

### 2.1.2. *Trabecular structures and the role of intertrabecular connectivity*

Healthy cancellous bone is a honeycomb-like structure which consists of highly connected networks of trabeculae. Osteoporotic bone, however, is characterized by thinner trabeculae that gradually lose their interconnections. Loss of intertrabecular connectivity in osteoporosis is considered to be a major contributor to loss of bone stiffness, and leads to increased bone fragility.[29]

Consider for example an idealized model of cancellous bone made of a cubic lattice of single-trabecula building-blocks that are arranged orthogonally, as in the left frame of Fig. 6. Provided that tissue-level mechanical properties, e.g., a tissue-level elastic modulus $E_t$ (Table 1) and a Poisson's ratio, are determined for each trabecula in the lattice model, and the Tb.Th is also defined, the apparent elastic modulus of the lattice $E_{cb}$ under external pressure can be calculated using the FE method, as the ratio of applied pressure to lattice strain.[28] The detailed modeling assumptions for such orthogonal lattice model will be discussed in subsequent sections. For now, let us consider the effect of loss of connectivity in the model as a result of simulated resorption or fracture of an individual trabecula owing to osteoporosis, on the apparent elastic modulus $E_{cb}$ of cancellous bone. To simulate such conditions, one center trabecula is removed from a cubic lattice which originally contained 144 trabeculae, 48 of which were aligned parallel to the direction of a compressive load. A dimensionless $E_{cb}$ property ratio defined as the ratio of $E_{cb}$ of cancellous bone with a discontinuity over the apparent elastic modulus of the intact lattice was determined to quantify the effect of loss of connectivity. Hence, if removal of a single center trabecula from the lattice does not influence the $E_{cb}$ of the lattice, the $E_{cb}$ property ratio approaches unity, but if removal of a trabecula is influential, the $E_{cb}$ property ratio drops below unity. Figure 7 provides the results for this analysis where the trabecula removed is either parallel to the direction of loading (as in the top left frame of Fig. 7) or perpendicular to the direction of loading. It is shown that removal of just one center trabecula that is parallel to the direction of loading (out of 48 trabeculae with the same orientation) causes the $E_{cb}$ property ratio to drop as low as $\sim$0.9, and this was consistent for lattices with different Tb.Th. In other words, loss of as few as $\sim$2% of trabeculae which align with the loading direction causes a decrease of $\sim$10% in $E_{cb}$. In contrast, loss of a center trabecula perpendicular to the direction of load barely influences $E_{cb}$ (>1%), as indicated by the property ratios which remained around unity for these simulations (although they tended to decrease slightly with a rise in Tb.Th, Fig. 7).

When a central trabecula is removed from a lattice model and the model is loaded in the direction of the missing trabecula, bending-related stress concentrations appear in the "necks" of neighboring trabeculae.[28] These focal stresses are $\sim$twofold the stresses in the "necks" of trabeculae in an intact lattice, and are likely to contribute to failure of the neighboring trabeculae on the long-term. Hence, loss of just one trabecula in the direction of load triggers a detrimental process in which trabeculae in the vicinity of the lost trabecula are overstressed, eventually fail, and thus overload their neighboring trabeculae, and so on.

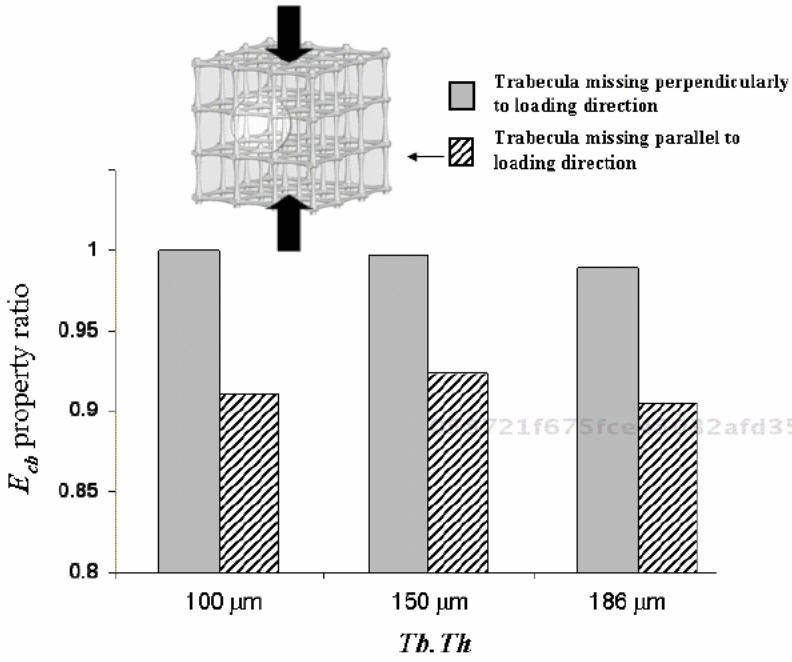


Fig. 7. Property ratios of apparent elastic modulus $E_{\mathrm{cb}}$ of cancellous bone with discontinuity over apparent elastic modulus of the intact lattice, for three orthogonal cubic lattices containing 144 identical trabeculae, of which 48 are aligned parallel to the direction of load. It is shown that loss of just one trabecula parallel to the direction of load reduces $E_{\mathrm{cb}}$ by ~10%; however, loss of one trabecula perpendicularly to the direction of load barely affects $E_{\mathrm{cb}}$.

It is important to note that the present simulations only consider loss of one trabecula at a cancellous bone site. This is particularly important when interpreting the results of the $E_{\mathrm{cb}}$ property ratio for removal of a trabecula perpendicularly to the direction of load. The present simulations did not identify a degrading effect of loss of just one trabecula perpendicularly to the loading direction on $E_{\mathrm{cb}}$. However, if at a certain central junction of the orthogonal lattice model all four trabeculae that are found perpendicularly to the direction of load are removed, that junction is not rigidly constrained anymore, and buckling, rather than bending, is likely to be the mechanism of local deformation (and possibly failure). Figure 8 illustrates this condition.

The Euler formula for the buckling load of a strut with fixed ends, applied for an individual trabecula,[15] states that

$$F_{\mathrm{c(critical)}} = 4\pi^2 \left( \frac{E_{\mathrm{t}} I_{\mathrm{t}}}{L^2} \right), \tag{4}$$

where $F_{\mathrm{c(critical)}}$ is the compressive load at which a trabecula buckles, $E_{\mathrm{t}}$ is the tissue-level elastic modulus of cancellous bone, $I_{\mathrm{t}}$ is the moment of inertia of the cross-section of the trabecula, and $L$ is the length of the trabecula. If a circular

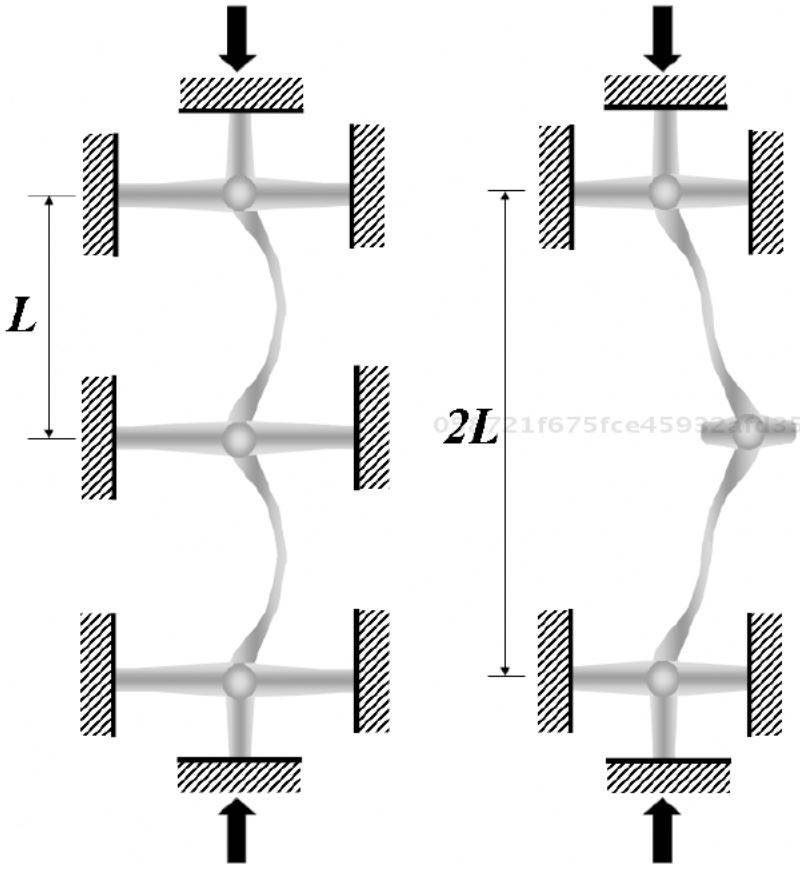


Fig. 8. The constraining of a trabecular junction by trabeculae perpendicular to the loading direction: The center trabecular junction in the left frame is constrained by trabeculae that are perpendicular to the direction of load. According to Euler's buckling theory, the critical force for buckling of individual trabeculae found in the direction of load in such case is fourfold greater than in the condition shown in the right frame, where perpendicular trabeculae at the central junction were all disconnected, and thus, the two trabeculae found in the loading direction buckle as a whole.

cross-section is assumed, such as in the trabecula building-block geometrical model described in the previous section, then $I_{\mathrm{t}}(z) = \pi[r(z)]^4/2$, where $r(z)$ is the local radius of the trabecula along the $z$-axis. To find the minimal force required for buckling $F_{\mathrm{c(critical)}}$ it is appropriate to use the minimal moment of inertia along the strut $I_{\mathrm{t(min)}}$. For the trabecula building-block model, this minimal moment of inertia occurs exactly at the center of the trabecula, where the radius of the trabecula is minimal ($r_{\mathrm{min}}$). Hence, substituting $z = 0$ in Eq. (2) yields that

$$r_{\mathrm{min}} = \pm\frac{1}{2}\left(\frac{2 \cdot \mathrm{Tb.Th} - \beta}{1 + \alpha}\right) \tag{5}$$

and $I_{t(min)} = \pi r_{min}^4/2$. Now employing the result in Eq. (4) to the geometrical building-block model of a trabecula we get

$$F_{c(critical)} = 2\pi^3 E_t \left(\frac{r_{min}^4}{L^2}\right), \tag{6}$$

where $2\pi^3 E_t$ is a constant. Accordingly, if a trabecular junction is constrained by trabeculae that are aligned perpendicularly to the direction of load, as in the left frame of Fig. 8, then the minimal force that will induce buckling of individual trabeculae in the lattice is proportional to $r_{min}^4/L^2$. However, if all perpendicular trabeculae at a junction are disconnected, as in the right frame of Fig. 8, then the two remaining trabeculae which share that junction (and which are situated in the direction of loading) buckle as a whole (Fig. 8). In such case, the effective length of the buckled strut is $2L$ (which is the total length of two adjacent trabeculae), and the minimal force that will induce buckling of these two trabeculae together is proportional to $r_{min}^4/4L^2$. Hence, in an orthogonal lattice model of cancellous bone, the constraining provided by trabeculae perpendicular to the direction of loading increases the bucking force resistance of trabeculae fourfold (Fig. 8).

Taken together, the analyses above highlight the role of trabecular connectivity in maintaining the stiffness and the strength of cancellous bone. Experimental approaches often fail to isolate the role of loss of connectivity among other osteoporotic changes, mainly due to large bone-to-bone heterogeneity (local variations of up to 100% in mechanical properties).[29] In contrast, FE modeling can be successful in studying the loss of connectivity independently of other factors, as demonstrated herein.

### 2.2. *Mechanical properties of cancellous bone*



The mechanical properties of cancellous bone can be investigated at the scale of individual trabeculae (tissue-level mechanical properties) or at the structural scale (apparent mechanical properties). Finite element modeling of cancellous bone requires knowledge of both. Tissue-level properties are required for definition of the constitutive behavior of the bone material in the model, and apparent properties are required for validation or verification of the results obtained from the FE simulations. The following sections review the mechanical properties of cancellous bone at both the tissue-level and the apparent scale.

#### 2.2.1. *Tissue-level properties*

In trabeculae, lamellae are not arranged concentrically as in osteons of cortical bone. Accordingly, at the tissue-level, cancellous bone material is generally treated as an isotropic, linear elastic material, with an effective tissue-level elastic modulus $E_t$ which considers the combined contributions of the organic and mineral phases

Table 2. Tissue-level elastic moduli $E_t$ of human cancellous bone reported in the literature.

| Reference | Bone origin | Testing method | Wet/dry | $E_t$ [GPa] |
|---|---|---|---|---|
| 32 | Femoral neck | FE back-calculation | Wet | $18 \pm 2.8$ |
| 33 | Proximal tibia | Bending (3-point) | Wet | 4.6 |
| 34 | T12 vertebrae | FE back-calculation | Wet | $5.7 \pm 1.6$ |
| 35 | T12 and L-1 vertebrae | Nanoindentation | Dry | $19.4 \pm 2.3$ |
| 36 | Distal femur | Buckling | Dry | $8.7 \pm 3.2$ |
| 37 | Proximal tibia | Buckling | Wet/dry | 11.4/14.1 |
| 38 | Femoral neck | Nanoindentation | Wet | $6.9 \pm 4.3$ |

of the trabecula material. This assumption is considered sufficient for most FE analyses of cancellous bone.[30]

Tissue-level elastic moduli $E_t$ of human cancellous bone were characterized in many experimental studies (Table 2); however, reported data range over an order of magnitude (~1–20 GPa), likely owing to the technical difficulties encountered when measuring properties at the small scale of trabeculae (length ~1 mm, thickness ~ 200 $\mu$m). Purely experimental methods used to determine elastic properties of individual trabeculae that include tensile, bending, and buckling tests on unmachined and micro-machined individual trabeculae, as well as microindentation and nanoindentation (Table 2). These methods should typically overcome major technical problems related to geometrical irregularity of individual trabeculae, possible damage to trabeculae when machining them to a standard geometry prior to testing, and the effects of micro-jigs for fixation of individual trabeculae or uniformity of loads applied to individual trabeculae. An alternative method to pure experimentation, developed by van Rietbergen and coworkers, is based on "reverse engineering" extrapolation of tissue-level $E_t$ from macro-scale specimens of cancellous bone, using an integrated experimental–computational procedure often called FE-back-calculation.[31] This procedure calculates the tissue-level modulus $E_t$ in a trial-and-error iterative process, which starts with an initial $E_t$ guess for a micro-computed tomography (micro-CT) or a micro-magnetic resonance imaging (micro-MRI) based FE model of a cancellous bone specimen, and is followed by recursive corrections to the initial $E_t$, corresponding to an actual experiment with the same specimen.[31] Results of $E_t$, classified according to the testing mode, are detailed in Table 2. Mean values of tissue-level elastic moduli are around 10 GPa for wet trabeculae and around 14 GPa for dry trabeculae across different testing methods (Table 2), where indentation or microhardness testing methods tend to produce greater $E_t$ values.

Considering a linear elastic behavior of cancellous bone at the tissue-level, a tissue-level Poisson's ratio $\nu_t$ should also be specified for a complete characterization of the isotropic linear elastic constitutive law. Direct measurements of Poisson's ratio at the trabecular scale are very difficult to obtain, owing to experimental limitations similar to those described in regard to $E_t$ measurements. Accordingly, it is generally accepted to assume that tissue-level Poisson's ratio of cancellous bone is similar to

that of macroscopic specimens of cortical bone, i.e., $\nu_t$ between 0.2 and 0.4, and in FE analyses, a midrange value of $\nu_t = 0.3$ is typically used.[39,40]

### 2.2.2. *Apparent properties*

Information on apparent elastic moduli of cancellous bone becomes relevant where it is desired to validate or verify the mechanical behavior of an FE model of the bone's microarchitecture. Specifically, FE analyses of the microarchitecture of cancellous bone can provide information on the distributions of deformations, strains, and stresses at the scale of individual trabeculae, but it can also provide the apparent (mean) deformation, strain, and stress at the scale of the whole specimen. A common approach for validation of such computational predictions will then be to compare the FE-predicted apparent elastic modulus (defined as the slope of the apparent stress versus apparent strain plot) with the apparent elastic modulus obtained in actual experiments conducted on the same specimen that was modeled, or with similar specimens. If sufficient agreement is shown, then it is concluded that model-predicted tissue-level deformation, strain, and stress distributions (in individual trabeculae) are also realistic.[28]

A literature review of experimental data reported for the apparent elastic moduli of adult human cancellous bone from the proximal femur, vertebrae, and glenoid demonstrates that the reported properties vary by over an order of magnitude (Table 3). Minimal reported values are around 50 MPa, and maximal ones are in the order of 3500 MPa.[11,41–46] Even within individual specimens, large ranges and high standard deviations were reported.[47] This substantial variability has been attributed mainly to the inhomogeneous trabecular bone structure,[47] but discrepancies may also relate to differences in testing protocols (e.g., specimen shape and size, specimen preparation, strain magnitudes, strain rate, etc.). Taken together, data in Table 3 show that cancellous bone in vertebrae has apparent elastic modulus $E_{cb}$ of up to 500 MPa, whereas cancellous bone in the proximal femur can be stiffer, with $E_{cb}$ of up to 3500 MPa.

Table 3. Apparent elastic moduli $E_{cb}$ of human cancellous bone reported in the literature.

| Reference | Bone origin | Testing method | Preservation | $E_{cb}$ [MPa] |
|---|---|---|---|---|
| 41 | Glenoid | Indentation | Embalmed* | 67–171 |
| 42 | Vertebrae | Compression | Fresh frozen | $63 \pm 10$ |
| 43 | Femoral neck | Compression | Fresh frozen | 200–2200 |
| 44 | Femoral head | Compression | Fresh frozen | 40–550 |
| 11 | Proximal femur | Compression | Fresh frozen | $635 \pm 265$ |
| 45 | Femoral neck | Compression | Fresh frozen | $120 \pm 40$ |
| 46 | Vertebrae | Tension | Fresh frozen | $349 \pm 133$ |
| 46 | Femoral neck | Tension | Fresh frozen | $2700 \pm 772$ |

*Embalming was shown to increase apparent elastic moduli of cancellous bone by a few percent, which is insignificant with respect to biological variations across anatomical sites and among individuals.[41]

Considering that a difference in tissue elastic modulus $E_t$ across anatomical sites could not be identified with current tissue-level measurement techniques (Table 2), the difference between $E_{cb}$ of proximal femora and vertebrae can be explained by the higher apparent density of cancellous bone in the proximal femur ($0.6 \pm 0.1$ g/cc) with respect to that in vertebrae ($0.2 \pm 0.05$ g/cc).[46] Moreover, it had been suggested that trabecular bone from the human proximal femur and vertebrae represent two architectural extremes, the first having a "plate-like" structure, and the second having a "rod-like" structure.[48] Consistently with this hypothesis, rod-like trabeculae are more susceptible to larger deformations, e.g., in buckling (Fig. 8).

In the context of FE modeling, another important apparent mechanical property of cancellous bone is its yield strain. An experimentally characterized apparent yield strain allows to maintain an FE simulation in the linear regime, by verifying that computationally predicted apparent strains in the model do not exceed the experimental yield strain of cancellous bone. Apparent yield strains for cancellous bone are experimentally determined using the offset method,[49] and reported values were shown to be generally uniform within an anatomic site but can vary across sites.[50] Taken together, compressive yield strains across different anatomical sites of cancellous bone are reported to be in the range of 0.5%–2.0%.[50,51] However, microdamage initiation in individual trabeculae may occur prior to the onset of a detectable apparent yield.[52] Thus, in FE simulations, it is practical to "keep on the safe side" and consider a linear elastic behavior at the tissue-level for apparent compressive strains which do not exceed 0.3%.[53]

To conclude the section on mechanical properties of cancellous bone, we note that (i) tissue-level elastic moduli $E_t$ (~10 GPa) are 100-fold to 10-fold the apparent elastic moduli $E_{cb}$ (~100–1000 MPa); (ii) apparent elastic moduli $E_{cb}$ depend on the anatomic site, likely due to microarchitectural differences (particularly in cancellous bone density, spatial arrangement of trabeculae, and shape of individual trabeculae); and (iii) linear elastic constitutive behavior of cancellous bone is expected for apparent strains lower than 0.5%.



### 2.3. *Finite element modeling of cancellous bone*

The FE method of analysis is based on dividing complex structures to elements with a simpler geometry, e.g., bricks, tetrahedrons or hexahedrons, which are connected through common nodes. The equations of equilibrium are analyzed for each element, and boundary displacement information is transferred to neighboring elements through the shared nodes, in an iterative process which eventually provides the distribution of deformations, as well as of strain and stress tensors in the whole structure. Review of the general-purpose FE method of analysis, the differential equations of element equilibrium, and the methods of programming an FE problem are outside the scope of this chapter. These topics are described in detail in dedicated FE textbooks.[54,55] This section complements these textbooks by focusing on the

particular issues related to application of the FE method to the microarchitecture of cancellous bone. Accordingly, the relevant assumptions, considerations, and approximations that are commonly used when applying FE to cancellous bone are discussed below.

### 2.3.1. *Concepts of finite element modeling as applied to cancellous bone*

Development of an FE model of the microarchitecture of cancellous bone generally requires four steps: (i) construction of the cancellous bone geometry at the microscopic scale and meshing of the microarchitecture to finite elements, (ii) assignment of mechanical properties to the bone tissue, (iii) determination of the loading mode and constraints, and (iv) validation of the strain and stress predictions of the model with respect to experimental measurements, typically of apparent mechanical properties.



The first step, of constructing the microscopic geometry of bone, requires that assumptions be made as to the level of detail at which cancellous bone geometry is represented. It was shown in previous sections that although individual trabeculae have irregular geometrical shape and although trabeculae are interconnected in a complex manner (Fig. 3), the structure of trabeculae can be idealized while keeping its fundamental geometrical characteristics, e.g., using the single-trabecula building-block (Fig. 6). Alternatively, with sufficiently large computer power it is now possible to reconstruct the realistic microarchitecture of cancellous bone, with the aid of micro-imaging methods such as micro-CT[56,57] or micro-MRI.[58,59] Regardless of whether trabeculae are idealized to a simplified shape or, are considered with their real curved surfaces, construction of the 3D geometry of the microarchitecture of cancellous bone must be based on imaging of the bone at the microscopic level. The resolution of images should be sufficient to identify the contours of individual trabeculae, i.e., it should be less than their characteristic thickness which is around 100 $\mu$m in humans. Several imaging methods which are able to produce such high resolution images are available for *in vitro* studies. Destructive methods include microscopy and histology (Fig. 3) which involve serial sectioning or milling for specimen preparation.[28] Non-destructive imaging methods are micro-CT[56,57] and micro-MRI.[58,59] Both micro-CT and micro-MRI can achieve a scan resolution in the range of 10–50 $\mu$m for a cancellous bone specimen with a characteristic face length of 1 cm (Fig. 9).[60,61] Techniques that were extensively used for automatic creation of FE meshes from the reconstructed microarchitecture of cancellous bone employ the voxel conversion or the "marching cubes" algorithms. Size of elements produced by these techniques is typically 50 $\mu$m or smaller, corresponding to the resolution in which contour data of trabeculae were acquired.[62] These methods are usually fast, and can be made fully-automatic. For example, the "marching cubes" algorithm simply converts image voxels representing cancellous bone tissue to equally shaped brick elements. Although a large number of elements is produced in this method

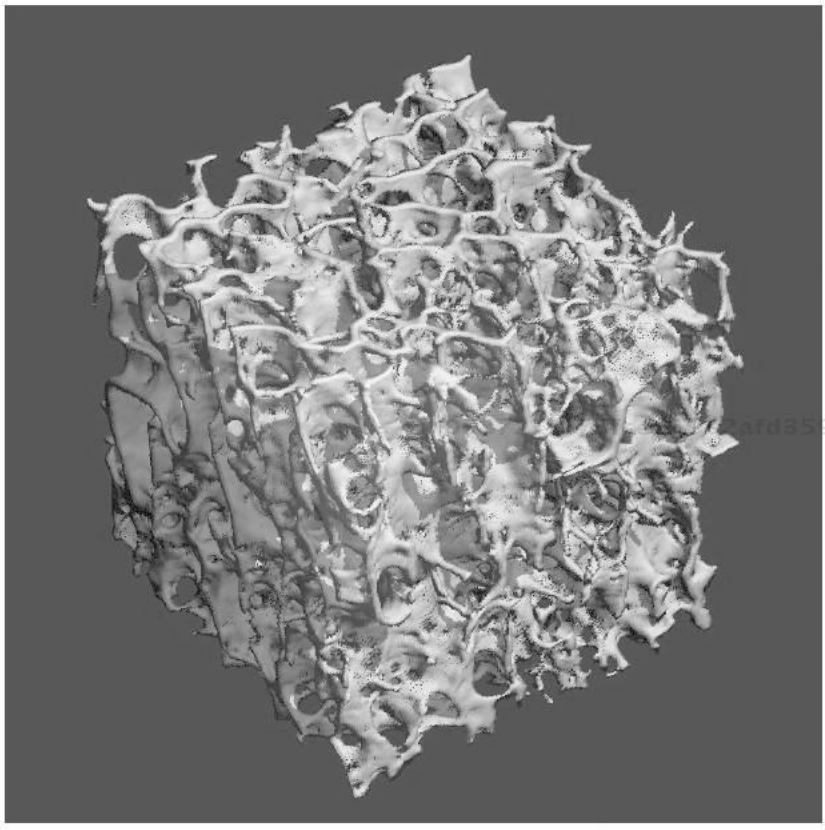

Fig. 9. Human cancellous bone specimen from the distal radius, reconstructed from a micro-computed-tomography (micro-CT) scan *in vitro*. The specimen was scanned at 30 $\mu$m resolution. Finite element (FE) meshing of this cubic specimen (with a face length of about 7.5 mm) produces 1–2 million elements (image courtesy of Dr. Bert van Rietbergen, Department of Biomedical Engineering, Eindhoven University of Technology, the Netherlands).

(in the order of $10^5$–$10^6$ elements per cubic centimeter), a special-purpose FE solver can deal with the problem within a reasonable computation time.[63]

The second step in the FE modeling, i.e., assigning tissue-level mechanical properties to the model, also requires some engineering simplifications. Generally, elements created in either the voxel conversion or the "marching cubes" method are considered at this microscopic level as a homogenous, linear-elastic and isotropic material. Accordingly, elements are assigned tissue-level elastic modulus $E_t$ and a Poisson's ratio $\nu_t$ based on experimental characterization of the mechanical properties of individual trabeculae (e.g., using bending, buckling, nanoindentation, etc.), as detailed in the previous section. Although FE solvers that are currently in the market are able to deal with anisotropic (e.g., transversally isotropic) constitutive properties for bone tissue, they are not currently implemented in

models, apparently owing to absence of experimental data on the distribution of tissue-level density or anisotropy in individual trabeculae.[60] Nevertheless, the assumption of a linear-elastic isotropic behavior of cancellous bone at the tissue-level was shown to provide adequate predictions of macroscopic (apparent) behavior of cancellous bone in many published studies, and is considered sufficient in most cases.[60]

The third step in the FE modeling of cancellous bone is to determine the loading mode and constraints in order to simulate a certain experimental condition (e.g., unconfined compression, Fig. 2) or to reproduce some physiological loading mode (e.g., compound compression and torsion as may occur in spinal cancellous bone). After solving the FE model for distributions of tissue strains and stresses, validation is necessary. Hence, the fourth and last step of modeling — validation — can address the macroscopic mechanical behavior of cancellous bone (apparent behavior), or the microscopic mechanical behavior of individual trabeculae (tissue-level behavior). Other than conventional mechanical testing to achieve validation at the apparent scale (Fig. 2), it is also possible to validate model predictions of tissue-level strains using the texture correlation technique which extracts displacement patterns from digitized contact radiographs of the samples under load.[64,65] For example, using texture correlation, approximately 2000 local strain values can be obtained from cancellous bone in a single human vertebra, which is detailed enough to allow validation of FE model predictions of strains in individual trabeculae in a single vertebra.[65]

### 2.3.2. *Micro-imaging-based cancellous bone models*

The micro-imaging-based FE analysis of cancellous bone microarchitecture was limited in its early stages (1990s) to small excised cancellous bone specimens, particularly because resolution of bone imaging *in vivo* was too coarse to allow identification of individual trabeculae.[63] The next step of evolution of these systems allowed micro-CT or micro-MRI reconstructions of cancellous bone microarchitecture *in vivo*, in small mammals (typically rodents).[66] The most recent advances in micro-imaging-based acquisition and processing techniques allow the 3D cancellous bone microarchitecture of humans to be analyzed *in vivo* at peripheral sites such as the distal radius or calcaneus.[59,67] Extension of micro-imaging-based methods to study typical osteoporotic fracture sites (e.g., the proximal femur or vertebrae) with sufficient resolution *in vivo* is not yet achievable, and hinges on further advances in detection sensitivity.[68] Nevertheless, technologies for reconstructing the microarchitecture of cancellous bone with micro-CT (Fig. 9) and micro-MRI *in vitro* and *in vivo* are constantly improving, and scanning resolutions decline. For example, it was shown that a micro-CT with high intensity and tight collimation synchrotron radiation is able to achieve spatial resolution of 1–2 $\mu$m *in vitro*.[66] Such resolutions provide the capability to assess details in trabeculae that are as small as resorption cavities produced by osteoclast cells.[66]

### 2.3.3. *Generic lattice cancellous bone models*

Micro-imaging-based FE models reconstructed from cancellous bone samples *in vitro* (Fig. 9) are highly useful in basic biomechanical research. However, *in vitro* studies are ineffective when it is desired to assess the mechanical performance of cancellous bone in individual osteoporotic (and other) patients. In order to obtain subject-specific mechanical properties of cancellous bone at sites susceptible to osteoporotic fractures (e.g., in vertebrae) non-invasively and in a robust and cost-effective manner, methods for *in vivo* acquisition of cancellous bone geometry are needed.

Nowadays, quantitative computed tomography (QCT) can be performed on clinical CT scanners to determine not only the bone mineral density (BMD), but also some apparent morphological properties of cancellous bone in patients (when the field of view of the imager is set to be at about the transverse cross-section of a single vertebra).[69] Specifically, the spatial resolution achievable *in vivo* by current whole-body QCT clinical imagers is just sufficient to reveal the apparent $V_f$, Tb.Th, and Tb.Sp[69,70] but not to reconstruct the shapes of individual trabeculae such as in micro-CT or micro-MRI studies.[31,56,60,63,67] The limitation on spatial resolution of whole-body QCT clinical imagers *in vivo* is due to the fact that projections blur the bone structure in the final QCT reconstructions. This blurring occurs because the minimum slice thickness currently achievable in humans *in vivo* ($\sim$1 mm) is $\sim$five times thicker than the average width of a trabecula ($\sim$200 $\mu$m) and about equal to the average intertrabecular dimension Tb.Sp found in normal subjects. Fortunately, however, with the aid of image processing methods, e.g., run-length encoding steps[71] or the ridge detection algorithm[72] which are now applied in large-scale clinical studies,[69,70] apparent morphological properties (e.g., $V_f$, Tb.Th, and Tb.Sp) can be extracted with sufficient accuracy from clinical QCT scans.

Apparent morphological properties are useful when it is desired to determine the equivalent mechanical properties of cancellous bone which correspond to the measured apparent morphological properties (for instance, the apparent elastic modulus of cancellous bone $E_{cb}$). This requires analysis of equivalent cancellous bone structures constructed according to the QCT-measured apparent morphological properties, rather than analysis of the real cancellous bone microarchitecture as in methods that analyze micro-CT or micro-MRI based reconstructions. Equivalent models of cancellous bone, called generic lattice bone models, are based on the observation that the microarchitecture of cancellous bone approximately conforms to a number of typical patterns consisting of 3D interconnected rods and plates.[22] A generic lattice model which is based on the single-trabecula building-block[28,53] is shown in Fig. 6. Other than being able to represent the mechanical properties of cancellous bone of an individual based on its apparent morphological parameters measured *in vivo*, generic lattice models offer several advantages. First, generic lattice models are not affected by local structural defects in individual trabeculae (which may be real defects

that are caused biologically or during specimen preparation, or be artifacts of the micro-imaging scan technique). Rather, generic lattice models produce the mechanical behavior of cancellous bone that is comprised of trabeculae with a smoothed "average" morphology, without considering atypical or abnormal shapes of individual trabeculae. Second, generic lattice models (Fig. 6) can be developed to very large sizes compared with micro-imaging-based reconstructions of cancellous bone (Fig. 9), because there is no limitation of the imaging field of view. Third, the computational power required for solving the FE problem in generic lattice models is substantially less than in micro-imaging-based models, since the irregular and potentially jagged geometries of each individual trabecula are not considered in the FE meshing. Fourth, the ability to produce and solve larger cancellous bone models allows to minimize the effect of boundary conditions on the mechanical behavior of the model, according to St. Venant's principle.[22] Fifth, when model size is less of a limitation, then FE analyses of whole human bones (e.g., vertebrae or the calcaneus) can be conducted economically, i.e., with reasonable CPU power and computation time. The sixth and last important feature of generic lattice models is their ability to determine the mechanical behavior of a "typical" rather than a specific cancellous bone sample.[28] In other words, actual experimental test or an FE analysis of a real cancellous bone specimen reconstructed from a micro-imaging scan provide a mechanical behavior that is specific to the particular bone that was studied.[22,28] It is extremely difficult to then generalize the mechanical behavior for a large population of bones or subjects. Generic lattice models, in contrast, may be used to characterize a more general mechanical behavior that should be expected for any specimen with apparent morphological properties as in the model.

Several generic lattice models of repeated cellular solid structures were developed to study the mechanical behavior of cancellous bone using different geometrical descriptions for the unit cell.[22,73–76] The more recent contributions accounted for the curved geometry of individual trabeculae rather than treating them as beams with uniform (circular or rectangular) cross-sections.[22,76] Specifically, Kim and Al-Hassani[76] considered differences between base and central thickness of trabeculae and used linear regression equations for relating thickness and separation of trabeculae with the age of bone. Most recently, Kowalczyk described the shape of unit cells using Bézier curves, which allowed to demonstrate a wide variety of microstructural patterns.[22] All generic lattice models in the literature were characterized by simplicity of formulation, and easy definition of boundary conditions that ensured repeatability of cell deformation and ability to parameterize the results.[22] However, apart from the studies of Dagan *et al.*[28] and Diamant *et al.*[53] who utilized the single-trabecula building-block which is based on anatomical microarchitectural measurements, none of the published generic models employed real microarchitectural statistical data to define the unit cell geometry.

Use of generic lattice models to represent the microarchitecture of cancellous bone also involves some limitations that should be discussed. In particular, when developing subject-specific models of the microarchitecture of cancellous bone,

model inputs include Tb.Th and Tb.Sp which are to be extracted from *in vivo* QCT scans of individuals. Hence, image acquisition and, image processing related limitations of current clinical QCT scans may affect the accuracy of Tb.Th and Tb.Sp evaluations and, consequently, may introduce some inaccuracies in predicted mechanical properties, e.g., in $E_{cb}$. For example, extraction of Tb.Th and Tb.Sp from clinical QCT is based on processing 2D slices of the actual 3D architecture[69] (unlike micro-CT and micro-MRI which are able to evaluate Tb.Th and Tb.Sp directly from the 3D solid reconstructions). Additionally, QCT scans may overestimate Tb.Th and Tb.Sp (with a stronger influence on Tb.Th) if the scanning voxel size is greater than 20 $\mu$m.[77] Although the typical scanning voxel size in commercial clinical QCT scanners to date is over 100 $\mu$m, image enhancement algorithms such as the run-length encoding steps[71] or the ridge detection algorithm[72] have the potential to reverse the overestimation effect, and such improvements are yet to be quantified. Overall, the resolution-related problems in defining apparent morphological parameter inputs for generic lattice cancellous bone models are expected to resolve during the upcoming years, with the continuous improvement in hardware and software of clinical QCTs.



## 3. Model Applications to Load-Bearing Phenomena in Normal and Osteoporotic Cancellous Bone

The final section of this chapter provides some practical examples in the FE modeling of the microarchitecture of cancellous bone. All the studies below employ the single-trabecula building-block, a standard (generic) model component for large-scale FE models of cancellous bone[28,53] which was described earlier in this chapter. The single-trabecula building-block is employed here to study several load-bearing phenomena in normal and osteoporotic cancellous bone, including studies of the apparent compression behavior of cancellous bone, the strain inhomogeneity in individual trabeculae, and buckling behavior of trabeculae.



### 3.1. *Compression behavior of cancellous bone*

In this application the apparent elastic modulus of cancellous bone $E_{cb}$ in vertebrae is calculated from a set of three physical and morphological properties of the bone that can all be assessed *in vivo*, in the clinical setting. These properties are the tissue BMD, the apparent Tb.Th, and the apparent Tb.Sp, which were previously measured in individuals with sufficient accuracy using commercial QCT clinical scanners (e.g., the GE CT-9800Q system).[69] The relations obtained herein allow to determine the $E_{cb}$ reflecting the individual's condition of a normal, an osteopenic, or a hypertrophic spinal cancellous bone. To obtain $E_{cb}$ as a function of tissue BMD, apparent Tb.Th, and apparent Tb.Sp, an orthogonal generic lattice model of cancellous bone in the spine which employs the single-trabecula generic

building-block is used (Fig. 6). To analyze lattices of various sizes and with different cancellous bone qualities, we developed a custom-made FE code (Visual C++ 6, Microsoft Co.). This code solves the apparent elastic modulus ($E_{cb}$) of any cubic orthogonal trabecular lattice similar to that in Fig. 6 under compression loading, depending on the three trabecula characteristics (tissue BMD, apparent Tb.Th, and apparent Tb.Sp). Being ideally orthogonal, under pure compression loading, these lattices best represent spinal cancellous bone, which closely follows orthogonal paths[78] and which supports mostly compression.[79] For orthogonal lattices, the trabecular separation, Tb.Sp, equals the (uniform) length of trabeculae in the lattice, $L$. The details of the FE code which runs parametric FE analyses to solve $E_{cb}$ from inputs of tissue BMD, apparent Tb.Th, and apparent Tb.Sp were provided elsewhere.[53] The fundamental calculation steps are described below:



- Uniform compression force $F$ is distributed over two opposite faces of the lattice. Each trabecular column now carries a load of $F_c = F/\#\text{columns}$ that generates a strain distribution $\varepsilon(z)$ in each vertical trabecula which is a function of the local cross-sectional area of the trabecula, $A_{Tb}$. Integrating strain $\varepsilon(z) = F_c/A_{Tb}(z)$ over the trabecular length $L = \text{Tb.Sp}$, we obtain the deformation of each vertical trabecula:

$$\begin{aligned}\delta_{Tb} &= \int_{-\frac{1}{2}\text{Tb.Sp}}^{\frac{1}{2}\text{Tb.Sp}} \varepsilon(z)\cdot dz \\ &= \frac{8\cdot F_c\cdot \text{Tb.Sp}\cdot(1+\alpha)^2}{25\cdot\gamma\pi(2\cdot\text{Tb.Th})-\beta)^2 E_t} \\ &\quad\times\left[\frac{10\cdot\tan(\gamma/2)+15\lambda\cdot\tan^{-1}(\lambda\cdot\tan(\gamma/2))[\tan^2(\gamma/2)+\eta]}{5\cdot\tan^2(\gamma/2)+1}\right], \qquad (7)\end{aligned}$$

where $\lambda = \sqrt{5}$ and $\eta = 0.2$. The tissue-level elastic modulus $E_t$ is calculated from the tissue BMD using the regression of Guo and Goldstein[80] as follows:



$$E_t = 24\cdot\text{BMD} - 3.73\,, \qquad (8)$$

where BMD units are in grayscale/mm$^2$ (image intensity). Considering that for a trabecular tissue density of 1.874 g/cc, the mineral fraction being 33.9% and the corresponding BMD being 0.34 grayscale/mm$^2$, it is possible to convert the image intensity units in the Guo and Goldstein paper[80] to g/cc. Equation (8) now becomes

$$E_t = 12.85\cdot\text{BMD} - 3.73\,, \qquad (9)$$

where $E_t$ is specified in GPa for a BMD value in g/cc.

- Equation (7) was solved using the FE method by approximating the curvature of an individual trabecula (characterized in Eq. (2) and depicted in Fig. 5) as a combination of 200 cylindrical elements with varying thicknesses.

- The compression deformation of the whole lattice is the sum of deformations of vertical trabeculae in a column under load $F_c$. The compression strain of the lattice is calculated from the definition of strain:

$$\varepsilon_{cb} = \frac{\sum_{i=1}^{\#\text{Trabeculae in a column}} \delta_{Tb}}{L_{cb}}, \tag{10}$$

where $L_{cb}$ is the undeformed face length of the lattice, and $\delta_{Tb}$ is the deformation of an individual vertical trabecula (from Eq. (7)). The corresponding average (apparent) compressive stress over the whole lattice is

$$\sigma_{cb} = \frac{F}{L_{cb}^2}, \tag{11}$$

where $L_{cb}^2$ is the cross-sectional area of the lattice.



- In each run, we incrementally increased $F$ from zero (in steps of 0.035 N) until reaching 0.3% strain of the lattice (i.e., a small strain analysis is maintained[50,51]). For each incremental load, we plotted the average lattice stress ($\sigma_{cb}$) versus the average lattice strain ($\varepsilon_{cb}$). The slope of the $\sigma_{cb}$–$\varepsilon_{cb}$ plot generated through that process is the apparent elastic modulus ($E_{cb}$) of the generic lattice model, which reflects the $E_{cb}$ of a cancellous bone specimen with the tissue BMD, apparent Tb.Th, and apparent Tb.Sp that were fed into the simulation.
- The volume of each trabecula in the lattice is specified in Eq. (3). The volume fraction ($V_f$) of bone tissue in the lattice is obtained from summing the volumes of all individual trabeculae and dividing that sum by the overall lattice volume $L_{cb}^3$. The apparent density of the lattice $\rho_{cb}$ is obtained from multiplying the volume fraction $V_f$ of the lattice by the tissue-level density of trabeculae $\rho_t$ as

$$\rho_{cb} = \rho_t \cdot V_f = \frac{\rho_t}{\text{Tb.Sp}^2} \cdot \pi \cdot \frac{(\beta - 2 \cdot \text{Tb.Th})^2}{4\gamma(1+\alpha)^2} \cdot (11\gamma + \sin 2\gamma - 12 \sin \gamma), \tag{12}$$



where $\rho_t = 1.99$ g/cc (for trabeculae in the vertebrae[21]).

We ran 5000 cases, using cubic lattices that contained 1344 trabeculae. Although in reality, the model parameters (tissue BMD, apparent Tb.Th, and apparent Tb.Sp) are not truly independent across subjects, we varied one parameter per simulation case to study the sensitivity of the model's predictions of apparent elastic modulus $E_{cb}$ to a change in each parameter. Figure 10 shows the results of $E_{cb}$ depending on apparent Tb.Th and apparent Tb.Sp for a constant tissue BMD of 0.62 g/cc (mean value for human cancellous bone[80]). The values of the morphological parameters Tb.Th and Tb.Sp in Fig. 10 represent lumbar spinal cancellous bone across ages of 10–100 years.[81]

A strong nonlinearity of $E_{cb}$ emerges in Fig. 10. The nonlinear relation of $E_{cb}$ to apparent Tb.Th and apparent Tb.Sp originates in Eq. (7). Specifically, in Eq. (7), Tb.Th appears in a polynomial expression (in power of 2) in the denominator,

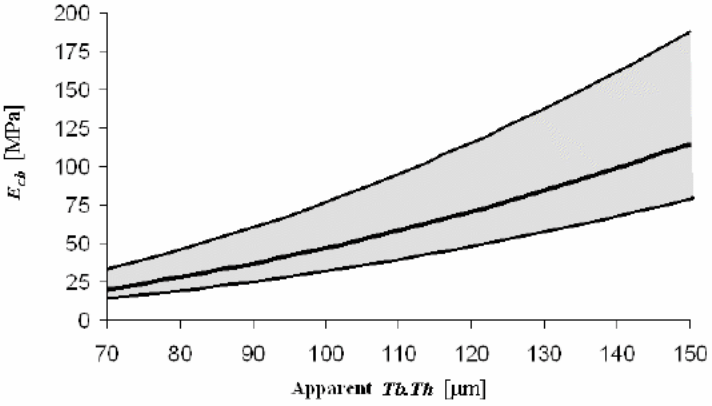


Fig. 10. Finite element (FE) predictions of the apparent elastic modulus of spinal cancellous bone $E_{cb}$ versus the apparent trabecular thickness Tb.Th. The thick central curve depicts FE model predictions of spinal $E_{cb}$ for Tb.Sp = 700 $\mu$m which was reported by Thomsen *et al.*[81] to be the mean Tb.Sp in the lumbar spine across ages of 10–100 years. Upper and lower shaded regions limit $E_{cb}$ for Tb.Sp values within one standard deviation from the mean. The value of one standard deviation of Tb.Sp = 150 $\mu$m was also adopted from Thomsen *et al.*[81] In all simulations, constant tissue BMD of 0.62 g/cc was assumed.[80]

and Tb.Sp concurrently influences the integration term and defines its limits. In contrast, tissue BMD linearly affects $E_{cb}$, because it correlates linearly with the tissue-level elastic modulus $E_t$ (Eq. (9)),[80] which is treated as a constant for the purpose of integration in Eq. (7). Accordingly, small tissue BMD variations (~10%) affect the predictions of $E_{cb}$ more weakly than do small changes in apparent Tb.Th and apparent Tb.Sp. For example, for mean morphological parameter values of Tb.Th = 120 $\mu$m and Tb.Sp = 700 $\mu$m which represent normal spinal cancellous bone, an increase in tissue BMD from 0.59 to 0.7 g/cc caused a linear rise of up to ~25 MPa in $E_{cb}$ over that tissue BMD range.

Validation of the present model can be achieved with respect to experimental studies in which both morphological and mechanical property measurements were taken from human spinal cancellous bone. For example, using high-resolution MRI, Majumdar *et al.* found that vertebral cancellous bone specimens with Tb.Th = 170 ± 20 $\mu$m and Tb.Sp = 1100 ± 70 $\mu$m had superior–inferior apparent elastic modulus of 66 ± 63 MPa under compression.[19] Using these apparent Tb.Th and Tb.Sp values as inputs for the present FE model results in a predicted $E_{cb}$ of 61 ± 22 MPa. Another example is a study of human lumbar cancellous bone by Cendre *et al.*, who found that vertebral specimens with Tb.Th = 261 ± 43 $\mu$m and Tb.Sp = 1348 ± 744 $\mu$m had apparent compressive elastic modulus of 134 ± 81 MPa.[82] Again, when these values are used for FE calculation with our generic lattice model, an overlapping apparent elastic modulus $E_{cb}$ of 100 ± 36 MPa is predicted. This very good agreement between the computational predictions and independent empirical observations demonstrates the ability of the

present generic lattice FE model to realistically predict $E_{cb}$ of spinal cancellous bone depending on its microarchitectural properties.

### 3.2. *Strain inhomogeneity in trabeculae*

The traditional interpretation of Wolff's law is that mass distribution and microstructural arrangement of trabeculae in cancellous bone are determined by the local mechanical stresses transferred to the bone. According to this interpretation, trabeculae are arranged on paths of equal ("iso") stress, called isostatics. This suggests that along each individual trabecular path, strains should be approximately uniform. Moreover, strains are expected to be rather uniform across different paths, since in healthy bones under physiological loads, paths do not spontaneously resorb or break, likely because they are subjected to a narrow range of stresses and strains.[83] However, recent micro-imaging-based FE studies of femoral cancellous bone by van Rietbergen *et al.* show considerable variation in tissue strains for the external loads acting on the femoral head during the stance phase of gait.[83] Strain magnitudes in an osteoporotic femoral head analyzed by micro-FE in the same study were ~70% higher and less uniformly distributed than those in the healthy femur.[83] These results lead to a subsequent research question: Is the inhomogeneity of tissue strains predominantly a consequence of structural differences between trabeculae (inter-trabecula strain variability), or is it caused by the curvatures of each individual trabecula (intra-trabecula strain variability)? Accordingly, in this application, the contribution of the shape of a trabecula to the intra-trabecula strain inhomogeneity is determined. Subsequently, FE modeling of individual trabeculae is employed to determine differences in intra-trabecula strain inhomogeneities between normal and thinner, osteoporotic-like trabeculae.

In order to study strain inhomogeneities in individual trabeculae by means of FE modeling, we employed our generic single-trabecula building-block again.[28,53] Empirically, we showed that the thickness at the edges of a mammalian trabecula is proportional to the minimal thickness at the center of the trabecula,[28] as demonstrated in the top panels of Fig. 4. One quantitative measure for the inhomogeneity of strains in an individual trabecula is the difference $\Delta\varepsilon$ between the maximal strain $\varepsilon_{max}$ and minimal strain $\varepsilon_{min}$ along the axis of the trabecula. Assuming first that small strain elasticity applies, and that a pure axial compressive force $F$ is acting on the edges of a trabecula building-block with an elastic modulus $E_t$, the strain inhomogeneity can be calculated from

$$\Delta\varepsilon = \frac{F}{E}\left(\frac{1}{A_{min}} - \frac{1}{A_{max}}\right), \tag{13}$$

where $A_{min}$ and $A_{max}$ are the minimal and maximal cross-sectional areas of the trabecula, respectively. The minimal and maximal cross-sectional areas of a single-trabecula building-block with nominal thickness Tb.Th can be calculated explicitly

from Eq. (2) when substituting $z = 0$ and $z = L/2$, respectively. However, considering that the single-trabecula building-block is characterized by a circular cross-section (Eq. (2)), Eq. (13) can be reformulated as

$$\Delta\varepsilon = \frac{4}{\pi}\frac{F}{E}\left(\frac{1}{t_{\min}^2} - \frac{1}{t_{\max}^2}\right). \tag{14}$$

Considering an empirical constant proportion factor $\phi$ between base and center thicknesses,[28] as shown to exist in Fig. 4 (top panels), it can be assumed that $t_{\max} = \phi \cdot t_{\min}$ for $t_{\min} > 0$. Accordingly, Eq. (14) becomes

$$\Delta\varepsilon = \frac{4F}{\pi E_{\mathrm{t}} \cdot t_{\min}^2}\left(1 - \frac{1}{\phi^2}\right). \tag{15}$$

Now let us consider two different trabeculae with center (minimal) thicknesses $t_{\min 1}$ and $t_{\min 2}$ and strain inhomogeneities $\Delta\varepsilon_1$ and $\Delta\varepsilon_2$, respectively. Let us also assume that trabecula #1 is thinner than trabecula #2, i.e., $t_{\min 1} < t_{\min 2}$ and that both trabeculae have the same modulus $E_{\mathrm{t}}$ and that they are both subjected to the same load $F$. For such case, Eq. (15) reveals that

$$\frac{\Delta\varepsilon_2}{\Delta\varepsilon_1} = \left(\frac{t_{\min 1}}{t_{\min 2}}\right)^2, \tag{16}$$

i.e., under pure compressive loading, the strain inhomogeneity in the thinner trabecula #1 ($\Delta\varepsilon_1$) must be greater than the strain inhomogeneity in the thicker trabecula #2 ($\Delta\varepsilon_2$).

In order to systematically study strain inhomogeneities in trabeculae with different profiles (Eq. (2)) which are subjected to more complex, compound loading modes (compression and shear and bending), we again employed our custom-made FE solver (Visual C++ 6, Microsoft Co.). This FE solver is able to approximate the profile shape of the single-trabecula building-block (Eq. (2)) using 200 cylindrical elements with varying thicknesses along the $z$-axis of the trabecula. The tissue-level elastic modulus $E_{\mathrm{t}}$ was set to 10 GPa in simulations considering both normal and osteoporotic trabeculae (Table 2).[28,83] We again analyzed strain inhomogeneities in trabeculae with dimensions that are characteristic of cancellous bone in the spine. In a first set of simulations, we studied strain distributions and strain inhomogeneities in individual trabeculae. Specifically, we considered normal trabeculae in the spine with Tb.Th of 180 $\mu$m and length of 1200 $\mu$m, osteoporotic spine trabeculae with Tb.Th of 120 $\mu$m and length of 2000 $\mu$m, and intermediate Tb.Th and length cases.[14,74] These trabeculae were subjected to identical loads — uniaxial compression force of 0.01 N and bending moment of $10^{-6}$ Nm — a combination which produced small tissue-level strains (less than 5%) in all simulation cases.

In a second set of simulations we studied strain inhomogeneities in statistical "populations" of trabeculae containing trabeculae with different Tb.Th but having the same length (1100 $\mu$m).[14] Specifically, we used Tb.Th in the range of 130–380 $\mu$m

(mean 180 $\mu$m) to represent normal vertebral cancellous bone, and Tb.Th in the range of 60–240 $\mu$m (mean 120 $\mu$m) to represent osteoporotic vertebral cancellous bone (Fig. 5).[14,74] Thickness distributions in normal and osteoporotic "populations" of trabeculae were set to be right-skewed (Fig. 4), as reported in experimental studies.[26,28]

All trabeculae in a "population" were again subjected to identical compressive and bending loads, of 0.1 N and $5 \times 10^{-5}$ Nm, respectively, and it was verified that these loads resulted small tissue-level strains (>5%) in all trabeculae.

Consistently with the conclusion derived from Eq. (16), the results for compound loading (compression and shear and bending) demonstrated that as trabeculae become thinner with the progression of osteoporosis, the strain inhomogeneity becomes wider and strain peaks grow higher. Figure 11(a) shows



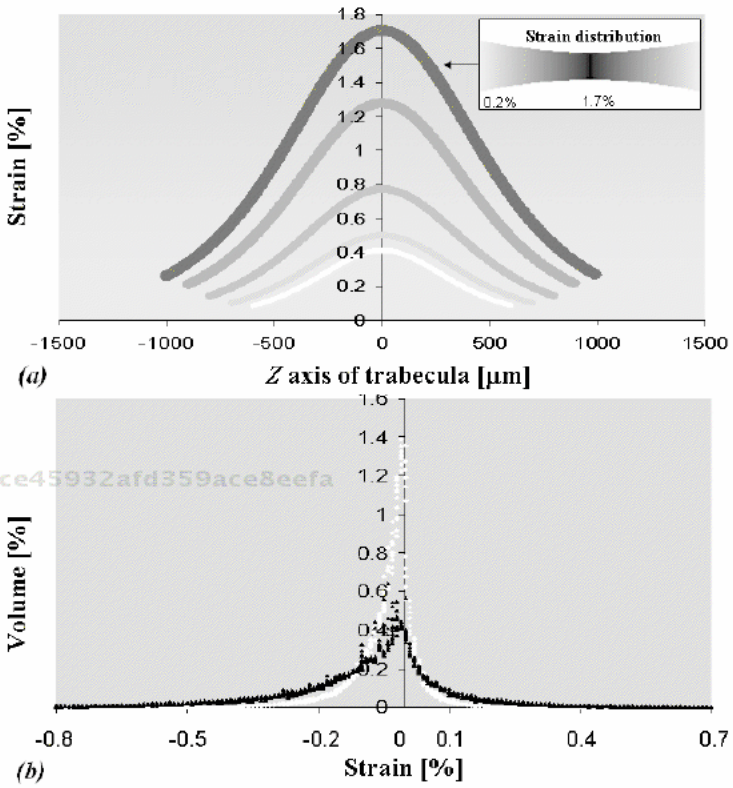


Fig. 11. Intra-trabecula and inter-trabecula strain inhomogeneities: (a) strain distributions along the longitudinal axes of normal (white line, Tb.Th = 180 $\mu$m, $L$ = 1200 $\mu$m) and osteoporotic (black line, Tb.Th = 120 $\mu$m, $L$ = 2000 $\mu$m) trabeculae. Strain distributions for intermediate Tb.Th and lengths are similarly plotted in grayscale. The strain distribution within a longitudinal cross-section of an osteoporotic trabecula is also depicted on the top right. (b) Volumetric distributions of strains in normal (white marks, Tb.Th = 130–380 $\mu$m) and osteoporotic (black marks, Tb.Th = 60–240 $\mu$m) "populations" of trabeculae. The length of all trabeculae in the model is identical, 1100 $\mu$m.

strain distributions in progressively thinning individual trabeculae. The strain inhomogeneity in the longest (2000 $\mu$m) and thinnest (120 $\mu$m) trabecula ($\Delta\varepsilon$ = ~1.4%) is nearly five-fold that in the shortest (1200 $\mu$m) and thickest (180 $\mu$m) trabecula ($\Delta\varepsilon$ =~0.3%).

Figure 11(b) shows the volumetric distribution of strains across "populations" of normal trabeculae (Tb.Th = 130–380 $\mu$m, length = 1100 $\mu$m) and osteoporotic trabeculae (Tb.Th = 60–240 $\mu$m, length = 1100 $\mu$m).[14,74] Consistently with the results for intra-trabecula strain inhomogeneities (Fig. 11(a)), the results for populations show that in normal cancellous bone strains are more uniform than in osteoporotic bone. For the thickness distributions in these simulations, strain inhomogeneity in the osteoporotic cancellous bone ($\Delta\varepsilon = 1.7\% \pm 1.4\%$) was more than threefold that in the normal cancellous bone ($\Delta\varepsilon = 0.5\% \pm 0.2\%$).

Taking these results together, our FE modeling of individual trabeculae and "populations" of trabeculae supports the hypothesis that when subjected to equivalent loads, thinner, osteoporotic-like trabeculae are found under substantially greater strain inhomogeneities (or strain gradients), compared with normal trabeculae. The present results also agree with the studies of van Rietbergen *et al.*,[83] and further indicate that intra-trabecula strain inhomogeneities may be a primary factor contributing to the effective strain inhomogeneities observed in their studies of femoral heads.[83] One important assumption in the present analyses is that osteoporotic bones are loaded as normal bones, but in real-life situations, osteoporotic patients may be less active, and this may be a compensating effect which reduces strain inhomogeneities in their cancellous bone. Additional FE studies, based on micro-imaging reconstructions of individual trabeculae, will now be required to distinguish between the contributions of intra-trabecula and inter-trabecula strain inhomogeneities to the overall reported increase in strain inhomogeneity with osteoporosis.[83]



### 3.3. *Buckling behavior of trabeculae*

Compression fractures in vertebrae are a serious health care problem among the aging population. The risk for vertebral compression fractures increases with age and with loss of cancellous bone density, trabecular thickness, and connectivity, and, accordingly, these fractures are often classified as osteoporotic fractures.[7] Vertebral compression fractures are considered to be a-traumatic. It is commonly believed that these fractures are the accumulative outcome of mechanical failure of many individual trabeculae which, until failure, functioned to support load in the inferior–superior direction of the vertebra.[84] Considering that each such individual trabecula in the spine bears mostly compression and bending, it is very likely that failure occurs in buckling when the ratio $r_{\min}^4/L^2$ drops below a critical threshold as a result of osteoporotic thinning and loss of horizontal constraints (Eq. (6) and Fig. 8). Trabeculae in normal spinal cancellous bone are 1000–1800 $\mu$m long, with Tb.Th

in the range of 130–180 $\mu$m.[74] Trabeculae in osteopenic spinal cancellous bone are effectively longer (due to loss of connectivity that eliminates horizontal constraining, as shown in Fig. 8), in the range of 1800–2000 $\mu$m, and their Tb.Th is reduced to 80–120 $\mu$m.[74] For these ranges of Tb.Th and $L$ dimensions, the slenderness ratio is less than 100, which indicates that inelastic buckling may be involved.[85] However, due to lack of experimental data on post-yield stiffness of individual trabeculae, the theory of elastic buckling is presently used to analyze buckling of trabeculae.[15] In this last application, the buckling behavior of individual trabeculae in cancellous bone is studied. Specifically, we aim at determining the critical load under which a macroscopic cancellous bone specimen fails owing to accumulative buckling-related failure of individual trabeculae. We also aim at comparing that critical load between normal and osteopenic bone microarchitectures. It should be considered here that the macroscopic failure load depends not only on the apparent Tb.Th and Tb.Sp in a cancellous bone specimen, but also, and strongly, on the intra-specimen variation in these properties.[15,86]



Let us consider a generic lattice model of spinal cancellous bone again, as shown in Fig. 6. However, unlike in previous applications, let us now also consider a non-uniform distribution of Tb.Th for trabeculae aligned parallel to the loading direction. In particular, let us consider a right-skewed Tb.Th distribution, which is typical for mammalian cancellous bone as demonstrated in Fig. 4 (center panels). Two such generic lattice models which included 100 trabeculae aligned with the direction of load were generated. In both, the length of trabeculae was uniform, 1000 $\mu$m, but the thickness of trabeculae differed. In the first model which represented normal spinal cancellous bone, Tb.Th values were distributed according to a right-skewed distribution (as in Fig. 4(b), right panel) around a mean Tb.Th of 180 $\mu$m. In the second model which represented osteopenic cancellous bone, Tb.Th values were also distributed as in Fig. 4(b) (right panel) but around a mean Tb.Th of 120 $\mu$m. Tissue-level moduli $E_t$ of 11 GPa were assigned to trabeculae with thicknesses greater than 120 $\mu$m, and slightly lower $E_t$ of 9.1 GPa were assigned to osteopenic trabeculae thinner than 120 $\mu$m (to consider the degrading effect of perforations by accelerated osteoclastic activity).[87] Identical compressive loads $F_{total}$ were then applied to both models. In each model, and across a layer of trabeculae (Fig. 6), the compressive load $F_{total}$ is shared among trabeculae aligned parallel to the loading direction. The fraction of the load borne by each individual trabecula with index $i$, which is defined by $(F_c/F_{total})_i$, approximately equals the ratio of the axial stiffness of that trabecula to the sum of axial stiffnesses of all trabeculae in the layer together, i.e.,



$$\left(\frac{F_c}{F_{total}}\right)_i [\%] = 100 \times \frac{E_t^i \cdot A_{Tb}^i}{\sum_j E_t^j \cdot A_{Tb}^j}, \tag{17}$$

where $A_{Tb}^i$ is the nominal cross-sectional area and $E_t^i$ is the tissue-level elastic modulus of trabecula $i$. Now approximating each trabecula as a cylinder with

nominal thickness $\mathrm{Tb.Th}^i$ we obtain

$$\left(\frac{F_\mathrm{c}}{F_\mathrm{total}}\right)_i [\%] = 100 \times \frac{E_\mathrm{t}^i \cdot \frac{\pi}{4} \cdot (\mathrm{Tb.Th}^i)^2}{\sum_j E_\mathrm{t}^j \cdot \frac{\pi}{4} \cdot (\mathrm{Tb.Th}^j)^2} = 100 \times \frac{E_\mathrm{t}^i \cdot (\mathrm{Tb.Th}^i)^2}{\sum_j E_\mathrm{t}^j \cdot (\mathrm{Tb.Th}^j)^2} \,. \quad (18)$$

The load actually transferred to each individual trabecula $i$ (Eq. 18) was compared with its Euler's critical load for buckling $F_{\mathrm{c(critical)}}$ (Eq. (6)). If the actual axial load applied to a trabecula exceeded $F_{\mathrm{c(critical)}}$, a buckling failure was considered to occur in that trabecula.

Equation (6) indicated that the maximal compressive force that an individual normal spinal trabecula in our generic lattice model could support without buckling was between 1.9 and 20 N. Likewise, the range of maximal compressive forces that could have been carried by an individual osteopenic trabecula was between 0.1 and 1.1 N. Now considering a "population" of trabeculae (with non-uniform right-skewed Tb.Th distribution), we observed that in the normal spinal cancellous bone model, 5% of the trabeculae failed in buckling under load of ~150 N, and 95% failed when the load reached ~3500 N. In the osteopenic spinal cancellous bone model, however, 5% of trabeculae failed already when ~15 N were applied, and 95% failed under a load of 600 N. The percentage of trabeculae that failed in buckling as function of the total compressive load $F_\mathrm{total}$ is shown in Fig. 12 for both generic lattice models (normal and osteopenic spinal cancellous bone). Although these models are not scaled to dimensions of real vertebrae, they do indicate that buckling failure of

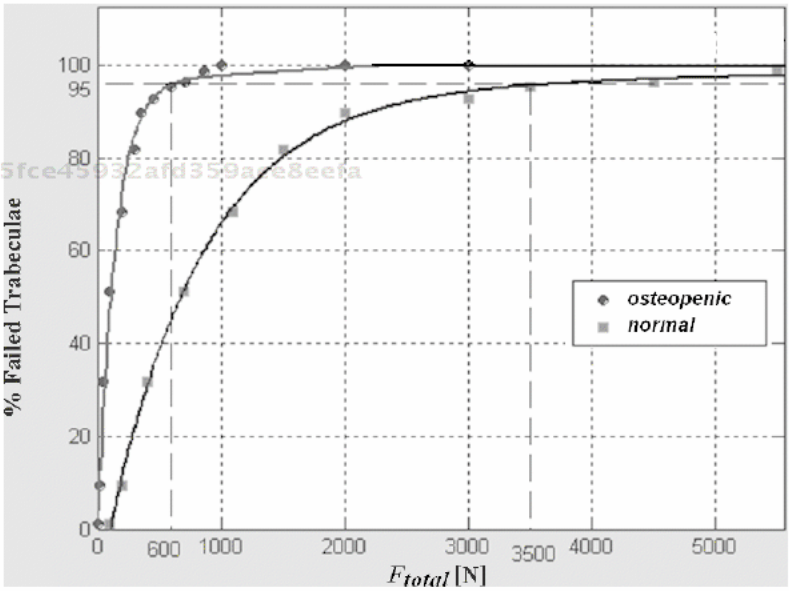


Fig. 12. Computational simulation results showing the percentage of spinal trabeculae oriented with the loading direction which failed in buckling, as function of the total compressive load $F_\mathrm{total}$ for generic lattice models of normal and osteopenic spinal cancellous bone.

5% of trabeculae in a normal vertebra requires as much as 10-fold the force that is required to cause the same extent of damage in an osteoporotic vertebra. This result demonstrates very well how the osteopenic cancellous bone microarchitecture promotes vertebral compression fractures under a-traumatic loads. One limitation that should be discussed, however, is that these simulations were quasi-static, rather than dynamic. In real-world situations, the spine is loaded dynamically and cyclically. Hence, if some trabeculae in an osteopenic spine fail in buckling under an a-traumatic load, the next cycle of load will be supported by fewer trabeculae, each of which bearing an increased load (Eq. (18)). Accordingly, the later cycle of load is expected to lead to a greater percentage of failed trabeculae compared with the early cycle, and unless the spinal load is reduced or the vertebra is somehow reinforced (e.g., through vertebroplasty), this damage spiral will continue to progress until the vertebra totally collapses. The presently proposed simulation method allows iterative calculation of the damage progression in cancellous bone models under cyclic loading, and studies are now underway in our laboratory to expand the FE generic lattice modeling approach in that direction.



## 4. Concluding Remarks

With today's imaging modalities and computer power, FE analysis of cancellous bone microarchitecture is becoming a surrogate for actual experiments. After reconstructing the real geometry of cancellous bone using micro-imaging-based methods, or after reconstructing an equivalent (generic lattice) geometry based on image analysis of apparent morphological properties, the macroscopic and microscopic mechanical behavior of cancellous bone can be investigated in a robust, economic, and controlled manner. Unlike the situation in laboratory experiments, where it is generally difficult to study the tissue-level strains and stresses in cancellous bone due to the small size of individual trabeculae, with FE analysis it is equally easy to study strains and stresses at the apparent and at the tissue scales. Considering also some other limitations of laboratory experiments such as insufficient specimen supplies, limited specimen sizes, difficulties in controlling boundary and loading conditions, considerable biological variability in both microarchitecture and tissue-level stiffness etc., it is expected that FE analysis will become at least as dominant as experimentation for evaluating the mechanical performance of cancellous bone. Practically, the growing number of studies which employs FE to analyze the microarchitecture of cancellous bone suggest that "numerical experiments" or "virtual experiments" are many times preferred over real experiments, due to the low cost and strictly controlled testing environment that FE analysis offers.



The applications of FE analysis of cancellous bone microarchitecture that were provided in this chapter concerned load-bearing phenomena in the apparent and tissue scales, and all employed a generic lattice modeling approach. Evidently, representation of the microarchitecture of cancellous bone as an equivalent

mechanical structure is a useful approach, which is able to reproduce the macroscopic mechanical behavior of bone as well as to shed light on tissue-level behavior. Specifically, since generic lattice modeling is insensitive to the above-listed problems of experimentation, of which many also exist in micro-imaging-based FE modeling (e.g., defects in specimens, limitations on specimen size, non-uniform boundary conditions, etc.), it offers unique strengths over the other methods.[22] One such strength is the ability to couple generic lattice modeling with *in vivo* medical imaging, which allows to provide patient-specific, anatomical-site-specific evaluation of bone mechanical properties that can be used for diagnostic and prognostic purposes in the clinical setting.[53]

Finite element modeling of the microarchitecture of cancellous bone not only provides fundamental information on the mechanical function of bone *per se*, but is also an important tool for understanding biological processes that govern the metabolism of bone. In the last decade we faced vast progress in bone cell biology research. Equally important was the progress in development of biomechanical theories that mathematically formulate the interactions between a mechanical stimulus on bone (strain, stress, strain energy, etc.), mechanosensory function of cells embedded in the bone (osteocytes), and build-up of new bone (by osteoblasts) or resorption of existing bone (by osteoclasts).[88] These theories generally assume that substantial and chronic changes in issue-level local strains, stresses, or strain energies in bone signal the osteocytes to transmit stimuli to the surface, where bone is formed or resorbed until the strains, stresses, or strain energies are normalized.[88] The formulation of these theories and the methods of coupling them with micro-imaging-based and generic lattice models of cancellous bone extend beyond the scope of this chapter, and the reader is referred to the literature which shows variant approaches as to the type of mechanical stimulus that controls the adaptation or remodeling (strain, stress, strain energy density, or strain energy per unit bone mass), the adaptation law (linear, non-linear), and the formulation of inter-cellular communication.[9,88–91]



In closure, FE modeling of the microarchitecture of cancellous bone is a powerful biomechanical tool to determine how the mechanical performance of cancellous bone degrades with osteoporosis. In the model applications provided herein, it was demonstrated how FE modeling can be employed to determine relations between morphological and mechanical properties at the microscopic (trabecula) level, the mechanical performance of individual trabeculae, and the effects on the macroscopic mechanical performance of cancellous bone. The concurrent developments in imaging technology, computer technology, and FE software capabilities show a great promise that in the near future FE analysis of the microarchitecture of cancellous bone will become a routine clinical procedure. In particular, FE modeling of cancellous bone to determine its apparent mechanical properties based on *in vivo* imaging seems useful for evaluating the fracture risk in osteopenic patients, and for monitoring the effect of pharmaceutical treatments on restoring bone stiffness and strength. Another promising application is in determining the timing for

intervention in patients who are candidates for vertebroplasty, spinal fusion, and other surgical procedures that are aimed at reinforcing or stabilizing cancellous bone structures. These applications, which are expected to promote orthopedic treatments substantially, depend on adaptation of the modeling approach to be patient-specific, and to be fast, robust, economical and easy to implement analyses in the clinical setting. Work in our laboratory is already oriented in these directions.[53]

## Acknowledgments

This study was supported (in part) by grant No. 5918 from the Chief Scientist's Office of the Ministry of Health, Israel. My students Michal Be'ery-Lipperman, Dor Dagan, Idit Diamant, Ronit Mann, and Sigal Portnoy are thanked for their contributions to this chapter.

## References

1. N. F. Ray, J. K. Chan, M. Thamer and L. J. Melton, *J. Bone Mine. Res.* **12** (1997) 24–35.
2. D. M. Black, J. P. Bilezikian, K. E. Ensrud, S. L. Greenspan, L. Palermo, T. Hue, T. F. Lang, J. A. McGowan and C. J. Rosen, *New Engl. J. Med.* **353** (2005) 555–565.
3. D. M. Kado, W. S. Browner, L. Palermo, M. C. Nevitt, H. K. Genant and S. R. Cummings, *Arch. Intern. Med.* **159** (1998) 1215–1220.
4. E. Seeman, *J. Appl. Physiol.* **95** (2003) 2142–2151.
5. B. L. Riggs, H. W. Wahner, E. Seeman, K. P. Offord, W. L. Dunn, R. B. Mazess, K. A. Johnson and L. J. Melton, *J. Clin. Invest.* **70** (1982) 716–723.
6. A. Weiss, I. Arbell, E. Steinhagen-Thiessen and M. Silbermann, *Bone* **12** (1991) 165–172.
7. L. J. Melton III, *Spine* **22** (1997) 2S–11S.
8. M. Singh, A. R. Nagrath and P. S. Maini, *J Bone Joint Surg. [Am.]* **52-A** (1970) 457–467.
9. M. Be'ery-Lipperman and A. Gefen, *Clin. Biomech.* **20** (2005) 984–997.
10. T. M. Keaveny and O. C. Yeh, *J. Musculoskel. Neuron. Interact.* **2** (2002) 205–208.
11. J. Homminga, B. R. McCreadie, T. E. Ciarelli, H. Weinans, S. A. Goldstein and R. Huiskes, *Bone* **30** (2002) 759–764.
12. J. Y. Rho, T. Y. Tsui and G. M. Pharr, *Biomaterials* **18** (1997) 1325.
13. P. K. Zysset, X. E. Gou, C. E. Hoffler, K. E. Moore and S. A. Goldstein, *J. Biomech.* **32** (1999) 1005.
14. S. Majumdar, M. Kothari, P. Augat, D. C. Newitt, T. M. Link, J. C. Lin, T. Lang, Y. Lu and H. K. Genant, *Bone* **22** (1998) 445–454.
15. P. Sutton-Smith, I. H. Parkinson, A. M. J. Linn, S. A. Kooke and N. L. Fazzalari, *Clin. Anat.* **18** (2005) 1–7.
16. T. E. Dufresne, P. A. Chmielewski, M. D. Manhart, T. D. Johnson and B. Borah, *Calcif. Tissue Int.* **73** (2003) 423–432.
17. E. Legrand, D. Chappard, C. Pascaretti, M. Duquenne, S. Krebs, V. Rohmer, M. F. Basle and M. Audran, *J. Bone Miner. Res.* **15** (2000) 13–19.

18. R. B. Ashman, J. Y. Rho and C. H. Turner, *J. Biomech.* **22** (1989) 895–900.
19. S. A. Goldstein, D. L. Wilson, D. A. Sonstegard and L. S. Matthews, *J. Biomech.* **16** (1983) 965–969.
20. M. Martens, R. van Audekercke, P. Delport, P. de Meester and J. C. Mulier, *J. Biomech.* **16** (1983) 971–983.
21. E. F. Morgan, H. H. Bayrakter and T. M. Keaveny, *J. Biomech.* **36** (2003) 897–904.
22. P. Kowalczyk, *J. Biomech.* **36** (2003) 961–972.
23. C. Lutz, P. Augat, D. Marsh, A. E. Goodship, R. A. Brand, G. Duda, T. Einhorn, E. H. Schemitsch, S. B. Goodman, T. M. Turner, R. D. Bloebaum, H. Alexander and J. T. Ryaby, *J. Orthop. Trauma* **14** (2000) 440–441.
24. E. A. Thorndike and A. S. Turner, *Frontiers Biosci.* **3** (1998) 17–26.
25. C. L. Zhang and F. A. Popp, *Med. Hypotheses* **43** (1994) 6–11.
26. M. Kothari, T. M. Keaveny, J. C. Lin, D. C. Newitt and S. Majumdar, *Bone* **25** (1999) 245–250.
27. R. J. Fajardo and R. Muller, *Am. J. Phys. Anthropol.* **115** (2001) 327–336.
28. D. Dagan, M. Be'ery and A. Gefen, *Med. Biol. Eng. Comput.* **42** (2004) 549–556.
29. R. Marcus and S. Majumder, in *Osteoporosis*, eds. R. Marcus, D. Feldman and J. Kelsey (Academic Press, San Diego, 2001), pp. 3–17.
30. J. Kabel, B. van Rietbergen, M. Dlastra, A. Odgaard and R. Huiskes, *J. Biomech.* **32** (1999) 673–680.
31. B. van Rietbergen, H. Weinans, R. Huiskes and A. Odgaard, *J. Biomech.* **28** (1995) 69–81.
32. H. H. Bayaktar, E. F. Morgan, G. L. Niebur, G. E. Morris, E. K. Wong and T. M. Keaveny, *J. Biomech.* **37** (2004) 27–35.
33. K. Choi, J. L. Kuhn, M. J. Ciarelli and S. A. Goldstein, *J. Biomech.* **23** (1990) 1103–1113.
34. F. J. Hou, S. M. Lang, S. J. Hoshaw, D. A. Reimann and D. P. Fyhrie, *J. Biomech.* **31** (1998) 1009–1015.
35. J. Y. Rho, M. E. Roy II, T. Y. Tsui and G. M. Pharr, *J. Biomed. Mater. Res.* **45** (1999) 48–54.
36. J. C. Runkle and J. Pugh, *Bull. Hosp. Joint Dis.* **36** (1975) 2–10.
37. P. R. Townsend, R. M. Rose and E. L. Radin, *J. Biomech.* **8** (1975) 199–201.
38. P. K. Zysset, X. E. Guo, C. E. Hoffler, K. E. Moore and S. A. Goldstein, *J. Biomech.* **32** (1999) 1005–1012.
39. P. K. Zysset, X. E. Guo, C. E. Hoffler, K. E. Moore and S. A. Goldstein, *Technol. Health Care* **6** (1998) 429–432.
40. B. van Rietbergen, R. Huiskes, H. Weinans, A. Odgaard and J. Kabel, in *Bone Structure and Remodeling*, eds. A. Odgaard and H. Weinans (World Scientific, Singapore, 1995), pp 137–145.
41. C. Anglin, P. Tolhurst, U. P. Wyss and D. R. Pichora, *J. Biomech.* **10** (1999) 1091–1107.
42. P. Augat, T. Link, T. F. Lang, J. C. Lin, S. Majumdar and H. K. Genant, *Med. Eng. Phys.* **20** (1998) 124–131.
43. X. Banse, C. Delloye, O. Cornu and R. Bourgois, *J. Biomech.* **29** (1996) 1247–1253.
44. S. J. Brown, P. Pollintine, D. E. Powell, M. W. Davie and C. A. Sharp, *Calcif. Tissue Int.* **71** (2002) 227–234.
45. B. Li and R. M. Aspden, *Osteoporosos Int.* **7** (1997) 450–456.
46. E. F. Morgan and T. M. Keaveny, *J. Biomech.* **34** (2001) 569–577.
47. G. D. Krischak, P. Augat, N. J. Wachter, L. Kinzl and L. E. Claes, *Clin. Biomech.* **14** (1999) 346–351.

48. T. Hildebrand, A. Laib, R. Müller, J. Dequeker and P. Rüegsegger, *J. Bone Mineral Res.* **14** (1999) 1167–1174.
49. C. H. Turner and D. B. Burr, *Bone* **14** (1993) 595–608.
50. E. F. Morgan, H. H. Bayraktar, O. C. Yeh, S. Majumdar, A. Burghardt and T. M. Keaveny, *J. Biomech.* **37** (2004) 1413–1420.
51. J. Sierpowska, M. A. Hakulinen, J. Toyras, J. S. Day, H. Weinans, J. S. Jurvelin and R. Lappalainen, *Physiol Meas.* **26** (2005) S119–S131.
52. S. Nagaraja, T. L. Couse and R. E. Guldberg, *J. Biomech.* **38** (2005) 707–716.
53. I. Diamant, R. Shahar and A. Gefen, *Med. Biol. Eng. Comput.* **43** (2005) 465–472.
54. O. C. Zienkiewicz, R. L. Taylor and J. Z. Zhu, *The Finite Element Method: Its Basis and Fundamentals.* 6th Edn. (Elsevier, Butterworth-Heinemann, Burlington, MA, USA, 2005).
55. I. M. Smith and D. V. Griffiths, *Programming the Finite Element Method*, 4th Edn. (John Wiley and Sons, Hoboken, NJ, USA, 2004).
56. B. Van Rietbergen, R. Muller, D. Ulrich, P. Ruegsegger and R. Huiskes, *J. Biomech.* **32** (1999) 443–451.
57. J. L. Kuhn, S. A. Goldstein, L. A. Feldkamp, R. W. Goulet and G. Jesion, *J. Orthop. Res.* **8** (1990) 833–842.
58. F. W. Wehrli, S. N. Hwang and H. K. Song, *Technol. Health Care* **6** (1998) 307–320.
59. B. R. Gomberg, F. W. Wehrli, B. Vasilic, R. H. Weening, P. K. Saha, H. K. Song and A. C. Wright, *Bone* **35** (2004) 266–276.
60. B. van Rietbergen, in *The Physical Measurement of Bone*, eds. C. M. Langton and C. F. Njeh (Institute of Physics Publishing, Bristol, UK, 2004), pp. 475–510.
61. M. Ito, *J. Bone Miner. Metab.* **23** (2005) 115–121.
62. D. Ulrich, B. van Rietbergen, A. Laib and P. Ruegsegger. *Technol. Health Care* **6** (1998) 421–427.
63. B. van Rietbergen, *Proc. ASME Bioengineering Conference*, Snowbird, Utah, USA, Vol. 50 (2001) 107–108.
64. B. K. Bay, *J. Orthop. Res.* **13** (1995) 258–267.
65. B. K. Bay, S. A. Yerby, R. F. McLain and E. Toh, *Spine* **24** (1999) 10–17.
66. Y. Jiang, J. Zhao, D. L. White and H. K. Genant, *Musculoskel. Neuron. Interact.* **1** (2000) 45–51.
67. B. van Rietbergen, S. Majumdar, D. Newitt and B. MacDonald, *Clin. Biomech.* **17** (2002) 81–88.
68. F. W. Wehrli, P. K. Saha, B. R. Gomberg, H. K. Song, P. J. Snyder, M. Benito, A. Wright and R. Weening, *Top. Magn. Reson. Imag.* **13** (2002) 335–355.
69. C. L. Gordon, T. F. Lang, P. Augat and H. K. Genant, *Osteoporos Int.* **8** (1998) 317–325.
70. S. Majumdar, H. K. Genant, S. Grampp, D. C. Newitt, V. H. Truong, J. C. Lin and A. Mathur, *J. Bone Miner. Res.* **12** (1997) 111–118.
71. E. P. Durand and P. Ruegsegger, *J. Comput. Assist. Tomogr.* **15** (1991) 133–139.
72. A. Laib, H. J. Hauselmann and P. Ruegsegger, *Technol. Health Care* **6** (1998) 329–337.
73. L. J. Gibson, *J. Biomech.* **18** (1985) 317–328.
74. H. J. Werner, H. Martin, D. Behrend, K. P. Schmitz and H. C. Schober, *Med. Eng. Phys.* **18** (1996) 601–606.
75. I. A. Anderson and J. B. Carman, *J. Biomech.* **33** (2000) 327–335.
76. H. S. Kim and T. S. Al-Hassani, *J. Biomech.* **35** (2002) 1101–1114.
77. D. G. Kim, G. T. Christopherson, X. N. Dong, D. P. Fyhrie and Y. N. Yeni, *Bone* **35** (2004) 1375–1382.
78. M. Nordin and V. H. Frankel, in *Basic Biomechanics of the Musculoskeletal System*, eds. M. Nordin and V. H. Frankel (Lea & Febiger, Philadelphia and London, 1989).

79. M. Lindh, in *Basic Biomechanics of the Musculoskeletal System*, eds. M. Nordin and V. H. Frankel (Lea & Febiger, Philadelphia and London, 1989).
80. X. E. Guo and S. A. Goldstein, *Forma* **12** (1997) 185–196.
81. J. E. Thomsen, E. N. Ebbesen and L. Moskilde, *Bone* **30** (2002) 664–669.
82. E. Cendre, D. Mitton, J. P. Roux, M. E. Arlot, F. Duboeuf, B. Burt-Pichat, C. Rumelhart, G. Peix and P. J. Meunier, *Osteoporos Int.* **10** (1999) 353–360.
83. B. van Rietbergen, R. Huiskes, F. Eckstein and P. Ruegsegger, *J. Bone Mineral Res.* **18** (2003) 1781–1788.
84. R. R. Recker, *Calcif. Tissue Int.* **53** (1993) S139–S142.
85. C. M. Wang, C. Y. Wang and J. N Reddy, *Exact Solutions for Buckling of Structural Members*, CRC Series in Computational Mechanical and Applied Analysis (CRC Press, Boca Raton, 2005), pp. 69–71.
86. O. C. Yeh and T. M. Keaveny, *Bone* **25** (1999) 223–228.
87. A. M. Coats, P. Zioupos and R. M. Aspden, *Calcif. Tissue Int.* **73** (2003) 66–71.
88. R. Huiskes, R. Ruimerman, G. H. van Lenthe and J. D. Janssen, *Nature* **405** (2000) 704–706.
89. T. Adachi, K. Tsubota, Y. Tomita and S. J. Hollister, *J. Biomech. Eng.* **123** (2002) 403–449.
90. R. Ruimerman, B. van Rietbergen, P. Hilbers and R. Huiskes, *Ann. Biomed. Eng.* **33** (2005) 71–78.
91. R. Ruimerman, P. Hilbers, B. van Rietbergen and R. Huiskes, *J. Biomech.* **38** (2005) 931–941.

# CHAPTER 4

# EFFECT OF STRESS RATIO AND STRESS FREQUENCY ON FATIGUE BEHAVIOR OF COMPACT BONE

S. ISHIHARA*,§, M. OTA*, B. L. DING*, C. FLECK†,
T. GOSHIMA* and D. EIFLER‡

*Department of Mechanical Engineering
University of Toyama, Gofuku 3190, Toyama 930-8555, Japan

†Institute of Materials Science and Engineering
Technical University of Berlin, Berlin, Germany

‡Institute of Materials Science and Engineering
University of Kaiserslautern, Kaiserslaautern, Germany
§ishi@eng.u-toyama.ac.jp

During bone's fatigue process, cracks generally initiate from inherent defects existing in the bone. Fatigue lives of bone specimens at different stress frequencies as well as at different stress ratios ($R$) were evaluated using a computer simulation under the assumption that the cracks initiated from the inherent defects in the bone. The S–N curves as well as the distributions of fatigue lives obtained by the simulations accurately conform with the experimental results. As strain thresholds representing fatigue failure of the bone specimens, values of 1500 $\mu\varepsilon$ for $R = -1$, 2500 $\mu\varepsilon$ for $R = 0.1$ and 4000 $\mu\varepsilon$ for $R = 10$ were extrapolated from the simulations. These values are in good agreement with experimental values reported in the literature. Such conformity indicates that the strain threshold for fatigue failure is associated with the threshold value for crack propagation.

*Keywords*: Compact bone; fatigue; computer simulation; stress ratio; stress frequency; crack propagation.



## Notation

| | |
|---|---|
| $a_i$ | Initial crack length ($\mu$m) |
| $C$ | The probabilistic variable |
| $da/dN$ | Crack growth rate (m/cycle) |
| $\Delta G$ | Strain energy release rate (MJ/m$^2$) |
| $\Delta G_C$ | Fracture toughness (MJ/m$^2$) |
| $\Delta G_{\mathrm{th}}$ | Crack growth threshold (MJ/m$^2$) |
| $\Delta K_{\mathrm{I}}$ | Stress intensity factor (Mode I) (MPa m$^{1/2}$) |
| $\Delta K_{\mathrm{II}}$ | Stress intensity factor (Mode II) (MPa m$^{1/2}$) |
| $\Delta\sigma$ | Stress range (MPa) |
| $\Delta\sigma_M$ | Bending stress range (MPa) |

| | |
|---|---|
| $\Delta\sigma_p$ | Axial stress range (MPa) |
| $\Delta\tau$ | Shear stress range (MPa) |
| $E$ | Young's modulus (GPa) |
| $E_0$ | Initial value of Young's modulus (GPa) |
| $E/E_0$ | Normalized specimen stiffness |
| $\varepsilon$ | Strain |
| $m$ | The probabilistic variable |
| $N_f$ | Number of cycles to failure |
| $N/N_f$ | Fatigue life ratio |
| $\nu$ | Poisson's ratio |
| $R$ | Stress ratio |
| $\sigma_{\max}$ | Maximum stress (MPa) |
| $\sigma_{\min}$ | Minimum stress (MPa) |
| $f$ | Stress frequency (Hz) |



## 1. Introduction

In daily life, bone is continually exposed to cyclic loads. Because of the geometry of the bones and the action of the muscles, the compressive forces due to supporting body weight induce bending moments with tensile, compressive, and torsional stress components. Thereby, bone is continually subjected to repeated loads with different stress amplitudes, mean stresses, and frequencies. Mean stresses as well as loading velocity have a strong influence on the deformation behavior and thereby on the resistance toward fatigue failure. In order to better understand the fatigue characteristics of bone, it is, therefore, necessary to study the effects of these loading parameters on the fatigue strength of bone.

Ishihara *et al.*[1–4] examined the effect of fatigue crack initiation and propagation behavior on the fatigue life in rotating bending tests on bovine bone at frequencies of up to 28 Hz. They ascertained that the effects of the frequency on the crack growth behavior and the fatigue lives were negligible in the rotating bending fatigue tests performed at a stress ratio of $-1$. Lafferty and Raju[5,6] examined the effect of frequency on the fatigue life of bovine compact bone also at a stress ratio of $-1$. They reported that the fatigue life of bone increased with increasing loading velocity for frequencies above 30 Hz. These experimental results were explained on the basis of the strain-rate-dependency of the mechanical properties of the bone. Carter and Caler[7] carried out tensile as well as completely reversed tension–compression fatigue tests using samples from a human femur. They reported that fatigue life of the bone was controlled by the time-dependent characteristics of the bone's mechanical properties. In contrast, in tensile and compressive fatigue experiments at low frequencies between 0.02 and 2 Hz, Caler and Carter[8] showed that time-dependent damage occurred at 0.02 Hz, while cycle-dependent damage occurred at 2 Hz. Obviously, a consensus regarding the effect of stress ratio on bone fatigue life has not yet been reached. The above short review further shows that, additionally,

the effect of stress ratio on bone fatigue life may depend in a complex way on the stress frequency.

Computer simulations concerning the fatigue properties of cortical bone have rarely been performed up to now. Studies using computer simulations[9,10] all consider cancellous bone. Gibson[9] modeled cancellous bone as cylindrical and trabecular structures to analyze the strength of the bone. She demonstrated the effect of bone density on the elastic modulus of the bone. Guo *et al.*[10] examined cancellous bone using two-dimensional finite element models in order to analyze damage storage in bone under both compressive fatigue and creep. They showed that a decrease in the apparent elastic modulus of bone during the fatigue process corresponded with an increase in microstructural damage.

During the fatigue process of bone under axial loading, cracks initiate and grow both in the interior and on the surface of the specimen. The fatigue process under axial loading is, therefore, different from that under rotating bending loading in which cracks predominantly generate on the specimen surface. One of the problems with axial fatigue tests is that we cannot observe the specimen's interior, but only the specimen's surface. Computer simulations are therefore useful in studying the fatigue mechanism under axial load.

In the present study, in order to examine the effect of stress ratio and stress frequencies on the fatigue characteristics of compact bone, a specimen of compact bovine bone was modeled as a two-dimensional beam structure consisting of hexangular osteons. The local stress distribution due to the application of an external load was calculated using two-dimensional finite element methods. During bone's fatigue process, cracks generally initiate from inherent defects such as Haversian and Volkmann canals and other bone vacuoles like canaliculi and lacunae existing in the bone.[1,2] Fatigue lives of the bone specimens at different stress levels were determined by computer simulation in which the crack propagation behavior was taken into consideration. The fatigue mechanism for compact bone and the effect of stress ratio and stress frequencies on bone's fatigue life are discussed in detail by comparing experimental and simulated results.

## 2. Modeling of Bone Tissue

Figures 1(a) and 1(b) show typical micrographs of transverse and longitudinal sections, respectively, of the compact bone of the bovine femur used in the present study. Figure 1(a) shows different osteons with their central Haversian canals. The osteons have a layered organization similar to that of annual rings in a tree. Irregularly shaped interstitial lamellae can also be observed between the osteons. The boundary between an osteon and the interstitial lamellae is called a cement line. Canaliculi can also be observed. In the longitudinal section (Fig. 1(b)), Volkmann canals are to be seen besides the other pores.

Figure 2(a) shows a longitudinal section of compact bone depicted as an aggregate of irregularly shaped cells (outlined in bold). In the model of the bone

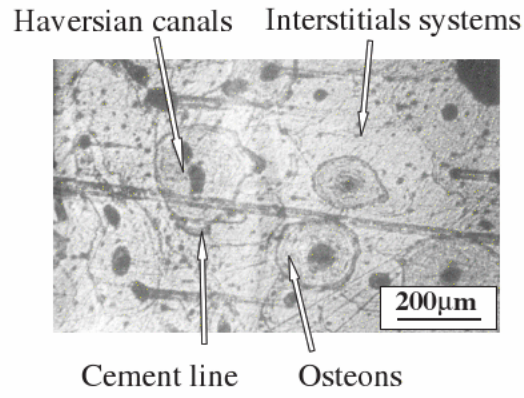


(a) Cross section of the specimen.

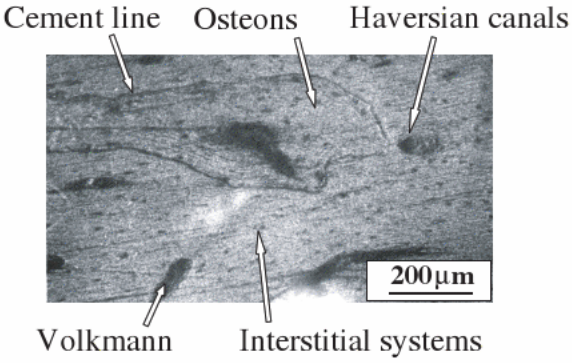


(b) Vertical section of the specimen.



Fig. 1. Photographs showing bovine bone tissue histology.

structure, these cells were assumed to have a regular size and shape as shown in Fig. 2(b).

The longitudinal microstructure of compact bone (Fig. 2) was then approximated as a two-dimensional frame structure consisting of perpendicular and diagonal members as shown in Fig. 3. In the analysis, only a quarter of the bone specimen was modeled because of the specimen's symmetry. In this approximation, bending stiffness ($EI$) was adjusted to be equal for both bone tissue and frame members, with $E$ and $I$ being Young's modulus and geometrical moment of inertia, respectively. Axial stress range $\Delta\sigma_p$, and bending moment $M_1$ and $M_2$ generated in the bone specimen by the external load $P$, as shown in Fig. 3, yield components for normal and shear stress.

The normal stresses act as driving forces for the propagation of mode I cracks in the specimen. On the other hand, shear stresses $\Delta\tau$ contribute to the driving

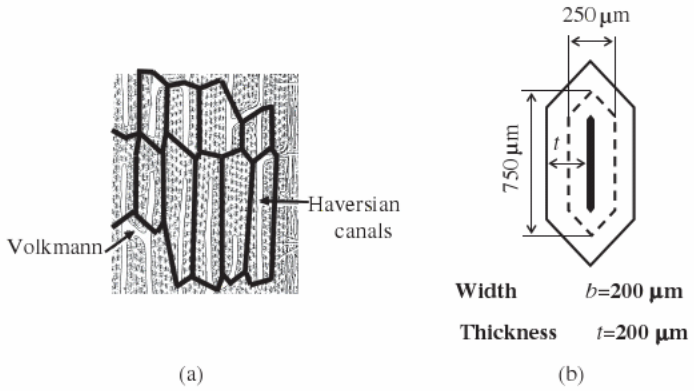


Fig. 2. Modeling of bone tissue in the present study.



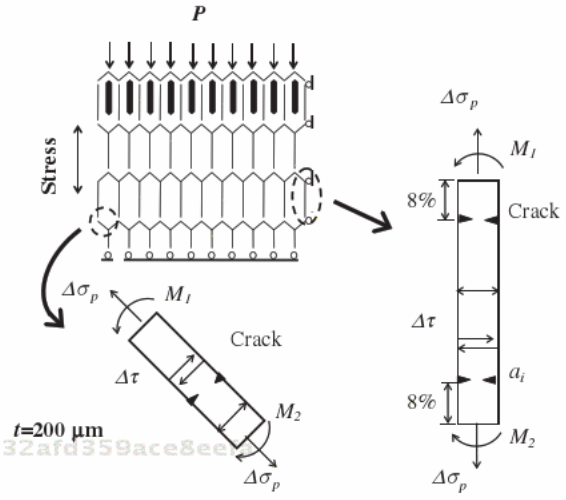


Fig. 3. FEM model of the specimen for calculation of normal as well as shearing stresses in the members.

force for mode II crack propagation. When a frame member is destroyed step by step during fatigue simulation, new stress values acting on the surviving members are recalculated using a plane frame analysis as finite element method (FEM). The number of elements and nodes was 122 and 94, respectively. As shown in Fig. 1(b), bone tissue can contain defects such as Haversian canals or Volkmann.

Cracks initiate from Haversian canals as well as from bone vacuoles.[3] For the computer simulation, it was further assumed that, cracks initiated from defects located at a distance of 8% (of the total length of the member) from each end in the perpendicular members, while in the diagonal members, cracks initiated from defects located at the middle of the frame.

These crack locations are schematically indicated in Fig. 3. The reason for this assumption is that the maximum stresses due to the external load in the perpendicular and diagonal members occur at the above locations. Though defects may exist at both sides (right or left) of the member, for simplicity, calculations were performed for a single defect with a maximum value of $\Delta G$. In the calculations, 32 8-node isoparametric elements were used. Calculations using 512 elements were also performed; however, the effect of the number of elements on both the value of maximum stress and its location was negligible.

## 3. Computer Simulation of Bone's Fatigue Process

A computer simulation of bone's fatigue process was performed, and its flowchart is shown in Fig. 4 and explained below. Latent flaws in the bone were simulated

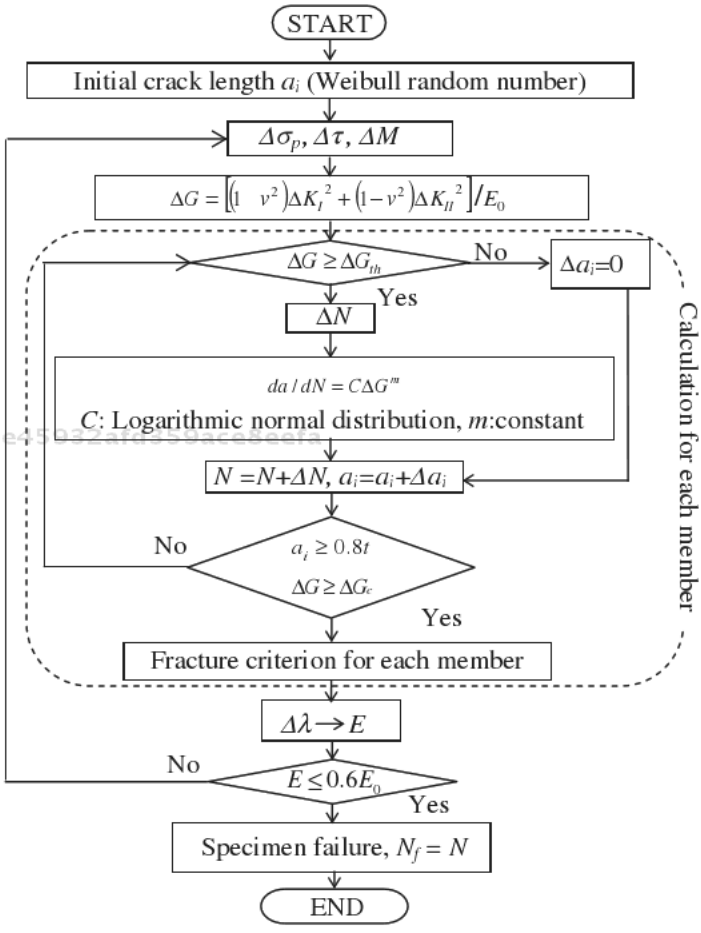


Fig. 4. Flowchart of the computer simulation of bone's fatigue process.

using the Monte Carlo method. These initial flaws in bone tissue were considered to be cracks. Cracks from these flaws were able to propagate when the level of energy release rate $\Delta G$ at the crack tip was larger than the threshold $\Delta G_{\mathrm{th}}$. New stress values acting on the surviving members were determined by FEM calculations when a member was destroyed by a crack formerly initiated and propagated from a defect. Then the simulation of fatigue crack propagation was repeated using these new stress values until the next member was destroyed. The final failure of the specimen was defined when its apparent Young's modulus decreased by 40% of the initial value. In the following, the role and function of each subroutine involved in the simulation program will be explained in detail. The related experimental results will be explained in detail in Sec. 4.



### 3.1. *Distribution of initial crack length*

Holes such as Haversian and Volkmann canals and other pores present in the bone tissue can be considered as cracks with lengths of $a_i$. Fluctuations in crack initiation are affected by the presence or absence of large defects in the specimen. The measured distribution of the initial crack lengths $a_i$,[3] shown in Fig. 5, was approximated by the three parameters of Weibull distribution expressed by the following equation:

$$F(a_i) = 1 - \exp[-(a_i - 7.7)^{1.31}/78.6]\,. \tag{1}$$

The unit for $a_i$ is $\mu$m. In the fatigue simulation, the initial crack length for each member was assigned using a Weibull random number expressed by Eq. (1).

### 3.2. *Calculation of the range of energy release rate $\Delta G$*



The values of axial stress range $\Delta\sigma_p$, shear stress range $\Delta\tau$, and bending stress range $\Delta\sigma_M$ induced by the external loading for each member were calculated using

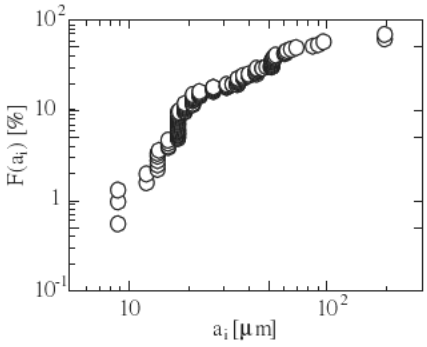


Fig. 5. The experimentally obtained distribution of the initial crack lengths $a_i$.[3]

finite element analysis. The stress intensity factors $K_{\mathrm{I}}$ for mode I cracks and $K_{\mathrm{II}}$ for mode II cracks were calculated using Eqs. (3) and (4), respectively, by assuming a semicircular crack shape. The energy release rate $\Delta G$ was calculated using Eq. (5).[3]

$$\Delta\sigma = \Delta\sigma_p + \Delta\sigma_m \,, \tag{2}$$

$$\Delta K_{\mathrm{I}} = 0.73\Delta\sigma\sqrt{\pi a_i} \,, \tag{3}$$

$$\Delta K_{\mathrm{II}} = 0.73\Delta\tau\sqrt{\pi a_i} \,, \tag{4}$$

$$\Delta G = [(1-\nu^2)\Delta K_I^2 + (1-\nu^2)\Delta K_{II}^2]/E_0 \,. \tag{5}$$

The parameters $\nu$ and $E$ are Poisson's ratio and Young's modulus of the bone, respectively.



### 3.3. *Threshold for crack propagation*

The crack for each member was made to propagate when the value of $\Delta G$ for the crack reached the crack growth threshold $\Delta G_{\mathrm{th}}$, which was determined by the experiment described in Chapter 4. The values are listed in Table 1.

$$\Delta G \geq \Delta G_{\mathrm{th}} \,. \tag{6}$$

### 3.4. *Crack propagation*

Paris law was used for the simulation of crack propagation[3,11]

$$\frac{da}{dN} = C\Delta G^m \,, \tag{7}$$

with $C$ and $m$ being material constants; their values are listed in Table 1. Their values were determined from the experimental results shown in Fig. 11. Generally spoken, both the values $m$ and $C$ are probabilistic variables. In the present study, $C$ was deemed to follow the logarithmic normal distribution with a mean value of $3.16 \times 10^{-2}$ and a standard deviation of 0.419[1] as shown in Fig. 6. The value $m$ is a constant 1.6 determined by regression of the experimental results.

Table 1. The values of parameters used in the computer simulation.

| | $R$ | $m$ | $C$ [m$^2$/N] | $\Delta G_{\mathrm{th}}$ [MJ/m$^2$] |
|---|---|---|---|---|
| | $-1$ | 1.5 | 3.16E-2 | 5E-6 |
| 0.1 | 0.3 Hz | 1.6 | 3.16E-2 | 5E-6 |
| | 20 Hz | 1.6 | 3.16E-2 | 4.5E-5 |
| 10 | 0.3 Hz | 1.6 | 3.16E-2 | 5E-6 |
| | 20 Hz | 1.6 | 3.16E-2 | 4.5E-5 |

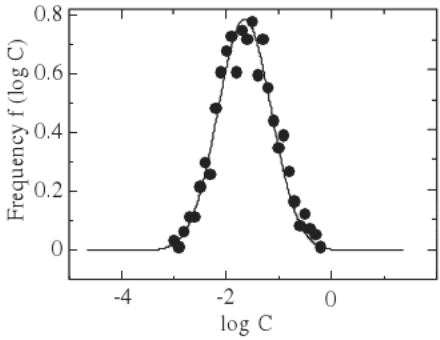


Fig. 6. The logarithmic normal distribution of parameter $C$. $(C = 3.16 \times 10^{-2} \pm 0.419)$.[1]



### 3.5. *Fracture criterion for each member*

The fracture for each beam member was assumed to occur when crack length $a_i$ reached 80% of the beam width, or when the range of energy release rate $\Delta G$ reached the bone's fracture toughness $\Delta G_c$.

$$a_i \geq 0.8t\,, \tag{8}$$

$$\Delta G \geq \Delta G_c\,. \tag{9}$$

### 3.6. *Criterion for specimen failure*

The displacement of the specimen due to loading was calculated using the finite element method in order to estimate an apparent Young's modulus $E$ for the specimen. The final fracture of the specimen was defined as occurring when the above apparent Young's modulus $E$ decreased by 40% from the initial value $E_0$.



$$E \leq 0.6E_0\,. \tag{10}$$

## 4. Specimen and Experimental Method

Completely reversed $(R = -1)$,[3,4] tensile $(R = 0.1)$, and compressive fatigue experiments $(R = 10)$ were performed at frequencies of 0.3 and 20 Hz using a servo-hydraulic fatigue testing machine. The stress waveform always was a sinusoidal as shown in Fig. 7. The tests were performed on compact bone specimens prepared from bovine femur. The specimen shape is shown in Fig. 8. The diaphysis of the femur was extracted by cutting off the bone-head and removing the marrow as shown in Fig. 9. Subsequently, specimens with cylindrical shape were machined with their long axis corresponding to the longitudinal direction and their smallest cross-sections corresponding with the central part of the femur. In order to facilitate observation of the specimen surface and also to remove flaws caused by the machining, the

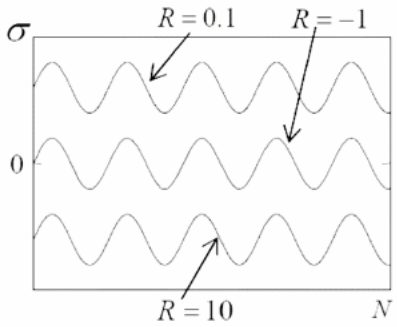


Fig. 7. Stress waveform employed in the present study.

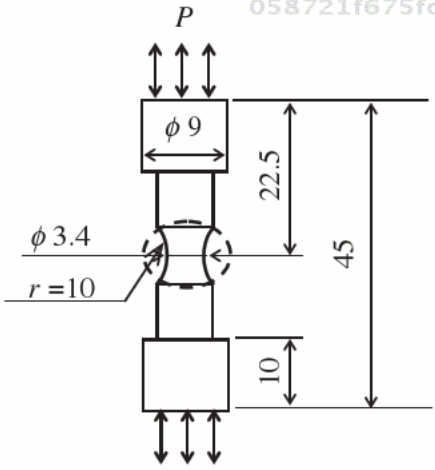




Fig. 8. Shape and dimensions of the specimens (mm).



specimen surfaces were polished with emery paper (#grit 1000 1500) and diamond paste before testing. To prevent the bone specimens from drying and decaying after processing, they were stored in 3% salt water and kept at 273 K until testing.

Successive observations of short crack propagation during the fatigue process were made using the replica method.[1,2,15] Therefore, the fatigue tests were interrupted at given numbers of cycles during the fatigue process. By observing the cracks recorded on the replicas with an optical microscope at a magnification of 400X, crack lengths were measured to obtain a crack propagation curve.

## 5. Effect of Stress Ratio

### 5.1. *Experimental results*

Figures 10(a) and 10(b)[3] show the relation between crack growth rate ($da/dN$) and stress intensity factor range $\Delta K$ for stress ratios $R = -1$ and $R = 0.1$, respectively.

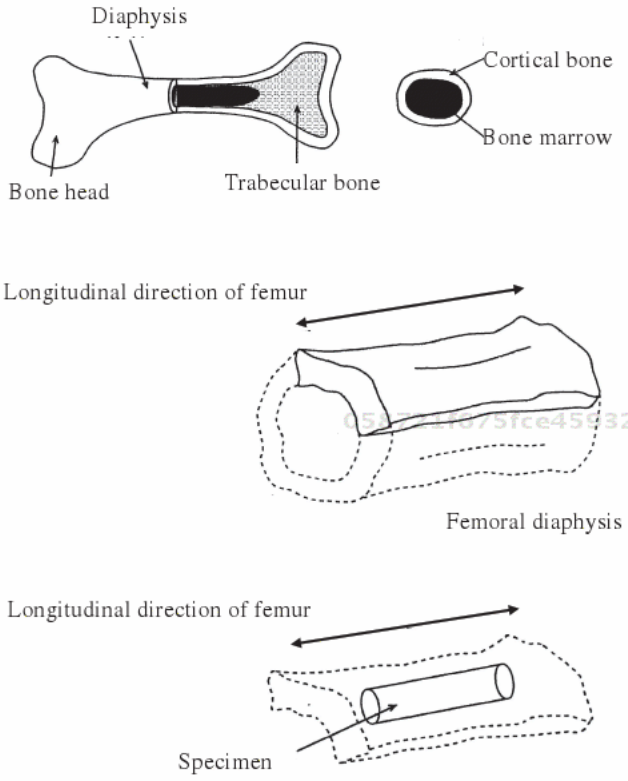


Fig. 9. Preparation of the specimen from femur.

The graphs apply to short surface cracks with lengths between 20 and 300 $\mu$m. The stress intensity factor $K_{\mathrm{I}}$ for mode I cracks was calculated using Eq. (3) by assuming a semicircular crack shape.

At $R = -1$, as shown in Fig. 10(a), the effect of frequency is very small in the relation $da/dN$ versus $\Delta K$. However, as can be seen in Fig. 10(b), at a stress ratio $R = 0.1$, there is a pronounced difference in this relation for testing at a frequency of 0.3 and 20 Hz. Furthermore, the crack growth rate at $R = -1$ differs from that at $R = 0.1$.

In the present study, the relation $da/dN$ versus $\Delta K$ was reconfigured as $da/dN$ versus $\Delta G$, with $\Delta G$ being the energy release rate. $\Delta G$ is used for the purpose of treating mode II crack propagation in compressive fatigue tests.

The stress intensity factor $K_{\mathrm{II}}$ for mode II crack propagation was calculated using Eq. (4) under the assumption of a semicircular crack shape. The energy release rate $\Delta G$ was calculated using Eq. (5).[3]

Figure 11 shows the relation $da/dN$ versus $\Delta G$ which was determined by the experiments performed at $R = -1$ and 0.1. In the following, we assume that this relation $da/dN$ versus $\Delta G$ can also be applied for compressive fatigue tests with $R = 10$.

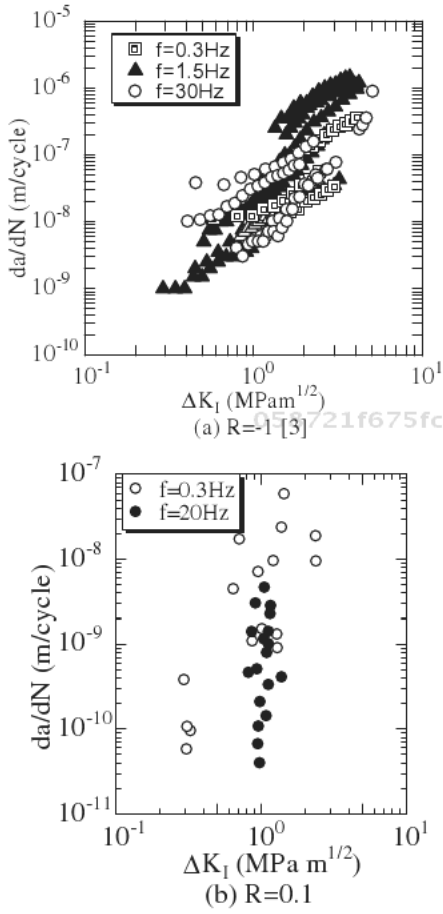


Fig. 10. Relationship between crack growth rate $da/dN$ and stress intensity factor range $\Delta K_I$.

Figure 12 shows the relationships between maximum stress ratios and fatigue lives for the three different stress ratios ($R = -1$, 0.1, 10). These relations were obtained for bovine compact bone at a frequency of 0.3 Hz. The results for equine bone obtained by Fleck and Eifler[13] at $R = -1$ and at a frequency of 5 Hz, and for human bone at a frequency of 2 Hz as reported by Pattin *et al.*[14] are also plotted in this figure. In Fig. 12, dimensionless stress expressed by $|\sigma_{\max}|/\sigma_b$ is used because the bending strengths or tensile strengths $\sigma_b$ for these bones differ. The values of $\sigma_b$ and Young's modulus $E$ for the three kinds of bones are shown in Table 2. In Fig. 12, the $S$–$N$ curves are shown separately, each curve dependent on a different stress ratio.

The values of threshold strain $\varepsilon_{\max}$ at which bone failure did not occur to a maximum number of cycles of $10^7$ cycles were determined for human bone by dividing the fatigue limit $\sigma_{\max}$ by the Young's modulus $E$. The values of $\varepsilon_{\max}$ are

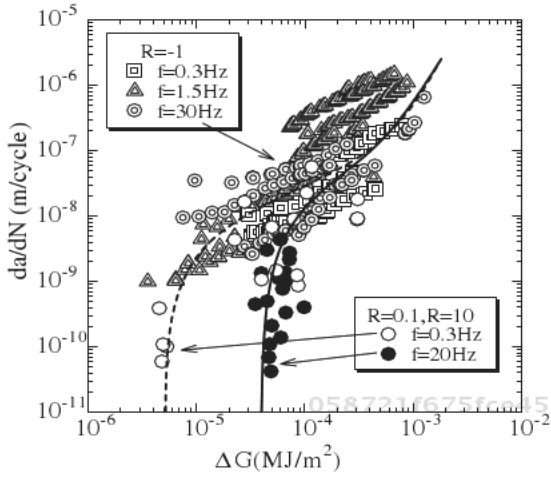


Fig. 11. Relationship between $da/dN$ and range of energy release rate $\Delta G$.

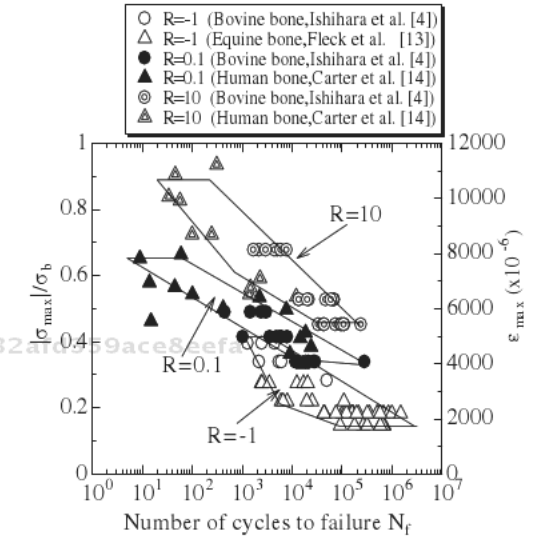


Fig. 12. Experimental relationships between dimensionless stress $|\sigma_{\max}|/\sigma_b$ and number of cycles to failure $N_f$ at 0.3 Hz.[4]

Table 2. The values of $\sigma_b$ and Young's modulus $E_b$ for three kinds of bones.

| Bovine[4] | Equine[13] | Human[14] |
|---|---|---|
| 265.7 | 273.9 | 165.7 |
| 23.0 | 23.7 | 22.4 |

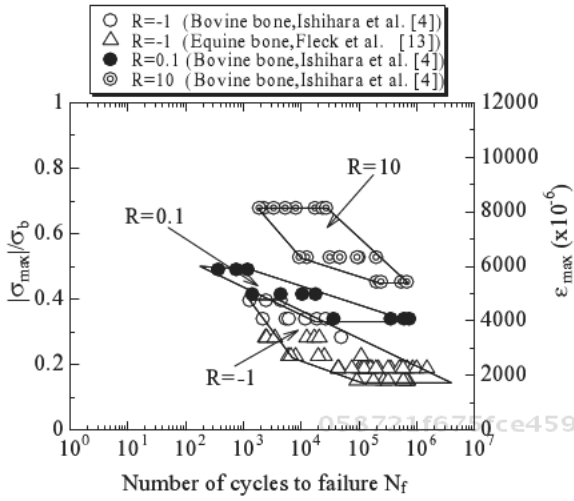


Fig. 13. Experimental relationships between dimensionless stress $|\sigma_{\max}|/\sigma_b$ and number of cycles to failure $N_f$ at 20 Hz.[4]

1594 $\mu\varepsilon$, 2455 $\mu\varepsilon$, and 3964 $\mu\varepsilon$ for $R = -1$, 0.1, and 10, respectively. These values are in good agreement with those in the literature[14] and correspond to the values which are applied to bone in daily life.

Figure 13 shows $S$–$N$ curves for a frequency of 20 Hz. A comparison of Fig. 12 with Fig. 13 shows that the fatigue life of bone loaded at a frequency of 0.3 Hz is shorter than that of bone loaded at a frequency of 20 Hz for the case of $R = 0.1$ and 10. However, at $R = -1$, fatigue lives $N_f$ for both cyclic speeds are almost equal. The effect of stress frequency on the fatigue life of bone will be discussed in more detail in Sec. 6.



## 5.2. *Comparison between simulation and experiment (stress ratio)*

### 5.2.1. *S–N curve*

Fatigue simulations for bovine bone were conducted under completely reversed tension–compression ($R = -1$), tensile ($R = 0.1$), and compressive fatigue loading ($R = 10$) at frequencies between 0.3 and 20 Hz. The $S$–$N$ curves estimated from the simulations are shown in Fig. 14. In this figure, the experimental data is represented by the hatched area for purposes of comparison. As can be seen from the figure, the simulated and experimental results agree very well. Furthermore, the dispersion of fatigue lives can be simulated by considering both the probabilistic distribution of $C$ in a crack growth rule and the distribution of initial flaw sizes as crack initiators in the program. The maximum strains $\varepsilon_{\max}$ for various $R$ ratios were obtained from the endurance limit, i.e., the stresses at which the specimens were not destroyed even by loading up to $10^7$ cycles. Their values are 1500 $\mu\varepsilon$ for $R = -1$, 2500 $\mu\varepsilon$ for $R = 0.1$, and 4000 $\mu\varepsilon$ for $R = 10$. These values are conforming with the experimental values.

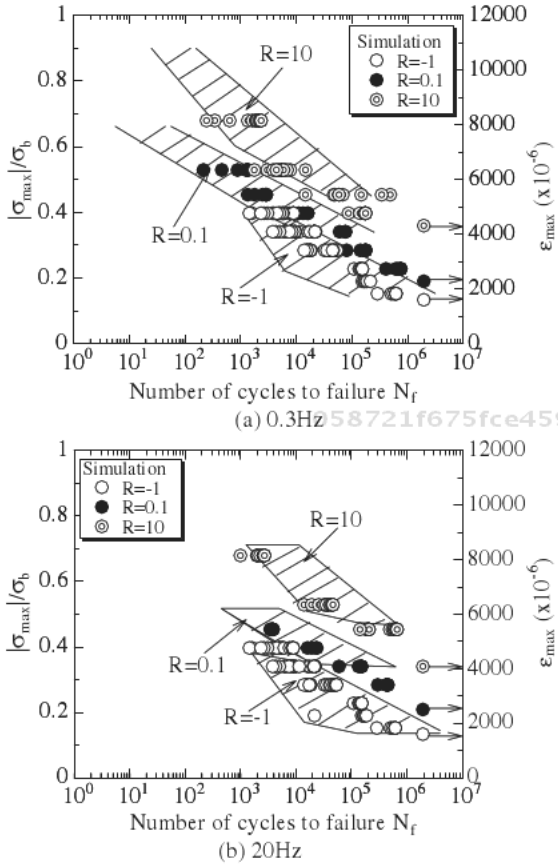


Fig. 14. Comparison between estimated $S$–$N$ curves in simulations with those obtained by experiments.



The fact that the simulated results correspond well with the experimental ones indicates that there is a strong relation between the threshold $\Delta G_{th}$ for crack propagation and the strain $\varepsilon_{max}$ at the fatigue endurance limit, since in the simulated $S$–$N$ curves, the fatigue endurance limit is determined by the value of threshold $\Delta G_{th}$ below which cracks do not develop.

### 5.2.2. *Variation of Young's modulus $E/E_0$ during fatigue process*

Figure 15 shows the relationship between $E/E_0$ and the fatigue life ratio, $N/N_f$, obtained from the simulation. In this figure, the smaller the $R$ ratio, the earlier the ratio $E/E_0$ decreases in the coarse of fatigue loading. This tendency can be seen more clearly in Fig. 15(a) for the lower maximum stress of 105 MPa than that in Fig. 15(b) for the higher maximum stress of 140 MPa.

In the previous studies,[4,13] for $R = -1$, a large number of smaller cracks were observed in addition to the dominant crack which causes the final failure of the

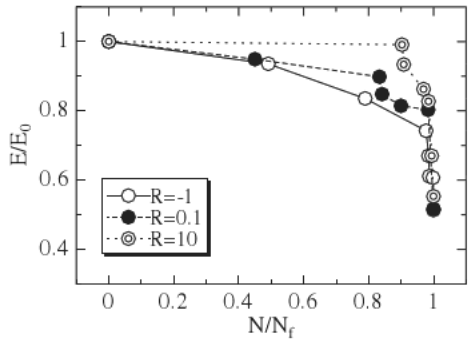


(a) 105MPa

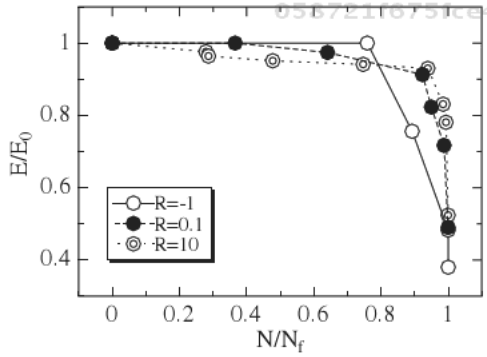


(b) 140MPa

Fig. 15. Variation of the specimen stiffness $E/E_0$ as a function of fatigue life ratio $N/N_f$.

specimen. On the other hand, for $R = 10$, much less cracks were initiated than that for $R = -1$. From these experimental results, it is clear that the specimen's rigidity may gradually decrease due to crack initiation in the early stage of fatigue life in the tests for $R = -1$, while for $R = 10$ where few cracks are initiated, a reduction in the specimen's stiffness is difficult to induce. However, in the latter case, once a crack is generated, a rapid failure of the specimen follows because fatigue damage is concentrated there.

## 6. Effect of Stress Frequency

### 6.1. *Experimental results*

#### 6.1.1. *Relationship between number of cycles to failure $N_f$ and maximum stress $\sigma_{\max}$*

Figures 16(a) and 16(b) show the experimental relationships between number of cycles to failure $N_f$ and maximum stress $\sigma_{\max}$ at an $R$ ratio of 0.1 for bovine compact bone at frequencies of 0.3 and 20 Hz, respectively. These figures were made by

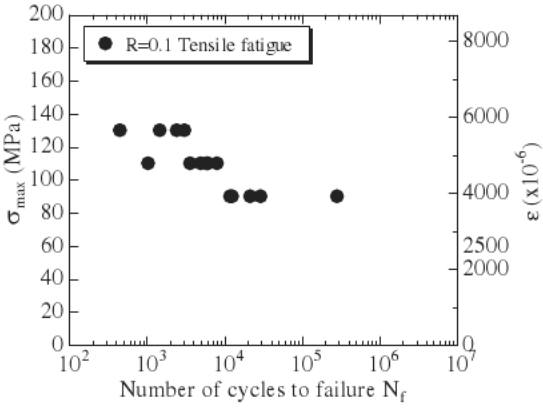


(a) f=0.3Hz



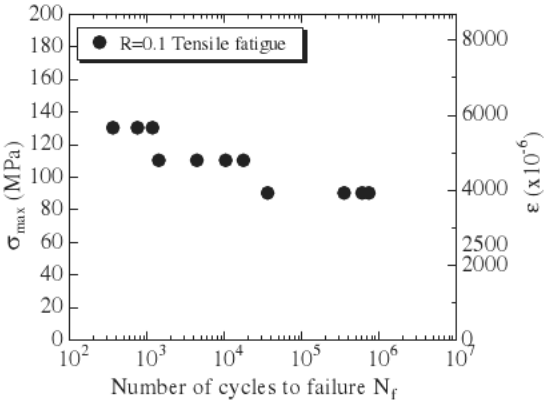


(b) f=20Hz

Fig. 16. Experimental relationship between maximum stress and number of cycles to failure $N_f$ for bovine bone at an $R$ ratio of 0.1 for stress frequencies of 0.3 and 20 Hz.



rearranging Figs. 12 and 13 in order to evaluate the effect of the stress frequency on the fatigue lives of the bone. The values of maximum strain $\varepsilon_{max}$ are also indicated along the vertical axis of these figures. When compared with Figs. 16(a) and 16(b), an effect of stress frequency on fatigue lives is not clearly observed at comparatively high stress region. However, the effect of stress frequency becomes marked with a decrease in the applied stress. For lower maximum stresses, the number of cycles to failure at a stress frequency of 0.3 Hz is shorter than those at 20 Hz.

Figure 17 shows the variation of fatigue life of bovine cortical bone specimens for a maximum stress of 90 MPa and an $R$ ratio of 0.1 as a function of stress frequency $f$. As can be seen from this graph, $N_f$ increases with an increase in stress frequency $f$, indicating a clear effect of stress frequency on the fatigue lives.

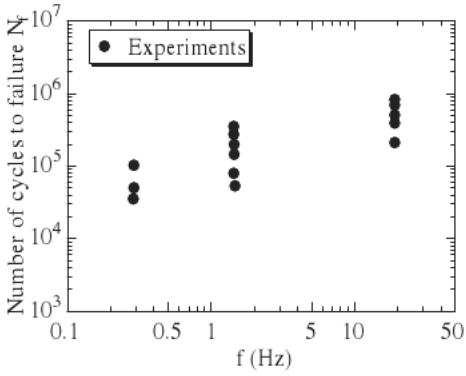


Fig. 17. Number of cycles to failure $N_f$ as a function of stress frequency $f$ obtained by experiments at $\sigma_{\max} = 90\,\mathrm{MPa}$, and $R = 0.1$.



6.1.2. *Crack propagation behavior for bovine cortical bone*

Figure 18 shows the relationships between stress intensity factor $\Delta K_{\mathrm{I}}$ and the rate of surface crack propagation $da/dN$ for $f = 0.3\,\mathrm{Hz}$ and $f = 20\,\mathrm{Hz}$. The stress intensity factor $\Delta K$ was calculated using expression (3) assuming crack shape as a semicircular one.

In the figure, trend lines, solid and broken lines, for the crack growth rate at each stress frequency are drawn. Due to the limited crack propagation data at $R = 0.1$ for higher crack growth rates, the trend line was determined by referring to the trend of the crack growth rate at an $R$ ratio of $-1$.[3] The estimated trend was indicated by the hatched area in the figure. As can be seen from the graphs, the crack growth rates differ clearly for stress frequencies of 0.3 and 20 Hz. The constants determined from this relation, $da/dN$ versus $\Delta K_{\mathrm{I}}$ will be used for the computer simulation of bone's fatigue process. The values will be given later.



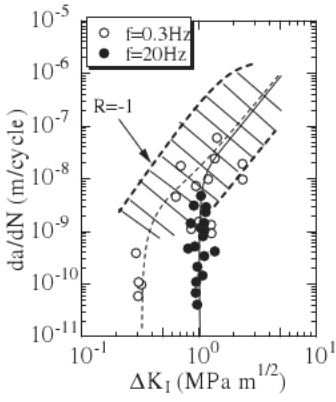


Fig. 18. Relationship between $da/dN$ and $\Delta K_{\mathrm{I}}$.

### 6.2. *Comparison between simulation and experiment*

#### 6.2.1. *S–N curve*

Figure 19 shows the $S$–$N$ curves for stress frequencies of 0.3 Hz and 20 Hz at $R = 0.1$, which were estimated from the computer simulation. In this figure, the experimental results are also shown by the hatched region for a comparison with the simulated results. As seen from this figure, the simulated and experimental results correspond well with each other. The fatigue limit $\varepsilon_{\max}$ is obtained as nearly 2500 $\mu\varepsilon$ from the computer simulation of the stress frequency of 20 Hz. This threshold value agrees well with the experimental finding[10] obtained in tensile fatigue tests on bone. On the other hand, the fatigue limit $\varepsilon_{\max}$ was obtained as 2000 $\mu\varepsilon$ from the computer simulation for a stress frequency of 0.3 Hz. The value is rather lower as compared



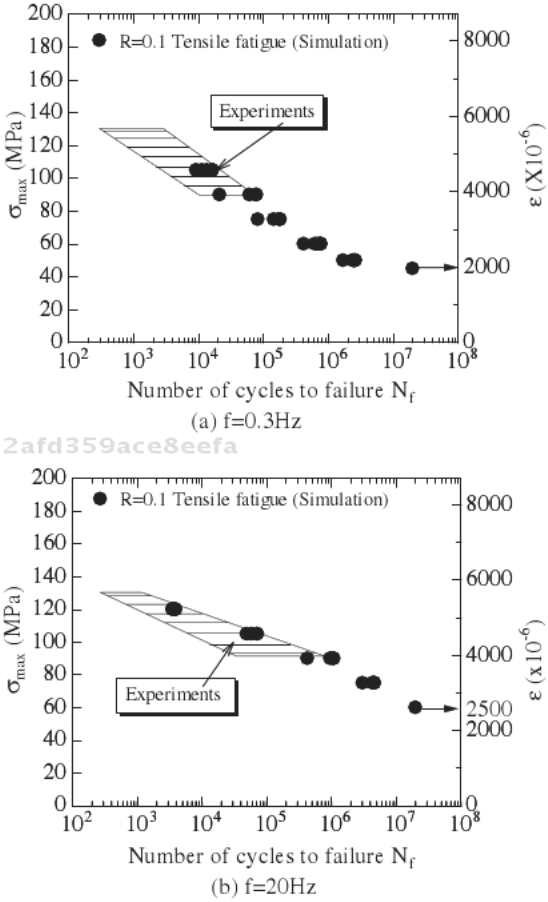


Fig. 19. $S$–$N$ curves obtained from the simulation.

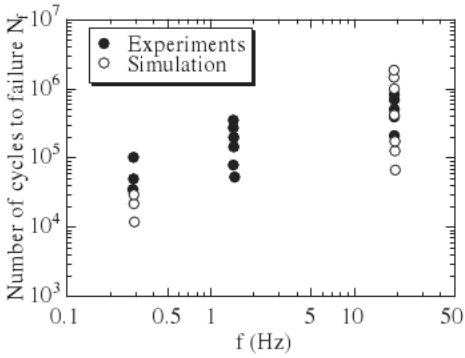


Fig. 20. Relation between $N_f$ and stress frequency $f$. Comparison between simulated and experimental data at $R = 0.1$ and $\sigma = 90\,\mathrm{MPa}$.



with that of 20 Hz. So, the experimentally obtained threshold strain values for bone fatigue failure are considered to have a strong correlation with the threshold values for the crack propagation.

### 6.2.2. *Estimated relation between fatigue lives $N_f$ as a function of stress frequency*

Figure 20 shows the relation between fatigue life $N_f$ and stress frequency $f$ calculated from the computer simulation. In the figure, the experimental results obtained at the conditions $\sigma_{\max} = 90\,\mathrm{MPa}$, $R = 0.1$ are plotted for comparison. As can be seen, a good correlation between the estimated and the experimental results was obtained. Both in the computer simulation and in the experiments, the fatigue life of the bone increases with an increase in the stress frequency. Viscoelastic effects within the bone are considered to be strongly related with the above phenomena. The restraining effect against a motion of body fluid by bone tissue becomes stronger with an increase in the stress frequency. As a result, mechanical properties of the bone are strengthened with an increase in the stress frequency. It is considered that the rate of fatigue crack propagation lowers remarkably by the above restraining effect, and fatigue life increases for higher stress frequencies as compared to the lower ones.

## 7. Conclusions

In order to examine the effect of stress ratio and stress frequency on the fatigue characteristics of compact bone, a specimen of compact bovine bone was modeled as a two-dimensional beam structure consisting of hexangular osteons. Fatigue lives of the bone specimens were determined by computer simulation in which crack propagation behavior was taken into consideration.

The conclusions obtained in the present study may be summarized as follows:

**Stress ratio**

(1) Computer simulations of the fatigue process for bovine, equine, and human bones were carried out under completely reversed, tensile, and compressive fatigue loading. The $S$–$N$ curves obtained by the simulations conform well with the experimental results.
(2) The simulation also enabled the derivation of the distribution of fatigue lives by considering both the probabilistic distribution of the constant $C$ in the crack propagation rule and the distribution of the initial flaws existing in the bone.
(3) With the strain threshold $\varepsilon_{\max}$ for fatigue failure of the bone specimen, values of $1500\,\mu\varepsilon$ for $R = -1$, $2500\,\mu\varepsilon$ for $R = 0.1$, and $4000\,\mu\varepsilon$ for $R = 10$ were estimated from the simulations. These data correlate well with the experimental values reported in the literature. Therefore, the strain threshold for fatigue failure corresponds well with the threshold value $\Delta G_{\text{th}}$ for crack propagation.
(4) Specimen stiffness diminishes during the fatigue process of the bone especially for lower stress amplitudes.



**Stress frequency**

(5) The fatigue life of bone under tensile fatigue loading increases with an increase in stress frequency. This is due to a reduction in the rate of fatigue crack propagation.
(6) Computer simulation of the tensile fatigue process for the bone was successively performed on the basis of the crack propagation behavior. The simulation predicts $S$–$N$ curves for different stress frequencies, which correspond well with the experimental ones. Scatter involved in the fatigue lives can also be simulated well by considering distributions of initial defect sizes from which cracks initiate and, further, of the distribution of the parameter $C$ which appears in the Paris-type crack propagation law.
(7) The threshold strains above which bone's fatigue fracture occurs were evaluated as $2000$–$2500\,\mu\varepsilon$ varying in dependence of the stress frequency. The values estimated by the computer simulation are considered to be reasonable since they correspond well with the experimental findings. The threshold strains are, therefore, considered to correlate strongly with the threshold for the crack propagation, since the computer simulation of the bone is based on the fatigue crack propagation within the bone tissue.



**Acknowledgment**

The authors express their thanks to Mr. Takazawa at T. M. C. Co., Ltd. for supporting this study.

## References

1. S. Ishihara, T. Goshima and Y. Nakamura, *Trans. Jpn. Soc. Mech. Eng.* **59**(A) (1993) 50–56.
2. S. Ishihara, T. Goshima, H. Higashikawa and M. Morino, *Trans. Jpn. Soc. Mech. Eng.* **61**(A) (1995) 1115–1121.
3. S. Ishihara, T. Goshima, H. Higashikawa and O. Nagamori, *Trans. Jpn. Soc. Mech. Eng.* **62**(A) (1996) 640–646.
4. S. Ishihara, T. Goshima and O. Nagamori, *Trans. Jpn. Soc. Mech. Eng.* **64**(A) (1998) 831–838.
5. J. F. Lafferty and P. V. V. Raju, *Trans. ASME* **101** (1979) 112–114.
6. J. F. Lafferty, *Aviation Space Environ. Med.* **49** (1978) 170–174.
7. D. R. Carter and W. E. Caler, *Trans. ASME* **105** (1983) 166–170.
8. W. E. Caler and D. R. Carter, *J. Biomech.* **22** (1989) 625–635.
9. L. J. Gibson, *J. Biomech.* **18** (1985) 317.
10. X. E. Guo, T. A. McMahon, T. M. Keaveny, W. C. Hayes and L. J. Gibson, *J. Biomech.* **27** (1994) 145–155.
11. T. M. Wright and W. C. Hayes, *J. Mater. Res. Symp.* **7** (1976) 637–648.
12. C. A. Pattin, D. R. Carter and W. E. Caler, *Trans. 36th Ann. Meet. Orthop. Res. Soc.* (1990), p. 50.
13. C. Fleck and D. Eifler, *J. Biomech.* **36** (2003) 179–189.
14. C. A. Pattin, D. R. Carter and W. E. Caler, *J. Biomech.* **29** (1996) 69–79.
15. S. Ishihara and A. J. McEvily, *Int. J. Fatigue* **24** (2002) 1169–1174.

# CHAPTER 5

# KINEMATIC ANALYSIS TECHNIQUES AND THEIR APPLICATION IN BIOMECHANICS

RITA STAGNI*,‡, SILVIA FANTOZZI*, ANDREA G. CUTTI†
and ANGELO CAPPELLO*

*Department of Electronics, Computer Science, and Systems
University of Bologna
Viale Risorgimento 2, 40136, Bologna, Italy

†INAIL Prosthesis Center — Research Area
Via Rabuina 14, 40054, Vigorso di Budrio, Bologna, Italy
‡rstagni@deis.unibo.it

Motion analysis is a fundamental instrument for the quantification of joint function during daily living activities. Several devices can be used for this purpose. An overview of some of these methods is here presented, focusing mainly on (i) stereophotogrammetry (flexible and widespread), (ii) 3D fluoroscopy (accurate but invasive), and (iii) inertial sensors (economic though not very accurate). The main advantages and limitations of these methods are outlined, paying particular attention to the errors which can affect the estimated kinematic variables. Finally, some applications are described in the field of error compensation, joint modeling, and upper limb motion analysis.

*Keywords*: Fluoroscopic analysis; stereophotogrammetry; knee joint modeling; inertial sensors; prosthesis; shoulder instability.



"the soul creates movement"
Aristotle (384–322 BCE)

## 1. Introduction

To Aristotle, living creatures were distinct by their ability to move themselves. The essential point of Aristotle's argument is that all living organisms possessed an internal will that allowed them to initiate and perform actions such as growth, regeneration, procreation, and movement. From the first simple reflex movements in the womb to the more complex movements after the birth, the child faces the challenge of the upright de-ambulation. Later the child masters his motility and learns that movement is not only life but also survival. The man uses motor ability to express intellectual values also such as aesthetical ones, creativity, and expression. Thus, movement is life, physical and intellectual.

Even though scientists have been fascinated by human motion from the earliest times, the first scientifically valid treatise on movement is considered "De Motu

Animalium" by Borrelli (1608–1679). Despite the technology limitations and the deficiency of scientific concept clear formalization, the founding of this work remained valid for the succeeding two centuries. By the beginning of the 20th century, new techniques became available for studying motion. Modern studies are based on three elements that can be traced back to this period when three major publications appeared: (i) the objective and accurate capture of motion,[2,3] (ii) the measurement of forces between the moving body and the environment,[2] and (iii) the approximation of skeletal segments by rigid links interconnected through a series of low-friction joints.[4] In the 1950s, the advent of high-speed photography, together with the emerging possibilities of digital computation, opened up new horizons for the study of normal human locomotion. Most recently, the advent of real-time data acquisition has led to an explosion of possibilities in this field and nowadays there are hundreds of human motion laboratories all over the world. For more details on history of bio-locomotion, see Refs. 5–8.



Human motion analysis, using three-dimensional kinematic measurement systems, is now an established technique of major importance in the clinical management of certain conditions. It has been shown to be a valuable tool for both clinical and fundamental research on a variety of musculo-skeletal disorders. The quantitative kinematic analysis is useful in many applications such as cerebral palsy, prosthetics and orthotics, upper limb motion, spinal motion, joint mechanics, and sport activities.

The main objective of this chapter is to show how to perform kinematic analysis of human motion and to illustrate some relevant applications. In Sec. 2, three methodologies for kinematics analysis will be described in detail. First of all, stereophotogrammetry, the most widely used technique in motion laboratories, will be presented (Sec. 2.1). Then a more accurate methodology, although more invasive and applicable only to a single joint, that uses X-ray images obtained by means of the fluoroscope will be depicted (Sec. 2.2). Finally, the principal aspects of a methodology using inertial sensors will be described (Sec. 2.3). This latter technique is less expensive than stereophotogrammetry, although less accurate. Mainly, it allows to perform the kinematic analysis of a subject in a very large field of view, thus in everyday living conditions.



In Sec. 3, a selection of possible applications of the kinematic analysis will be described. First, Soft Tissue Artifact (STA) quantification and compensation for the upper and lower limb will be depicted (Sec. 3.1). Then the use of kinematic analysis for knee modeling and for the functional evaluation of shoulder orthopedic patients and upper limb amputees will be shown.

## 2. Methods

### 2.1. *Stereophotogrammetry*

Optoelectronic stereophotogrammetry is designed to reconstruct the 3D position in the laboratory reference frame of light emitting (active) or reflecting (passive)

spherical objects, called markers. The system is generally composed of a minimum of two TV-cameras, and the position of each marker, reconstructed for each acquired frame, allows to determine the trajectory of that marker. In order to reconstruct the position of a marker, the system exploits the knowledge of the 2D coordinates of the centroid of the markers on the image plane of each TV-camera, and the knowledge of the pose of each TV-camera.

Considering the condition sketched in Fig. 1, the 3D coordinates of the centroid of marker P can be reconstructed from the knowledge of the 3D coordinates of the two nodes (N1 and N2), the position and orientation of the two image planes, and the 2D coordinates of the projections P1 and P2, on the two image planes respectively, considering the rules of optic projection.

The scheme reported in Fig. 2(a) shows the logic flow for the estimation of the 3D coordinates of a generic marker. The system parameters include the pose of the image planes, the position of the foci, and the parameters modeling the image distortion, introduced by the optics of the cameras. Thus, in order to reconstruct the position of the markers, the system parameters have to be estimated (Fig. 2(b)). This estimation is performed by means of a procedure, which is called *Stereophotogrammetric System Calibration*. This procedure exploits the knowledge of the geometry of a calibration object (in which the relative position of the markers



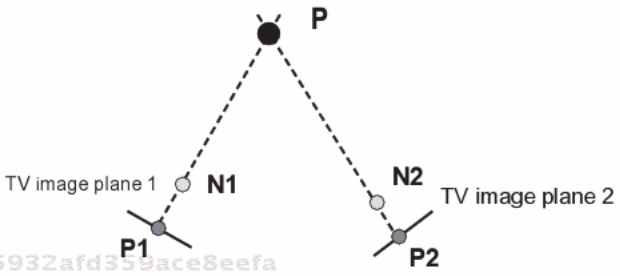


Fig. 1. Sketch of the projection of the marker on the image planes of the TV-cameras.

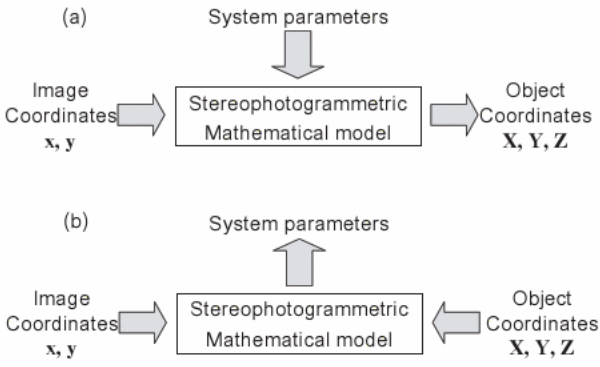


Fig. 2. Logic schemes for the markers coordinates reconstruction (a) and system calibration (b) procedures of the stereophotogrammetric system.

is known). The geometry of the calibration objects and the specific characteristics of the calibration procedures vary from system to system.

In general, optoelectronic stereophotogrammetry is the most conventional and versatile instrument adopted for the reconstruction of the kinematics of the body segments in motion analysis. In order to reconstruct body kinematics from the 3D trajectories of markers, they have to be properly positioned on the body surface, according to an acquisition protocol depending on the specific applications.[9] The estimate of the joint kinematics implies, for definition, the reconstruction of the relative position and orientation of the anatomical reference frames associated to the relevant body segments. Generally, this consists in calculating the time variations, during the execution of the motor task of interest, of six scalar quantities, three for orientation and three for translations, defined with respect to articular or anatomical reference frames properly. In order to obtain this information from the trajectories of the markers, provided by the stereophotogrammetric system, it is necessary to fulfill the following steps:

(i) Starting from the position of the markers in the laboratory $\mathbf{p}_i(t)_{\text{glo}} = (X_i(t); Y_i(t); Z_i(t))_{\text{glo}}$, $i = 1, 2, \ldots, m$, build a Technical Reference Frame (TF) for each body segment:

$$[{}^{\text{glo}}\mathbf{R}_{\text{tec}}(t), {}^{\text{glo}}\mathbf{T}_{\text{tec}}(t)] = f(\mathbf{p}_{1,2,\ldots,m}(t)_{\text{glo}}),$$

where ${}^{\text{glo}}\mathbf{R}_{\text{tec}}(t)$ and ${}^{\text{glo}}\mathbf{T}_{\text{tec}}(t)$ represent the orientation matrix and the position method of the TF associated to the segment at instant $t$.

(ii) Determine the coordinates of the Anatomical Landmarks (AL) with respect to the TF of the corresponding bony segment:

$$\mathbf{a}_j(t)_{\text{tec}} = (x_j(t); y_j(t); z_j(t))_{\text{tec}}, \quad j = 1, 2, \ldots, N_a.$$

(iii) Reconstruct the coordinates of the ALs with respect to the global reference frame of the laboratory:

$$\mathbf{a}_j(t)_{\text{glo}} = {}^{\text{glo}}\mathbf{R}_{\text{tec}}(t)\mathbf{a}_j(t)_{\text{tec}} + {}^{\text{glo}}\mathbf{T}_{\text{tec}}(t), \quad j = 1, 2, \ldots, N_a.$$

(iv) Reconstruct the position and orientation of each Anatomical Reference Frame (AF) with respect to the laboratory reference frame for each instant of time $t$:

$$[{}^{\text{glo}}\mathbf{R}_{\text{ana}}(t), {}^{\text{glo}}\mathbf{T}_{\text{ana}}(t)] = f(\mathbf{a}_{1,2,\ldots,N_a}(t)_{\text{glo}}).$$

(v) Calculate for each joint the relative position and orientation of the AF of the two relevant segments according to a proper convention:

$$[\boldsymbol{\theta}(t), \mathbf{T}_{dp}(t)] = f({}^{\text{glo}}\mathbf{R}_{\text{ana}}(t)_{\text{prox}}, {}^{\text{glo}}\mathbf{T}_{\text{ana}}(t)_{\text{prox}}, {}^{\text{glo}}\mathbf{R}_{\text{ana}}(t)_{\text{dist}}, {}^{\text{glo}}\mathbf{T}_{\text{ana}}(t)_{\text{dist}}),$$

where $\boldsymbol{\theta}(t)$ and $\mathbf{T}_{dp}(t)$ are the orientation (flexion–extension — Fl/Ex, ab–adduction — Ab/Ad, internal–external rotation — In/Ex) and position vector of the distal with respect to the proximal reference frame.

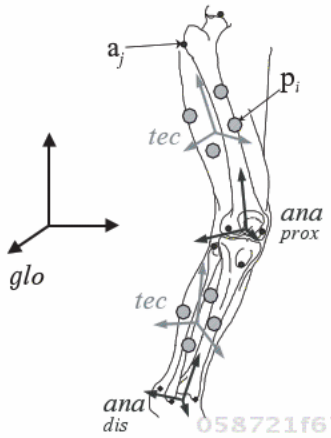




Fig. 3. Laboratory, technical, and anatomical reference frames for the lower limb.

In Fig. 3, the TF and AF of the distal and proximal segments of the knee joint are represented.

This procedure is totally general and can be realized in different ways, depending on the acquisition and elaboration protocol implemented. We will refer to the C.A.S.T. (Calibrated Anatomical System Technique) protocol.[10] In this protocol the first two steps correspond to the so-called *anatomical calibration*. The TF in this context is determined once for all in the calibration configuration and the local coordinates of the ALs are considered time-invariant.

The accuracy of the joint kinematics reconstructed according to this procedure is of fundamental importance for the exploitation of the results in operative conditions, such as during the clinical decision process. Different types of errors can occur and affect this accuracy:



(a) Instrumental errors;
(b) Errors in the identification of the local coordinates of the ALs;
(c) Errors due to STA.

While instrumental errors can be quantified and possibly compensated, the errors in the identification of the ALs and those derived from STA are systematic, thus, much more complex to be quantified, limited, and compensated.

### 2.1.1. *Instrumental errors*

Even in static condition, the reconstructed coordinates of the markers result time-variant, due to errors proper of the measurement system.[11] These errors propagate to the calculated pose of the TF (${}^{\text{glo}}\mathbf{R}_{\text{tec}}(t)$ and ${}^{\text{glo}}\mathbf{T}_{\text{tec}}(t)$), thus to the joint kinematics $[\boldsymbol{\theta}(t), \mathbf{T}_{dp}(t)]$. Experience recommends that these errors are quantified before each experimental session by means of *ad hoc* tests, in order to estimate how

they could compromise the measurement. According to the characteristics of the error, different techniques can be adopted to limit its effects.

Two types of instrumental errors are possible: *systematic* or *random*. *Systematic errors* are always associated to a model of the measurement system of limited validity, or to inaccuracies in the calibration of the system (inaccurate estimate of the parameters of the model), or to the non-linearities which the calibration cannot take into account (inadequate model). For instance, a model of the cameras should not neglect the distortion introduced by the optics, which influences the elaboration of the images.[12] The magnitude of systematic errors depends on the amplitude of the field of view and on the position of the marker within this field of view.[13] The calibration of the system must reduce the systematic instrumental errors. It must be performed as accurately as possible by the operator and repeated if necessary in order to preserve the performance of the instrument even when no meaningful modification in the configuration has been introduced.



*Random errors* can be introduced by electronic noise, by the flickering, associated to the imprecision in the conversion of the image of the marker into image coordinates of its centroid, and by the quantization intrinsic of the digitalization process, transforming the image coordinates of the marker into digital values.[11,14]

Data of human motion usually have a limited frequency spectrum, to which the wide band additive instrumental noise is superimposed. This worsens significantly the signal–noise ratio of the signals obtained through numeric differentiation, such as velocity, and acceleration. Since the end of the 1970s, a large number of studies were focused on the treatment of noise in this condition.[12,15–28] Most of these studies investigated the source and the statistic characteristics of instrumental errors, proposing a large variety of filtering and smoothing techniques. In order to better adapt to the characteristics of the signal and of the noise, filtering methods in the time and frequency domains have been recently proposed,[12,15,18,19,21,22,26,28–30] using optimization procedures for the determination of the filtering parameters, such as the cut-off frequency. All these methods assume that the human motion signals are stationary. This assumption might not be realistic in contexts as sport activities, where sudden variations in the frequency content of the kinematic signal can occur. Thus, the choice of a single cut-off frequency cannot provide a non-polarized estimate of the position, and in particular of velocity and acceleration. For the estimation of impact phenomena time–frequency analysis is more suitable,[31,32] as it guarantees a substantial improvement in estimation of velocity and acceleration with respect to traditional techniques.



It is realistic to suppose that the calibration of the system works well in correcting systematic instrumental errors and that good filtering techniques are available, simply following the indications of the producers. Nevertheless, the performance of the system, in terms of accuracy and precision, can depend on a variety of factors. These include not only the adequacy and quality of the system itself, but also the parameters associated to the specific setup adopted in the laboratory, such as the number and position of the cameras, the size of the

measurement volume, the size and shape of the adopted calibration object, and also the care taken in performing the calibration procedure. The producers declare that the accuracy in the reconstruction of the coordinates of the marker within a given measurement field is approximately 1:3000 of the main diagonal of the calibrated volume. Schmid[33] refers a reachable accuracy in distances ranging, for available commercial systems, from 0.09% to 1.77% of the measurement field. The reported values are largely acceptable for human motion analysis applications. Nevertheless, the determination of the accuracy and precision in the measure of the position of the marker deserves an *ad hoc* estimation in routine laboratory practice.[11] Actually, the understanding of the limits of the available analysis system is essential for the proper application of the estimates of the segment and joint kinematics.[34] Thus, the system user, before each experimental session, should perform an estimate of the instrumental errors performing spot-checks, i.e., simple tests to verify the maintenance of the performance of the system. Several tests of this sort were proposed in the literature, assuming for the estimate of the error different reference measurements, based both on objects with markers at known distance.[11,35–37] and known trajectories of markers.[38–40]



### 2.1.2. *Anatomical landmarks misplacement*

When the pose of the TF has been estimated as accurately as possible, that is limiting the propagation of the experimental errors, the corresponding pose of the AF can be estimated by means of a registration procedure, which is called anatomical calibration.[10,41,42] The ALs can be both *internal* and *sub-cuetaneous*. Generally their identification is not precise, introducing a misplacement error:

$$\hat{\mathbf{a}}_{j,\mathrm{tec}} = \mathbf{a}_{j,\mathrm{tec}} + \mathbf{e}_{j,\mathrm{tec}}\,, \quad j = 1, 2, \ldots, N_a\,,$$

where $\mathbf{a}_{j,\mathrm{tec}}$ are the real coordinates of the AL $j$, $\mathbf{e}_{j,\mathrm{tec}}$ is the misplacement error associated to the AL $j$, and $\hat{\mathbf{a}}_{j,\mathrm{tec}}$ are the estimated coordinates of the AL $j$.



This error affects the precision in the estimate of the pose of the AF:

$$\begin{aligned}[{}^{\mathrm{glo}}\mathbf{R}_{\mathrm{ana}}(t), {}^{\mathrm{glo}}\mathbf{T}_{\mathrm{ana}}(t)] &= f(\hat{\mathbf{a}}_{1,2,\ldots,N_a}(t)_{\mathrm{glo}}) \\ &= f({}^{\mathrm{glo}}\mathbf{R}_{\mathrm{tec}}(t)\hat{\mathbf{a}}_{1,2,\ldots,N_a,\mathrm{tec}} + {}^{\mathrm{glo}}\mathbf{T}_{\mathrm{tec}}(t)) \\ &= f({}^{\mathrm{glo}}\mathbf{R}_{\mathrm{tec}}(t)(\mathbf{a}_{1,2,\ldots,N_a,\mathrm{tec}} + \mathbf{e}_{j,\mathrm{tec}}) + {}^{\mathrm{glo}}\mathbf{T}_{\mathrm{tec}}(t))\end{aligned}$$

and consequently the estimate and the interpretation of joint kinematics.

The misplacement of the *sub-cutaneous ALs* through palpation can be caused by three main factors: (i) the palpable ALs are actually not geometrical points but surfaces, which are sometimes large and irregular; (ii) a soft tissue layer, of variable thickness and composition, covers the ALs; (iii) the identification of the AL location depends on the palpation procedure adopted.

Della Croce *et al.*[43] presented an extensive study regarding this problem, reporting: (a) the precision in the determination of the AFs of the lower limb,

(b) the effect of ALs misplacement on the pose of the AFs, and (c) the effect of the AFs pose error on joint kinematics. The precision in the determination of the AFs pose of the pelvis and lower limb was assessed, considering subjects wearing markers attached directly on the skin, evaluating the inter- and intra-operator variability for experienced physical-therapists. This study pointed out that inter-operator variability (several identifications performed by several operators) is larger than intra-operator variability (several identifications performed by the same operator). This is probably due to the different interpretation by each operator of the ALs identification procedure. The largest dispersion was observed for the great trochanter, with a root mean square error up to 18 mm. The tibial ALs were, generally, more accurate. The reported results can be used as guidelines for the selection of the ALs, which can be more suitable for the definition of AFs. The choice should exclude the most critical ALs, in order to minimize errors and their propagation to joint kinematics.

The *internal ALs* are not associated to bone prominences, that can be palpated from the outside. Among internal ALs, the hip joint center (HJC) and the center of the gleno-humeral head (GH) are certainly the most commonly used. The hip is modeled as a spherical joint. The accuracy and precision in the identification of the HJC are crucial in order to determine the error propagated to the hip and knee kinematics and dynamics.[44–49] The flow diagram describing how HJC misplacement propagates to relevant kinematics and dynamics is shown in Fig. 4.

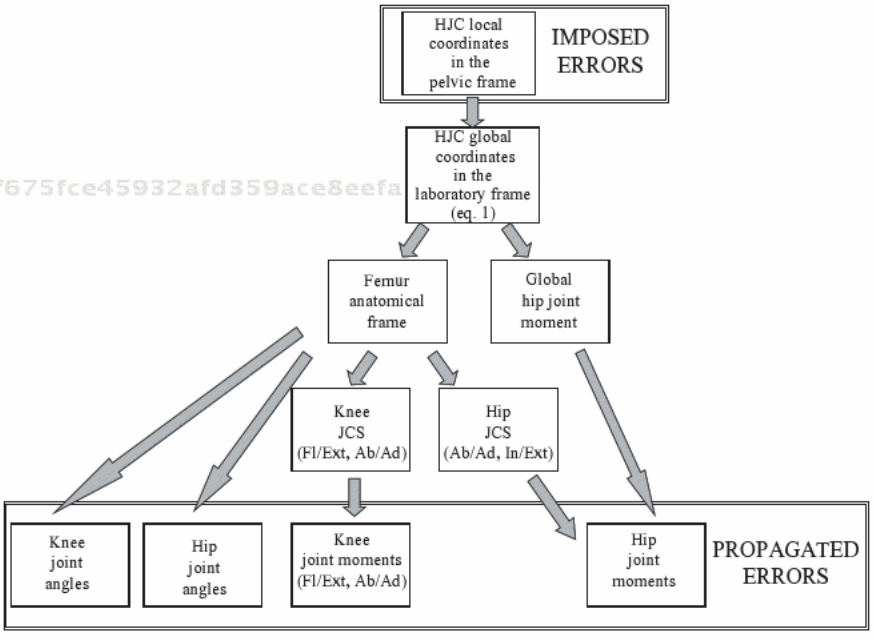


Fig. 4. Diagram of the HJC misplacement propagation to hip and knee joints angles and moments.[49]

The position of the HJC can be estimated using either a functional.[41] or a geometrical approach.[50–52] The functional approach[41] is based on the assumption that the HJC is the centre of the relative 3D motion of the femur with respect to the pelvis. Using this method, without STA, it is possible to estimate a reliable position of the HJC, almost independently from the type of motion, if the range of motion is appropriately wide.[53–55] The error in the estimate of the HJC position can reach 10 mm performing a 15° rotation and 5 mm with a 30° rotation.[55] The functional method requires the execution of an *ad hoc* exercise during the motion analysis experimental session. It can be applied only to subjects who exhibit a sufficient range of motion at the hip joint, and it can be affected by STA. Nevertheless, it is the only viable method for the subject-specific identification of the HJC, independently from differences due to deformities, age, gender, and anthropometry.

The performance of the functional method was compared[56] with RSA HJC identification on 11 subjects. An error of 12 mm was reported, which is lower than the error obtained using most conventional geometrical methods,[50,51] showing errors up to 23 and 21 mm. The estimate obtained with the two geometrical methods[50,51] resulted also polarized: antero-superiorly[50] and medially.[51] Thus, when a proper range of motion at the hip can be acquired, the functional method should be preferred. When this is not possible, geometrical methods must be adopted, paying particular attention to the anthropometric characteristics of the subject.

Any estimation method of the HJC position implies a certain error, thus the error affected results must be interpreted critically and carefully for the clinical decision process.

Given the fundamental role of the HJC in motion analysis, special attention was paid to the effects of the misplacement of this AL.[46,49] The hip moments are the most affected by HJC misplacement.[49] The effect of HJC misplacement on hip moments and hip and knee rotation angles is negligible.

The estimation of the center of the GH is fundamental for the analysis of the upper-limb kinematics.[1] As discussed in Ref. 57 GH is assumed to lie at the geometric center of the humeral head. The GH is mainly estimated by regression equations[58,59] or by functional methods.[60,61] Stokdijk *et al.*[60] could determine that these lasts (no matter if based on sphere fitting or helical axis) are more reliable *in vivo* than regression equations; furthermore, indications were also provided for their higher accuracy, even if definitive conclusions could not be drawn *in vivo* due to a luck of gold-standard. The drawback of the functional methods is that they require additional movements to the patient, which require time to be acquired and the ability of the patient himself to perform them. If this is the case, regression methods remain the solution.

The misplacement of ALs propagates through the calculus to the pose of the AFs, thus to the joint angles. This phenomenon is particularly critical for angles characterized by small ranges during motion. In order to analyze this phenomenon several methods have been used in the literature: (1) experimental errors applied

to devices with controlled joint kinematics[62]; (2) experimental errors applied to simulated joint kinematics[43]; (3) simulated errors applied to joint kinematics or mechanics[46,48,63,64]; (4) mathematical approach for a sensitivity analysis.[65]

The analyses performed, focusing mainly on the kinematics of the knee, pointed out that even small errors in the alignment of the AFs produce critical errors on joint kinematics.[62] The most critical rotations at the knee resulted to be the In/Ex and the Ab/Ad rotation angles, observing a propagated error depending on the amount of flexion.[43] The amount of propagated error was considered relevant with respect to the range of motion. The same thing happens at the hip and ankle.

Obviously, the criticality of error propagation to joint kinematics depends on the adopted angular convention. Woltring[66] performed a sensitivity analysis comparing the results obtained using the cardan angles and the attitude vector, which resulted more robust. Unfortunately, although more reliable this convention lacks physiological interpretability.



In summary, the misplacement of the ALs is a critical issue in the processing of motion analysis data. Even small ALs misplacement errors can result in relevant errors on the joint kinematics, in particular for angles characterized by small ranges.

In order to minimize the effects of this source of error, very little can be done in addition to pay particular attention to the calibration procedure of the ALs.

### 2.1.3. *Soft tissue artifact*

Acquisition and elaboration protocols for motion analysis are usually based on the erroneous assumption that the markers associated to a body segment are rigidly attached to the underlying bony segment. Actually, *in vivo* passive and active deformable tissues are interposed between the markers and the underlying targeted bony segment: skin, fat, and muscles. This leads to relative motion of the markers with respect to the bony segment during the execution of the motor task; thus the position of AF in the TF is time-variant:



$$\hat{\mathbf{a}}_j(t)_{\text{tec}} = \mathbf{a}_{j,\text{tec}} + \mathbf{e}^{\text{ATM}}(t)_{\text{tec}}\,, \quad j = 1, 2, \ldots, N_a\,,$$

where $\mathbf{a}_{j,\text{tec}}$ is the position of the AF during the calibration, while $\mathbf{e}^{\text{ATM}}(t)_{\text{tec}}$ is the motion of the AF during the execution of the motor task. This phenomenon is called STA. Inertia, deformation, skin sliding, occurring mainly close to the joints,[67] gravity, and deformations caused by the contraction of muscles contribute interdependently to STA. Because of its own characteristics, STA has the same frequency content of the kinematics to be analyzed, thus its effect, unlike stereophotogrammetric errors, cannot be limited by means of smoothing techniques. Thus, STA was recognized as the most critical source of error in motion analysis.[68]

Several studies focused on the characterization of this phenomenon, attempting to evaluate the motion $\mathbf{e}^{\text{ATM}}(t)_{\text{tec}}$. This knowledge could allow to compensate the effect of STA.

The problem of how STA can be quantified and compensated is described with more detail in Sec. 3.1.

### 2.2. *Single-plane fluoroscopy*

The methods based on stereophotogrammetry, described in the previous sections, are limited by the large artifact introduced by the motion of the skin with respect to the underlying bone.[68] The errors involved can be as large as a few centimeters for joint translations and several degrees for rotations.[67] From 1990s, in order to achieve higher accuracy, radiographic images have been used to evaluate motion in replaced human joints. For total knee replacement kinematics analysis, single-plane video-fluoroscopy has been successfully used.[69–75] More recently, in order to achieve higher accuracy, lower than 0.5 mm and 0.5°, a dual orthogonal fluoroscopy system was developed[76] and applied to evaluate *in vivo* motion of total knee replacement.[77] In this section, only single-plane fluoroscopy will be analyzed.



Nevertheless, the kinematic analysis using fluoroscopy can be applied only to a single joint at a time and not to the whole body like with the stereophotogrammetry and it is also an invasive procedure.

With respect to traditional radiography, a reduced X-ray dose is sufficient to form the image, which however shows a lower quality in terms of resolution and distortion. The incident X-ray beam strikes an image intensifier producing an image that is converted into an electronic signal by a television camera. This signal can be visualized on a monitor, recorded on a tape or even collected on a computer using frame grabber boards. Video-fluoroscopy is well suited for kinematics analysis of human joints because a sequence of X-ray images can be collected during the execution of a specific task (Fig. 5). On each image, the projection of bones on the image plane can be identified.



#### 2.2.1. *The fluoroscope device*

Early fluoroscopic procedures produced visual images of low intensity, which required the radiologist's eyes to be dark adapted and restricted image recording. In the mid-1950s, the X-ray image intensifier (XRII), which considerably brightened fluoroscopic images and enabled the radiologist to visualize the output image with no need of dark adaptation,[78] was commercially introduced. The intensified visual image is easily captured by film and television camera tubes.

An XRII consists of the following major components: an input window, an input phosphor and a photo cathode, several electrostatic focusing lenses, an accelerating anode, an output phosphor screen, and a protective vacuum case (Fig. 6). An XRII has two major functions: (a) to intercept the X-ray photons and convert them into visible light photons, and (b) to amplify or intensify this light signal. The XRII creates a large gain (or intensification) in luminance at the output screen compared with that at the input screen. The XRII is located opposite to the

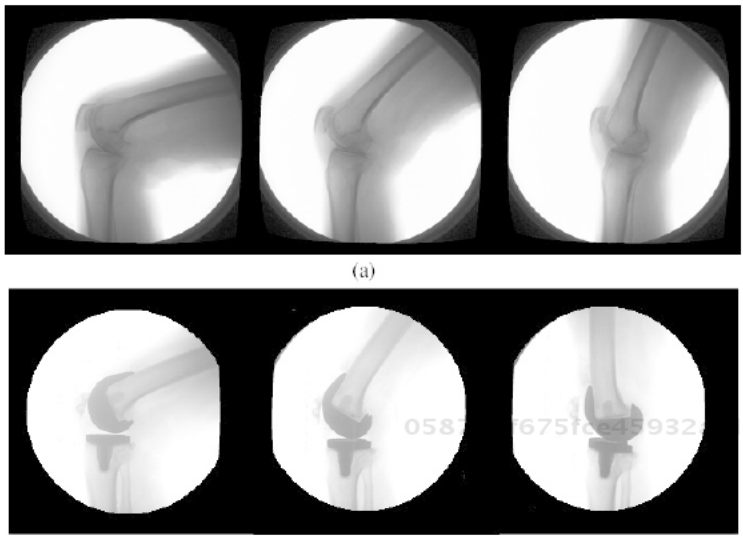


Fig. 5. Sequence of fluoroscopic images during rising from a chair of a normal subject (a) and of a subject treated by a total knee replacement (b).

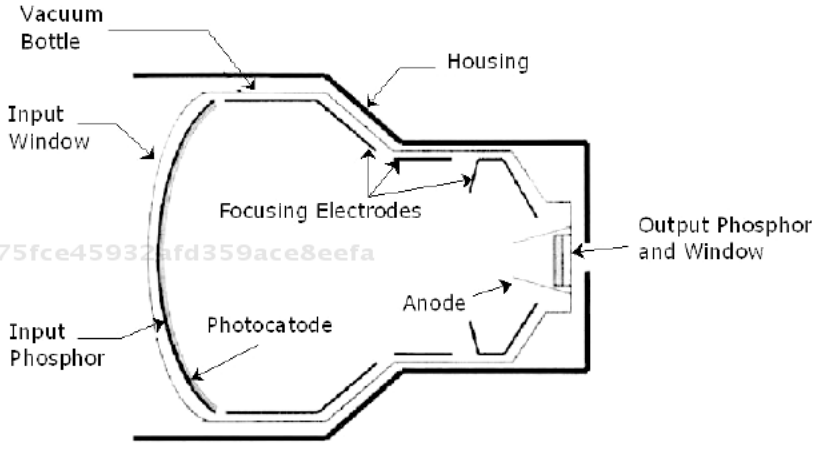


Fig. 6. Cross-sectional diagram of an XRII shows its major components.

X-ray tube. The XRII is contained in a cylindrical protective case because it is a very delicate device under high vacuum, and needs to be handled with care. The operational principles of an XRII can be briefly described as follows. X-ray photons penetrate the input window of the vacuum case. The input phosphor absorbs the X-ray photons and converts them into optical photons (a phenomenon called luminescence). These optical photons are converted into photoelectrons at

the photo cathode. The photoelectrons are accelerated by electric field produced by strong electric potential difference of the XRII and are collected at the output phosphor. Each accelerated electron produces many optical photons at the output phosphor.

XRII systems are commonly used for digital planar image acquisition in radiology. However, even the best XRII system hardware cannot deliver images free of artifact. Lag, vignetting, veiling glare, and geometrical distortions are introduced. Some of these artifacts are caused by improper calibration and can usually be corrected. In particular, the latter will be discussed with more details as its correction is typically performed during elaboration of fluoroscopic images for quantitative estimation of human joint kinematics. With ordinary sizes of the XRII, the images are affected by geometric distortion which causes a variation in magnification up to 5%–10%.[79] The geometric distortion has two main sources: the projection of the X-ray beam onto the curved input surface of the XRII and the deflection of the electrons inside the XRII caused by any external magnetic field. The former produces the typical "pincushion" distortion. The latter source may produce a sigmoidal distortion if the orientation of the XRII is parallel to the external magnetic field.[80] Larger XRII are more sensitive to the electromagnetic fields, causing a larger sigmoidal distortion. Manufactures include a highly conductive mu-metal shield that lines the canister in which the vacuum bottle is positioned to reduce the effect of sigmoidal distortion.

To characterize the geometric distortion of the specific XRII used, an image of a rectilinear calibration grid placed on the input screen of the XRII is commonly used.[81–83] The grid consists of either wires, transparent holes or small opaque objects.[83] A number of approaches can be distinguished in the procedures that correct the distortion. The more effective approach uses analytical function to map distorted positions to undistorted positions. This is performed either locally for each quadrilateral or triangular patch[84] identified by four or three grid points respectively, or globally.[82,83] In some cases a radially symmetric distortion is assumed,[81,85] thereby ignoring the typical sigmoidal component. The global techniques, based on polynomials[82] or based on thin-plate splines,[86] avoid discontinuities from one patch to the other and show better performances with respect to any local synthetic and real images. When the distortion has a local nature or is predominantly sigmoidal, the thin-plate splines global correction technique shows better performances with respect to global techniques based on polynomials.[86]

### 2.2.2. *Pose estimation*

In human joint kinematics analysis using video-fluoroscopy, the problem is to estimate for each bi-dimensional (2D) fluoroscopic image the 3D position and orientation (pose) of both the distal and proximal extremities of bones that constitute the joint. The problem can therefore be formulated as the estimation

of the full six degrees-of-freedom (DOF) pose of an object, with a well-known geometry from a single projection view. Originally, this technique was applied to estimate the *in vivo* kinematics of total knee replacement, therefore the object was the CAD model of femoral and tibial prosthetic components. Easily the technique was later applied to other total joint replacements; such as the ankle[87] and the hip.[88] Recently, using the Nuclear Magnetic Resonance or Computed Tomography for the reconstruction of the bone extremities geometry, this methodology has also been used to estimate *in vivo* kinematics of normal lower limb joint.[89] or of particular knee prosthesis.[90]

In the following paragraphs the two main approaches of *in vivo* kinematics analysis using video-fluoroscopy will be described in the specific field of total knee replacement kinematics. The technique, even if described in the total knee replacement application, can be used for normal joint, just taken into account two differences: (1) the object geometry is not given from the company but must be estimated in some way, and (2) the 2D projection of the object has more information as not only the contour of the silhouette but also the gray scale of the image region inside the contour can be used for the alignment (Fig. 5).



2.2.2.1. 3D/3D alignment approach

The problem of 3D model-based pose estimation from 2D projections has been largely faced in computer vision. In an extensive study, Lavallée and colleagues[91,92] proposed an algorithm for the 3D pose estimation of smooth free-form objects from a general number of planar video images, and tested the application of the general technique to two X-ray images in the field of computer-assisted surgery. The object pose results from the alignment of the object model with all image projections. The alignment is based on the minimization of the distance between model and projection rays. Distances are pre-computed in an "octree" distance map for faster pose estimation. Because object models may not be too much accurate as typically obtained from 3D segmentation on medical images, two image projections are advised to reach the necessary accuracy in the estimation of the object pose.



The 3D/3D alignment approach is a simplified version of the algorithm proposed by Lavallée and Szeliski.[92] In TKR 3D kinematics analysis using single plane video-fluoroscopy, the perfect knowledge of the geometry of the two prosthesis components is necessary together with the relevant projection on the image plane. When a non-symmetric object is imaged by a non-orthogonal camera, a unique projection is produced for each 3D pose of the object. The assumption is that a single image, together with the knowledge of the 3D geometry, is sufficient for the complete six DOF estimation of the object. Although femoral and tibial components are symmetric with respect to the sagittal plane in most of the prosthesis designs, false poses due to symmetry can be rejected by the expected smoothness of the knee joint motion. The pose estimation of prosthesis components from a single view can be obtained by aligning the 3D object model in order to

obtain a corresponding projection as observed in the X-ray image. The alignment between model and image is intended to be the condition that replicates the image formation. In the image formation process, X-rays pass through the object to generate image's projection points. For contour points X-rays must be tangent to the component. The camera model defines projection lines that analytically represent X-rays. For pose estimation, the object model must be aligned with the projection, that is projection lines coming from contour points must be tangent to the model surface (Fig. 7). A projection line is tangent to the model when the minimum distance from the surface is zero. Using distances, the definition of a cost function which represents the alignment is straightforward and the pose estimation is formulated in a nonlinear minimization problem, which is solved by an iterative procedure.

Going into more details of this approach, three elaboration steps can be identified: (a) projection model and calibration, (b) image acquisition and processing, and (c) pose estimation.

*Projection model and calibration.* As previously described, in video-fluoroscopy, X-rays are emitted from a source, passing through the object and then striking the input phosphor. The light produced by the phosphor screen is then converted into an image by a TV system. X-rays are attenuated depending on the density of materials; so high-density metallic TKR components appear very dark on a fluoroscopic image. A perspective projection model can represent the fluoroscope. In perspective projection model, a pinhole camera forms the image. X-rays are considered straight lines emitted by a point source of uniform radiation in all



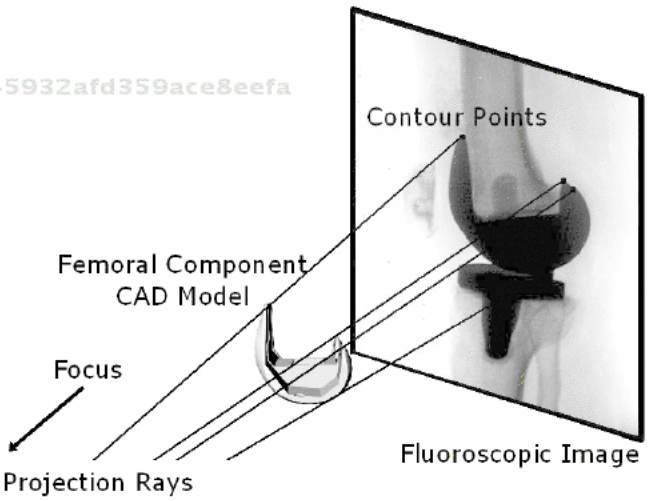


Fig. 7. Sketch of the model for image generation process: projection lines from the contour points must be tangent to the object model when the model is in the right pose. In the frame, a typical video-fluoroscopy image taken from an *in vivo* examination in a TKR patient.

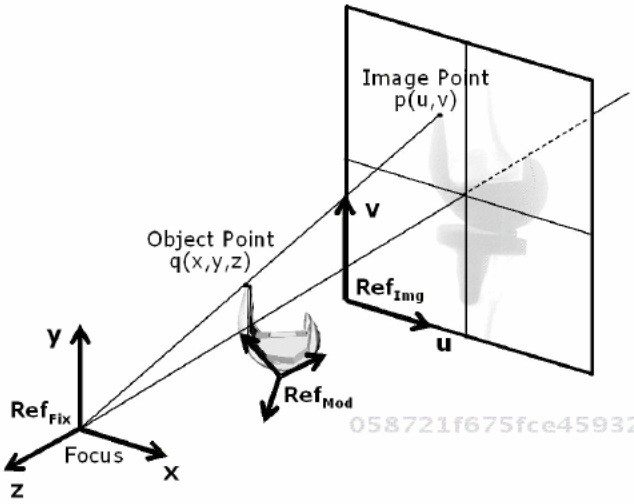


Fig. 8. Perspective projection camera model and reference coordinate systems.

directions. The projection model defines a function $F$ that maps 3D points, ${}^{\mathrm{Fix}}\mathbf{q}$, in the camera-embedded fixed coordinate system, $\mathrm{Ref}_{\mathrm{Fix}}$, to 2D points, $\mathbf{p}$, in the image coordinate system, $\mathrm{Ref}_{\mathrm{Img}}$:

$$F : \mathrm{Ref}_{\mathrm{Fix}} \rightarrow \mathrm{Ref}_{\mathrm{Img}}$$
$$F({}^{\mathrm{Fix}}\mathbf{q}(x,y,z)) = \mathbf{p}(u,v)\,,$$

where $x, y, z$ are the 3D spatial coordinates and $u, v$ the 2D plane coordinates (Fig. 8). The inverse function $F^{-1}$ defines, for each image point, a straight 3D line, ${}^{\mathrm{Fix}}l(\mathbf{p})$, joining $p$ to the camera focus. The position of the camera focus with respect to the image plane is fixed and calibrated at the beginning of each experimental session.



*Image acquisition and processing.* Images are first corrected for geometric distortion. To extract the prosthesis component contours from the collected image, a Canny's edge detector is applied.[93] The edge detector detects contour points according to grey scale values. In X-ray images, pixel values depend on the density of the structures the rays pass through before reaching the image plane and on the X-ray doses. Spurious edges are detected and erased.

*Pose Estimation.* As previously stated, the key point in this approach is to look at the tangent condition between projection lines and model surface. When distance between line and model is defined by the minimum Euclidean distance between each point of the line and each point of the surface, projection rays are tangent to the object when their distance to the model is zero. The tangent condition therefore corresponds in practice to the minimum distance condition. Surface points are defined in a third reference system, $\mathrm{Ref}_{\mathrm{Mod}}$, embedded with the model. To evaluate distance values, the transformation that maps points in $\mathrm{Ref}_{\mathrm{Fix}}$ to $\mathrm{Ref}_{\mathrm{Mod}}$ must be

applied to ray points. Let us indicate:

$$\begin{aligned} {}^{\mathrm{Fix}}\mathbf{P}_{\mathrm{Mod}} &= [\vartheta_x \quad \vartheta_y \quad \vartheta_z \quad T_x \quad T_y \quad T_z]^T \,, \\ {}^{\mathrm{Fix}}\mathbf{R}_{\mathrm{Mod}} &= \mathbf{R}(\vartheta_x, \vartheta_y, \vartheta_z) \,, \\ {}^{\mathrm{Fix}}\mathbf{T}_{\mathrm{Mod}} &= [T_x \quad T_y \quad T_z]^T \,, \end{aligned} \tag{1}$$

respectively the pose vector, the orientation matrix, and the position vector of $\mathrm{Ref}_{\mathrm{Mod}}$ with respect to $\mathrm{Ref}_{\mathrm{Fix}}$. The Euler $x$–$y$–$z$ convention is used for the $\vartheta_{x,y,z}$ to $\mathbf{R}$ transform. The inverse transformation to be applied is

$${}^{\mathrm{Mod}}\mathbf{q} = {}^{\mathrm{Mod}}\mathbf{R}_{\mathrm{Fix}}\,{}^{\mathrm{Fix}}\mathbf{q} + {}^{\mathrm{Mod}}\mathbf{T}_{\mathrm{Fix}} \,, \tag{2}$$

where ${}^{\mathrm{Mod}}\mathbf{q}$ is the position in $\mathrm{Ref}_{\mathrm{Mod}}$, ${}^{\mathrm{Mod}}\mathbf{R}_{\mathrm{Fix}} = {}^{\mathrm{Fix}}\mathbf{R}_{\mathrm{Mod}}^{-1}$, and ${}^{\mathrm{Mod}}\mathbf{T}_{\mathrm{Fix}} = -{}^{\mathrm{Fix}}\mathbf{R}_{\mathrm{Mod}}^{-1}\,{}^{\mathrm{Fix}}\mathbf{T}_{\mathrm{Mod}}$. The distance between the ray of the contour point $\mathbf{p}_i$ and the model surface, $S$, is defined as

$$d(\mathbf{p}_i, S) = \min_{\substack{{}^{\mathrm{Mod}}\mathbf{q} \in {}^{\mathrm{Mod}}l(\mathbf{p}_i) \\ \mathbf{s} \in S}} [\pm \| {}^{\mathrm{Mod}}\mathbf{q} - \mathbf{s} \|] \tag{3}$$

where negative values apply when the ray point ${}^{\mathrm{Mod}}\mathbf{q}$ is internal to the surface. According to Eq. (3), the distance of a ray that crosses the surface is therefore negative.

For a faster computation of the distance between projection rays and model Euclidean distance maps are pre-computed and stored. A distance map represents an object, assigning to each point of the volume around and internal to the object the corresponding distance from the surface. Using distance maps, the distance of a point belonging to a projection ray from the model surface can be computed by a trilinear interpolation of the eight map points closest to the point. The ray-to-model distance can therefore be easily found as the minimum value of the distance for a set of points that belong to the projection ray. Distance maps are represented by 3D arrays whose values are the vector distances from the closest point of the object.

The 3D alignment condition for the object is obtained by minimizing a cost function parameterized by the pose vector, $\mathbf{P}$, and defined as the sum of the squared ray-to-surface distances:

$$\mathrm{SSD}(\mathbf{P}) = \sum_{i=1}^{N} d^2(\mathbf{p}_i, S) \,, \tag{4}$$

where $N$ is the number of contour points. The procedure iterates until the difference between two successive values of the cost function is smaller than a certain threshold. When the minimum is reached, the pose vector is the estimate of the object pose.

Computer simulation and *in vitro* tests using real knee prosthesis show that the accuracy with which relative orientation and position of the components can be estimated is better than 1.5° and 1.5 mm, respectively.

2.2.2.2. 2D/3D alignment approach

In the 2D/3D alignment approach the estimation of the six DOF is performed minimizing the similarity between the fluoroscopic image and the 2D computer simulated projection of the known object. The accuracy gained with this approach is comparable with the previous one.

Banks and Hodge[69,72,94] use a template matching technique for TKR pose estimation. The authors developed a library of contours of each prosthesis component rendered at several different poses. The contours extracted from every X-ray image are compared with each element of the library to find the best match. To reduce the size of the library, only out-of-plane rotations are taken into account for template matching. Each template in the library is obtained by rendering the object model at different out-of-plane rotations with steps of 1°. A transformation is then applied to each template in order to normalize for size and in-plane position and orientation. In the matching process the collected image is first normalized and then compared with every template in the library to find the best match. Rotation and translations of the image and translation in the direction perpendicular to the image plane are then computed. Fourier descriptors are used to represent library templates and projection contours. Each contour pixel is considered as a complex value; if the contour is continuously traced, it could be seen as a periodic complex function, and Discrete Fourier Transform is applied.



The group of the Rocky Mountain Musculoskeletal Research Laboratory (Denver, USA) uses a similar approach.[75,95] The difference can be identified in the representation of templates and collected image projection, and in the matching process. Areas are used instead of contours: library templates are binary images with a fixed number of pixels and therefore with the same area. The normalization is performed reducing the image projection to the fixed number of pixels of library templates. More recently, the same group has developed another technique based on the same approach[96]: the match between the real fluoroscopic image and the predicted image, generated rendering the object model, is evaluated using weighted combination of pixel values comparison and of edges overlap. Robust optimization algorithm, simulated annealing, is used to find the global minimum.[96] This last technique, as the 3D/3D alignment approach, does not perform any prior segmentation of the image, as no closed contour is required.



## 2.3. *Inertial sensors*

As discussed in the previous section, stereophotogrammetric systems have become a reference for motion analysis. However, their use presents a number of drawbacks:

(1) acquisitions are restricted to the calibrated working space, precluding the possibility of long-term monitoring in natural environments;
(2) they are difficult to install in small rooms, such as ambulatories;
(3) markers occlusion can preclude proper data acquisition;
(4) they are generally very expensive.

A possible solution to overcome these problems is represented by the use of inertial sensors, i.e., accelerometers and gyroscopes, alone, together, or combined with other type of sensors, such as magnetometers.[97,98] Even if not immune from limitations,[99] an increasing number of publications[100,101] are highlighting their role as the emerging technology for motion analysis.

In the next two sections a brief description of accelerometers and gyroscopes is given, with particular reference to their realization as microelectromechanical systems (MEMS).[102] It then follows a section dedicated to the application of these sensors in motion analysis.

### 2.3.1. *Accelerometers*

An accelerometer is a device which is able to sense the acceleration of the body to which it is attached, by transforming it into an electrical signal. As discussed in Ref. 97, in its simplest form a single axis accelerometer can be thought as a mass (usually referred to as proof-mass), suspended by a spring in a housing. Assuming the spring in its linear region, Hooke's law models its behavior: the spring will then exhibit a restoring force ($F$) proportional (with coefficient $k$) to the amount it has been expanded or compressed ($x$):

$$F = kx\,.$$

Combining Hooke's law with the second law of Newton applied on the accelerometer proof-mass, the following equation is valid:

$$F = ma = kx\,,$$

where $m$ is the mass of the proof-mass and $a$ is the acceleration. The acceleration $a$ which displaces the mass $m$ of $x$ will therefore be equal to $a = kx/m$.

The problem of measuring an acceleration is thus turned into the problem of measuring a displacement. More realistically, accelerometers can be modeled as a mass-spring-dumper system, which is then governed by the following equation:

$$\ddot{x} + \frac{d}{m}\dot{x} + \frac{k}{m}x = a\,,$$

where $x$ is the displacement of the mass, $d$ the damping factor, and $k$ the spring constant. This system is thus described by a second order transfer function. This means that in the development, application-specific consideration must be done, e.g., to optimize the resonance frequency, the quality factor, keeping the mechanical noise due to Brownian motion as limited as possible.[103]

A variety of transduction mechanisms have been used in MEMS accelerometers, e.g., piezo-resistive, capacitive, tunneling device, resonant device, and thermal device. A detailed analysis of MEMS technology issues is available in Refs. 102 and 103.

Main problems affecting MEMS accelerometers are due to thermal effects and mechanical wear.[104] Low frequency drifting, e.g., due to bias and scale factor drifts,

resulted in having a more relevant effect than high frequency errors, e.g., due to sensor jolting or impact spikes.[98] Modeling equations for the device may vary depending on assumptions: for details see Refs. 98, 104, and 105.

Accelerometers are mostly used in human movement analysis for vibration sensing or, as described in the following sections, as inclinometers.

### 2.3.2. *Gyroscopes*

Gyroscopes are angular rate sensors. As discussed in Refs. 97, 102, 103, and 106, different designs exist, but each one is based on the principle of a vibrating mass undergoing an additional vibration caused by the Coriolis effect.

When a mechanical element is made to oscillate by the application of an alternating force, and the oscillating body is placed in a rotating reference frame, a so-called Coriolis force appears, which produces a secondary oscillation perpendicular to the primary oscillation motion. By sensing the secondary vibration, the angular velocity can be measured. The Coriolis force $F_c$ is given by:

$$\vec{F}c = 2m \cdot \vec{v} \wedge \vec{\omega}\,,$$

where $m$ is the mass of the vibrating element, $v$ is the vibration velocity, and $\omega$ is the rate of turn to be measured; $\omega$ can be computed if the acceleration due to the Coriolis effect is sensed.

Thermal effects are the predominant source of error in gyroscopes, leading to consistent drifting (one of the quality parameters of gyroscopes is drifting, expressed as °/s or °/h). A detailed description of MEMS gyroscopes can be found in Ref. 103. It is sufficient here to say that classical examples of vibrating gyros are tuning forks, i.e., tunes that are connected to a junction bar. The actuation mechanisms used to drive the vibrating structure in resonance are primarily electrostatic, electromagnetic, or piezoelectric.

Modeling equations for the device may vary depending on assumptions: for details see Refs. 98, 104, and 105.

Gyroscopes are usually applied for orientation measurement in conjunction with techniques for compensating the thermal drifting of the offset.

### 2.3.3. *Application in human movement analysis*

Historically,[99] the application of accelerometers and gyroscopes for inertial navigation systems of ships, submarines and airplanes became widespread in the 1950s. Although their potentials for human movement analysis was demonstrated in the '70s,[107] due to weight and physical dimension, their application became feasible in the 1990s, with the advent of MEMS. Nowadays, in parallel to constant improvement in the microelectronic side (which will probably lead to the construction of accelerometers and gyroscopes integrated in a single chip[108]), a growing number of research groups are active in the definition of acquisition

protocol for activity monitoring, ergonomic studies, measurement of neurological disorderss,[109] and, more generally, for upper and lower limb kinematic analysis. The strategies applied to reach these targets can be divided into two groups:

(1) Sensors are placed on the body (typically thigh, ankle, foot, trunk, and wrist), and features of their output signals (both in the frequency and time domain) are linked to relevant biomechanical events (e.g., heel strike or toe off), postures (e.g., walking, stairs climbing, laying), or parameters (e.g., gait symmetry), by means of an *a priori* knowledge base, pattern recognition, or data-mining techniques. This strategy has been widely applied for activity monitoring (here, including falling detection), gait analysis, neurological disorder assessment (e.g., tremor),[110] ergonomics,[111,112] posture control, and biofeedback systems).[113–115]

Activity monitoring has historically been one of the first application of accelerometers,[116] leading to the definition of well established and validated protocols and data processing,[117–121] which can count on commercially available systems such as Vitaport2 (Temec, Instruments), or Physilog©.[119] Even though mobility received much attention, activity monitoring was also applied to the upper limb.[122,123]

Considering gait analysis, gait events correlation with accelerometric and gyroscopic signals can be found, for example, in Auvinet *et al.*[124] (which reports gait reference data acquired through accelerometry over 282 people).[119,125–127] Through autocorrelation and frequency analysis, instead Moe-Nilssen and Helbostad[128] and Yack and Berger[129] could assess the symmetry and the stability of gait.

(2) The reconstruction of the complete joint kinematics is searched for, by computing the relative orientation of sensing units placed on adjacent segments. This strategy still presents open problems which are attracting the effort of different research groups. As demonstrated by Giansanti *et al.*,[130] it is not feasible to reconstruct the position and orientation of a rigid body just using accelerometers. In particular, position reconstruction appeared critical. Offset fluctuations (due to temperature and mechanical wear) and the fact that the device measures the sum of body acceleration and gravity are reported as critical factors.[104,107] If accelerometers have to be used as inclinometer (i.e., measuring the roll and pitch with respect to a global vertical axis),[116] the body accelerations must be small compared to gravity, otherwise the computation of the orientation of the sensing axis with respect to the global vertical axis becomes impossible. Luinge *et al.*[104] demonstrated that the accuracy of an inclination estimate can be greatly increased using a Kalman filter and a model of the spectrum of the acceleration.

Similar to accelerometers, Aminian *et al.*,[125] using triaxial gyroscopes, have demonstrated the possibility to compute hip and knee joint angles in the sagittal plane, by combining the detection of gait events with a simple biomechanical model of the lower limb in the sagittal plane. Similarly Najafi *et al.*[131] have demonstrated

the application of gyroscopic systems for computing the trunk tilting. Gyroscopes are, in fact, insensitive to gravity, and the integration of angular velocity can provide variation of orientation. Even more than accelerometers, however, they pose problems of thermal drifting, which must be compensated to obtain reliable measurement. A discussion concerning pros and cons for accelerometric versus gyroscopic systems can be found in Ref. 125.

If both accelerometers and gyroscopes are considered, the complete description of orientation can be obtained (further literature details can be found to this regard in Refs. 132 and 133). After compensating for the thermal drifting of the gyroscopes, in fact, Giansanti and coworkers[107] found it possible to estimate both position and orientation with a system formed by a triaxial accelerometer and gyroscope, for very short activities (stand-to-sit, sit-to-stand, gait-initiation): errors were found lower than 30 mm and 2° during the 4 s acquisitions and lower than 6 mm and 0.2° during the effective duration of a locomotor task. In the aim of obtaining a driftless orientation for longer periods, Luinge *et al.*[105] designed and evaluated a Kalman filter that signals from one triaxial accelerometer and one triaxial gyroscope. In particular, the inclination information was calculated from both the gyroscope and the accelerometer. The Kalman filter used the difference between the inclinations measured by the two sensors, together with an error model, to estimate the orientation and offset errors in a statistical, most-likely manner. These orientation errors and offset errors were then used to correct the orientation and offset at each time-step. To check for the accuracy of the orientation obtained from the inertial sensors through the Kalman filter, this orientation was compared with that measured by a stereophotogrammetric system. The orientation error from the comparison was divided into heading and inclination errors. Results indicated that for acquisitions of 120 s, an orientation drift was still present, due to heading error, which could be drawn back to an incomplete compensation of the thermal drifting in the gyroscopes. For applications in which the heading is important, additional sensors or assumptions are required. For example, biomechanical constraints on the joints between segments can be used.[134] Magnetic field sensors may make the heading observable, but have the disadvantage of being difficult to use near ferromagnetic metals.[105] Roetenberg *et al.*[109] demonstrated that the introduction of a magnetometer in the sensing unit and a compensation algorithm for ferromagnetic material interference allows for accurate and driftless orientation estimations. The compensation resulted in a significant difference ($p < 0.01$) between the orientation estimates with compensation of magnetic disturbances in comparison to no compensation or only gyroscopes. The average static error was 1.4 (standard deviation — 0.4) in the magnetically disturbed experiments. The dynamic error was 2.6 root mean square. Commercial solutions based on sensors fusion are available on the market, for example, through Xsens Technologies (Enschede, The Netherlands) and InterSence Inc. (Burlington, MA).

Current research appears to be focused on development of even more sophisticated Kalman filtering technique specifically designed for human movement

analysis,[98] development of new systems for position and orientation sensing in long-term acquisitions,[97] and finally, on the design of protocols for upper and lower limb kinematics and dynamics analysis. To this regard, one of the main problem to solve is to link relevant anatomical systems of reference to the local sensing units embedded frames. Possible solutions appear to be the application of functional methods[12,135] and postural calibration methods as discussed in Refs. 134 and 136. Considering motion analysis application, the assessment of acquisition accuracy for the specific protocol is recommended. To this regard, Cutti *et al.*,[137] have recently proposed a simple method for determining the static and dynamic accuracy of inertial sensors systems explicitly considering the problem of estimating the relative kinematics between sensing units and the dependence of inertial sensors systems accuracy on the task performed (e.g., due to problems related to acceleration profiles).



## 3. Applications

### 3.1. *Soft tissue artifacts: Quantification and compensation*

The description of joint kinematics during daily living activity is the main aim of human motion analysis. Stereophotogrammetry allows for the reconstruction of the trajectories of markers or fixtures, on which markers are mounted, attached to the skin of the body segments to be analyzed. These trajectories are used to calculate the pose of the underlying bony segments, with the erroneous assumption that markers and bony segments are rigidly connected. It is well known that markers on the surface of the body move with respect to the underlying bones because of the interposition of soft tissues. This interposition is the origin of two different sources of error: anatomical landmarks misplacement and STA. The latter has been recently recognized to be the major source of error in human motion analysis.[68] Because of its origin STA is necessarily associated to the specific marker-set and experimental protocol adopted. Inertial effects, skin deformation and sliding, gravity and muscle contraction interdependently contribute to this phenomenon. This artifact has a frequency content similar to that of bone movement and is therefore not possible to distinguish between them by means of any filtering technique. A quantification of STA is thus necessary in order to critically consider motion analysis results and indications for the clinical decision process, and to develop methods for STA compensation to improve bone pose estimation accuracy.

#### 3.1.1. *Upper limb*

As already pointed out, one of the main problems in the acquisition of accurate kinematic data with motion analysis systems based on skin-mounted sensors is the rigid component of the STA. Considering the upper-extremity, Schmidt *et al.*[138] and Cutti *et al.*[139] quantified it for axial rotations of forearm and humerus, these being the movements most affected.[67]

In their study, Schmidt and co-authors defined two clusters of three markers, one on a cuff wrapped around the distal forearm and one on a rigid plate on the hand. Based on anatomical landmark calibrations, they defined systems of reference for forearm and hand, resulting in a joint coordinate system for the wrist. The hand system of reference was assumed as being able to provide the exact amount of prono-supination (Pr/Su) when the wrist was straight. On the contrary, the forearm cluster was assumed to be affected by the artifact. Consequently, the artifact was measured as the apparent wrist internal–external rotation during forearm Pr/Su, i.e., the apparent rotation of the hand with respect to the forearm. Over 10 subjects, the artifact led to high underestimations of the Pr/Su, ranging from 17% to 43%.

In Ref. 139, the artifact during humerus In/Ex was assessed, together with the influence of humerus orientation and elbow flexion on it. Three clusters of four markers were attached on the thorax, humerus, and forearm of six subjects. Bone embedded systems of reference and joint coordinate systems were defined following the International Shoulder Group recommendations. In particular, for the humerus two systems of reference were considered. The former, referred to as H1, was entirely based on anatomical landmarks calibrated with respect to the humerus cluster of markers: H1 was therefore affected by the artifact to be measured. The other system of reference, H2, was computed from the orientation of the long axes of humerus and forearm. This property and the development of an *ad hoc* processing algorithm, allowed to consider H2 to be almost artifact-free, thus providing the gold-standard for the measurement of the In/Ex. Subjects were acquired while performing cyclical humerus axial rotations while flexing–extending the elbow, in 12 different orientations of the humerus with respect to the thorax. The artifact was found to be a constant fraction of the In/Ex performed, ranging from 21% to 48% (best and worst case for the set of subjects). Humerus orientation and elbow flexion comparably affected the artifact, with coefficients of variations from 2.38% up to 16.44% for humerus orientation and from 3.65% up to 14.43% for elbow flexion. If both effects are neglected, the average artifact ranged for the subjects from 25% up to 45% with limited coefficients of variations (less than 11%), mostly due to a compensatory effect between elbow flexion and humerus orientation (Fig. 9).



Given the entity of the artifact, compensation techniques were searched for Schmidt and co-workers, based on the same method applied for assessment, proposed a technique for compensating the artifact during Pr/Su. The percentage factor which estimated the artifact was used as a multiplicative factor for correcting the angular measure obtained from the forearm cluster in a generic task, during which the wrist cannot be usually maintained straight and thus the hand cannot provide a reliable measure of Pr/Su.

Cutti and co-workers, instead, focused on the compensation of the humerus axial rotation. The proposed technique, firstly validated *in vitro*,[140] then *in vivo*,[141] was based on the use of the H2 definition for the humerus. As stated above, this system of reference is almost "artifact free"; however, being its definition based on the orientation of the humerus and forearm long axis, it results kinematically

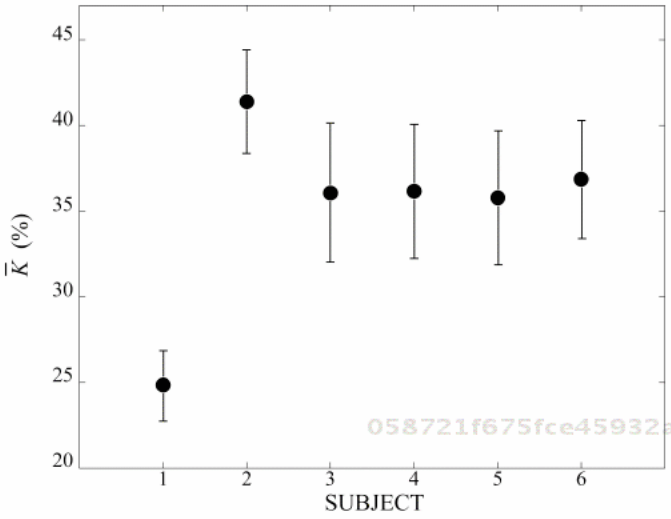




Fig. 9. Artifact magnitude ($K$) during humerus internal–external rotation: mean (±1 standard deviation) value among all the humeral orientations and elbow flexion–extension angles for all the six subjects examined in Ref. 139.

coupled with the elbow orientation. This means that an elbow Fl/Ex or Pr/Su induces an apparent variation of the humerus In/Ex. An algorithm, suitable for real-time applications, was designed to solve this problem. The *in vivo* validation involved six healthy subjects who performed five arm-movement tasks with different combinations of elbow Fl/Ex and Pr/Su. All takes were executed with the humerus as steady as possible. In this particular pose, the axial rotation measured by the humerus system of reference H1 could be assumed as the gold-standard. For each task the similarity between the gold standard pattern (of H1) and the axial rotation pattern of H2 before and after the application of the compensation algorithm was evaluated; the similarity was assessed computing three parameters, which quantify differences in the explained variance, gain, phase, and offset. In addition, the RMSE between the patterns was used as a global similarity estimator. Results showed that before application of the algorithm, patterns were almost uncorrelated, opposite in phase, different in gain, with a high offset and a RMSE averaged over the tasks of 9° (Fig. 10). After the application, for four out of five tasks, patterns were highly correlated, in phase, with almost equal gain and limited offset; the mean *RMSE* decreased to 3°.



Limited efficacy of the technique was found only for compensating the effects of the pure Pr/Su on the kinematic coupling. However, these effects were found to be limited and avoidable by computing the long axis of the forearm with a functional method.[135,142]

Finally, Roux and co-workers[143] applied to the upper extremity the Global Optimization technique proposed by Lu and O'Connor.[144] This is an optimization method for the determination of the positions and orientations of multi-link

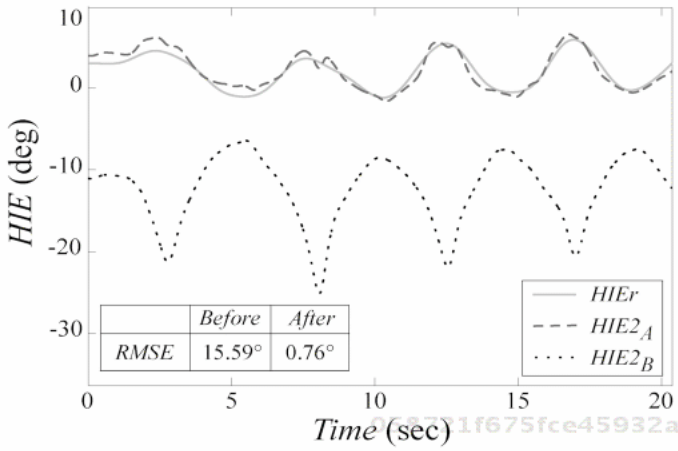


Fig. 10. Example showing the decoupling of the humerus axial rotation measured by H2 from the elbow flexion–extension. The real internal–external rotation pattern (HIEr) is compared to the one obtained from H2 before (HIE2A) and after (HIE2B) the application of the algorithm proposed in Ref. 141.

musculoskeletal models from marker coordinates. It is based on the minimization of the weighted sum of squared distances between measured and model-determined marker positions; the model imposes joint constraints. After defining an upper limb model, Roux *et al.*[143] validated the technique in simulation, by compensating for an imposed artifact over humerus In/Ex and forearm Pr/Su movement. Results reported showed a significant reduction of the artifact.

### 3.1.2. *Lower limb*

Given the importance of the functional integrity of the lower limbs for the human locomotor system, motion analysis was largely applied for the quantification of their biomechanics, producing a number of studies quantifying the motion and loads at the hip, knee, and ankle joints during the execution of various activities in healthy and pathological subjects.

STA was recognized to be extremely critical with respect to the reliability of the lower limbs motion data, thus several studies have been performed to quantify the motion of skin markers with respect to the underlying bony segments using intra-cortical pins,[145–155] external fixators,[67,156] percutaneous trackers,[64,157,158] and Roentgen photogrammetry.[159–161] All these attempts to quantify STA have important limitations. Intracortical pins, external fixators and percutaneous trackers provide a reliable measurement of bony segment motion, but they limit and alter skin motion. Methods exploiting Roentgen photogrammetry, either X-ray pictures or fluoroscopy, do not limit skin motion, but they do not usually allow for a full 3D tracking of skin markers. Even when 3D trajectories[161] can be estimated, the very limited fluoroscopic field of view confines the trackable markers to small

areas around the joints. In particular, X-ray pictures allow for the description of STA in 2D only and in static conditions and not during the execution of motor tasks. The wide range of techniques used, the different motor tasks analyzed, and the limitations observed in these experiments are likely to have caused the large discrepancies reported in these studies.

In order to overcome all these limitations STA was quantified on the thigh and shank combining traditional stereophotogrammetry with modern 3D-kinematics reconstruction from fluoroscopic images.[162] This technique gave a description of STA in unconstrained skin conditions and during the execution of motor tasks typical of daily living. The extent to which STA propagates to knee rotation angles was also assessed in order to determine the effect of STA on relevant kinematic variables routinely reported.

According to Stagni *et al.*,[162] all shank markers exhibited almost the same amount of displacement in the three directions during the execution of different motor tasks. Displacement of skin markers in the corresponding anatomical frames is generally larger on the thigh than on the shank. In general, STA is both subject- and task-dependent[153] (see Fig. 11).

The evaluation of STA propagation to knee rotations demonstrated that joint kinematics evaluation is strongly affected by the choice of the cluster of markers. In particular, while STA propagation to the Fl/Ex angle is limited, the measure of In/Ex and Ab/Ad in particular can be invalidated by RMS errors up to 117% and 192% of the corresponding range, respectively. The differences in the way of propagation demonstrate the subject- and task-specificity of the phenomenon,

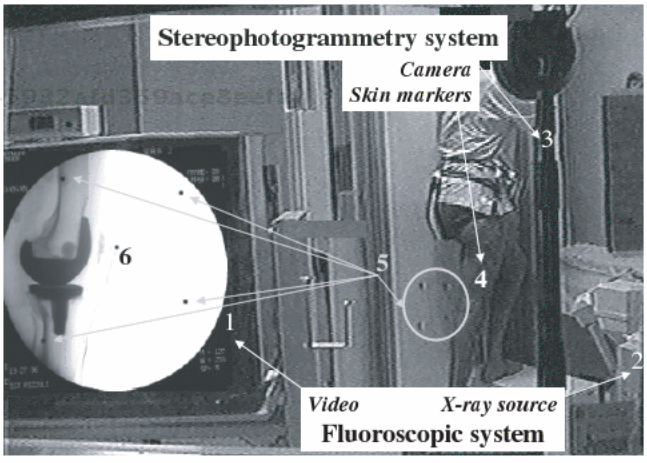


Fig. 11. Experimental setup. (1) Real-time visible feedback of the fluoroscopic images acquired; (2) X-ray source of the fluoroscope; (3) one of the five cameras of the stereophotogrammetric system; (4) skin markers on the lateral aspect of the thigh and the shank; (5) the four specialized radiopaque/reflecting markers for spatial registration; (6) the specialized radiopaque/reflecting marker for temporal synchronization.[162]

but the criticality of the propagation of STA to In/Ex and Ab/Ad is common to subjects and motor tasks, and can nullify the usefulness of these measurements in the interpretation of gait analysis data.

These results are difficult to compare with those reported in the literature because of the different techniques used, the large variability in the subjects analyzed, the different motor tasks performed and the location of the skin markers. Most of other studies reporting quantification of STA have analyzed walking and running using external fixators,[156] or intracortical pins[150,154,155] or percutaneous trackers,[64,157,158] or peculiar non-daily living motor tasks using intracortical pins.[146,149] or Roentgen photogrammetry.[161] All the studies using external fixators, intracortical pins, and percutaneous trackers reported STA up to 20 mm,[153] thus much smaller than the ones reported by Stagni *et al.*[162] Nevertheless, STA measured using Roentgen photogrammetry[161] was up to 42 mm only in the sagittal plane for a marker placed on the distal thigh (Fig. 12). This result supports the hypothesis that pins or fixators strongly limit the realistic quantification of STA during daily living activities. Moreover, the motion of skin markers of these studies was not quantified in those positions which have been shown to be the most, such as the proximal–posterior area of the thigh. The hypothesized limitation to STA given by



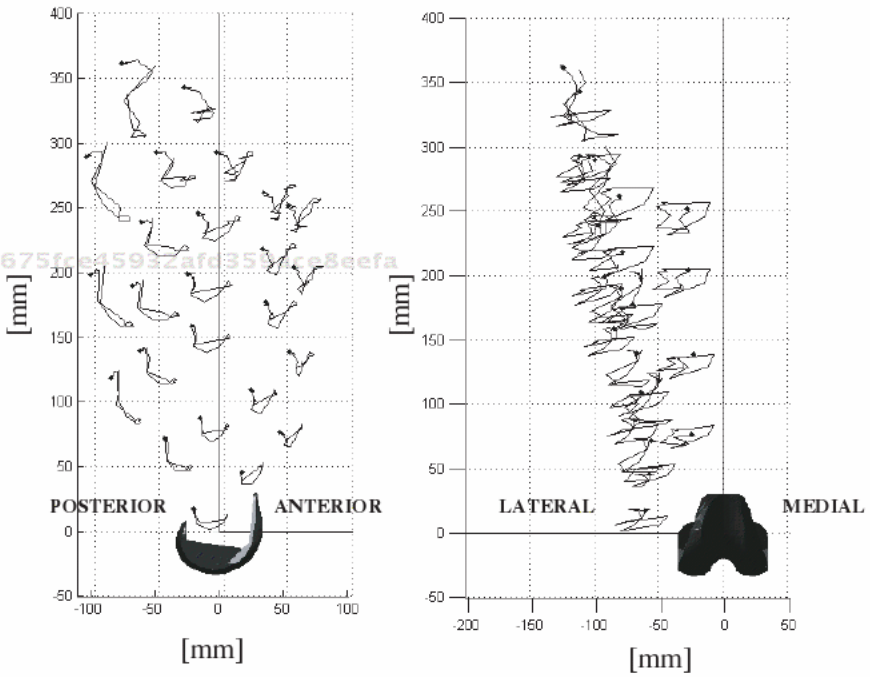


Fig. 12. Sagittal (left) and frontal (right) view of skin marker trajectories in the corresponding bone-embedded anatomical frames for the thigh, for subject #2 during the execution of STS motor task. The varying shade of gray of the trajectory of the marker represents the time-flow from sit (black) to stand (dark gray) and back to sit (light gray).[162]

the use of pins or fixators justifies also the smaller error propagated to knee rotations reported in these studies (i.e., 10% on Fl/Ex, 20% on Ab/Ad, and 100% on In/Ex[67]). Although these differences, the criticality of STA propagation to Ab/Ad and In/Ex with respect to Fl/Ex is in agreement with Ref. 162. Finally, when different motor tasks were analyzed the STA was assessed to be task-dependent as reported in the present study.

Stagni *et al.*[162] pointed out that no precise indication can be given for careful positioning of the skin markers in order to limit STA propagation to knee rotations. The small sample of analyzed subjects did not allow for large generalization of the results of STA propagation to knee kinematics. Anyway, the extremely different behaviors observed even in those two subjects suggested that not even the amount of STA is a good indication of its effect on knee rotations. The amplitude of STA in subject #2 was larger than in subject #1, but its propagation to knee rotations was less critical. This can be explained observing how STA affects the orientation of the cluster with respect to the underlying bony segment: larger deformations on skin marker clusters do not necessarily correspond to larger changes in the skin–bone relative orientation. The only possible general suggestion is not to position the thigh cluster in the proximal area of the thigh.

In conclusion, regarding the quantification of STA on the lower limbs, whereas the calculation of Fl/Ex at the knee by means of external markers can be considered acceptably reliable, this is not true for In/Ex and Ab/Ad. In order to improve the performance of stereophotogrammetry-based human motion analysis, devising validated STA compensation methods is felt necessary. This compensation method should take into account the STA characteristics of the specific subject and motor task.

Several such methods have been proposed in the literature. STA can be considered as the sum of two contributions: deformation of the surface marker cluster and the rigid displacement of the cluster with respect to the underlying bony segment. Some of the proposed compensation methods take into account only the former.[163–165] Their performance in the estimation of the bone pose is comparable with a least squares optimization of the marker cluster position and orientation.[166] Other methods are aimed at coping also with the rigid displacement of the cluster with respect to the underlying bone. Lu and O'Connor,[144] rather than seeking optimal rigid body transformation on each segment of the lower limb individually, imposed model-based constraints to the joints connecting each couple of segments. The implementation proposed assumes the simple ball and socket constraint for each joint and it is therefore not subject-specific and thus not suited for the study of pathologies or joint prostheses. This kind of global approach was assessed to provide smooth curves but still erroneous curves for joint rotations. With a similar approach, a biomechanical model of the human body has been used to minimize the distances between marker 2D projections on the TV camera planes and the corresponding back projected markers located on the body.[167] Estimation of the model parameters for each specific subject is not straightforward, joints are still assumed as elementary kinematics pairs, and computer simulation was only performed for validation.

Another category of methods is aimed explicitly at detecting STA effects from the specific subject under analysis. The dynamic calibration technique[168] uses *ad hoc* movements, to be performed by the subject, to characterize the specific STA and to determine the correlation between flexion–extension joint angles and surface marker displacement in a bone-embedded frame. The technique is time-consuming both for acquisition and elaboration of the additional movements, and it is too demanding for routine human motion analysis. The multiple landmark calibration method[169] recommends a double calibration of the anatomical landmarks at the two extremes of the expected range of motion. The positions of anatomical landmarks between these configurations are calculated by linear interpolation in time. This technique is subject-specific, not time-consuming, and has a very simple implementation. However, it was observed[170] that its major limitation is the linearity assumption, as it does not take into account the true dependence of the STA on the motion pattern during the execution of the motor task.



An evolution of the original multiple landmark calibration method[169] for STA compensation was proposed[171] with Fl/Ext angle interpolation, and its performance was assessed *in vivo* at the knee joint on experimental data of real and known STA. The analysis performed on two subjects and three different motor tasks showed that the new method significantly improved the reliability of the calculated knee joint angles, in particular of Ab/Ad and In/Ext angles, that are in general the most critically affected by STA. The most important improvement produced by the proposed double calibration was on the calculation of joint translations, traditionally considered not reliable when obtained from optoelectronic stereophotogrammetry. Compensated translations were very close to the fluoroscopy-based gold-standard. In particular, the AP translation, which is the most relevant in certain clinical decision processes,[172] was found to have a residual mean value of the RMSE in percentage of the range lower than 14%. The extremely good performance in the calculation of knee translations is also the main improvement introduced by the new double calibration with Fl/Ext angle interpolation with respect to the previously proposed one,[169] based on time interpolation (Fig. 13). No relevant further computational time is required by the implementation of the double calibration procedure.



It was assessed[171] that the main contribution of the double calibration to the compensation of STA was given by the interpolation of the position of the ALs in the technical frame, rather than the interpolation of the shape of the cluster. This shows that the most critical source of error is the rigid motion of the cluster with respect to the underlying bone, rather than the relative deformation of the cluster itself. Thus, any compensation method taking into account only the deformation of the cluster is not expected to perform significantly better than a simple least squares minimization algorithm. Finally, the double calibration with Fl/Ex angle interpolation was assessed to be still effective when ALs misplacement is present on the thigh and shank.[173]

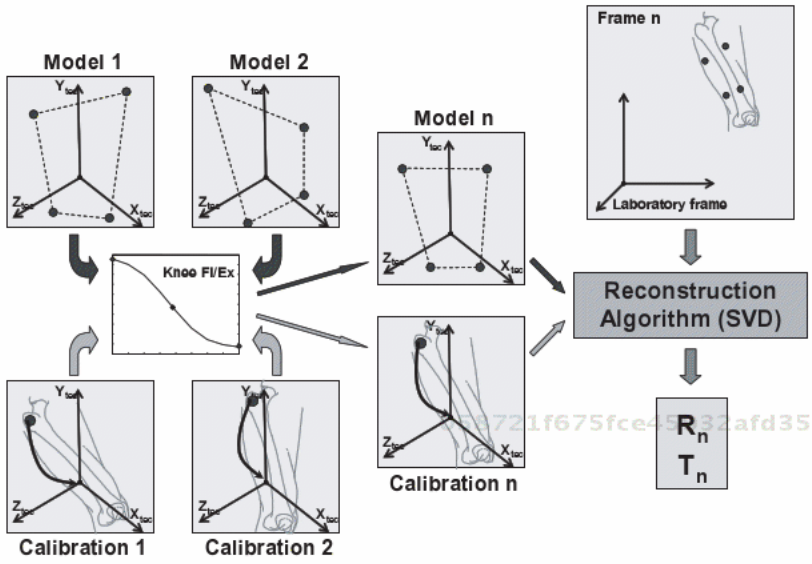


Fig. 13. Sketchy representation of the double calibration approach based on the flexion–extension angle interpolation.[171]

### 3.2. *Joint modeling*

The knee is a key joint of the human locomotor system. The restoration of its function is of fundamental clinical interest, regarding both joint replacement and surgical reconstruction of the main anatomical structures. This interest is demonstrated by over 8 million of injury-related visits for knee symptoms (physicians and emergency room), 381 000 total knee replacements and 12 000 other repair of cruciate ligaments performed in the United States in 2002, as reported by the American Association of Orthopaedic Surgeons (AAOS), and the 16 743 total knee replacements performed in Italy in 1998 according to data of the Italian Health Ministry. An accurate knowledge of the mobility and stability of the whole articular structure, as well as of its different anatomical structures, is a fundamental prerequisite for the development of effective reconstructive surgery, new prosthetic designs, and new rehabilitation procedures. The need for this deeper knowledge led to a bulk of *in vitro*[174–177] and *in vivo* studies,[178,179] which allowed to clarify several aspects of the physiological behavior of this complex joint.

The *in vitro* testing explained the kinematics of the knee: it is a joint with 1° of unresisted freedom; its motion is described by a mobile instantaneous helical axis, which moves forward in extension and backward in flexion.[174,176,177]

The cruciate ligaments were, moreover, assessed to guide the motion. They maintain articular surfaces just in contact, while articular surfaces keep the cruciate ligaments just tight and almost isometric along the range of motion.[175] Other ligaments stabilize the joint; they restore the proper tensioning of the cruciate ligaments when external loads are applied. *In vitro* testing allows to directly

observe and measure different aspects of joint mechanics, but not in physiological conditions. During its normal function, the knee lets the shank move with respect to the thigh, maintaining the stability of the structure under articular load and torque. These are the result of several contributions: the intersegmental contact load, ligament tensioning, loads applied by muscles, and the inertia of body segments. All these contributions are strongly dependent on the analyzed motor task, as well as on the physical characteristics of the subject. Thus, if we want to quantify the contribution of each anatomical structure in determining the physiological function of the knee, modeling is the only possible solution, as direct measurements cannot be performed.

The problem of knee modeling has been approached at different levels of complexity.

Bidimensional models were designed in order to investigate the role of the cruciate ligaments in simple conditions, such as isometric quadriceps contraction (Fig. 14).[181–184] Three-dimensional models, including articular surfaces and ligaments, were also designed. Even these more complex models were applied in conditions far away from those of the physiological knee.[185–189] The natural evolution of this approach is inserting the model into a context, which allows to evaluate the boundary conditions of the knee-structure during the performance of a simple task of daily living.[190] A "macro-model" like this, which includes not only the anatomy of the knee (articular surfaces, cartilage, ligaments) but also how other body segments and muscles stress it in physiological conditions, should consider several anatomical and mechanical aspects. Moreover, it should try to take into account the effect of error sources, which could alter the results, even in the unavoidable mathematical simplification.

Concerning anatomical definition, the geometry of articular surfaces should be reconstructed. This can be done calculating a three-dimensional model of the bone segment from Computer Tomography or Magnetic Resonance imaging.[180,191,192]



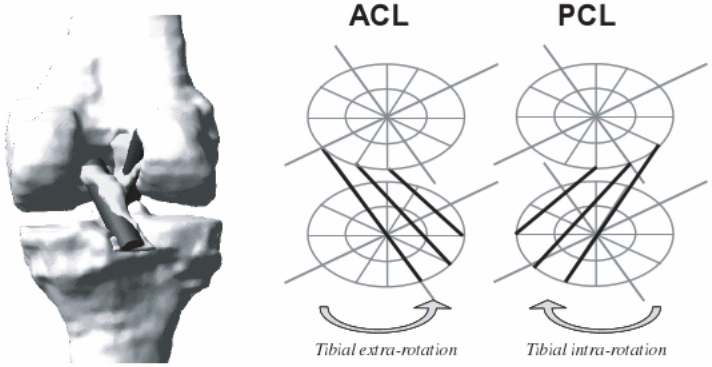


Fig. 14. Modeling sketches for the cruciate ligaments.[180]

The position and geometry of ligaments and muscles insertions should be correctly mapped too. This can be done through the three-dimensional reconstruction of segmented soft tissues, obtained with Nuclear Magnetic Resonance, which has to be properly registered with data obtained with other imaging techniques (computer tomography, fluoroscopy, stereophotogrammetry).[193–195] Moreover, the lines of action of the main muscular groups, and how they change during the execution of the motor task, have to be defined. The solution for this problem was described for the upper limb as based on the morphological description of the muscle bellies.[196–198] Concerning the definition of the mechanics of the structure, ligaments have to be modeled. Their fibers are traditionally represented with nonlinear springs, working in parallel, paying particular attention to geometrical distribution.[188,191,199–202] A model of the muscular actuators has to be defined too. It should allow determining the load applied by each muscle.



A modified Hill model (Fig. 15) was usually applied for this purpose.[203] More complex models, which better describe muscle physiology, are certainly possible, but the higher complexity does not usually lead to meaningful better performance.[204] The description of the intra-articular contact is part of the mechanical characteristics of the joint too. In order to simplify the problem, it can be modeled as a punctual contact between two rigid bodies, which can then be modified in order to take into account the thickness and the mechanical behavior of the cartilage.[200] A model built according to these criteria can be used to quantify the role of the different anatomical structures, once the joint kinematics is known during the chosen motor task. In order to limit error sources, the relative kinematics between the femur and the tibia–fibula should be reconstructed with an accuracy, which can be obtained from cine-fluoroscopic images, when the geometry of bony segments is known.[72,205,206]

The calculation of loads can be performed solving a direct dynamics problem, when the kinematics is known and the model defined.[190,207] This approach does not control, but, through serial integration, amplifies errors, which are superimposed on several inputs. On the other hand, when ground reaction forces are known, the solution can be found through an inverse dynamics problem,[208,209] in order to exploit data redundancy and to better control the model.



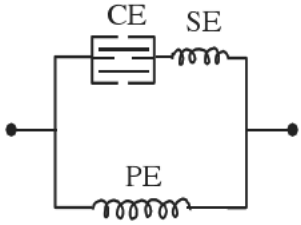


Fig. 15. Hill model for the muscle.

### 3.3. *Kinematic analysis of the upper extremity*

In the following two sections, examples of kinematic analysis of the upper extremity are presented. In the former, it is shown how movement analysis can help assessing both upper-extremity amputees while using their myoelectric prosthesis and the prosthesis itself, with implications for physical therapy and for prosthesis development. In the latter example, a kinematic analysis of a post-surgical patient treated for shoulder instability is reported. The analysis allowed an in-depth study of the evolution of the patient's compensatory movement with implications for his rehabilitation program.

#### 3.3.1. *Assessment of an above-elbow amputee and his innovative prosthesis*

Through stereophotogrammetric systems it is possible to acquire the 3D joint kinematics of a patient while performing everyday activities. These data, combined with a biomechanical model of the anatomical structures under investigation and clinical rating scales, can form the basis for an objective assessment of the patient motor ability. When the subject acquired is an amputee fitted with a new prosthetic arm, the information provided can be useful not only for the practitioner but also for the prosthesis designer. The aim of this work was to give an example of this kind of clinical/technology assessment, presenting the case study of a young trans-humeral amputee fitted with the first prototype of an innovative myoelectric elbow. In particular, the analysis was intended to quantitatively evaluate:

(1) the kinematic performances of the electro-mechanic elbow, when controlled *in vivo* by the patient EMG signals;
(2) how the patient controls the prosthesis, in order to identify critical movements and prevent potential disorders.



##### 3.3.1.1. Subject description and prosthesis setup

The subject involved in the experimental sessions (after giving his informed consent), was a young adult (initials G. F.) who underwent the first proximal trans-humeral amputation in 2003 due to a work-related trauma. By the time of acquisition he had been using the prosthesis for four months. G. F. controlled the elbow Fl/Ex with contractions of the trapezius and deltoid, respectively.

##### 3.3.1.2. Motion analysis protocol and data analysis

G. F. was acquired with a VICON 460 stereophotogrammetric system (Vicon Motion Capture, Oxford, UK) with six video cameras, while performing five elbow Fl/Ex trials with different loads on the hand: 0 kg, 0.52 kg, 1 kg, 2 kg, and 3 kg. For every trial, at least two consecutive Fl/Ex cycles were repeated. To analyze the electro-mechanic elbow performances, the relative motion of the forearm with respect to the third distal had to be tracked. Since G. F. engaged the elbow with

contractions of trapezius and deltoid, possible critical movements could arise from excessive motion of the head and shoulder girdle, leading to early deterioration of the sterno-clavicular, acromio-clavicular, and scapulo-thoracic joints (hereinafter referred together as the "shoulder"), and cervical rachis problems. Given these considerations, 20 retro-reflective markers were attached on the head, thorax, socket, third-distal, and forearm, thus defining an open kinematic chain with seven active degrees of freedom (Figs. 16(a) and 16(b)), associated to the neck, shoulder, and elbow joints. To define the mobility of these joints, a system of reference (SoR) had to be defined for each segment. For the head, thorax and shoulder girdle these were obtained through the "calibration" of relevant anatomical/prosthetic landmarks with respect to the correspondent cluster of markers.[10,57,136,139,210] For the definition of the third-distal and the forearm SoR, we combined the use of well-identifiable landmarks, with a functional, optimization-based method,[30] which enables to compute the real axis of rotation of the elbow (Fl/Ex) and of the hand (Pr/Su).[135,136] Joint angles were then obtained decomposing the relative orientation of adjacent segments using appropriate sequences of Euler angles: FL/Ex and Pr/Su for the elbow, Fl/Ex, lateral flexion (LF), and axial rotation for the neck and protraction–retraction (Pr/Re) and elevation–depression (El/De) for the shoulder.

Using the shoulder angles and their first derivative, we identified in each trial the following phases: elbow flexion, transition from flexion to extension, and elbow

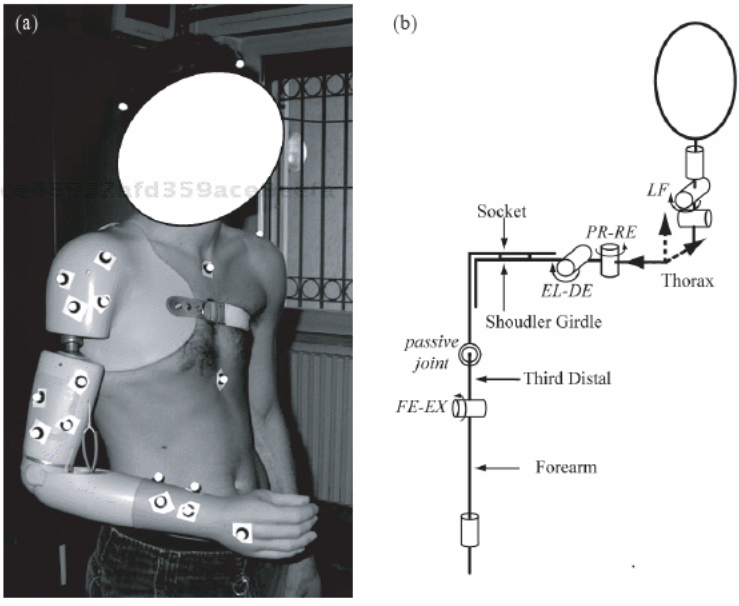


Fig. 16. (a) Marker-set used: markers on the left acromion and the hand are used for visualization purposes only. Not visible in the figure: markers on the 7th cervical and 8th thoracic vertebra and on the left and posterior part of the head; (b) kinematic model of the amputee with the prosthesis.

extension. In each phase, the head, shoulder, and elbow patterns were analyzed in terms of excursion and velocity.

3.3.1.3. Elbow performance

Elbow Fl/Ex patterns for the different loads tested are shown together in Fig. 17. Given the high level of repeatability found in the gesture, only one representative

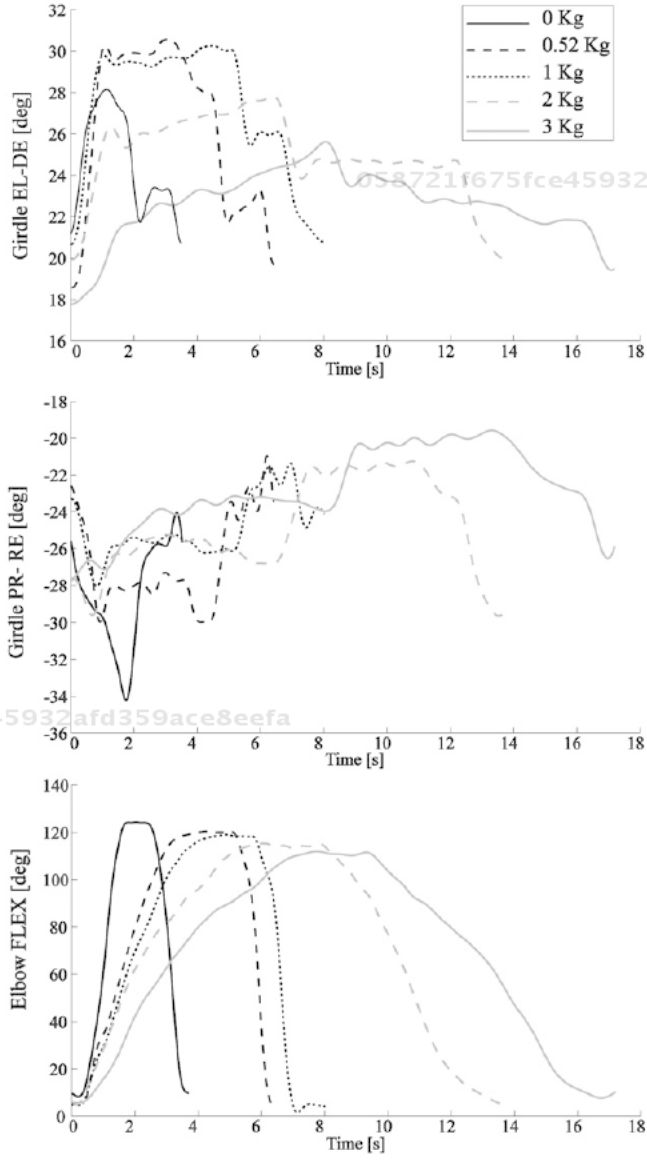


Fig. 17. Shoulder girdle elevation–depression (top), protraction–retraction (middle), elbow flexion–extension (bottom) for the different loads tested.

curve among the repetitions is reported for every load. The mean range of elbow Fl/Ex observed was 115° (coefficient of variation: 4%), which decreased of about 11° changing the load from 0 to 3 kg. The minimum elbow extension ranged from 2° (1 kg) to 8° (0 kg), while the maximum flexion from 112° (3 kg) to 126° (0 kg). For the 0 kg condition, the mean velocities reached in flexion was 77.4°/s; this decreased to 14.8°/s for 3 kg. The mean velocities in extension was 88°/s for 0 kg and 19°/s for 3 kg. The range of motion measured resulted smaller than that of an able-bodied subject (140°–150°) but for light loads, it appeared to be adequate for most feeding activities.[211] The results obtained were reported to the prosthesis developers who could compare them with similar results obtained from *in vitro* tests.

#### 3.3.1.4. Subject movements for prosthesis control



The macroscopic effects of the trapezius (for flexion) and deltoid (for extension) contractions are reported in Fig. 17: the elbow flexion appears to be activated by a shoulder elevation and retraction, while the extension by a shoulder depression and protraction. An exception was the slight girdle protraction for elbow flexion with 2 and 3 kg, which was however followed by a higher protraction for extension. Shoulder motion usually ranged from 11° to 8°, both for El/De and Pr/Re, generally tending to decrease with the increase of the load. While the shoulder motion tended to decrease, with increasing loads the duration of the contraction tended to increase, almost doubling from 0.52 to 2 kg. The elbow Fl/Ex was also followed by 8°–12° of LF of the head toward the shoulder during flexion.

The characteristic of the gesture recorded (frequent, incongruous, asymmetric, and repetitive), suggest a monitoring of the patient for cumulative trauma disorder syndromes, which may lead to irritation of the tendinous and peritendinous structure and chronic muscular fatigue. This latter problem may also result in a decrease in the quality of the EMG signals acquired by the prosthesis sensors.



### 3.3.2. *The evolution of compensation strategies in a patient with shoulder instability*

As soon as patients who underwent surgery for shoulder instability begin active mobilization, a reduced shoulder range of motion (RoM) and an altered scapulo-humeral rhythm can be observed. In particular, an abnormal kinematics of the shoulder girdle (defined as the fictitious segment connecting the sterno-clavicular with the gleno-humeral joint), is generally evident during arm elevation, involving range and/or timing of El/De and Pr/Re. One of the target of rehabilitation is therefore the recovery of an adequate shoulder RoM while trying to remove these compensatory movements. To this regard, unfortunately, the usual clinical rating scales for assessment of shoulder impairment, i.e., Constant and ASES,[212] do not provide full support to monitor the results of the rehabilitative intervention. In fact, even though recording information about the overall shoulder mobility, they do not describe the compensation strategy. Quantitative motion analysis with

extraction of kinematic indexes appears to be a possible solution to overcome these limitations.[213,214] The aims of this section are therefore: (1) to present a simple motion analysis protocol for monitoring the girdle compensatory movements in patients with shoulder impairment; (2) to report and discuss the case study of a post-surgical patient treated for shoulder instability, assessed integrating the Constant scale with the motion analysis protocol.

#### 3.3.2.1. Motion analysis protocol

The motion analysis protocol was intended to quantitatively assess, e.g., through a stereophotogrammetric system, the RoM and the coordination between shoulder girdle and humerus motion during four activities of the Constant scale: hand-behind-head and full shoulder flexion in the sagittal plane, hand-to-top-of-head and full shoulder adduction in the frontal plane. The patient had to be acquired while performing the activities after one and three weeks of active/active-assisted mobilization (AQ1, AQ2). Assuming the shoulder of one side of the body unimpaired (i.e., as the subject-specific gold-standard), in each acquisition each activity had to be repeated five times, firstly with the right and then with the left arm. From the biomechanical viewpoint, being interested in the orientation of the shoulder girdle with respect to the thorax and of the humerus with respect to the shoulder girdle, upper arms were modeled as open kinematic chains each formed by three segments (thorax in common, shoulder girdle, and humerus), with five degrees of freedom: two describing the mobility of the shoulder girdle,[213] and three of the gleno-humeral joint (Fig. 18). The thorax and humerus bone embedded systems of reference (SoR) were defined following the ISG recommendations[1]: H1 for the humerus; $z$ axes pointing backward. For the (right) girdle, the $x$ axis was assumed from IJ to GH, the $z$ as the cross-product of $x$ and the $y$ axis of the thorax and the $y$ consequently. Through a static trial at the beginning of AQ1 and AQ2, the girdle and humerus SoRs were then reoriented in order to be parallel to that of the thorax when the subject stood in the upright position, arms along the body, neutral pronation: in this posture, therefore, all joint angles were zero. The axes of the left side SoRs were oriented to give rise to joint angles with the same sign of the right side. Joint angles were obtained decomposing the relative orientation of adjacent segments using appropriate sequences of Euler angles: Pr/Re and El/De for the shoulder girdle, Fl/Ex, Ab/Ad, and In/Ex, or Ab/Ad, Fl/Ex, and In/Ex for the gleno-humeral joint during almost sagittal and frontal tasks, respectively. In order to track the segments SoR during motion with a stereophotogrammetric system (Vicon 460, six cameras), four markers were placed on the thorax anatomical landmarks, while four on the humerus of each side to form a technical cluster (Fig. 18(b)). Anatomical calibrations were then performed as described in Ref. 139.

For both AQ1 and AQ2, for each activity and side, the RoM of shoulder girdle and gleno-humeral joint were computed, as well as the angle–angle plots describing the coordination between the girdle degrees of freedom and the gleno-humeral

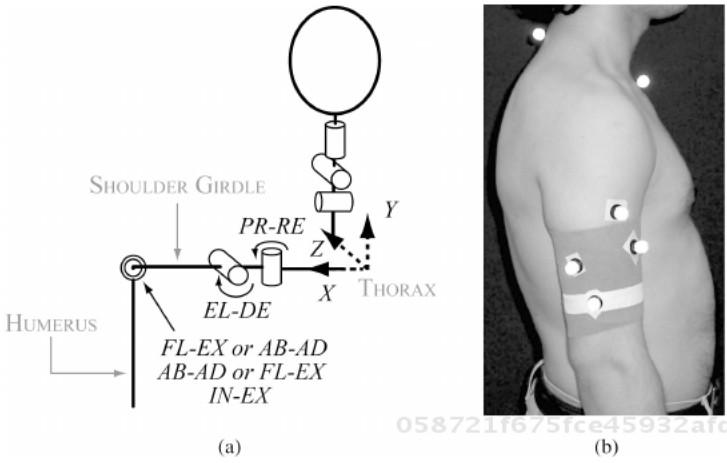




Fig. 18. (a) Open kinematic chain modeling the right arm and (b) marker-set used. Markers on the xiphoideus process (PX) and in the 8th thoracic vertebra (T8) are not visible.

ones.[213–215] Corresponding angle–angle plots from AQ1 and AQ2 for the impaired and sound sides were then superimposed to check for the evolution in the girdle–humerus coordination of the impaired shoulder in time and with respect to the unimpaired one.

3.3.2.2. Patient description

A 21-year-old man, initials E.G., participated in the study, after signing an informed consent. E.G. underwent an arthroscopic surgery at the left shoulder with capsula repairing and plications for an instability following recurrent episodes of scapulo-humeral dislocation in the past three years. He was acquired with the motion analysis protocol, as well as clinically assessed with the Constant (for impairment) and DASH[216] (for disability) rating scales the same day of the two acquisitions. The clinical questions we had to answer were, whether the active and active-assisted mobilization followed by E.G. was effectively (1) increasing the shoulder RoM, (2) restoring a girdle–humerus coordination consistent with the right unaffected side, and (3) the level of disability was decreasing.

3.3.2.3. Results

The Constant scales for the patient's impaired side in AQ1 and AQ2 are reported in Table 1(a), evidencing a good improvement, mostly due to an increased RoM. The DASH scale remained almost unchanged, decreasing from 26.66 to 25.83, mostly due to the impossibility to practice the usual sport, to lift loads, and to sleep without pain. The motion analysis acquisitions confirmed the overall RoM improvements of the gleno-humeral joint (Table 1(b)). In addition, the angle–angle plots brought in evidence the kinematic patterns of the girdle with respect to the humerus motion.

Table 1. (a) Constant scales for E.G. I1 and I2 refer to the impaired side in AQ1 and AQ2, respectively. U refers to the unimpaired side. (b) Gleno-humeral RoM. For the hand-to-top-of-head task the AB–Ad and FL–Ex angles are reported. A reduction in this latter indicates a more frontal (i.e., better) execution of the task. Sagittal hand-behind-head RoM is included in the forward elevation activity.

(a)

| | E.G. | | |
|---|---|---|---|
| Item | I1 | I2 | U |
| Pain | 10 | 10 | 15 |
| Activity level | 0 | 4 | 10 |
| Positioning | 2 | 8 | 10 |
| Forward Elev | 4 | 6 | 10 |
| Lateral Elev | 4 | 6 | 10 |
| External Rot | 2 | 4 | 10 |
| Internal Rot | 6 | 10 | 10 |
| Power | 1 | 4 | 8 |
| Score | 29 | 52 | 93 |

(b)

| | E.G. | | | | | |
|---|---|---|---|---|---|---|
| Activity | I1 | | I2 | | U | |
| Forward Elev | 99° | | 121° | | 179° | |
| Lateral Elev | 52° | | 61° | | 158° | |
| Hand-to-top-of-head | 53° | 55° | 86° | 61° | 136° | 29° |



Exemplificative of the E.G. behavior were found the plots for the forward flexion task, which are reported in Fig. 19.

3.3.2.4. Discussion and conclusions

Looking for a widely applicable and fast protocol, the acquisition of the single motion of clavicle and scapula was not considered, this requiring additional specialized instrumentation and generally being very time-consuming.[215,217] Considering the definition of the SoRs, the reorientation of the girdle and humerus ones was performed to enhance the interpretability of the results, remaining more adherent to clinical expectations. Coming to the results, the DASH scale pointed out the unchanged disability level of the patient. This is reasonable given the absence in the therapy of force regaining exercises. Considering the exemplificative forward flexion task, an increased gleno-humeral RoM could be observed consistently with Constant. However, E.G. showed, between the two acquisitions, very similar coordination patterns for the impaired side, which remained far from that of the sound side. Moreover, the increased RoM in AQ2 impaired pattern was followed by an increased girdle elevation, and by a Pr/Re pattern which drifted away from the sound. Similar results were obtained from the other activities, even if not observing a worsening of the Pr/Re. From the results obtained it can be stated therefore that the therapy applied for E.G. increased the RoM while increasing the entity of the girdle abnormal motion. Since E.G. came from a three years' history of shoulder dislocation, longer term results are expected. However, an increment in the execution of proprioceptive and scapulo-humeral coordination exercises could be recommended. It can be concluded therefore that the motion analysis protocol have positively integrated the Constant scale, explicating the relation between a general

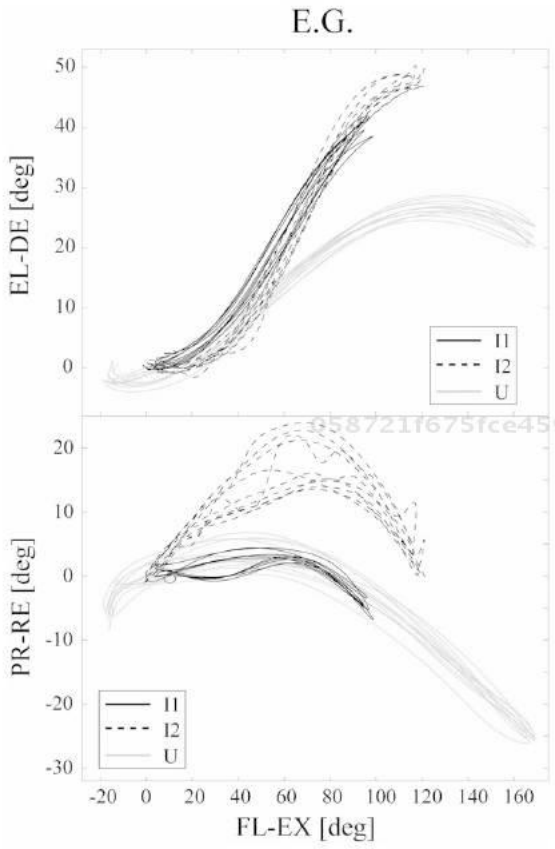


Fig. 19. Plots showing the coordination between the gleno-humeral flexion and girdle motion during the forward flexion activity. Shown are the overlapped patterns of the impaired side in AQ1 and AQ2 (denoted as I1 and I2 in the plots), compared to the unimpaired side for AQ2 (denoted as U), which was consistent with the one found for AQ1. For each acquisition and side, the patterns of the three central repetitions are reported, out of the executed five.

increment in gleno-humeral RoM and the underlying girdle–humerus coordination, with implications for the rehabilitation program.

## 4. Conclusions

Motion analysis is a key instrument for the quantification of joint function in healthy and pathological subjects. This knowledge is of fundamental importance to support the clinical decision process and for the development, as well as for the evaluation, of new surgical and rehabilitative procedures. Several devices can be used for the quantification of motion, and the best method to be used for this quantification depends on the field of application and accuracy required for the specific purpose. Stereophotogrammetry is certainly the most common method adopted, as well

as the most flexible to different applications. Nevertheless, this instrument must be used carefully and critically, because several errors can propagate to the final results, which are the segmental and joint kinematics. Among the different types of errors, the instrumental ones are certainly the least critical, because they can be identified and corrected by means of a proper calibration of the system and proper smoothing techniques. Serious is instead the effect of the ALs misplacement and of the STA, whose identification and correction are much more difficult. Thus, motion analysis results obtained using stereophotogrammetry can be exploited for clinical purposes, but they must be interpreted critically, taking errors into account. Some STA compensation methods improve significantly the quality of the results, but particular care must be paid in the implementation of such methods. On the other hand, errors introduced by ALs displacement are still a critical issue.

For the analysis of specific joints, such as the knee, 3D fluoroscopy provides much better accuracy, but this is associated to more invasiveness of the analysis, and to a more limited field of application, depending on the limited field of view.

On the contrary, the less expensive methodology that used inertial sensors permits the analysis of subjects in a very large field of view, but with an accuracy lower than stereophotogrammetry.

In these limitations, instruments adopted for the analysis of human motion can be used for a number of applications both in the clinical and in the research area, allowing to gain a deeper understanding of the biomechanics of human joints during daily living activities.

## Acknowledgments

The authors, gratefully acknowledge the help of M. Eng. Michele Raggi, M. Eng. Pietro Garofalo, M. D. Maria Vittoria Filippi, M. Eng. Andrea Giovanardi, and M. Eng. Angelo Davalli for their support in the development of the case studies presented in the upper-extremity application section; and M. Eng. Luigi Bertozzi for his support in the analysis of knee models. The clinical trials presented in this chapter were supported by Regione Emilia-Romagna. PRRIITT Misura 3.4 Azione A in the framework of the Starter Project.

## References

1. G. Wu, F. C. van der Helm, H. E. J. Veeger, M. Makhsous, P. van Roy, C. Anglin, J. Nagels, A. Karduna, K. McQuade, X. Wang, F. W. Werner and B. Buchholz, *J. Biomech.* (2005) 981–992.
2. E. J. Marey, *Animal Mechanism: A Treatisie on Terrestrial and Aerial Locomotion* (1873).
3. E. Muybridge, *Animal in Motion* (1887).
4. W. Braune and O. Fischer, *The Human Gait* (1987).
5. A. Cappozzo, M. Marchetti and V. Tosi, *Biolocomotion: A Century of Researches Using Moving Pictures* (1992).

6. D. H. Sutherland, *Gait Posture* (2001) 61–70.
7. D. H. Sutherland, *Gait Posture* (2002) 159–179.
8. D. H. Sutherland, *Gait Posture* (2005) 447–461.
9. A. Cappozzo, U. D. Croce, A. Leardini and L. Chiari, *Gait Posture* (2005) 186–196.
10. A. Cappozzo, F. Catani, U. D. Croce and A. Leardini, *Clin. Biomech. (Bristol., Avon.)* (1995) 171–178.
11. U. D. Croce and A. Cappozzo, *Med. Biol. Eng. Comput.* (2000) 260–266.
12. H. J. Woltring and R. Huiskes, *Biomechanics of Human Movement: Applications in Rehabilitation, Sport and Ergonomics* (1990).
13. F. Gazzani, *J. Biomech.* (1993) 1449–1454.
14. H. Furnée, *Three-Dimensional Analysis of Human Locomotion* (1997).
15. A. Cappello, P. F. La Palombara and A. Leardini, *Int. J. Biomed. Comput.* (1996) 137–151.
16. A. Cappozzo, T. Leo and A. Pedotti, *J. Biomech.* (1975) 307–320.
17. J. H. Challis, *J. Biomech.* (1995) 733–737.
18. M. D'Amico and G. Ferrigno, *Med. Biol. Eng. Comput.* (1992) 193–204.
19. S. Fioretti and L. Jetto, *Int. J. Systemat. Sci.* (1989) 33–53.
20. F. Gazzani, *Int. J. Biomed. Comput.* (1994) 57–76.
21. H. Hatze, *J. Biomech.* (1981) 13–18.
22. H. Hatze, *Human Movement Sci.* (1984) 5–25.
23. H. Lanshammar, *Prosthet. Orthot. Int.* (1982) 97–102.
24. H. Lanshammar, *J. Biomech.* (1982) 459–470.
25. K. Soudan and P. Dierckx, *J. Biomech.* (1979) 21–26.
26. H. J. Woltring, *Adv. Eng. Software* (1986) 104–113.
27. H. J. Woltring (1995) 79–99.
28. G. A. Wood, *Exerc. Sport Sci. Rev.* (1982) 308–362.
29. J. H. Challis, *Med. Eng. Phys.* (1995) 83–90.
30. H. J. Woltring, *Biomechanics of Human Movement* (1990).
31. A. Georgakis, L. K. Stergioulas and G. Giakas, *Med. Biol. Eng. Comput.* (2002) 625–633.
32. G. Giakas, L. K. Stergioulas and A. Vourdas, *J. Biomech.* (2000) 567–574.
33. O. A. Schmid, *Biomed. Tech. (Berl)* (2001) 50–54.
34. K. J. Deluzio, U. P. Wyss, J. Li and P. A. Costigan, *J. Biomech.* (1993) 753–759.
35. Y. Ehara, H. Fujimoto, S. Miyazaky, S. Tanaka and S. Yamamoto, *Gait Posture* (1995) 166–169.
36. Y. Ehara, H. Fujimoto, S. Miyazaky, M. Mochimaru, S. Tanaka and S. Yamamoto, *Gait Posture* (1997) 251–255.
37. J. P. Holden, S. Selbie and S. J. Stanhope, *Gait Posture* (2003) 205–213.
38. A. Cappozzo, U. Della Croce, F. Catani, A. Leardini, S. Fioretti and M. Maurizi, *Stereometric System Accuracy Test (CAMARC II)* (1993).
39. A. Cappello, A. Leardini, M. G. Benedetti, R. Liguori and A. Bertani, *IEEE Trans. Rehabil. Eng.* (1997) 388–393.
40. D. G. Everaert, A. J. Spaepen, M. J. Wouters, K. H. Stappaerts and R. A. Oostendorp, *Arch. Phys. Med. Rehabil.* (1999) 1082–1089.
41. A. Cappozzo, *Hum. Movement Sci.* (1984) 25–54.
42. A. Cappozzo, V. Camomilla and M. Donati (2003) 4–7.
43. U. Della Croce, A. Cappozzo and D. C. Kerrigan, *Med. Biol. Eng. Comput.* (1999) 155–161.
44. A. Cappozzo, *Biological and Biomechanical Performance of Biomaterials* (1986).
45. R. D. Crowninshield, R. C. Johnston, J. G. Andrews and R. A. Brand, *J. Biomech.* (1978) 75–85.

46. M. P. Kadaba, H. K. Ramakrishnan and M. E. Wootten, *J. Orthop. Res.* (1990) 383–392.
47. G. R. Pennock and K. J. Clark, *J. Biomech.* (1990) 1209–1218.
48. H. K. Ramakrishnan and M. P. Kadaba, *J. Biomech.* (1991) 969–977.
49. R. Stagni, A. Leardini, A. Cappozzo, B. M. Grazia and A. Cappello, *J. Biomech.* (2000) 1479–1487.
50. A. L. Bell, D. R. Petersen and R. A. Brand, *Human Movement Sci.* (1989) 3–16.
51. I. R. B. Davis, S. Ounupuu, D. Tyburski and J. R. Gage, *Human Movement Sci.* (1991) 575–587.
52. G. K. Seidel, D. M. Marchinda, M. Dijkers and R. W. Soutas-Little, *J. Biomech.* (1995) 995–998.
53. V. Camomilla, A. Cereatti, G. Vannozzi and A. Cappozzo, *J. Biomech.* (2006) 1096–1106.
54. A. Cereatti, V. Camomilla and A. Cappozzo, *J. Biomech.* (2004) 413–416.
55. S. J. Piazza, N. Okita and P. R. Cavanagh, *J. Biomech.* (2001) 967–973.
56. A. Leardini, A. Cappozzo, F. Catani, S. Toksvig-Larsen, A. Petitto, V. Sforza, G. Cassanelli and S. Giannini, *J. Biomech.* (1999) 99–103.
57. C. Anglin and U. P. Wyss, *Proc. Inst. Mech. Eng. [H]* (2000) 541–555.
58. C. G. Meskers, F. C. van der Helm, L. A. Rozendaal and P. M. Rozing, *J. Biomech.* (1998) 93–96.
59. I. A. Murray, *Determining Upper-Limb Kinematics and Dynamics During Everyday Tasks* (1999).
60. M. Stokdijk, J. Nagels and P. M. Rozing, *J. Biomech.* (2000) 1629–1636.
61. H. E. Veeger, F. C. van der Helm, L. H. Van der Woude, G. M. Pronk and R. H. Rozendal, *J. Biomech.* (1991) 615–629.
62. S. J. Piazza and P. R. Cavanagh, *J. Biomech.* (2000) 1029–1034.
63. L. Cheze, *J. Biomech.* (2000) 1695–1699.
64. K. Manal, I. McClay, J. Richards, B. Galinat and S. Stanhope, *Gait Posture* (2002) 10–17.
65. H. J. Woltring, *J. Biomech.* (1994) 1399–1414.
66. H. J. Woltring, K. Long, P. J. Osterbauer and A. W. Fuhr, *J. Biomech.* (1994) 1415–1432.
67. A. Cappozzo, F. Catani, A. Leardini, M. G. Benedetti and U. Della Croce, *Clin. Biomech. (Bristol., Avon.)* (1996) 90–100.
68. T. P. Andriacchi and E. J. Alexander, *J. Biomech.* (2000) 1217–1224.
69. S. A. Banks, G. D. Markovich and W. A. Hodge, *J. Arthroplasty* (1997) 297–304.
70. J. B. Stiehl, D. A. Dennis, R. D. Komistek and P. A. Keblish, *Clin. Orthop.* (1997) 60–66.
71. S. A. Banks, *Models Based 3-D Kinematic Estimation from 2-D Perspective Silhouettes: Application with Total Knee Prosthesis* (1992).
72. S. A. Banks and W. A. Hodge, *IEEE Trans. Biomed. Eng.* (1996) 638–649.
73. S. A. Banks, G. D. Markovich and W. A. Hodge, *Am. J. Knee. Surg.* (1997) 261–267.
74. W. A. Hoff, R. Komistek and D. A. Dennis (1996) 181–186.
75. W. A. Hoff, R. D. Komistek, D. A. Dennis, S. M. Gabriel and S. A. Walker, *Clin. Biomech. (Bristol., Avon.)* (1998) 455–472.
76. G. R. Hanson, J. F. Suggs, A. A. Freiberg, S. Durbhakula and G. Li, *J. Orthop. Res.* (2006) 974–981.
77. G. Li, J. Suggs, G. Hanson, S. Durbhakula, T. Johnson and A. Freiberg, *J. Bone Joint Surg. Am.* (2006) 395–402.
78. J. W. Coltman, *Radiology* (1948) 359–367.

79. B. G. Brown, E. Bolson, M. Frimer and H. T. Dodge, *Circulation* (1977) 329–337.
80. U. Solzbach, H. Wollschlager, A. Zeiher and H. Just (1989) 355–357.
81. S. Rudin, D. R. Bednarek and R. Wong, *Med. Phys.* (1991) 1145–1151.
82. E. Gronenschild, *Med. Phys.* (1997) 1875–1888.
83. R. Fahrig, M. Moreau and D. W. Holdsworth, *Med. Phys.* (1997) 1097–1106.
84. J. M. Boone, J. A. Seibert, W. A. Barrett and E. A. Blood, *Med. Phys.* (1991) 236–242.
85. E. J. Morton, P. M. Evans, M. Ferraro, E. F. Young and W. Swindell, *Br. J. Radiol.* (1991) 747–750.
86. S. Fantozzi, A. Cappello and A. Leardini, *Med. Phys.* (2003) 124–131.
87. R. D. Komistek, J. B. Stiehl, F. F. Buechel, E. J. Northcut and M. E. Hajner, *Foot Ankle Int.* (2000) 343–350.
88. D. A. Dennis, R. D. Komistek, E. J. Northcut, J. A. Ochoa and A. Ritchie, *J. Biomech.* (2001) 623–629.
89. D. A. Dennis, M. R. Mahfouz, R. D. Komistek and W. Hoff, *J. Biomech.* (2005) 241–253.
90. S. A. Banks, B. J. Fregly, F. Boniforti, C. Reinschmidt and S. Romagnoli, *Knee. Surg. Sports Traumatol. Arthrosc.* (2005) 551–556.
91. A. Hamadeh, S. Lavallee and P. Cinquin, *Comput. Aided Surg.* (1998) 11–19.
92. S. Lavallee and R. Szeliski, *IEEE Trans.Pattern Anal. Machine Intell.* (1995) 378–390.
93. J. Canny, *IEEE Trans. Pattern Anal. Machine Intell.* (1986) 679–698.
94. S. A. Banks and W. A. Hodge, *J. Arthroplasty* (2004) 809–816.
95. J. B. Stiehl, R. D. Komistek, D. A. Dennis, R. D. Paxson and W. A. Hoff, *J. Bone Joint Surg. Br.* (1995) 884–889.
96. M. R. Mahfouz, W. A. Hoff, R. D. Komistek and D. A. Dennis, *IEEE Trans. Med. Imaging* (2003) 1561–1574.
97. D. Roetenberg, *Inertial and Magnetic Sensing of Human Motion* (2006).
98. A. M. Sabatini, *IEEE Trans. Biomed. Eng.* (2006) 1346–1356.
99. G. Welch and E. Foxlin, *IEEE Computer Graphics and Applications* (2002) 24–38.
100. P. Bonato, *IEEE Eng. Med. Biol. Mag.* (2003) 18–20.
101. K. Aminian, *Computational Intelligence for Movement Sciences* (2006), pp. 101–138.
102. M. Gad-el-Hak, *The MEMs Handbook* (2005).
103. N. Yazdi, F. Ayazi and K. Najafi, *Proc. IEEE* (1998) 1640–1659.
104. H. J. Luinge and P. H. Veltink, *IEEE Trans. Neural Syst. Rehabil. Eng.* (2004) 112–121.
105. H. J. Luinge and P. H. Veltink, *Med. Biol. Eng. Comput.* (2005) 273–282.
106. H. J. Luinge, *Inertial Sensing of Human Movement* (2002).
107. D. Giansanti, G. Maccioni and V. Macellari, *IEEE Trans. Biomed. Eng.* (2005) 1271–1277.
108. S. Nakamura, *IEEE Sensors* (2005) 939–942.
109. D. Roetenberg, H. J. Luinge, C. T. Baten and P. H. Veltink, *IEEE Trans. Neural Syst. Rehabil. Eng.* (2005) 395–405.
110. M. Hallett, *Mov. Disord.* (1998) 43–48.
111. H. J. Busser, W. G. de Korte, E. B. Glerum and R. C. van Lummel, *Ergonomics* (1998) 1519–1526.
112. C. F. Estill, L. A. MacDonald, T. B. Wenzl and M. R. Petersen, *Ergonomics* (2000) 1430–1445.
113. L. Chiari, M. Dozza, A. Cappello, F. B. Horak, V. Macellari and D. Giansanti, *IEEE Trans. Biomed. Eng.* (2005) 2108–2111.

114. M. Dozza, L. Chiari and F. B. Horak, *Arch. Phys. Med. Rehabil.* (2005) 1401–1403.
115. M. Dozza, L. Chiari, B. Chan, L. Rocchi, F. B. Horak and A. Cappello, *J. Neuroeng. Rehabil.* (2005) 13.
116. P. H. Veltink and R. C. van Lummel, *Dynamic Analysis Using Body-Fixed Sensors* (1994).
117. J. B. Bussmann, W. L. Martens, J. H. Tulen, F. C. Schasfoort, van den H. J. Berg-Emons and H. J. Stam, *Behav. Res. Methods Instrum. Comput.* (2001) 349–356.
118. P. H. Veltink, H. B. Bussmann, W. de Vries, W. L. Martens and R. C. van Lummel, *IEEE Trans. Rehabil. Eng.* (1996) 375–385.
119. K. Aminian, P. Robert, E. E. Buchser, B. Rutschmann, D. Hayoz and M. Depairon, *Med. Biol. Eng. Comput.* (1999) 304–308.
120. B. Najafi, K. Aminian, A. Paraschiv-Ionescu, F. Loew, C. J. Bula and P. Robert, *IEEE Trans. Biomed. Eng.* (2003) 711–723.
121. A. Paraschiv-Ionescu, E. E. Buchser, B. Rutschmann, B. Najafi and K. Aminian, *Gait Posture* (2004) 113–125.
122. A. Vega-Gonzalez and M. H. Granat, *Arch. Phys. Med. Rehabil.* (2005) 541–548.
123. G. Uswatte, W. H. R. Miltner, B. Foo, M. Varma, S. Moran and E. Taub, *Stroke* (2000) 662–667.
124. B. Auvinet, G. Berrut, C. Touzard, L. Moutel, N. Collet, D. Chaleil and E. Barrey, *Gait Posture* (2002) 124–134.
125. K. Aminian, B. Najafi, C. Bula, P. F. Leyvraz and P. Robert, *J. Biomech.* (2002) 689–699.
126. K. Aminian, C. Trevisan, B. Najafi, H. Dejnabadi, C. Frigo, E. Pavan, A. Telonio, F. Cerati, E. C. Marinoni, P. Robert and P. F. Leyvraz, *Gait Posture* (2004) 102–107.
127. W. Zijlstra and A. L. Hof, *Gait Posture* (2003) 1–10.
128. R. Moe-Nilssen and J. L. Helbostad, *J. Biomech.* (2004) 121–126.
129. H. J. Yack and R. C. Berger, *J. Gerontol.* (1993) M225–M230.
130. D. Giansanti, V. Macellari, G. Maccioni and A. Cappozzo, *IEEE Trans. Biomed. Eng.* (2003) 476–483.
131. B. Najafi, K. Aminian, A. Paraschiv-Ionescu, F. Loew, Y. Blanc and Ph. Robert, *Gait Posture* (2001) 119–120.
132. K. Aminian, *Computational Intelligence for Movement Sciences: Neural Networks and Other Emerging Techniques* (2006).
133. R. E. Mayagoitia, A. V. Nene and P. H. Veltink, *J. Biomech.* (2002) 537–542.
134. H. J. Luinge, P. H. Veltink and C. T. Baten, *J. Biomech.* (2007) 78–85.
135. D. J. Veeger, B. Yu and K. N. An, *Proc. 1st Conf. ISG* (1997).
136. A. G. Cutti, *Motion Analysis Assessment of Upper Extremity Motor Ability* (2006).
137. A. G. Cutti, A. Giovanardi, L. Rocchi and A. Davalli, in press (2007).
138. R. Schmidt, C. Disselhorst-Klug, J. Silny and G. Rau, *J. Biomech.* (1999) 615–621.
139. A. G. Cutti, G. Paolini, M. Troncossi, A. Cappello and A. Davalli, *Gait Posture* (2005) 341–349.
140. A. G. Cutti, A. Cappello and A. Davalli, *J. Mech. Med. Biol.* (2005) 1–15.
141. A. G. Cutti, A. Cappello and A. Davalli, *Clin. Biomech. (Bristol., Avon.)* (2006) S13–S19.
142. S. S. H. U. Gamage and J. Lasenby, *J. Biomech.* (2002) 87–93.
143. E. Roux, S. Bouilland, A. P. Godillon-Maquinghen and D. Bouttens, *J. Biomech.* (2002) 1279–1283.
144. T. W. Lu and J. J. O'Connor, *J. Biomech.* (1999) 129–134.
145. M. A. Lafortune, *The Use of Intra-Cortical Pins to Measure the Motion of Knee Joint During Walking* (1984).

146. M. A. Lafortune and M. J. Lake (1991) 55–56.
147. M. A. Lafortune, P. R. Cavanagh, H. J. Sommer, III and A. Kalenak, *J. Biomech.* (1992) 347–357.
148. A. S. Levens, V. T. Inman and J. A. Blosser, *J Bone Joint Surg.* (1948) 859–872.
149. D. Karlsson and A. Lundberg, *Proc. 3rd Int. Symp. 3D Anal. Hum. Mov.* (1994).
150. C. Reinschmidt, A. J. van Den Bogert, B. M. Nigg, A. Lundberg and N. Murphy, *J. Biomech.* (1997) 729–732.
151. C. Reinschmidt, A. J. van Den Bogert, N. Murphy, A. Lundberg and B. M. Nigg, *Clin. Biomech. (Bristol., Avon.)* (1997) 8–16.
152. G. K. Cole, B. M. Nigg, J. L. Ronsky and M. R. Yeadon, *J. Biomech. Eng.* (1993) 344–349.
153. J. Fuller, L. J. Liu, M. C. Murphy and R. W. Mann, *Human Movement Sci.* (1997) 219–242.
154. H. J. Yack, J. Houck, T. Cudderford, M. Pierrynowski and K. Ball, *Gait Posture* (2000) 148–149.
155. P. Westblad, K. Halvorsen, T. Hashimoto, I. G. Winson and A. Lundberg (2000) 49–51.
156. C. Angeloni, A. Cappozzo, F. Catani and A. Leardini, *Proc. VIII Meeting European Society of Biomechanics* (1992).
157. J. P. Holden, J. H. Orsini, K. L. Siegel, T. M. Kepple, L. H. Gerber and S. J. Stanhope, *Gait Posture* (1997) 217–227.
158. K. Manal, I. McClay, S. Stanhope, J. Richards and B. Galinat, *Gait Posture* (2000) 38–45.
159. B. A. Maslen and T. R. Ackland, *Clin. Biomech.* (1994) 291–296.
160. R. Tranberg and D. Karlsson, *Clin. Biomech. (Bristol., Avon.)* (1998) 71–76.
161. M. Sati, J. A. de Guise, S. Larouche and G. Drouin, *The Knee* (1996) 121–138.
162. R. Stagni, S. Fantozzi, A. Cappello and A. Leardini, *Clin. Biomech. (Bristol., Avon.)* (2005) 320–329.
163. L. Cheze, B. J. Fregly and J. Dimnet, *J. Biomech.* (1995) 879–884.
164. K. A. Ball and M. R. Pierrynowski, *Proc. SPIE — The Int. Society of Optical Engineering, BiOS'98* (1998).
165. E. J. Alexander and T. P. Andriacchi, *J. Biomech.* (2001) 355–361.
166. R. Stagni, S. Fantozzi, A. Leardini and A. Cappello, *Springer Verlag Lect. Note Comp. Sci.* (2003) 293–301.
167. P. Cerveri, A. Pedotti and G. Ferrigno, *Human. Movement Sci.* (2003) 377–404.
168. L. Lucchetti, A. Cappozzo, A. Cappello and C. U. Della, *J. Biomech.* (1998) 977–984.
169. A. Cappello, A. Cappozzo, P. F. La Palombra, L. Lucchetti and A. Leardini, *Human Movement Sci.* (1997) 259–274.
170. T. P. Andriacchi, E. J. Alexander, M. K. Toney, C. Dyrby and J. Sum, *J. Biomech. Eng.* (1998) 743–749.
171. A. Cappello, R. Stagni, S. Fantozzi and A. Leardini, *IEEE Trans. Biomed. Eng.* (2005) 992–998.
172. D. M. Daniel and M. L. Stone, *Knee Ligaments: Structure, Function, Injury, and Repair* (1990).
173. R. Stagni, S. Fantozzi and A. Cappello, *Gait Posture* (2006) 137–141.
174. L. Blankevoort, R. Huiskes and A. de Lange, *J. Biomech.* (1990) 1219–1229.
175. J. J. O'Connor, T. L. Shercliff, E. Biden and J. W. Goodfellow, *Proc. Inst. Mech. Eng. [H]* (1989) 223–233.
176. D. R. Wilson, J. D. Feikes, A. B. Zavatsky and J. J. O'Connor, *J. Biomech.* (2000) 465–473.

177. D. R. Wilson, J. D. Feikes and J. J. O'Connor, *J. Biomech.* (1998) 1127–1136.
178. R. D. Komistek, D. A. Dennis and M. Mahfouz, *Clin. Orthop.* (2003) 69–81.
179. M. A. Freeman and V. Pinskerova, *Clin. Orthop.* (2003) 35–43.
180. L. Bertozzi, R. Stagni, S. Fantozzi and A. Cappello, *Springer Verlag Lect. Note. Comp. Sci.* (2006) 831–838.
181. H. S. Gill and J. J. O'Connor, *Clin. Biomech. (Bristol., Avon.)* (1996) 81–89.
182. T. W. Lu and J. J. O'Connor, *Proc. Inst. Mech. Eng. [H]* (1996) 71–79.
183. A. B. Zavatsky, D. J. Beard and J. J. O'Connor, *Am. J. Sports. Med.* (1994) 418–423.
184. A. B. Zavatsky and J. J. O'Connor, *Proc. Inst. Mech. Eng. [H]* (1993) 7–18.
185. R. A. Huss, H. Holstein and J. J. O'Connor, *Proc. Inst. Mech. Eng. [H]* (1999) 19–32.
186. S. D. Kwak, L. Blankevoort and G. A. Ateshian, *Comput. Meth. Biomech. Biomed. Eng.* (2000) 41–64.
187. T. J. Momersteeg, L. Blankevoort, R. Huiskes, J. G. Kooloos, J. M. Kauer and J. C. Hendriks, *J. Biomech.* (1995) 745–752.
188. T. J. Mommersteeg, L. Blankevoort, R. Huiskes, J. G. Kooloos and J. M. Kauer, *J. Biomech.* (1996) 151–160.
189. T. J. Mommersteeg, R. Huiskes, L. Blankevoort, J. G. Kooloos, J. M. Kauer and P. G. Maathuis, *J. Biomech.* (1996) 1659–1664.
190. S. J. Piazza and S. L. Delp, *J. Biomech. Eng.* (2001) 599–606.
191. R. Stagni, S. Fantozzi, M. Davinelli and M. Lannocca, *Springer Verlag Lect. Note Comp. Sci.* (2004) 1073–1080.
192. D. Testi, C. Zannoni, A. Cappello and M. Viceconti, *Comput. Meth. Prog. Biomed.* (2001) 175–182.
193. M. A. Audette, F. P. Ferrie and T. M. Peters, *Med. Image Anal.* (2000) 201–217.
194. J. B. Maintz and M. A. Viergever, *Med. Image Anal.* (1998) 1–36.
195. L. Montanati, F. Taddei, S. Martelli, A. Leardini, M. Manfrini and M. Viceconti, (2006) S46.
196. B. A. Garner and M. G. Pandy, *Comput. Meth. Biomech. Biomed. Eng.* (2001) 93–126.
197. B. A. Garner and M. G. Pandy, *Comput. Meth. Biomech. Biomed. Eng.* (2000) 1–30.
198. B. A. Garner and M. G. Pandy, *Comput. Meth. Biomech. Biomed. Eng.* (1999) 107–124.
199. L. Blankevoort and R. Huiskes, *J. Biomech. Eng.* (1991) 263–269.
200. L. Blankevoort, J. H. Kuiper, R. Huiskes and H. J. Grootenboer, *J. Biomech.* (1991) 1019–1031.
201. A. B. Zavatsky and J. J. O'Connor, *Proc. Inst. Mech. Eng. [H]* (1992) 135–145.
202. A. B. Zavatsky and J. J. O'Connor, *Proc. Inst. Mech. Eng. [H]* (1992) 125–134.
203. F. E. Zajac, *Crit. Rev. Biomed. Eng.* (1989) 359–411.
204. M. L. Audu and D. T. Davy, *J. Biomech. Eng.* (1985) 147–157.
205. D. A. Dennis, R. D. Komistek, W. A. Hoff and S. M. Gabriel, *Clin. Orthop.* (1996) 107–117.
206. S. Zuffi, A. Leardini, F. Catani, S. Fantozzi and A. Cappello, *IEEE Trans. Med. Imaging.* (1999) 981–991.
207. M. G. Pandy, *Ann. Rev. Biomed. Eng.* (2001) 245–273.
208. D. W. Risher, L. M. Schutte and C. F. Runge, *J. Biomech. Eng.* (1997) 417–422.
209. C. F. Runge, F. E. Zajac, III, J. H. Allum, D. W. Risher, A. E. Bryson, Jr. and F. Honegger, *IEEE Trans. Biomed. Eng.* (1995) 1158–1164.
210. C. L. Koerhuis, J. C. Winters, F. C. van der Helm and A. L. Hof, *Clin. Biomech. (Bristol., Avon.)* (2003) 14–18.

211. M. A. Buckley, A. Yardley, G. R. Johnson and D. A. Carus, *Proc. Inst. Mech. Eng. [H]* (1996) 241–247.
212. P. Pynsent, J. Fairbank and A. Carr, *Outcome Measure in Orthopedics* (1994).
213. P. W. McClure, L. A. Michener and A. R. Karduna, *Physical Therapy* (2006) 1075–1090.
214. N. Klopcar and J. Lenarcic, *Clin. Biomech. (Bristol., Avon.)* (2006) S20–S26.
215. A. R. Karduna, P. W. McClure, L. A. Michener and B. Sennett, *J. Biomech. Eng.* (2001) 184–190.
216. E. Finch, D. Brooks, P. W. Stratford and N. E. Mayo, *Physical Rehabilitation Outcome Measures* (2002).
217. G. R. Johnson, P. R. Stuart and S. Mitchell, *Clin. Biomech. (Bristol., Avon.)* (1993) 269–273.

This page intentionally left blank

# CHAPTER 6

# STRUCTURAL ANALYSIS OF SKELETAL BODY ELEMENTS: NUMERICAL AND EXPERIMENTAL METHODS

ELISABETTA M. ZANETTI
*Department of Industrial and Mechanical Engineering*
*University of Catania, V.le Andrea Doria 6, 95125 Catania, Italy*
*elisabetta.zanetti@diim.unict.it*

CRISTINA BIGNARDI
*Department of Mechanical Engineering, Politecnico di Torino*
*Corso Duca degli Abruzzi 24, 10129 Torino, Italy*
*cristina.bignardi@polito.it*

This chapter deals with the structural analysis of bone elements, performed both numerically and experimentally. Among numerical techniques, the finite element method is discussed at length, focusing on its applications to bone biomechanics. The main steps involved in the method are analyzed from the practical perspective, and guidelines about dealing with commonly recurring problems are provided. As for experimental methods, considerable space is devoted to full-field techniques, with special attention to the lesser-known method of thermoelastic stress analysis. The main aim of this chapter is to illustrate how numerical and experimental methodologies can complement each other, explaining why it is beneficial to pursue both approaches.

## 1. Introduction: The Origins of Structural Biomechanics

Until the late Middle Ages, man's understanding of his own anatomy was extremely sketchy: up to the 14th century, the dictates of the Church made it impossible to dissect human cadavers and thus increase anatomical knowledge. With the end of the medieval interlude and the rise of humanism, the limitations of Neoplatonism and Averroism began to be overcome, and the first attempts were made to provide a mechanical explanation for the behavior of the human body. Leonardo da Vinci (1452–1519) first directed his attention to the anatomy of the head and brain, later (in around 1490) studying the proportions of the human body. It was perhaps at this point that he passed from simply describing human nature to exploring the mathematical relationships behind it. In the second half of the first decade of the 16th century, he investigated the skeleton, studying limbs and entire systems from the hand to the spinal column, and drawing bone elements seen from all sides and in cross-section. In addition, he investigated muscles and tendons as well as paid attention to other organs.

Critics have often asked whether Leonardo was only an observer of nature or an anatomist or even a physiologist. As he himself noted in a page of the Codice Atlantico, however, 'We must understand what is man, and what is life,' indicating that his interest did not stop with the organ in itself, but encompassed its function. Though Leonardo did not yet have the basics of Galileo's modern science, he used his knowledge of mechanics and anatomy to examine the mechanics of walking, jumping, sitting, and rising from a chair. He was thus careful to describe both form and function and, in his own way, was without doubt a technologist of genius.

The turning point in the history of biomechanics came with the Iatromechanical School, which had the merit of considering the human organism as subject to immutable physical laws. The founders and leaders of this movement were Santorio Santorio (1561–1630), Gian Alfonso Borelli (1608–1679), and Giacomo Baglivi (1666–1707).



The most important insight of the Iatromechanical School, which led to the more extreme theoretical concept of Giacomo Baglivi, was the so-called 'human machine,' or in other words a mechanical system consisting of many small machines making up the various organs, whose mechanical malfunction is the cause of illness.

After this period of keen intuition, which was not in any case followed by concrete applications because of the difficulties involved in biological and mechanical investigation, engineering and medicine gradually grew apart, each taking its own way almost until the present day.

Modern biomechanics got its start thanks to technological advances toward the end of World War II when the United States poured enormous resources into systematic investigations aiming at the rehabilitation of war veterans. These resources were put to good use by researchers from the natural sciences, engineering, physics, and mathematics. Biomechanics, which marks the passage from qualitative to quantitative, thus springs from humanitarian considerations in the service of health care, rather than as an academic exercise.[1]



## 2. Numerical Analysis

Mathematical studies can be analytical or numerical. The former are based on closed form solutions for geometrically simplified models, in which bone is modeled with uniform section beams.[1–9] It was initially believed that results which could be used for prosthesis design could be obtained with minimum effort and cost. Analyses were conducted with different types of approximation, all focusing on prosthesis stem–bone coupling with or without interposed cement: this structural situation was often approached in the light of the classic beam on elastic foundation theory, in many cases assuming both the sections and the stiffness of the elastic connecting layer to be constant,[9] or considering material and geometrical properties to vary along the length of the beam, which calls for a semi-analytical approach, and possibly one based on special functions.[5]

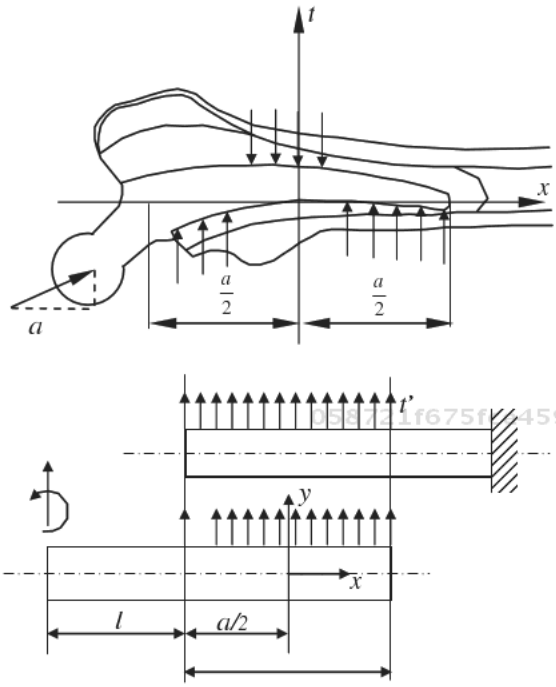


Fig. 1. Simplified representation of a femur–prosthesis coupling for the analysis of load transfer.[5]

Published theoretical studies of this mechanical coupling can be classified on the basis of the types of stress addressed in the investigation.[10]

The flexural part of the phenomenon was addressed by Gola and Gugliotta[5] (Fig. 1), Huiskes and Slooff,[11] and Huiskes[9]; while most two-dimensional analyses, including those by Mc Neice and Amstutz,[12] Wood,[13] and Svensson *et al.*[14] dealt with the coupled axial and flexural phenomena. The axial part of the problem was investigated by Huiskes,[9] whose analysis was based on the assumption that the cement transmits the tangential stresses fully and at all points.

More complete analyses which also take torsional phenomena into account were performed by Röehrle *et al.*,[15] Crowninshield *et al.*,[16] and Tarr *et al.*[17]

In reality, it soon became apparent that the approximations so produced were not valid, precisely because they did not account for the problem's physical complexity in terms of material anisotropy and the bone–stem system shape.

One of the basic mathematical tools that engineering makes available to biomechanics is finite element discretization, which is used to analyze the stress and strain conditions of geometrically complex structures consisting of anisotropic, nonhomogeneous, and nonlinear materials, subjected to complex load and constraint systems (Fig. 2).

The Finite Element Method (FEM) is a well-established numerical technique, whereby the stress pattern on complex structures can be calculated when the

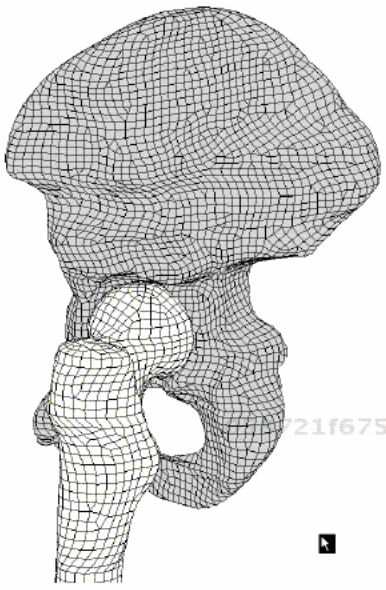

Fig. 2. Finite element model of a hip joint.

analytical solution cannot be obtained. A complex volume is subdivided into many elementary volumes called finite elements; these elementary volumes are connected to each other through node points at which equilibrium and congruency equations are written. The displacements inside each elementary volume are approximated by means of basis functions, whose parametric values can be calculated from nodal displacements and, if necessary, nodal strains. The stiffness of an elementary volume can be calculated from its basis function and its material properties; the set of all elementary volume stiffness gives the stiffness matrix of the whole structure. Once this stiffness matrix is known, nodal displacements can be derived from nodal forces and *vice versa*. Nodal strains can be obtained by derivation of nodal displacements and, lastly, nodal stresses can be calculated from nodal strains thanks to the elasticity matrix of the material in question. The finite element method guarantees the equilibrium of forces and the continuity of displacements. The continuity of stresses and of strains is not generally assured, however, thus providing a good test of the quality of results.

As in the case of analytical studies, the first applications of the finite element method were designed to investigate the mechanical behavior of the bone–prosthesis system: from the outset, it was understood that one of the most important mechanisms behind implant failure, aseptic loosening, was due to structural causes. The main structural problems affecting prosthetic implants derive from the fact that the bone–prosthesis system couples elements of different stiffness, producing complex structural conditions in the proximity of bone resection and stiffness discontinuity.

A comprehensive review of the problems that this sector tackled in the early years is given in Refs. 18 and 19, which discuss both technical aspects and clinical results, providing an extensive bibliography. Briefly summarized, the development of these applications began with the use of two-dimensional or axially symmetric models for parametric analyses designed to identify the optimal shape of the prosthesis stem in relation to the stress state of the cement or bone coupled to it. Examples of this work include the first finite element studies of the coupled femur and prosthesis performed by Mc Neice and Amstutz[12,20] in 1975, and the later investigations by Forte,[21] Bartel *et al.*,[22–25] and Andriacchi *et al.*[26] These models, however, often did not take the bone's circumferential continuity into account, as there was no connection between medial cortical bone and lateral cortical bone.

A more realistic analysis was presented in 1976 by Hampton *et al.*,[27] who joined the medial and lateral cortical bone with transverse connecting elements. This advance in modeling technique was followed by Svensson *et al.*,[14] who in 1977 presented a two-dimensional model which yielded a distribution of the stresses on the bone surface that was in qualitative agreement with the results of experimental strain-gage tests by Brockhurst.[28] These authors were also the first to investigate the influence of prosthesis stem–cement interface conditions, simulating the possibility of relative slip; by contrast, earlier studies had assumed a rigid connection at the interface.

The first detailed finite element analysis of the proximal femur with implanted prosthesis was probably that conducted by Röehrle *et al.* in 1977–1979.[15,29,30] Their models were three dimensional with adequately fine mesh, and also took the bone's dishomogeneity in various areas — but not its anisotropy — into account. These authors considered both the case in which the prosthesis interfacing with the cement can slip, and that in which the two interfaces are rigidly connected. These models were used for comparative studies in order to assess certain specific prosthesis designs, to clarify the calcar's support function, and to evaluate the effect of different stiffness on the part of the intermediate cement layer. These studies were followed by other three-dimensional investigations, all benchmarks in the early years of applying the numerical method to this type of problem: Crowninshield *et al.*,[16,31–33] Tarr *et al.*,[17,34] Rohlmann *et al.*,[35] Valliappan *et al.*,[36] Hampton *et al.*,[37] Lewis *et al.*,[38] and Vichnin and Batterman.[39] Making comparison between the results obtained by these authors is difficult, as there are significant differences between the models they used as regards density, geometry, material properties, and loading conditions. Though the work of many of these authors was verified experimentally by applying strain gauge techniques, the latter were usually employed on the outer surface of the bone, and could not be correlated with the stress changes in the bone and the cement that occur with changes in the geometry of the prosthesis stem. In the majority of these studies, cortical bone and spongy bone were assumed to be homogeneous, isotropic materials exhibiting linear elastic behavior, while the interfaces were often considered to be rigidly connected to each other. The effects of cortical bone anisotropy were investigated by Valliappan *et al.*[36] and by Vichnin and Batterman.[39]

The nonlinear effects of loosening at the prosthesis stem–cement interface were studied by Huiskes and Shouten in 1980[40] and by Hampton *et al.* in 1981[41] on the basis of realistic, experimentally determined cement–stem bond failure characteristics.

In 1983, Rohlmann *et al.*[42] determined the stress distribution in a femur with implanted prosthesis, conducting a parallel strain gauge analysis. This study considered different loading conditions, and the interface elements were regarded as rigidly connected to each other. An interesting aspect of this work was its discussion (the first of its kind) of the usefulness of simulating muscle contribution.

In 1985, Calderale and Garro[43] conducted a comparative study with prostheses of differing lengths implanted in a fine three-dimensional model of the femur. This study employed a first rudimental schematization of the spongy bone to investigate the actual stresses on the bone trabeculae, and identified the most highly stressed bone–stem interface areas.



Starting in the late 1970s, the success of studies conducted on the stem–femur coupling inspired investigators to apply the finite element method to the pelvis–acetabulum coupling,[44–47] as well as to other joint prostheses such as those for the knee and ankle.[48–59]

Today, this method is widely used in orthopedics, where ever-higher computing power and improved software make increasingly sophisticated applications possible.

While developments in theoretical stress analysis research have made it clear that three-dimensional finite element discretization is the best way to obtain meaningful results, passing from beam models to three-dimensional finite element models is reasonable only if the results do not simply give information about load transfer, but also provide details of local stress concentrations. This requires that the model be fine-tuned as regards material parameters as well as geometry. An overview of how this can be accomplished will be given in the following pages, where we will look at the main steps through which a finite element analysis can be processed:



- Preparation of the geometrical model
- Subdivision of the whole volume in finite elements (meshing)
- Assignment of the mechanical properties of the material
- Choice of element type
- Setting boundary conditions: loads and constraints
- Choice of the type of solution (static, dynamic, linear, nonlinear, etc.)
- Analysis of results (post-processing).

### 2.1. *The geometrical model*

Two different cases should be considered: numerical structural analysis can address a generic case, or can be carried out to analyze a specific patient.

In the first case, a generic geometric model should be built which is representative of a full class. In most cases, this is accomplished using data from

the "Visible Human Project"[60] or geometrical models which reproduce the synthetic bones produced by Sawbones (Sawbones Europe AB, Sweden).[61] This approach is advantageous because these geometries are a true standard for the biomechanical community, so the results thus obtained can be compared with those produced by other researchers. A further advantage is that many of these models are already shared by the biomechanics community and can be freely downloaded from the Web: the International Society of Biomechanics (ISB), for example, has a link where 3D bone models are shared,[62] and is not the only institution which provides such a feature.

In cases where a patient-specific model is being sought or the generic model needs to be created from scratch, the most accurate technique for obtaining morphological information, together with the pattern of bone density, consists of processing CT scans[63,64]: CT files are analyzed by special software in order to obtain the contours of each volume of interest (e.g., spongy bone and cortical bone), slice by slice. These contours are then exported to the 3D CAD software in order to interpolate contours by means of surfaces which will delimit the volumes concerned. This procedure can produce very good results: Kang *et al.*[65] report precision errors of less than 1% for trabecular and total volumes and less than 2% for cortical thickness.

In a recent work,[66] the authors also proposed an alternative procedure based on radiographs, noting that CT scans are by no means universally used: not all hospitals have the necessary equipment, nor can all countries afford the procedure's high cost. Above all, hospital managers usually regard CT scans as unnecessary for pre-operative planning and even less essential for follow-up assessment (Fig. 3). The main limitation of radiographic images is obviously that they can give only a projective view, whereas CT scans permit faithful 3D reconstruction, section by section. This limitation was partially overcome by basing the patient-specific 3D model on a pre-existent 3D model of an average femur. The basic assumption of this method was that femoral sections remain similar among different patients if they are cut perpendicularly to the geometrical longitudinal axis, formed by the shaft axis, the neck axis, and a fillet between them. A distinctive feature of the method is that the neck-shaft angle of the reconstructed model is the same as in

Fig. 3. Composite femurs.

the radiograph. The cortical outer and inner diameters as measured on the frontal plane are respected, while neck length and femur length assessed on the frontal plane are the same as in the radiograph. This procedure is biased by errors, especially in the lateral plane. In the authors' opinion, however, these errors are not so great as to make this procedure useless: in fact, it should not be regarded as an alternative to CT scans, but as an alternative to standardized models, which, in most cases, would entail much larger errors.

### 2.2. *Volume meshing*

The discretization into elements, called the 'mesh,' is not uniform and is established in accordance with the type of investigation concerned and thus calls for a good deal of experience and a feeling for the structure's physics.



Though the meshing operation is usually carried out by FE software, it is seldom possible to achieve a good mesh using fully automated procedures: the ability of the operator is fundamental. A few words are in order concerning this operation, because the quality of results is heavily dependent on mesh quality.

Most automatic meshers are only capable of generating tetrahedral meshes. It should be borne in mind that tetrahedra are quite "bad" finite elements (they are too "stiff"): they give poor performance unless they are very small, well shaped, and if possible have 10 nodes. On the whole, a high element density is needed to give acceptable results, and this leads to increased solver time. Hexahedra are a better alternative, though, unfortunately, meshes of this kind can only be obtained semi-automatically: in the authors' experience, the most effective way to obtain a good mesh is first to identify a longitudinal direction, then to mesh a plane section perpendicular to the longitudinal direction, and lastly to extrude the plane mesh along the lateral surfaces of the model.



Many alternative meshing procedures are described in the literature. These procedures, which can be implemented whenever a 3D model is derived from CT scans, are based on a voxels-to-hexahedra correspondence. Voxel-based as opposed to contour-based algorithms are capable of automated mesh generation on the basis of the image data. Their geometric precision is nevertheless limited, and these model representations often have jagged edges. Many works in the literature address these problems through specially designed software.[67,68] Another limitation is that voxel-based meshes are typically uniform: all elements have the same size, which is not dependent on the stress field. This involves a higher-than-necessary number of elements and, consequently, high computational costs.

Once the mesh has been generated, it must be checked in order to avoid highly distorted elements: each FE software package has its own specific functions for performing this check. In general, the elements should be as "equiangular" as possible, e.g., should be equilateral triangles or regular tetrahedra. Highly distorted elements such as long, thin triangles or squashed tetrahedra can lead to numerical stability problems caused by round-off errors and do not guarantee convergence.

### 2.2.1. *Notch effect*

Another important aspect is that the elements should be sized according to stress gradients: a finer mesh should be created wherever stress concentrations are expected, e.g., near holes, sharp edges, discontinuities in the material, localized contacts, and so on. Being able to foresee which mesh size will be sufficient calls for extensive experience. The safest procedure is iterative, continuing to refine the mesh until results converge. The effort involved is not always worthwhile, as the notch effect has already been studied and quantified for many typical geometries (such as small holes)[69,70]: in such cases, it is more advantageous (and often more correct) to simulate the geometry of bone without the notch, and then multiply the calculated stress by the tabulated intensification factor.



## 2.3. *Bone mechanical properties*

Numerical studies usually have one of two different aims: assessing a "standard" or "average" behavior or performing a patient-specific study where individual characteristics must be taken into account. This paragraph will discuss the information needed to simulate both "standard" bone behavior or patient-specific bone behavior.

It is important to bear in mind that mechanical properties depend on a range of factors, including the particular bone concerned, the individual and skeletal area to which it belongs (Fig. 4),[71] the species, age and sex of the subject (Fig. 5),[72] the bone's stress history, and any pathologies it is subject to. For any given individual, moreover, the bone's characteristics will change with time. Experimental data, in addition to depending on the objective factors listed above, also depend on whether measurements are performed *in vivo* or *in vitro* and, in the latter case, on the method used to preserve the material. Likewise influential are such test conditions



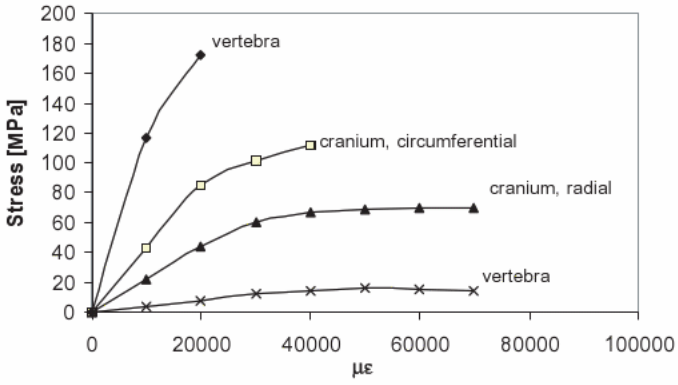


Fig. 4. Stress–strain curves, relative to different human bone segments, tested in compression. Circumferential and radial direction are referred to intact bone segments.

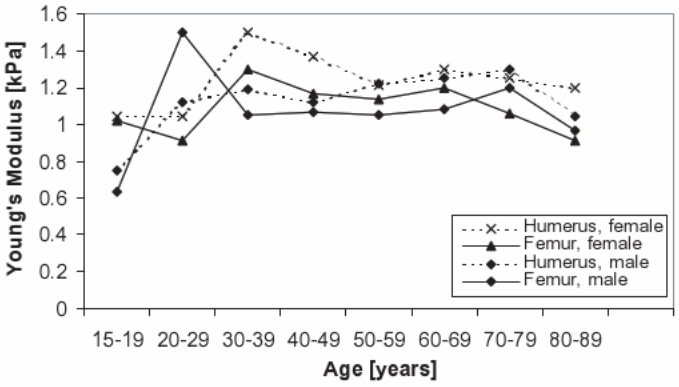


Fig. 5. Pattern of the Young modulus toward age for the femur and the humerus in males and females.

as the type of load, the direction of load application relative to the bone's structural organization, test temperature, and measurement or load errors.[73]

On the whole, though an extensive literature is now available concerning bone characteristics, the data which emerges is far from uniform. Table 1 shows several mechanical properties of cortical bone determined using different techniques by various authors.[74] Table 2 shows the values for modulus of elasticity and strength found by various authors for spongy bone.[75]

Unfortunately, it will be noted that the values show an enormous degree of scatter, which creates a number of problems for the technologist.

### 2.3.1. *Bone density and the main mechanical properties*

Analyses performed by Carter and Hayes,[76,77] who considered spongy bone and cortical bone as a single material whose apparent density (i.e., the ratio of bone tissue mass to total volume, including the spaces occupied by nonmineralized tissue) varies over a wide range, demonstrated that the bone's compressive strength is proportional to the square of apparent density and that the modulus of elasticity in compression is proportional to the cube of apparent density. Since then, a significant amount of experimental work has been focused on establishing empirical relationships between bone mechanical properties and apparent density. Local bone tissue density can be determined *in vivo* using a number of densitometric techniques, including quantitative computerized tomography,[78] dichromatic bone densitometry, and videodensitometric analysis of X-ray images. Establishing a relationship between CT output (Hounsfield units) and bone mechanical properties is particularly attractive because it would make it possible to obtain nonhomogeneous finite element models directly from CT. Unfortunately, no correlation has yet been found between the bone modulus and the CT number,[79] so a noninvasive method for establishing bone properties still remains a challenge.

Table 1. Bone mechanical properties, measured by different authors with different methods; FL stands for fibrous-lamellar bone; HS stands for Haversian systems; 1,2,3 refer, respectively, to radial, circumferential, and axial directions; the numbers enclosed in brackets were obtained assuming axial-symmetry.

| | Direction | Reilly and Burstein | Currey | Van Buskirk and Ashman | Bonfield and Grynpas | Reilly and Burstein | Currey | Reilly, Burstein and Frankel | Knets, Krauya and Vilks | Van Buskirk and Ashman |
|---|---|---|---|---|---|---|---|---|---|---|
| Species | | Cow | Cow | Cow | Cow | Cow | Cow | Man | Man | Man |
| Histology | | FL | FL | ? | ? | HS | HS | HS | HS | HS |
| Method | | Mech | Mech | Ultra | Ultra | Mech | Mech | Mech | Ultra | Ultra |
| Young's | 3 | 26.5 | 25.9 | 21.9 | 17 | 22.6 | 20.3 | 17.0 | 18.4 | 21.5 |
| modulus | 2 | 11.0 | | 14.6 | 11 | 10.2 | | 11.5 | 8.5 | 14.4 |
| [MPa] | 1 | (11.0) | | 11.6 | (11) | (10.2) | | (11.5) | 6.9 | 13.0 |
| Shear | 23 | 5.1 | | 7.0 | | 3.6 | | 3.3 | 4.9 | 6.6 |
| modulus | 13 | (5.1) | | 6.3 | | (3.6) | | (3.3) | 3.6 | 5.8 |
| [MPa] | 12 | | | 5.3 | | | | | 2.4 | 4.7 |
| Poisson's | 31 | 0.41 | | 0.21 | | 0.36 | | | 0.32 | 0.40 |
| ratio | | | | | | | | | | |
| | 32 | 0.41 | | 0.31 | | 0.36 | | 0.41 | 0.31 | 0.33 |
| | 21 | | | 0.38 | | 0.51 | | (0.41) | 0.62 | 0.42 |

Table 2. Review of the mechanical properties of trabecular bone, assessed by different authors and with different methods.

| Region | Year | Storage method | Specimen geometry | Test detail | Mechanical properties |
|---|---|---|---|---|---|
| Proximal tibia | 1974 | Fresh frozen | 5 mm slabs | 0.785 $cm^2$ indenter | Str 1.8–63.6 MPa |
| | 1976 | Dried defatted | $0 \times 14 \times 9\ mm^3$ | Uniaxial stress | Str 0.2–6.7 MPa<br>Mod 1.4–79 MPa |
| | 1977 | Fresh frozen | Cylindrical; diameter = 10.3 mm; height = 5 mm | Uniaxial strain, variable strain rate | Str 1.5–45 MPa<br>Mod 10–500 MPa |
| | 1982 | Dried defatted | 5–6 mm cubes | Rewetted, orthogonal preyield, uniaxial stress | Str 1.5–6.7 MPa<br>Mod 8–457 MPa |
| | 1983 | Fresh frozen | Cylindrical; diameter = 7 mm; height = 5 mm | Uniaxial stress | Str 1–13 MPa<br>Mod 4–430 MPa |
| | 1985 | Fresh frozen | 5 mm slabs | 2.5 mm needle indenter | Str 13.8–116 MPa |
| | 1986 | Fresh frozen | 8 mm cubes | Orthogonal preyield, uniaxial stress | Str 0.52–11 MPa<br>Mod 5–552 MPa |
| Distal femur | 1973 | Fresh frozen | Cylindrical; diameter = 9.5 mm; height = 5 mm | Uniaxial stress; elastic and viscoelastic | Mod 413–1516 MPa |
| | 1974 | Fresh frozen | 5 mm slabs | 0.785 $cm^2$ indenter | Str 2.25–66.2 MPa |
| | 1977 | Fresh frozen | Cylindrical; diameter = 5 mm; height = 8 mm | Uniaxial stress, variable strain rate | Str 0.98–22.5 MPa<br>Mod 59–2942 MPa |
| | 1986 | Fresh frozen | 8 mm cubes | Orthogonal preyield, uniaxial stress | Str 0.56% 18.6 MPa<br>Mod 7.6–800 MPa |
| Proximal femur | 1949 | Fresh | Cylindrical; diameter = 0.25 in.; height = 0.25 in. | Crushing test | Fail 105–382 lb |
| | 1961 | Embalmed | 2.5 × 0.79 cm prism | Uniaxial stress | Str 0.21–14.82 MPa<br>Mod 20.7–965 MPa |
| | 1974 | Fresh | Cylindrical; diameter = 4.8 mm; height = 9.5 mm | Uniaxial stress, 37°C | Str 0.15–13.5 MPa<br>Mod (ave.) 344.7 MPa |
| | 1980 | Fresh frozen | 5 mm cubes | Orthogonal preyield, uniaxial stress | Str 120–310 MPa<br>Mod 1000–9800 MPa |
| | 1983 | Fresh frozen | Cylindrical; diameter = 8 mm; height = 10 mm | Uniaxial stress | Str 0.45–15.6 MPa<br>Mod 58–2248 MPa |
| | 1986 | Fresh frozen | 8 mm cube | Orthogonal preyield, uniaxial stress | Str 2.1–16.2 MPa<br>Mod 49–572 MPa |

### 2.3.2. *Bone anisotropy*

From the mechanical standpoint, bone is a composite material, consisting of low-modulus collagen embedded in hydroxyapatite, which has a high modulus of elasticity. This gives the material anisotropic properties: in other words, its mechanical properties differ according to the direction considered.[74,80] In 1952, Dempster and Liddicoat[81] were among the first to investigate bone anisotropy. They performed compression tests in small cubes of human cortical bone in various directions (longitudinal, transverse, and radial). Though their specimen geometry and preparation technique drew criticism, results indicated that in long bones the modulus of elasticity in the longitudinal direction is approximately twice that in the other two directions.

This result was confirmed by quasi-static tensile tests performed by Reilly and Burstein[82] on strain gauged fresh specimens of human and bovine bone, sampled in the longitudinal, radial, and circumferential directions.



A noninvasive technique for evaluating the type of spongy bone structural organization in any bone element is optical Fourier analysis.[83,84] This technique applied to the observation of X-ray images shows spongy bone architecture, which is difficult to evaluate with visual observations alone.

### 2.3.3. *Influence of strain rate*

Ultimate stress and elastic modulus values depend on strain rate, i.e., bone is a viscoelastic material.[85] For example, it has been calculated[86] that at a strain rate such as that occurs during trauma, a human tibia can absorb 45% more energy than can be absorbed with a slow strain rate. As strain rate increases, Young's modulus $E$ and ultimate stress increase, while ultimate strains and yield strains decrease. All these data should be taken into account whenever a dynamic simulation or a crash simulation is being performed.[87]



### 2.3.4. *Influence of age on bone mechanical properties*

The properties of bone have been analyzed at different ages. Analyses indicate that tensile strength and Young's modulus increase up to 40 years of age, while breaking strains decrease with age. Though a child's bones have a lower modulus of elasticity and bending strength than that of the adult bone, they show greater total strain before fracture and absorb more energy.[88] Burnstein suggested that from the structural standpoint this reduction in breaking strains is the most important change that takes place in bone over time. In tensile tests, this property was found to decrease by 5% per decade in the femur and by 7% in the tibia. This decrease is responsible for a reduction of 32% and 42%, respectively, in the tensile energy which can be absorbed prior to failure by the femur and the tibia between the third and ninth decade of life.[89] The decrease in tensile strength over time has been observed in both the femur and the tibia, where the strength loss is in the order of 2% and 1%, respectively, every 10 years.

2.3.5. *Influence of sex on bone mechanical properties*

Mechanical properties have not been found to differ significantly by sex, though after 50 years of age, bone density increases in men and decreases in women.[90]

2.3.6. *Effect of temperature*

As high temperatures are developed at the bone–cement interface in cemented prosthesis implants,[91] a knowledge of bone's mechanical behavior at various temperatures can be useful. Bonfield and Li[92] tested cortical bone at temperatures between −58°C and 90°C, determining its strain characteristics; they demonstrated that the modulus of elasticity decreases as temperature rises, while the anelastic component is independent of temperature.



2.3.7. *Element type*

The choice of element type has been touched on in the preceding paragraphs. For 3D models, the most common element types are four-node tetrahedra and eight-node hexahedra. Ten-node tetrahedra are preferable to four-node tetrahedra, and, in most cases, hexahedra are the best option. Where the 3D structures can be represented as a shell, plane elements should be preferred to solid ones: this option should be considered, for example, whenever the cortical bone is very thin. In such cases, in fact, plane elements are much more powerful than solid ones because they include two fundamental degrees of freedom which are out-of-plane bending: a thin shell is very likely to bend!

Specific applications may require special elements. Very frequently, two different bodies (the bone and the prosthesis, for example) cannot be cemented because they do not move together. In these cases, the contact (with or without friction) must be simulated. Contact elements guarantee two main features: relative displacements are allowed, and only compressive reactions can be exchanged between the two bodies. Different formulations can be chosen, using either node-to-node, node-to-face, or face-to-face contact elements.[93] The first formulation requires the point of contact to be known *a priori* and is capable of simulating only a limited amount of sliding. The last formulation is the most general, but also the most onerous in terms of computational demand. It should be emphasized that all formulations require that many numerical parameters be specified. Depending on the type of contact algorithm in use, these parameters may include contact stiffness, convergence norm and tolerance, co-penetration monitoring, over-relaxing factors, etc. All these parameters cannot be immediately related to physical entities[94] and therefore cannot be estimated on the basis of the materials and surface finish involved. Though this makes identifying them quite complicated, it must be done by means of experimental tests because analysis results have been shown to be very sensitive to these parameters.[94]

Another finite element formulation which should be mentioned is that used for anisotropic materials. For these elements, the reference system used to define the material's elasticity matrix must be specified. In particular, when the material is considered to be orthotropic, it is necessary to define the orientation of the main axes of orthotropy. Not infrequently, detailed finite element models claim to allow for orthotropic behavior, but leave the main axes of orthotropy in alignment with the general system reference: there can be little doubt that a solution of this kind is worse than considering the material to be isotropic. To achieve a sound simulation, the principal axes of orthotropy should be aligned with the mean trabecular orientation.



### 2.4. *Boundary conditions: Loads and constraints*

In general, loads and constraints should be located at the points where muscle forces or contact forces are applied in physiological conditions. A second consideration is that the impact of constraint distribution on results decreases as their distance increases.

Determining how and where loads will be applied involves many problems: physiological activities vary widely, and it not possible to simulate them all. In addition, not all muscle actions can be simulated, so it is necessary to select the most significant one, and the magnitude and directions of these forces must be assessed. Lastly, the points or areas where these forces are to be applied must be identified.

The choice of physiological activities which are to be simulated depends on the type of analysis being performed: if the strength of an orthopedic structure is to be checked, the heaviest activities should be considered; if, and this is the most common case, fatigue and remodeling phenomena are being analyzed, the most recurrent activities (typically gait for the lower limb) should be simulated.



While most data concerning joint and muscle load amplitudes, directions, and application points can be found in the literature, several guidelines can be given.

The first observation is that the number of loads which need to be simulated depends on the analysis: when micromovements between a prosthesis and bone are being studied, for instance, the most relevant loads are those which are applied on the prosthesis, which is the stiffer component. Conversely, if bone remodeling is being simulated, it is quite important to simulate most of the forces as well as their distribution on a full area; otherwise, certain bone volumes would appear to be under-loaded and consequently would resorb.

The second observation is that the musculoskeletal system is statically indeterminate: kinematic analyses and force platform measurements cannot be used to assess single muscle forces without making rather broad assumptions about muscle activation strategies. This is also true for the most complex experimental analyses where EMG signals are also considered, or certain internal reactions are

measured with an instrumented prosthesis.[95] Consequently, simulating forces whose importance is secondary involves the risk of simply adding numerical noise to the model, with no true benefit.

To provide an example of the issues discussed above, we will now consider the hip joint.

Most studies concern the analysis of fatigue, wear, and bone remodeling, and address the most recurrent activity, i.e., gait and single-leg stance, in particular.

Static analysis of the single-leg stance was performed in the 1930s by Pauwels.[96] The forces acting on the free body include three main coplanar forces: the force of gravity (ground reaction force) against the foot, which is transmitted to the femoral condyles; the force produced by contraction of the abductor muscles; and the joint reaction force on the head of the femur. This static system can be easily solved and makes it possible to identify the magnitude and the orientation of abductor muscle force (approximately two times the body weight, angled 21° from the vertical) and joint force magnitude (about 2.75 times the body weight, angled 16° from the vertical). This is the loading condition which is most commonly implemented in finite element analysis, and has sometimes been scaled $\times 1.5$ in order to take dynamic effects into account. Recently, however, the amount of data regarding muscle loading of the femur has increased considerably,[97] and these forces can thus be more realistically represented in FE analysis. Recent investigations of bone remodeling around hip implants have clearly demonstrated the bone conserving effect of additional muscle forces in the vicinity of their areas of attachment.[98] Additionally, it has been proved that simplified, concentrated load cases generate unrealistic displacement results and high strain magnitudes, exceeding the physiological range.[99] A standardized muscle femur model has been introduced and validated[100]; its use should be considered as an option because it makes it possible to compare results based on different load configurations across various studies.



### 2.5. *Linear and nonlinear analyses*

Analysis becomes nonlinear in any of the following main cases:

— The material's behavior is not linear: the stress–strain curve is not linear. Elasto-plastic behavior is not linear, whereas anisotropic behavior may be.
— Contact elements have been used.
— Large displacements are expected.

The last case has seldom been considered, though many bones undergo large displacements under physiological stresses. This implies that the geometry of the structure changes together with moment arms.

Figure 6 illustrates how results may change between a linear and a nonlinear analysis in the latter case, considering a simple model made of two angled trusses.

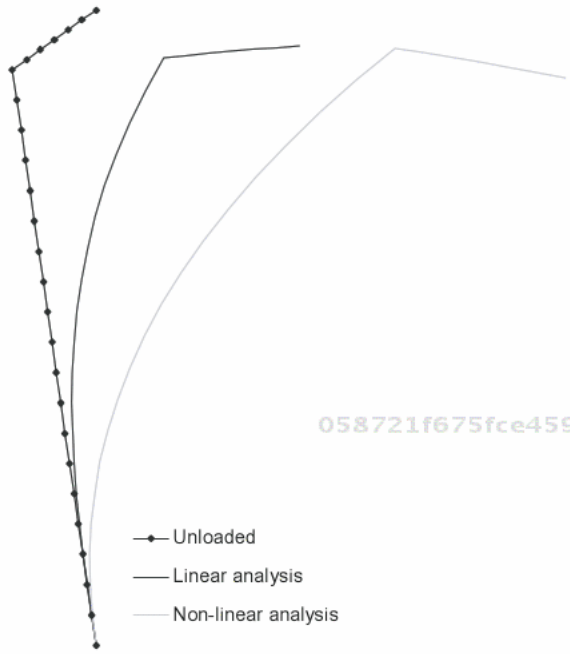


Fig. 6. Deformed shape, calculated from linear and nonlinear analysis; the lower end is fully constrained, the higher end is completely free.

Accordingly, nonlinear analyses may be advisable even when the material's behavior is linear and there are no nonlinear boundary conditions.

### 2.6. *Dynamic analyses*

The finite element method is also suitable for dynamic biomechanical problems.

Dynamic analyses can be performed in order to study vibration modes of whole bones and skeletal segments, or in order to simulate high speed loads as in impact and crash tests. For example, the effects of a head-on automobile crash on the driver have been extensively studied. Here, the model involves discretizing part of the vehicle, the occupant, and bone elements such as the femur and pelvis.[101] Stresses and strains in the femur and pelvis caused by the head-on collision have been computed with these models.

The most crucial aspect of dynamic simulations is damping estimation. This is well known to be the most influential parameter around the resonance frequency, though little experimental data can be found in the literature.

### 2.7. *Post-processing*

The first step of post-processing should consist in checking the quality of results. A good indicator of numerical convergence can be obtained from analyzing strain

discontinuity between adjacent elements. As mentioned in the first paragraph, finite elements only guarantee the continuity of displacements; as the solution gets closer to the "true" value, strain discontinuity drops.

Special care should be taken at those points where stress concentrations occur: it is advisable to keep on refining the mesh until convergence is reached.

Final validation of a finite element model can be achieved only through experimental tests, as will be discussed in the next chapter.

Once a model has been validated, the results can be analyzed. FE results can yield a huge amount of information; the main problem is being able to summarize it!

The first aspect that must be considered is that a stress tensor (consisting of six components in the 3D space) is available, node by node. It is often useful to convert this tensor to a scalar in order to have full-field maps. The simplest way to do so is to make use of the so-called "equivalent stresses," i.e., von Mises stresses, maximum principal stresses, maximum deviatoric stresses, and so on. However, care should be taken to identify the most significant indicator; in particular, it should always be remembered that ultimate bone strength is very different between tensile and compressive stresses, and orthotropic materials have specific equivalent stress formulations. Hoffmann's[102] 3D isotropic failure criterion was applied to the multiaxial test data, along with data from uniaxial compression tests, indicating a compressive strength approximately three times the tensile strength.[103]



Once the most interesting points have been identified using full-field maps, it is always advisable to analyze the full stress tensor in these points in order to understand the stress flow and how the structure is loaded. For example, if the equivalent von Mises stress has been used (as do most investigations in the literature), further stress tensor analysis can make it possible to assess the sign of principal stresses.

Another aspect is that the stress value measured at the most highly stressed nodes should be weighted according to the kind of loading: fatigue situations and sudden loads are much more dangerous, as in static or quasi-static conditions, plastic phenomena take place which redistribute stresses over a wider area. In these cases, the actual magnitude of an equivalent stress is less important than how wide an area is affected by overloading.



In specifically orthopedic applications, the stress field should be judged in relation to the effort that the bone will have to make in order to adapt itself: the farther we are from physiological conditions, the heavier the stress distribution will be. This concept will be further developed in the following section.

## 2.8. *Notes on bone remodeling*

Bone is a living material which adapts and remodels itself according to its mechanical environment.[104] This implies that bone's apparent density, and geometrical and mechanical properties can change with the passing of time.

This behavior can be simulated, assuming an optimality function whose deviation from the physiological condition gives the bone change rate.[105] The mechanical properties of finite elements and the position of external nodes are updated according to this rate, step by step, and a new numerical iteration is started where bone stresses are recalculated and a new bone change rate is obtained. This procedure is repeated until convergence has been reached.

Bone remodeling is usually implemented in finite elements by means of routines which update the elements' properties, according to stress results of the previous iteration.

All these simulations generally require that a number of parameters be estimated: the "optimal stimulus," the function which describes bone remodeling rate, the extreme stress values which determine overloading, and so on. A serious numerical approach cannot overlook the problem of validating these models. For example, the final outcome of an arthroprosthesis can be correctly forecast only if the huge amount of postoperative follow-up is carefully examined. Only a thorough analysis of the past can allow scientists to calibrate the routines designed to predict the future.[106] The literature contains several attempts to evaluate remodeling objectively on the basis of quantitative methods applied to follow-ups: the most recent ones are based on DPA[106] and on CT scans,[107] though almost all available postoperative follow-ups employ radiographs. Most methods based on bone remodeling assessment on X-rays are semi-quantitative because they evaluate geometrical magnitudes quantitatively, while density variations are evaluated through visual inspection with qualitative criteria. We recently proposed a quantitative densitometric evaluation procedure employing standard radiographs. This procedure is now being used to investigate long-term remodeling in patients with total hip prostheses.[108–110]



## 3. Experimental Analysis

### 3.1. *Specimens*

The development of experimental studies in orthopedic biomechanics has been hampered by the problems of specimen availability, specimen collection and preservation methods (as widely reported in the literature[111]), and variability. All these issues will be briefly summarized below, where a viable solution will be suggested.

#### 3.1.1. *Wet bone and dry bone*

The mechanical properties of wet bone differ substantially from those of dry bone. Indeed, significant changes in these properties have been observed within an hour or less from the time bone is removed.[112] Dry bone behaves elastically up to failure, while wet bone shows a wide zone of plastic behavior. Consequently, wet bone requires a much higher ultimate strain energy than dry bone.

### 3.1.2. *Specimen variability*

One of the greatest difficulties in biomechanical experimentation arises from the fact that it is not possible to obtain two identical specimens. Dealing with the femur, Noble *et al.*[113] demonstrated the high geometrical variability of bone shape and the impossibility of finding definite relationships between parameters. This has significant statistical repercussions: if a normal distribution of the property under investigation is assumed and its variance is regarded as equal to its average value,[114,115] it follows that an accuracy of 10% can be achieved with a 95% confidence level only if more than 400 specimens are analyzed. The problem of specimen availability is thus aggravated, while the experimental effort involved becomes prohibitive. For the same reason, biomechanical science has been slow to gain knowledge: the results achieved by different researchers could seldom be compared and discussed because in most cases different specimens were used, and the sample size was limited to fewer than 10 specimens.



### 3.1.3. *A viable solution: Synthetic bones*

Synthetic specimens have become available in recent years. Manufactured by Sawbones (Sawbones Europe AB, Sweden),[116] these specimens not only reproduce the shape of an "average" bone, but also replicate its main mechanical properties. This is a watershed for experimental work in orthopedic biomechanics: since the introduction of synthetic bone, experiments can be repeated on substantially identical specimens, and the results of different research studies can be compared without having to perform analyses on huge populations. Though this is the most important advantage, several other aspects should be mentioned: specimens can be readily acquired, there are no preservation problems, no need for hydration during the experiment, and none of the ethical issues are associated with the use of natural bone.



Synthetic bones have been improved and modified since the first generation was introduced, and are now in their third-generation. Both second-generation and third-generation bones are currently produced. Second-generation types reproduce cortical bone with a glass fiber mat immersed in epoxy resin, while third-generation bones are more detailed from the geometrical point of view; cortical bone consists of short, randomly oriented glass fibers immersed in epoxy resin. In both cases, spongy bone is made of polyurethane foam. Second-generation bones include the femur, the tibia, and the humerus, while a synthetic pelvis was added for third-generation bones.

These bones were validated as regards both their geometry[117] and their mechanical properties.[118–121] Generally speaking, validation was aimed at demonstrating that certain specific properties measured on synthetic bones fell within the associated physiological range of variation. In particular, mechanical tests demonstrated that macroscopic behavior such as displacement under certain loading conditions was well reproduced, but also that stress/strain distribution on the bone surface could be considered realistic.

### 3.2. *Loading and constraining*

The experimental setup whereby structural properties are assessed must be carefully designed in order to achieve significant, repeatable, fully determined tests. Some general guidelines will be given below, and femur analysis will be discussed by way of example.

#### 3.2.1. *Simple constraining*

Basic mechanics has clearly established that only simply constrained systems are fully determined. Though this might seem obvious, over-constrained setups are not infrequently adopted in order to secure a bone element in a certain, known position. As explained by Paul,[122] "no conclusions on structural loading stresses and strains can be drawn from test setups which are statically undetermined." Though it is true from the theoretical standpoint that indeterminate systems can be calculated by taking elastic equations into account, it is very difficult in practice to obtain a correct estimate of support elasticity, a parameter that can have a major influence on results.

Static indeterminacy brings two main problems: the most serious is that the experimental setup is not completely known, and its exact replication consequently cannot be checked. The second problem is that whenever load cells are to be used, they cannot be oriented parallel to the constraining force orientation, and thus will not be correctly installed: they will measure only one component of the load (i.e., the component along the load cell axis), and this measurement will be biased by other components due to cross-talk.

#### 3.2.2. *Large displacements*

All orthopedic joints are known to be heavily stressed: depending on the joint concerned, maximal loads can be as much as two to five times the body weight. Large deformations occur when these loads are applied on bones: as most bones are not straight, these loads result in flexural moments and large rotations. This must be taken into account when designing an experimental setup, because it means that the simple "small displacement" hypothesis, which is so often adopted for structural analysis in classical mechanics, cannot be used. This can lead to important geometrical changes as load is increased: for example, moment arms may change significantly, producing very different stress patterns.

If cameras or IR thermocameras are to be used, the same pixel coordinates on the screen will not identify the same point on the bone; in any case, unconstrained degrees of freedom will permit large generalized displacements.

#### 3.2.3. *Simulation of muscle forces*

Identifying the most relevant forces which need to be simulated is not simple. Joint force is regarded as the base condition, and was the first to be taken into account.

In the 1940, simple models were developed for each single joint, according to a well-established procedure[123]:

- three forces were identified;
- the first was the joint force, whose point of application was given;
- the second was the weight force, and this was completely known as regards its point of application (the center of mass), magnitude, and direction;
- the third force was the most important muscle force, whose point of application and direction were assigned on the basis of anatomical sites;
- the equilibrium of forces and moments was imposed;
- the point of application, magnitude, and direction of all three forces were determined.



According to these models, more complex experimental setups simulated both the joint force and a relevant muscle force.

Sophisticated new experimental tests have recently been performed using force-platforms, video recordings of movements, and, in the most advanced cases, instrumented prostheses.[124] Combined with numerical models, these experimental methods have made it possible to estimate the pattern of many muscle forces during daily activities. This has further complicated the setup used in experimental structural analysis, where more than one muscle force has been simulated. However, as a more sophisticated solution is not always a better solution, the following guidelines should be borne in mind:

- It is important to simulate only those forces which are well known, as doing otherwise will only add noise.
- The primary issue in a loading system is its repeatability: this aspect can never be sacrificed or the experimental tests will be meaningless.
- If dynamic loading is to be applied, a stiff loading system must be implemented. In addition, multiple forces will require multiple actuators, making the setup very complex.
- The experimental setup should be appropriate for the information being sought. If bone-implant micromovements are to be measured, for example, only the loads applied on the stiffer component (the prosthesis) are relevant; conversely, if the stress pattern on a whole bone is being studied, more than one muscle force is likely to have an influence.
- In many cases, it is advisable to forgo a faithful reproduction of actual conditions in favor of a more simple and robust experimental setup. In fact, experimental tests can be used simply in order to validate a numerical model where a greater variety of detailed loading conditions will be introduced.

### 3.2.4. *An example: Femur loading*

We will now examine a very simple example: an experimental setup for the femur which simulates only the joint force.

Figure 7 shows four different loading conditions for the femur, all of which can be found in published articles.[125–128] The first condition on the left, as illustrated in Fig. 7(a), should be avoided if possible: the femur is over-constrained, and the loading system is statically indeterminate. The lower constraint gives a vertical force whose magnitude is known, as it is equal to the force applied by the machine. However, the lower fixture can also give a lateral force and a moment which is not known *a priori*. These indeterminate "secondary" forces can become relevant because of large deformations occurring in the femur in the course of loading (a vertical force over 1000 N is usually applied).



Figure 7(b) illustrates a better setup which is statically determinate. A minor flaw is that the reaction force is known to pass through the upper and lower hinges; consequently, it is not parallel to the machine axis, and the load cell measurement can be biased by cross-talk.

Figures 7(c) and 7(d) show substantially equivalent experimental setups. Both are simply constrained, and the load cell is correctly mounted; the difference is that the setup shown in Fig. 7(c) leaves translational degrees of freedom to the femur head, while that shown in Fig. 7(d) leaves translational degrees of freedoms to the femoral condyles. In both cases, significant translations are likely to take place as a result of large femur deformations. This means that the stress pattern of the proximal (Fig. 7(c)) or distal (Fig. 7(d)) side of the femur changes noticeably as load increases because the arm of the applied force changes. Consequently, the

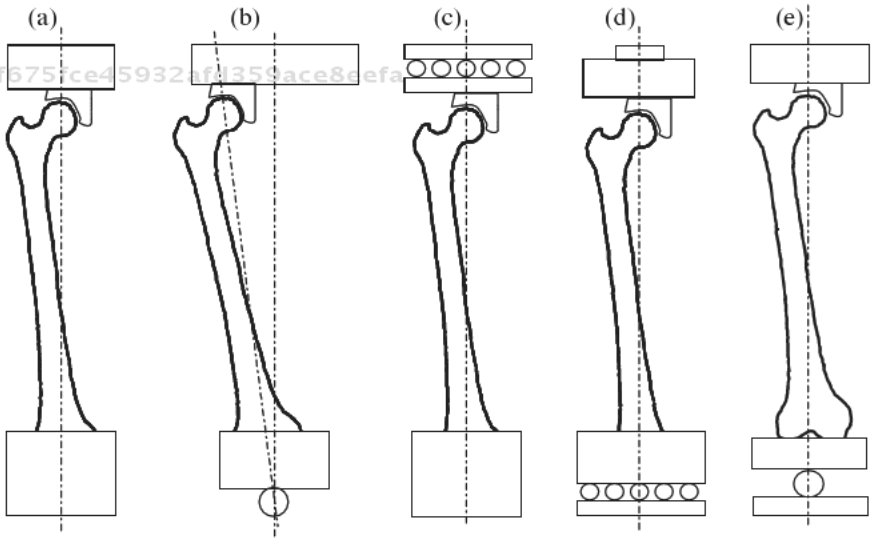


Fig. 7. Different loading setup for the femur.

setup shown in Fig. 7(d) might be more advisable when the proximal femur is being studied and *vice versa*. The last image (Fig. 7(e)) shows an alternative solution with a simply constrained loading system, leaving only rotational degrees of freedom. This configuration avoids all complications generated by large displacements taking place during the test.

When muscle forces are not simulated, the bipedal condition is more closely replicated, while unilateral stance is generally judged to be the most representative loading condition because it is very frequent and involves large stresses. However, loading setups of this kind can be used to validate numerical models where more physiological conditions can be successively simulated.

### 3.3. *Instrumentation*



The goal of mechanical tests on bones is to assess the stress/strain pattern in bone. Appropriate transducers must be used in order to obtain this information. Experimental techniques can be classified in two main categories: the first includes all sensors whereby all tensor components of stress or strain can be measured locally, while the second includes full-field experimental techniques. Full-field experimental techniques make it possible to visualize the stress pattern on a full area. The obvious advantage is that very complete information can be gathered: this can be useful in gaining an understanding of load transmission from a prosthesis to the bone, in validating finite element models or synthetic bones, or in locating the most highly stressed areas. The most serious drawback is that stresses are tensorial variables and cannot be fully represented by a single scalar. Full-field representations, in fact, are related to a scalar given by a combination of principal stresses. In this sense, full-field techniques are the exact opposite of local measurements (e.g., such as those effected using strain gauges): the former gathers partial information on a full area, while the latter technique provides very detailed information on one single point. Stress tensor assessment in the most highly stressed points is an example of how these techniques can cooperate: here, full-field techniques pinpoint which areas are the most heavily stressed, while strain gauges give a full representation of stress tensor. Another example is related to finite model validation: full-field techniques can make it possible to assess if the general stress pattern is properly represented, as well as if numerical values are sound; strain gauges can then be used to validate more localized effects such as notch factor, contact stresses, etc.

A broad overview of commonly used experimental techniques will be given below. The lesser-known full-field techniques will also be discussed in greater detail, though no attempt will be made at providing an exhaustive description.

### 3.4. *Strain gauges*

Strain gauges have been widely used whenever the local strain tensor is to be measured: there can be no doubt that they are the most important transducers

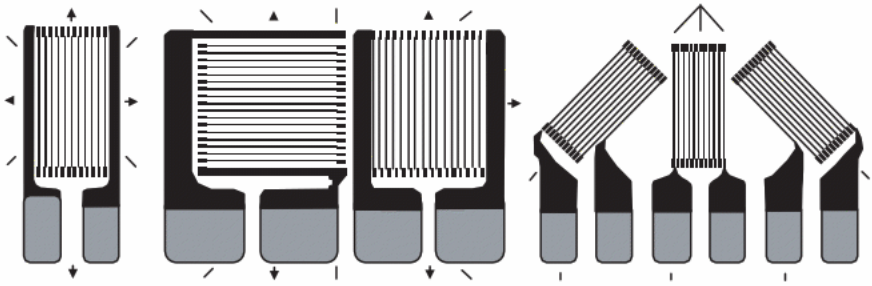

Fig. 8. Uniaxial strain gauge (left); biaxial strain gauge (center), triaxial strain gauge (right).

in experimental stress analysis (Fig. 8). Strain gauges are small electrical resistors which have the property of changing their resistance under strain, and which can be attached to the surface of an object in order to measure strain in that object. One strain gauge is sufficient in uniaxial strain fields; two strain gauges are sufficient in a biaxial strain field if the principal stress directions are known; three strain gauges are necessary in all other conditions. A transducer made of three strain gauges is a "rosette." Strain gauges are sensitive both to mechanical and to thermal strains; thermally produced strains can be compensated when more than one arm of the measuring Wheatstone bridge is active and appropriate connections have been designed.

Many researchers have used the strain gauge technique for experimental investigations.[129–136] The first to apply strain gauges to the bone of a live animal were Gurdjian and Lissner.[129] Lanyon *et al.*[133] attached strain gauge washers to the calcaneal bone of a sheep *in vivo*, calculating the amount and direction of major strains. The same technique was subsequently used[134] to measure the strains occurring on the anteromedial surface of a human tibia during walking and running. Since then, numerous studies have been performed, and there can be no doubt that strain gauges are a well-established experimental technique.

The three primary specifications when selecting strain gauges are operating temperature, the state of strain (including gradient, magnitude, and time dependence), and the stability required by the application. Frequency response is adequate to most applications, while minor drawbacks include the need for contact with the surface (where strain gauges are adhesive-bonded), the minimum size which cannot be less than 0.1 mm, and the need for regular balance.

### 3.5. *Photoelasticity*

Normally, isotropic substances can become birefringent when under stress. Birefringence is a property whereby a ray of light passing through a birefringent material exhibits two refractive indices. The difference in the refractive indices leads to a relative phase delay between the two component waves generated by a ray

of plane polarized light which passed through the photoelastic material. It can be demonstrated that this phase delay is proportional to the difference between principal stresses. The two waves are then brought together in a polariscope, where optical interference produces a fringe pattern which depends on the relative phase delay. Photoelasticity can produce two main types of information: the map of the difference of principal stresses, and the pattern of isostatic curves.

Two main techniques can be applied: transmission photoelasticity and reflection photoelasticity.

For the transmission photoelasticity technique, a transparent plastic scale model must be constructed. The technique is thus of very limited utility in biomechanics because such a model is often incapable of providing a full, accurate representation of the actual component: behaviors like anisotropy and homogeneity are difficult or impossible to model accurately.



Problems connected with modeling and load simulation can be avoided by using the reflection photoelastic technique, in which a birefringent plastic coating is bonded to the structure with a reflective adhesive. The polarized light must therefore pass through the coating twice. In biomechanics applications, the main disadvantage of the technique is that the complexity of bone geometries with edges and corners makes the coating difficult to produce. Milch[137] and Pawels[138] introduced this application, which was used by Refior *et al.*[139] to study femoral implant behavior (Fig. 9). These authors concluded that reflection photoelasticity



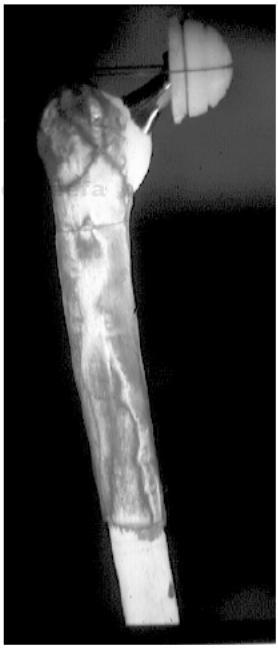

Fig. 9. Photoelastic analysis of an implanted femur.

is a valid procedure, though preparation is time-consuming, and results are difficult to evaluate quantitatively.

A further aspect which should be mentioned is that photoelasticity has been primarily used for static stress analyses, even though high-speed photographic techniques now make it possible to conduct dynamic analyses as well.

### 3.6. *Laser holography*

Holographic interferometry is a noninvasive method used to analyze the mechanical displacement affecting an object undergoing distortion: the diffraction pattern produced by high-intensity laser illumination of a component is recorded photographically. When the image is reconstructed from the diffraction pattern, it will overlie the object exactly if the latter has not changed its position. Conversely, if the object has moved slightly or has been deformed, interference fringes may be observed, the number and spacing of which depend on the amount of displacement. A pulsed laser can be used for dynamic applications.

The equipment is quite expensive, and the experimental setup is very complex and requires painstaking work. However, the theoretical accuracy should be better than 1 $\mu$m.

Some applications of this experimental technique in orthopedics are described in Ref. 140 they include comparative analyses of structures (such as implanted femurs[141]), analysis of deformations in bones such as the hip[142] or the pelvis,[143] and experimental assessment of fracture healing or fixation.[144]

This technique cannot be used to make straightforward structural considerations because output information concerns displacement only: differentiation or even double differentiation is required in order to obtain information about strains and stresses.



### 3.7. *Thermoelastic stress analysis*

This experimental technique analyzes temperature variations induced by a dynamic load. It is known that a specimen changes its temperature when subjected to cyclic stresses. If the strain is elastic, the temperature change is produced by two main effects: elastoplasticity and thermoelasticity. The first phenomenon is due to microplasticity and energy dissipation inside a material, which causes mechanical energy to be converted into heat. Thermoelasticity can be explained by means of the first law of thermodynamics, whereby an increase in volume under adiabatic conditions is associated with a decrease in temperature, and *vice versa*.[145] Thermoelasticity and elastoplasticity produce very different temperature patterns. The first induces a periodic temperature change, synchronous with loading history and proportional to the actual load amplitude, while thermoplasticity produces a continuous temperature increment, which is related to both load amplitude

and the number of cycles performed, and persists until thermal equilibrium is reached. The thermoelastic effect is usually neglected in standard thermography, because it induces very small temperature changes compared to elastoplasticity, but it is the object of stress analysis because it is proportional to the amplitude of the first stress invariant (sum of principal stresses). Full-field thermoelastic stress measurement requires suitable instruments which have a highly sensitive infrared detector (sensitivity is about 1/1000 of a degree) that makes it possible to measure the small temperature change. With dedicated software, the portion of the temperature signal which is coherent with loading history can be isolated.[146,147]

In biomechanics, Thermoelastic Stress Analysis (TSA) is an attractive technique because it can be used to obtain full-field stress maps and does not require special specimen preparation[127,139]: it is sufficient to surface the femur with a black paint. Few applications for this technique can be found in the literature. A preliminary study was performed by Vanderby and Kohles,[148] who analyzed uniaxially loaded cortical bone cubes. They demonstrated that there is a significant linear relationship between TSA and mechanical parameters such as stress, strain, first strain invariant, and strain energy density, but they did not address the problem of calibration. In a later work, the same authors applied thermography to canine femora,[149] calibrating the results on the basis of strain gauge readings; unfortunately, it is not clear how results might be affected by anisotropy. Duncan[127] introduced an extensive critical analysis of TSA's advantages and disadvantages, and subsequently performed a similar study which analyzed a fresh human femur and calibrated the results against strain gauge readings. He mentions the problem of bone anisotropy, suggesting it should not invalidate the results. In the loading system employed for this study, the femoral head is constrained with a spherical hinge, while the condylar end is free to translate; abductor muscles are simulated by means of a suitable belt. This system has the disadvantage that large displacements are allowed, which means that it could be difficult to focus the camera on the same exact point during the loading cycle, especially in the condylar area. Kruger-Franke *et al.*[125] describe another investigation which considered dried human femurs; here, TSA results were compared with strain gauge measurements to demonstrate their quantitative value. A more recent study by Refior *et al.*[139] applied TSA to fresh femurs. In this case, the surfaces could not be coated with black paint: this is a major shortcoming of the experimental procedure, since emissivity cannot be regarded as constant over the entire specimen. Results were assessed from a qualitative standpoint and were compared to photoelastic maps, finding good agreement. However, no details are given about how the authors made allowance for the fact that photoelastic maps reproduce the pattern of the difference of main strains, while thermoelastic maps reproduce the pattern of the first strain invariant (i.e., the sum of main strains). On the whole, few authors (mainly Duncan[127]) have pointed out that TSA cannot be applied straightforwardly to anisotropic materials, and none has clarified which anisotropic materials can still be examined in a quantitative, rigorous way with this

technique. This aspect will be clarified below, where thermoelastic stress analysis will also be applied on a synthetic femur and the calibration factor for this material will be estimated on the basis of strain gauge measurements.

### 3.8. *Thermoelastic stress analysis of anisotropic materials*

If a thin laminate and a plane stress field are assumed, the following thermoelastic equation holds[146]:

$$\Delta T = -\frac{T}{\rho C_\sigma}(\alpha_{ii}\Delta\sigma_{ii} + \alpha_{jj}\Delta\sigma_{jj})\,, \tag{1}$$

where $ii, jj =$ principal directions; Eq. (1) can be rewritten in general coordinates:

$$\rho C_\sigma \frac{\Delta T}{T} = -(\alpha_{xx}\Delta\sigma_{xx} + \alpha_{yy}\Delta\sigma_{yy} + \alpha_{xy}\Delta\sigma_{xy})\,. \tag{2}$$

This is the most general formulation; we can simplify the problem by considering an orthotropic material.

If the preceding equation is written in the orthotropic reference system $ij$, it becomes[150]

$$\Delta T = K_m T(\Delta\sigma_{ii} + \alpha_m \cdot \Delta\sigma_{jj})\,; \quad K_m = -\frac{\alpha_{ii}}{\rho C_\sigma}\,; \quad \alpha_m = \frac{\alpha_{jj}}{\alpha_{ii}}\,. \tag{3}$$

In fact, the shear stress may not be zero in the orthotropic reference system, but is multiplied by term $\alpha^{ij}$ which is equal to zero.

The last equation indicates that it is impossible to apply thermoelastic stress analysis to composite materials (and consequently also to anisotropic materials), since the same principal stresses can result in different signal output as the direction of the principal reference system changes relative to the orthotropic reference system. However, there is a special case, i.e., when expansion coefficients measured in the direction of weft and warp are almost identical. Under this special condition, the thermoelastic signal is again proportional to the first stress invariant, as in the orthotropic case. This condition needs to be carefully checked; one method is to apply thermoelastic stress analysis on specimens for uniaxial tensile tests which have the same geometry, but were obtained at different directions with respect to orthotropic axes.

#### 3.8.1. *Application of TSA on second-generation femurs*

The cortical bone of second-generation composite femurs consists of a fiberglass-fabric reinforced epoxy. Unfortunately, full characterization of the composite synthetic femur material could not be performed because this would have required specimens constructed with a different fiber orientation. Specimens obtained from the diaphysis showed fibers at ±45°, and were used to verify the flexural elastic

modulus specified by the producer and in the calibration required for thermoelastic stress analysis. The flexural elastic modulus was determined to be 14.5 GPa, very close to the 14.2 GPa declared by the producer. Calibration for thermoelastic analysis was then undertaken, applying 10 and 20 MPa uniaxial stress fields. The calibration procedure was repeated, increasing the load frequency from 1 to 20 Hz and measuring 20 points on each specimen for each frequency. The standard deviation of stress levels measured on these points for each frequency never reached 0.8 MPa and is less than 0.7 MPa for 10 Hz measurements. This variability (3.5% on a 20 MPa range) is large, but it cannot be attributed to the precision error alone: composite materials themselves are not uniform. Another interesting aspect is that its absolute value (0.7 MPa) remains the same if loading amplitude is doubled. The calibration constant was evaluated on the basis of the 20 Hz test, because the higher the testing frequency, the better the approximation of adiabatic conditions that can be reached. After calibrating all measurements, an estimated stress amplitude was calculated for each test in order to be able to evaluate bias errors: a 10 Hz frequency was sufficient to produce the required adiabatic condition (giving a bias error which is lower than 0.08 MPa as an absolute value, and 0.4% as a percentage value on a 20 MPa range).

As mentioned earlier, calibration has been performed on the basis of specimens obtained from the diaphysis; in actual fact, however, synthetic femurs are quite inhomogeneous, so calibration constants may vary from point to point. However, this bias is common among all experimental techniques: the stress/strain relationship in strain gauges may vary from point to point, and the same holds true for the photoelastic constant.

A synthetic femur was analyzed, applying a vertical load on its head by means of a spherical mold, and constraining the condyles by a congruent mold. A spherical hinge was placed between this mold and the base of the loading machine in order to avoid constraining moments, while the head center was vertically aligned with the condyles' center to keep lateral loads from arising. Figure 10 shows the anterior stress pattern: the femur diaphysis shows tensional stresses on the lateral side and compressive stresses on the medial side. This is due to flexural moments produced by the femoral head, which is offset with respect to the diaphysis. Epiphysis and condylar ends show both areas in tension and in compression. The spatial resolution of Fig. 10 may appear to be insufficient, though in fact the measurement spot had a diameter of 1.34 mm and spot spacing of 2.02 mm. The problem, however, does not lie with the IR thermocamera's physical limitations (according to the producer, the camera can reach 0.5 mm), but is one of time: around 30 min were required to acquire each of these images. The IR thermocamera was a SPATE 9000 unit and features a sensor which scans the entire analyzed area. Higher resolution images were obtained for a portion of the femur by reducing the distance between it and the IR thermocamera (Fig. 11). In this case, spot diameter was 0.75 mm, and spot spacing was 1.2 mm; particular care was needed in order to avoid displacements in the direction perpendicular to the lens axis. Spurious border effects are more apparent than in the previous images. When detailed analyses are performed, it is

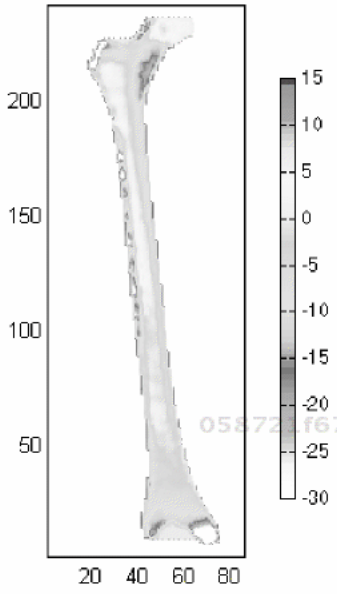


Fig. 10. TSA results: anterior femur.

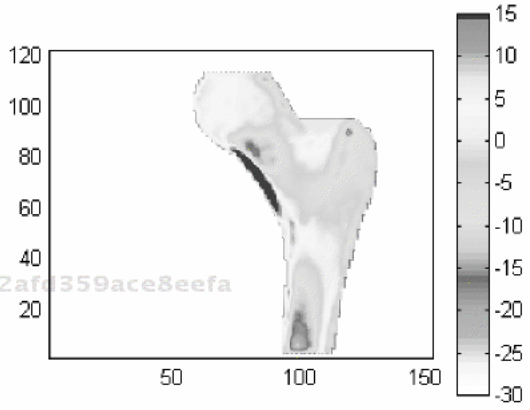


Fig. 11. TSA results: detailed image of the proximal femur.

advisable to use the "motion compensator" device in order to move the focal point along the appropriate direction, according to load variations. This device can be profitably used only in detailed analyses; otherwise, different points would call for very different compensation, which is not possible since the same motion is applied during acquisition of the whole image.

### 3.8.2. *Application of TSA on third generation femurs*

Third-generation composite femurs consist of short E-glass fibers and epoxy resin, a material that is likely to show isotropic behavior. Full characterization

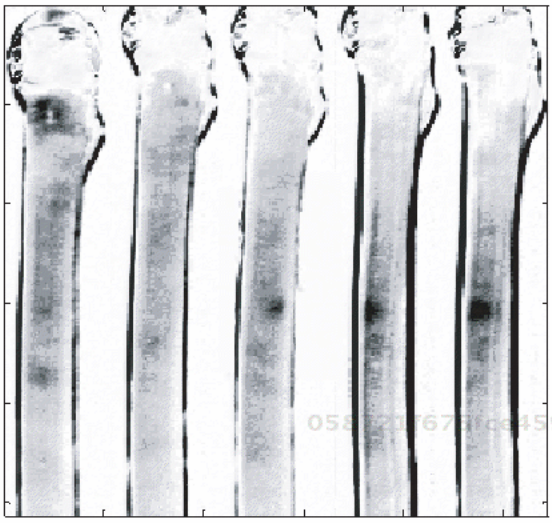

Fig. 12. TSA results: lateral view of femurs implanted with different head offset.

would have required specimens cut from the same sheet at several different orientations; for this material, however, the authors considered that tests performed at two orthogonal directions would be sufficient to confirm the hypothesis of isotropy. Results showed that the two calibration factors were very similar (37.93 and 37.42 MPa/K, respectively), confirming material isotropy and permitting straightforward application of TSA.

The same loading rig described in the previous section was employed; the analyzed specimens consisted of synthetic femurs which were implanted by orthopedic surgeons.

Figure 12 illustrates the lateral images obtained from the same implanted femurs with different head offsets: the larger this offset, the higher and more distal the observed peak stress. Figure 13 shows the anterior view of a full femur: as can be seen, spatial resolution is higher than in Fig. 11. In this case, a Deltatherm thermoelastic camera was employed which includes a full array of sensors, thus eliminating scanning times and permitting better spatial resolution.

### 3.9. *Dynamic analysis of bones*

From the 1970s onward, a number of investigations have addressed the vibration modes of bone segments. These investigations have been based on the impulse response concept: a structure responds to an external impulse by its own free vibration motion, which is determined by the spatial distribution of mass, stiffness, and damping properties over the structure and by the boundary conditions, i.e., the connections with the surroundings.

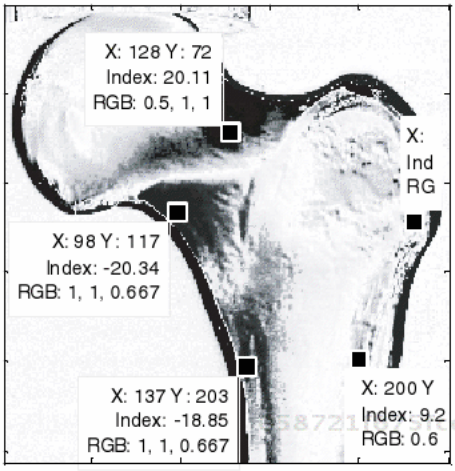


Fig. 13. TSA results: proximal femur.

Frequency response testing is performed in order to determine the free vibration characteristics of the structure and hence its physical properties and/or boundary conditions. In bone biomechanics, these tests are used to evaluate bone behavior in different conditions (e.g., fracture healing and osteoporosis) or to obtain structural information about the bone–implant system, as compared to bone alone. Free vibration characteristics of bone can be used in analyzing motor vehicle drivers and passenger comfort as regards interaction with vehicle-induced vibrations. Another application is the evaluation of potential occupational injuries such as those resulting from the use of pneumatic hammers or, more generally, from moderate loads that are continually repeated throughout the working day. Yet another application is the evaluation of bone response to specific dynamic loading situations such as impact during automobile or sports accidents.[151]

The early investigations in the field were steady state frequency response tests, i.e., tests using a harmonic force input signal with increasing angular frequency. For example, the resonant frequencies of human ulnas were determined by varying the frequency of the harmonic input signal to a modified loudspeaker, used as a shaker, and measuring the bone response with an accelerometer.[152] The frequency values obtained on a number of human subjects were claimed to correlate significantly with the degree of osteoporosis. Thompson[153] and Orne[154] made driving point impedance measurements on the ulna *in vivo*. The impedance head was driven by an electromagnetic shaker and pressed against the ulna using a balance–counterweight system.

Alongside the development of numerical methods, rapid progress in digital data processing techniques and the implementation of Fast Fourier Transform routines have made it possible to determine frequency response functions using an impact or random noise signal as force input and thus analyze a wide frequency range in one

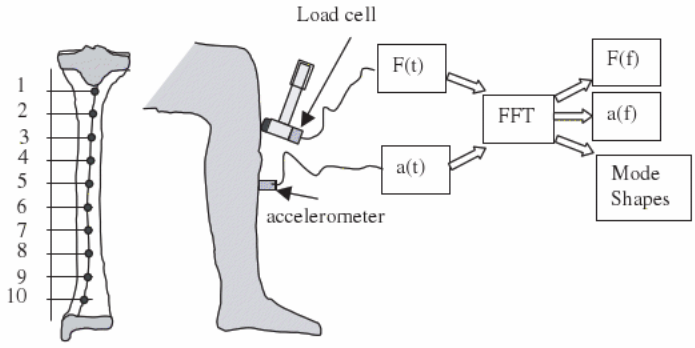


Fig. 14. Experimental setup for modal testing.



simple test.[155] The development of modal analysis software has made it possible to determine all modal parameters experimentally on excised bones as well as bones *in vivo*.[156] In one of the first studies of this kind, modal parameters for the tibias of 20 men were measured. For this purpose, frequency response measurements were made in eight points along the medial face, with the tibia hanging loosely with a knee angle of 90° (Fig. 14). This study revealed a bending mode at 300–350 Hz which was interpreted as the first bending mode in the plane of minimum bending stiffness.[157]

Various teams have studied the application of dynamic response testing in fracture healing monitoring.[158–162] Sonstegard and Matthews[159] made time domain analyses of the acceleration signals in two points at both sides of the fracture. The characteristic parameters used in this study were the amplitude ratio, the curve slope ratio, and the propagation velocity. The results obtained on seven dogs, the left radius of which was surgically fractured, showed that the examined parameters varied over time. Similar studies have been carried out to evaluate osteoporosis.[160,162,163] Many studies have been published concerning the response of bone elements to impact and vibrations. Most of these studies concern the skull and the lumbar spine as part of investigations of car crash traumatology and comfort.

In studies of vibration transmission from vehicle seats to the body, intravertebral movements have been measured *in vivo* by means of transducers linked to lumbar segments with needles. Major rotations and axial movements were measured at a frequency of 5 Hz. There are different criteria and many parameters for determining the severity of an injury to a body structure segment. The terms injury criteria levels or human tolerance levels denote the magnitude of loading of a living body just sufficient to produce a specific type of injury. The magnitude of loading should be expressed in terms of physical parameters (force, acceleration, strain, and pressure) which, when applied to a living body, are capable of producing a change in the physiological or mechanical state of some parts of this body.

The fracture tolerance of mandible, jaw, cheekbone, and nose have been measured, as they have for the skull.[164–166]

For the lower limbs, two different types of investigation are performed: one type addresses the strength and consequently the tolerance levels of each individual component, while the other evaluates the behavior of the entire patella–femur–pelvis system. Overall, data obtained from these investigations point to a threshold force of 6.2 kN.[167] For the femur alone, the tolerance level to axial load would appear to be 10 kN. Impact tests on the patella performed with different impact masses and impact speeds have indicated that fractures of this element are highly influenced by impact speed. The tibia has a low impact strength; transversal load tests have given limit load values between 3 and 9.8 kN depending on the extension of the impact area, and a limit fracture bending moment of 200 Nm.

The head–neck system has been dynamically studied using *in vivo* and *in vitro* experimental methods as well as mathematical methods.[166,168,169] An *in vitro* study of the dynamic response of the head and cervical spine to axial impact loading explored the inertial effects of the head and torso on cervical spine dynamics.[170] Numerous experimental studies have attempted to establish the functional relationship between the impact parameters and the resultant stress, strain, pressure, linear and angular acceleration, etc., in the tissues of the head and neck.

## 4. Conclusions

By this time we can consider proved that bone can be studied, from the mechanical point of view, as an engineering material. We have arrived at this technological interpretation when it became possible to make experimental measures on human body tissues suitable for characterizing them mechanically, giving results in numerical and graphical forms, similar to those available for engineering materials; in other words, it was possible to move from a qualitative study to a quantitative study of the human body.

The knowledge of the mechanical characteristics of bone tissue and of the whole bone elements, particularly as regards its behavior under load, is without doubt fundamental for studying it in various physiological and pathological conditions, looking for substitution materials, and for investigating possibilities of coupling with other materials and devices.

This chapter illustrates how the structural analysis of skeletal body elements can be performed both numerically and experimentally. However each approach has its own limitations: numerical models can be very complex and consequently need to be validated; experimental tests cannot faithfully reproduce the real conditions and require simplifications, in most cases. On the basis of these assumptions, both approaches still remain necessary and complementary.

The above regards bone analysis from a purely mechanical point of view; however, bone, unlike engineering materials, is alive and subject to remodeling in response to stress. Also this particular behavior can be studied in biomechanics with models suitable for simulating the phenomenon.

In the last 40 years many authors have been attending to the quantitative characterization of biological tissues and organs and, particularly, of bone. This work is an attempt to offer an overview of the methods adopted and of the most significant conclusions reached.

## References

1. P. M. Calderale, *XXIII AIAS* (*Associazione Italiana Analisi Sollecitazioni*) *Conf.*, Rende (1994), p. 15.
2. P. M. Calderale, M. M. Gola and A. Gugliotta, *1st Mediterranean Conf. Medical Biological Engineering*, Sorrento II/1. 77 (1977).
3. G. Barberi, M. M. Gola, A. Gugliotta and P. M. Calderale, *Acta Orthop. Belgica* **46** (1980) 728.
4. G. Barberi, M. M. Gola, A. Gugliotta and P. M. Calderale, *Eng. Med.* **7** (1978) 172.
5. M. M. Gola and A. Gugliotta, *J. Strain Anal.* **14** (1979) 29.
6. P. M. Calderale, M. M. Gola and A. Gugliotta, *2nd Meeting Europ. Soc. Biomech.*, Strasbourg (1979), p. 1.
7. P. M. Calderale, M. M. Gola and A. Gugliotta, *Biomechanics VII*, Warsawa (1979), p. 373.
8. P. M. Calderale, M. M. Gola and A. Gugliotta, *Adv. Biomater.*, Vol. 3 (J. Wiley & Sons, 1980), p. 113.
9. R. Huiskes, *Acta Orthop. Scand.*, suppl. (1980) 185.
10. C. Bignardi, P. M. Calderale, M. M. Gola and A. Gugliotta, in *Bioingegneria della riabilitazione*, eds. T. Leo and G. Rizzolatti (Patron Ed., Bologna, 1987), p. 295.
11. R. Huiskes and T. J. Slooff, *Pauwels Symposium*, Berlin (1979).
12. G. M. Mc Niece and H. C. Amstutz, *Biomechanics V*, ed. P. Komi (Baltimore, 1976).
13. R. D. Wood, PhD thesis (Univ. of New South Wales, Australia, 1975).
14. N. L. Svensson, S. Valliappan and R. D. Wood, *J. Biomech.* **10** (1977) 581.
15. H. Röehrle, R. Scholten and W. Sollbach, *Pauwels Symp.*, Berlin (1979).
16. R. D. Crowninschield, R. A. Brand and R. C. Johnston, *25th Ann. Meet. Orthop. Res. Soc.*, S. Francisco (1979).
17. R. R. Tarr, J. L. Lewis, D. Jaycox, A. Sarmiento, J. Schmidt and L. L. Latta, *25th Ann. Meet. Orthop. Res. Soc.*, S. Francisco (1979).
18. I. C. Clarke, T. A. W. Gruen, R. R. Tarr and A. Sarmiento, *Int. Conf. Finite El. Biomech.*, ed. B. R. Simon, Tucson (1980), p. 487.
19. R. Huiskes and E. Y. S. Chao, *J. Biomech.* **16** (1983) 385.
20. G. M. Mc Niece and H. C. Amstutz, *22nd Ann. Meet. Orthop. Res. Soc.*, New Orleans (1976).
21. M. R. Forte, *21st Ann. Meet. Orthop. Res. Soc.*, S. Francisco (1975).
22. D. L. Bartel and G. A. Ulsoy, *21st Ann. Meet. Orthop. Res. Soc.*, S. Francisco (1975).
23. D. L. Bartel and E. Samehyek, *22nd Ann. Meet. Orthop. Res. Soc.*, New Orleans (1976).
24. D. L. Bartel and S. G. Desormeaux, *Symp. Retrivial and Analysis of Orthopaedic Implants Proc.*, eds. A. Weinstein, E. Horowitz and A. W. Ruff (1976).
25. D. L. Bartel and S. G. Desormeaux, *22nd Ann. Meet. Orthop. Res. Soc.*, New Orleans (1976).
26. T. P. Andriacchi, J. O. Galante, T. B. Belytschko and S. J. Hampton, *J. Bone Joint Surg.* **58A** (1975) 618.
27. S. J. Hampton, T. P. Andriacchi, J. O. Galante and T. B. Belytschko, *29th ACEMB*, Boston (1976).

28. P. J. Brockhurst, Centre for Biomedical Eng. Report, Univ. of New South Wales, Australia (1975).
29. H. Röehrle, R. Scholten, W. Sollbach, G. Ritter and A. Grunert, *Arch. Orthop. Unfall-Chir.* **89** (1977) 49.
30. R. Scholten, H. Röehrle and W. Sollbach, *South Afr. Mech. Eng.* **28** (1978) 220.
31. R. D. Crowninschield, R. A. Brand, R. C. Johnston and J. C. Milroy, *J. Bone Joint Surg.* **62A** (1980) 68.
32. R. D. Crowninschield, R. A. Brand, R. C. Johnston and J. C. Milroy, *Clin. Orthop. Rel. Res.* **146** (1980) 71.
33. R. D. Crowninschield, R. A. Brand, R. C. Johnston and D. R. Pedersen, *Clin. Orthop. Rel. Res.* **158** (1981) 270.
34. R. R. Tarr, I. C. Clarke, T. A. Gruen and A. Sarmiento, in *Finite Element in Biomechanics*, eds. R. H. Gallagher, B. R. Simon, P. C. Johnson and J. F. Gross (John Wiley, New York, 1982), p. 345.
35. A. Rohlmann, R. Kolbel and G. Bergmann, *Pauwels Symp.*, Berlin (1979).
36. S. Valliappan, S. Kjellberg and N. L. Svensson, *Int. Conf. Finite El. in Biomech*, ed. B. R. Simon, Tucson (1980), p. 528.
37. S. J. Hampton, T. P. Andriacchi and J. O. Galante, *J. Biomech.* **13** (1980) 443.
38. J. L. Lewis, G. M. Kramer, R. L. Wixson and M. J. Askew, *27th Ann. Meet. Orthop. Res. Soc.*, Chicago (1981).
39. H. H. Vichnin and S. C. Batterman, *28th Ann. Meet. Orthop. Res. Soc.*, Chicago (1982).
40. R. Huiskes and R. Y. Shouten, in *1980-Advances in Bioengineering*, ed. V. C. Mow (ASME, New York, 1980).
41. S. J. Hampton, T. P. Andriacchi, L. F. Draghanich and J. O. Galante, *27th Ann. Meet. Orthop. Res. Soc.*, Chicago (1981).
42. A. Rohlmann, U. Mossner, G. Bergmann and R. Kolbel, *J. Biomech.* **16** (1983) 727.
43. P. M. Calderale and A. Garro, *Int. Conf. Experimental Mechanics*, Beijing (1985).
44. R. Vasu, D. R. Carter and W. H. Harris, *J. Biomech.* **15** (1982) 155.
45. D. R. Carter, R. Vasu and W. H. Harris, *J. Biomech.* **15** (1982) 165.
46. D. R. Pedersen, R. D. Crowninshield, R. A. Brand and R. C. Johnston, *J. Biomech.* **15** (1982) 305.
47. H. Oonishi, *27th Ann. Meet. Orthop. Res. Soc.*, Chicago (1981).
48. J. L. Lewis, *Workshop on Internal Joint Replacement*, Chicago (1977), p. 127.
49. W. C. Hayes, *Workshop on Mechanical Failure of Total Joint Replacement*, Chicago (1978), p. 159.
50. H. H. Vichnin, W. C. Hayes and P. A. Lotke, *25th Ann. Meet. Orthop. Res. Soc.*, Chicago (1979).
51. M. J. Askew and J. L. Lewis, *J. Biomech. Eng.* **103** (1981) 239.
52. S. C. Shrivastava, A. M. Ahmed, D. L. Burke and S. Salomon, *26th Ann. Meet. Orthop. Res. Soc.*, Chicago (1980).
53. K. Murase, R. D. Crowninshield, D. R. Pedersen and T. S. Chang, *J. Biomech.* **16** (1983) 13.
54. D. L. Bartel, A. H. Burstein, E. A. Santavicca and J. N. Install, *J. Bone Joint Surg.* **64A** (1982) 1026.
55. J. L. Lewis, M. J. Askew and D. P. Jaycox, *J. Bone Joint Surg.* **64A** (1982) 129.
56. H. Röehrle, W. Sollbach and J. Gekeler, in *Biomechanics: Principles and Applications*, eds. R. Huiskes, D. H. Van Campen and J. R. De Wijn (Martinus Nijhoff, The Hague, 1982), p. 305.
57. D. H. Van Campen, H. W. Croon and J. Linwer, *25th Ann. Meet. Orthop. Res. Soc.*, Chicago (1979).

58. H. W. Croon, D. H. Van Campen, J. Klok and R. Miehlke, in *Biomechanics: Principles and Applications*, eds. R. Huiskes, D. H. Van Campen and J. R. De Wijn (Martinus Nijhoff, The Hague, 1982), p. 313.
59. P. S. Walker, J. S. Rovick, A. Garg and S. Seijong, *SOMA* (1986), p. 6.
60. M. J. Ackerman, V. M. Spitzer, A. L. Scherzinger and D. G. Whitlock, *Medinfo* 8 Pt 2 (1995) 1195.
61. L. Cristofolini, M. Viceconti, A. Cappello and A. Toni, *J. Biomech.* **29** (1996) 525.
62. http://sirio. cineca. it/hosted/LTM-IOR/back2net/ISB_mesh/isb_mesh. html.
63. H. Weinans, D. R. Sumner, R. Igloria and R. N. Natarajan, *J. Biomech.* **33** (2000) 809.
64. F. Adam, D. S. Hammer, D. Pape and D. Kohn, *Arch. Orthop. Trauma Surg.* **122** (2002) 262.
65. Y. Kang, K. Engelke and W. A. Kalender, *IEEE Trans. Med. Imag.* **22** (2003) 586.
66. E. M. Zanetti, V. Crupi, C. Bignardi and P. M. Calderale, *Med. Biol. Eng. Comput.* **43** (2005) 181.
67. S. K. Boyd and R. Muller, *J. Biomech.* **39** (2006) 1287.
68. J. Kaminsky, T. Rodt, A. Gharabaghi, J. Forster, G. Brand and M. Samii, *Med. Eng. Phys.* **27** (2005) 383.
69. A. H. Burstein, J. Currey, V. H. Frankel, K. G. Heiple, P. Lunseth and J. C. Vessely, *J. Bone Joint Surg.* **54A** (1972) 1143.
70. V. H. Frankel and A. H. Burstein, *Orthopaedic Biomechanics* (Lea & Febiger, Philadelphia, 1970).
71. J. H. McElhaney, N. M. Alem and V. L. Roberts, *ASME, Publ. 70-WA/BHF-2*, New York (1970).
72. O. Lindahl and A. G. H. Lindgren, *Acta Orthop. Scand.* **39** (1968) 129.
73. F. G. Evans, in *Mechanical Properties of Bone*, ed. Charles C. Thomas, Springfield (1973).
74. J. D. Currey, *The Mechanical Adaptation of Bone* (Princeton University Press, 1984).
75. S. A. Goldstein, *J. Biomech.* **20** (1987) 1055.
76. D. R. Carter and W. C. Hayes, *Science* **194** (1976) 1174.
77. D. R. Carter and W. C. Hayes, *J. Bone Joint Surg. Am.* **59** (1977) 954.
78. R. J. McBroom, W. C. Hayes, W. T. Edwards, R. P. Goldberg and A. A. White, *J. Bone Joint Surg.* **67A** (1985) 1206.
79. M. Cuppone, B. B. Seedhom, E. Berry and A. E. Ostell, *Calcif. Tissue Int.* **74** (2004) 302.
80. J. D. Currey, *Biorheology* **2** (1964) 1.
81. W. T. Dempster and R. T. Liddicoat, *Am. J. Anat.* **91** (1952) 331.
82. D. Reilly and A. Burstein, *J. Biomech.* **8** (1975) 393.
83. C. E. Oxnard, *Am. Cleft. Palate J.* **23** (1987) 110.
84. C. E Oxnard, *J. Biomech.* **26**(Suppl. 1) (1993) 63.
85. J. H. McElhaney, *J. Appl. Physiol.* **21** (1966) 1231.
86. V. H. Frankel and A. H. Burstein, in *Biomechanics and Related Bio-Engineering Topics*, ed. R. M. Kenedi (Pergamon Press, New York, 1965), p. 381.
87. P. J. Arnoux, D. Cesari, M. Behr, L. Thollon L and C. Brunet, *Traffic Inj. Prev.* **6** (2005) 288.
88. J. D. Currey and G. Butler, *J. Bone Joint Surg.* **57A** (1975) 810.
89. A. H. Burstein, D. T. Reilly and M. Martens, *J. Bone Joint Surg.* **58A** (1976) 82.
90. O. Lindahl and A. G. H. Lindgren, *Acta Orthop. Scand.* **38** (1967) 133.
91. J. N. Wilson and J. T. Scales, *Clin. Orthop.* **72** (1970) 145.
92. W. Bonfield and C. H. Li, *J. Biomech.* **1** (1968) 323.

93. M. Viceconti, R. Muccini, M. Bernakiewicz, M. Baleani and L. Cristofolini, *J. Biomech.* **33** (2000) 1611.
94. M. Bernakiewicz and M. Viceconti, *J. Biomech.* **35** (2002) 61.
95. G. Bergmann, G. Deuretzbacher, M. Heller, F. Graichen, A. Rohlmann, J. Strauss and G. N. Duda, *J. Biomech.* **34** (2001) 859.
96. F. Pauwels, ed., *Der Schenkelsbruch: Ein Mechanisches Problem* (Ferdinand Enke, Germany, 1935).
97. C. Bitsakos, J. Kerner, I. Fisher and A. A. Amis, *J. Biomech.* **38** (2005) 133.
98. J. R. Britton, L. A. Walsh and P. J. Prendergast, *Clin. Biomech.* **18** (2003) 637.
99. K. Polgar, H. S. Gill, M. Viceconti, D. W. Murray and J. J. O'Connor, *Proc. Inst. Mech. Eng. [H]* **217** (2003) 173.
100. K. Polga, H. S. Gill, M. Viceconti, D. W. Murray and J. J. O'Connor, *Proc. Inst. Mech. Eng. [H]* **217** (2003) 165.
101. P. M. Calderale, A. Garro and G. L. Lorenzi, *IVth IRCOBI Conf.*, Goeteborg (1979), p. 305.
102. O. Hoffmann, *J. Comp. Mater.* **1** (1967) 200.
103. J. L. Stone, G. S. Beaupre and W. C. Hayes, *J. Biomech.* **16** (1983) 743.
104. D. R. Carter, D. Fyhrie and T. E. Orr, *J. Biomech.* **22** (1989) 231.
105. G. S. Beaupre and W. C. Hayes, *J. Biomech. Eng.* **107** (1985) 249.
106. J. Kerner, R. Huiskes, G. H. van Lenthe, H. Weinans, B. van Rietbergen, C. A. Engh and A. A. Amis, *J. Biomech.* **32** (1999) 695.
107. M. Lengsfeld, D. Gunther, T. Pressel, R. Leppek, J. Schmitt and P. Griss, *J. Biomech.* **35** (2002) 1553.
108. A. L. Audenino, P. M. Calderale and E. M. Zanetti, *Med. Eng. Phys.* **18** (1996) 382.
109. A. L. Audenino, P. M. Calderale and E. M. Zanetti, *J. Real-Time Imag.* **3** (1997) 399.
110. A. L. Audenino, P. M. Calderale and E. M. Zanetti, *Med. Eng. Phys.* **19** (1997) 495.
111. F. Linde and H. C. Sorensen, *J. Biomech.* **26** (1993) 1249.
112. E. D. Sedlin and C. Hirsch, *Acta Orthop. Scand.* **37** (1966) 29.
113. P. C. Noble, J. W. Alexander, L. J. Lindahl, D. T. Yew, W. M. Granberry and H. S. Tullos, *Clin. Orthop. Rel. Res.* **235** (1988) 148.
114. G. T. Shybut, M. J. Askew, R. Y. Hori and S. D. Stulberg, *Proc. Inst. Med. Chic.* **33** (1980) 95.
115. R. D. Crowninshield, D. R. Pedersen and R. A. Brand, *J. Biomech. Eng.* **102** (1990) 230.
116. http://www. sawbones. com.
117. P. T. Bianco, J. E. Bechtold. R. F. Kyle and R. B. Gustilo in *Proc. Biomechanics Symp.*, eds. P. A. Torzilli and M. H. Friedman (ASME, New York, 1989), p. 297.
118. L. Cristofolini, M. Viceconti, A. Cappello and A. Toni, *J. Biomech.* **29** (1996) 525.
119. J. A. Szivek and R. L. Gealer, *J. Appl. Biomater.* **2** (1991) 277–280.
120. L. Cristofolini and M. Viceconti, *J. Biomech.* **33** (2000) 279.
121. A. Heiner and T. Brown, *J. Biomech.* **34** (2001) 773.
122. J. P. Paul, *Med. Eng. Phys.* **23** (2001) 435.
123. V. H. Frankel and M. Nordin, in *Basic Biomechanics of the Skeletal System*, eds. V. H. Frankel and M. Nordin (Lea & Febiger, Philadelphia, USA, 1980), p. 129.
124. G. Bergmann, F. Graichen and A. Rohlmann, *J. Biomech.* **26** (1993) 969.
125. M. Kruger-Franke, A. Heiland, W. Plitz, H. J. Refior, *Z. Orthop. Ihre Grenzgeb.* **133** (1995) 389.
126. J. B. Finlay, D. G. Chess, W. R. Hardie, C. H. Rorabeck and R. B. Bourne, *J. Orthop. Res.* **9** (1991) 749.

127. J. L. Duncan, in *Strain Measurement in Biomechanics*, eds. A. W. Miles and K. E. Tanner (Chapman & Hall, London, 1992), p. 157.
128. L. Cristofolini, M. Viceconti, A. Cappello and A. Toni, *J. Biomech.* **29** (1996) 525.
129. E. S. Gurdjian and H. R. Lissner, *J. Neurosurg.* **1** (1944) 393.
130. F. G. Evans, *Am. J. Phys. Anthropy* **11** (1953) 413.
131. G. V. B. Cochran, *J. Biomech.* **5** (1972) 119.
132. V. L. Roberts, *Exp. Mech.* **6** (1966) 1.
133. L. E. Lanyon, *J. Biomech.* **6** (1973) 41.
134. L. E. Lanyon, W. G. J. Hampson, A. G. Goodship and J. S. Shan, *Acta Orthop. Scand.* **46** (1975) 256.
135. L. E. Lanyon and D. G. Baggott, *J. Bone Joint Surg.* **58B** (1976) 436.
136. D. R. Carter, D. J. Smith, D. M. Spengler, C. H. Daly and V. H. Frankel, *J. Biomech.* **13** (1980) 27.
137. H. Milch, *J. Bone Joint Surg.* **22** (1940) 621.
138. F. Pawels, Uber die bedeutung der bauprinzipien des stutz-und bewegungsapparates rur die deansprunchungder rohrenknochten, *Acta Anat.* **12** (1951) 207.
139. H. J. Refior, C. Schidlo, W. Plitz and S. Heining, *Orthopedics* **25** (2002) 505.
140. J. C. Shelton and D. M. Katz, *J. Med. Eng. Technol.* **15** (1991) 209.
141. D. M. Katz, S. Blatcher and J. C. Shelton, *Med. Eng. Phys.* **20** (1998) 114.
142. M. T. Manley, J. Gurtowski, L. Stern, M. Halioua and T. Bowins, *Trans. ORS* **8** (1983) 99.
143. D. Vukicevic, S. Vukicevic, I. Vinter and K. Sankovic, in *Optics in the Biomedical Sciences*, eds. G. von Bally and P. Greguss (Springer, Berlin, 1982), p. 138.
144. J. C. Shelton, D. Gorman and W. Bonfield, *J. Mater. Sci. Mater. Med.* **1** (1990) 146.
145. W. Thomson (Lord Kelvin, 1853), *Trans. Roy. Soc. Edinburg* **20** (1853) 261.
146. B. J. Rauch and R. E. Rowlands, in *Handbook of Experimental Mechanics*, ed. A. S. Kobayashi (VCH Publishers, New York, 1993), Chap. 14.
147. A. L. Audenino, V. Crupi and E. M. Zanetti, *Exp. Tech.* **28** (2004) 23.
148. R. Vanderby Jr and S. S. Kohles, *J. Biomech. Eng.* **113** (1991) 418
149. S. S. Kohles and R. Vanderby Jr, *Med. Eng. Phys.* **19** (1997) 262.
150. S. T. Lin and R. E. Rowlands, *Exp. Mech.* **35** (1995) 257.
151. G. Van der Perre, in *Functional Behavior of Orthopaedic Biomaterials*, eds. P. Ducheyne and G. H. Hastings (CRC Press, 1984), p. 99.
152. J. M. Jurist, H. D. Hoeksema, D. A. Blacketter, R. K. Snider and E. R. Garner, *Orthopaedic Mechanics, Procedures and Devices* — Vol. 3, Chap. 1, eds. D. W. Ghista and R. Roaf (Academic Press, London, 1981).
153. J. A. Thompson, *Aerosp. Med. Assoc. Annu. Sci. Meet.*, Las Vegas (1973), p. 133.
154. D. J. Orne, *J. Biomech.* **7** (1974) 250.
155. J. Péters, *Int. Seminar Modal Analysis*, eds. H. Van Brussel and R. Snoeys (Katholieke Universiteit Leuven, 1977), p. 18.
156. G. Van der Perre, R. Van Audekercke, J. Vandecasteele, M. Martens and J. C. Mulier, *Am. Soc. Mech. Eng. Biomech. Symp.*, eds. W. C. Van Buskirk and S. L. Y. Woo (ASME, New York, 1981), p. 173.
157. J. Vandecasteele, G. Van der Perre, R. Van Audekercke and M. Martens, in *Mechanical Factors and the Skeleton*, ed. I. Stokes (John Libbey, London, 1980), p. 98.
158. E. Markey and J. M. Jurist, *Wis. Med. J.* **73** (1974) 62.
159. D. A. Sonstegard and L. S. Matthews, *J. Biomech.* **9** (1976) 689.
160. C. R. Steele and A. F. Gordon, in *Advances in Bioengineering, Am. Soc. Mech. Eng. Symp.* (ASME, New York, 1978), p. 85.

161. J. L. Surber, K. G. Kitchen, H. H. Doemland, J. J. Ketzner and D. H. Stanley, *Biomed. Sci. Instrum.* **15** (1979) 31.
162. M. Cornelissen, P. Cornelissen and G. Van der Perre, in *Biomechanics: Principles and Applications* (*Developments in Biomechanics*), Vol. 1, eds. R. Huiskes, D. H. Van Campen and J. R. de Wijn (Martinus Nijhoff, The Hague, Netherlands, 1982), p. 213.
163. J. M. Jurist, *Phys. Med. Biol.* **15** (1970) 417.
164. T. B. Khalil, D. C. Viano and D. L. Smith, *J. Sound Vib.* **63** (1979) 351.
165. C. Christmann and F. Holzweissig, *Anat. Anz.* **142** (1978) 229.
166. W. Goldsmith, in *Biomechanics: Its Foundations and Objectives*, eds. Y. C. Fung *et al.* (Prentice-Hall, Englewood Cliffs, 1972), p. 585.
167. Human Tolerance to Impact Conditions as Related to Motor Vehicle Design (Society of Automotive Engineers, Warrendale, 1980).
168. T. B. Khalil and R. P. Hubbard, *J. Biomech.* **10** (1977) 119.
169. E. S. Gurdjian, H. R. Lissner, F. G. Evans, L. M. Patrick and W. G. Hardy, *Surg. Gynecol. Obstet.* **113** (1961) 185.
170. R. W. Nightingale, J. H. McElhaney, W. J. Richardson and B. S. Myers, *J. Biomech.* **29** (1996) 307.

This page intentionally left blank

# CHAPTER 7

# INDENTATION TECHNIQUE FOR SIMULTANEOUS ESTIMATION OF YOUNG'S MODULUS AND POISSON'S RATIO OF SOFT TISSUES

PONG-CHI CHOI, HANG-YIN LING and YONG-PING ZHENG*
*Department of Health Technology and Informatics*
*The Hong Kong Polytechnic University*
*Kowloon, Hong Kong, China*

Young's modulus and Poisson's ratio are the important parameters for representing the mechanical properties of soft tissue. Indentation test is an *in vivo*, non-invasive and convenient technique for measuring the tissue properties. In this chapter, two methods for the simultaneous estimation of Young's modulus and Poisson's ratio of soft tissues using indentation are presented. With the consideration of the finite deformation effect, the first method is based on the use of two sized indentors for conducting two different indentation tests, whereas the second one is only a single indentation test. Finite element (FE) analysis was used to demonstrate the feasibility of these two methods. The FE results were found to be comparable to the one shown in the previous literatures. It was revealed that finite deformation effect is of vital importance in the estimation of the Young's modulus and Poisson's ratio. Simultaneous estimation of these two parameters is necessary for achieving an accurate measurement of the Young's modulus.

*Keywords*: Soft tissue; Young's modulus; Poisson's ratio; indentation; finite element analysis.



## 1. Introduction

Indentation testing has been widely used as a non-destructive, quick, and quantitative diagnostic tool for assessing the mechanical properties of soft human tissues *in vivo*, such as articular cartilage, skin, and subcutaneous tissues. For the assessment of the articular cartilage, changes in the tissue stiffness would provide an early warning of cartilage degeneration.[1,2] Moreover, any pathological changes in the mechanical properties of the skin and subcutaneous tissues would also give some implications on various diseases like edema, tissue proliferation, and abnormal calcification.[3–5] Motivated by the need of the quantitative assessment of the tissues, many research efforts have been focused on the development of various indentation instruments in the past decades.[6–9]

*Correponding author.

Tissue thickness ($h$), indentation force ($P$), and tissue deformation ($w$) are the essential parameters that we need to measure before or during the indentation test. $h$ can be measured before the test by using needle punch,[10] optical or ultrasound methods.[6,11] During the test, both $P$ and $w$ can be recorded simultaneously with various approaches. $P$ can be obtained from strain gauges[6] and fiber optic sensor,[12] while $w$ can be measured by a displacement transducer-linearly variable differential transformer (LVDT),[13] spatial sensors[14] or ultrasonic methods.[1,6,15,16] By knowing these three parameters, the Young's modulus of tissue can be calculated by the following equation in the case of using a flat ended cylindrical indentor,[17]

$$E = \frac{(1-v^2)}{2a\kappa(v, a/h)} \cdot \frac{P}{w}\,, \tag{1}$$

where $E$ is Young's modulus, $P$ is indentation force, $v$ is Poisson's ratio, $w$ is tissue deformation, $a$ is indentor radius, $h$ is tissue thickness, and $\kappa$ is a scaling factor, which depends on the aspect ratio ($a/h$) and $v$. It is reminded that this equation is only valid for the infinitesimal indentation problem of a thin elastic layer bonded on a rigid half-space. The tissue was assumed to be linear elastic, homogenous, and isotropic. Only the numerical solution of $\kappa$ has been presented for $0.3 \leq v \leq 0.5$. Later, Jurvelin[18] further estimated $\kappa$ for which $v$ is smaller than 0.3. By considering the effects of finite deformation, Zhang *et al.*[19] reported a new table of $\kappa$ by using nonlinear finite element (FE) analysis. It was found that $\kappa$ increased almost linearly with the tissue deformation. Their results obtained from the infinitesimal deformation were comparable with that reported by Hayes *et al.*[17]

A constant Poisson's ratio in the range of 0.3–0.5 has been widely accepted to study the mechanical properties of tissues.[20,21] However, cautions have to be taken when this assumption is applied over different body sites, in patients with different diseases and ages since the Poisson's ratio may vary from individual to individual and from site to site. The estimated error of Young's modulus may be greatly increased due to the incorrect assumption of Poisson's ratio. Many methods have been introduced to measure the Poisson's ratio of tissues. In particular, optical and mechanical methods have been used to measure the Poisson's ratio of articular cartilage.[22] In the optical measurements, an axial load was applied and the strain in the lateral direction was then measured using microscope in order to calculate the Poisson's ratio. On the other hand, confined and unconfined compressions were conducted by the mechanical method to determine the aggregate modulus ($H_a$) and Young's modulus ($E$), respectively. The Poisson's ratio can be estimated using the following equation:

$$H_a = \frac{1-v}{(1+v)(1-2v)} \cdot E\,. \tag{2}$$

Although these two methods can be used to determine the Poisson's ratio effectively, they can only work *in vitro* but not *in vivo*.

*In vivo* measurement of the Poisson's ratio can be achieved by using a recent approach, in which both Young's modulus and Poisson's ratio can be estimated simultaneously via two indentation tests with two different sized indentors.[23] Rearranging Eq. (1) with two sets of force-deformation relationship obtained from the indentation tests with two different sized indentors, the Poisson's ratio can then be estimated by the following equation:

$$\frac{P_1/w_1}{P_2/w_2} = \frac{a_1}{a_2} \cdot \frac{\kappa(a_1/h, v)}{\kappa(a_2/h, v)}, \tag{3}$$

where the subscripts 1 and 2 represent the indentors 1 and 2, respectively. Since Eq. (3) was derived based on Eq. (1), Eq. (3) is only valid for the infinitesimal indentation. However, it is difficult to control the indentation with the infinitesimal indentation in practice and such infinitesimal deformation and load cannot be easily measured by some available sensors. From the experimental and numerical results reported by Jin and Lewis,[23] the indentation deformation was found to be about 2%–10% of the tissue thickness, instead of infinitesimal deformation. In this case, the assumption of infinitesimal indentation might cause some significant errors on those results.



In this study, two methodologies are introduced for the simultaneous estimation of Young's modulus and Poisson's ratio of soft tissues using indentation techniques by considering the finite deformation effect. The first one is to use two different sized indentors for performing two different indentation tests, while another one is to exploit a single indentation test only. The feasibility of the proposed methods is demonstrated in virtue of a FE analysis. The accuracy of the FE model for the indentation tests is validated by means of comparing the results from the previous literatures in the case of the infinitesimal indentation.[17,18] In the study of the two different sized indentors, both Young's modulus and Poisson's ratio were calculated from the simulated indentation data with and without considering the finite deformation effect. The importance of the finite deformation effect on the calculation of these two parameters is highlighted. By using the single indentation test method, the relationship between the Poisson's ratio and deformation dependent indentation stiffness for different aspect ratios is established. In virtue of the simulated force-deformation data, the Young's modulus and Poisson's ratio can than be calculated based on this relationship.



## 2. Methodologies

In the present study, the finite deformation effect is considered for the simultaneous estimation of Young's modulus and Poisson's ratio of soft tissue for both methods. According to the study from Zhang *et al.*,[19] Eq. (1) can be improved by taking into

account of the finite deformation effect as

$$E = \frac{(1-v^2)}{2a\kappa_n(a/h, v, w/h)} \cdot \frac{P}{w}\,. \tag{4}$$

In this equation, $\kappa_n$, a deformation-dependent scaling factor, depends not only on the aspect ratio $(a/h)$ and Poisson's ratio $(v)$, but also on the deformation ratio $(w/h)$. Moreover, it revealed that $\kappa_n$ almost linearly depends on the tissue deformation $(w)$.[19]

### 2.1. *Two different sized indentors*

In the indention of using two different sized indentors, Eq. (3) can be rewritten as follows:



$$f(a_1/h, a_2/h, v) = \frac{P_1 w_2 a_2}{P_2 w_1 a_1}\,, \tag{5}$$

where $f(a_1/h, a_2/h, v)$ is the ratio between the two $\kappa$ values with the same Poisson's ratio but different aspect ratios with two different radii of indentors. For the given radii of indentors and tissue thickness, $f$ is a function only dependent on the Poisson's ratio and can be obtained from the table of $\kappa$ for different $a/h$ and $v$ given by Hayes *et al.*[17] Figure 1 shows the nonlinear relationship between $v$ and $f$ when $a_1$, $a_2$, and $h$ are equal to 4.5, 9, and 4.5 mm, respectively. Using Eq. (5) and Fig. 1, the Poisson's ratio $v$ can be calculated from the force and deformation pairs obtained from the FE analysis.



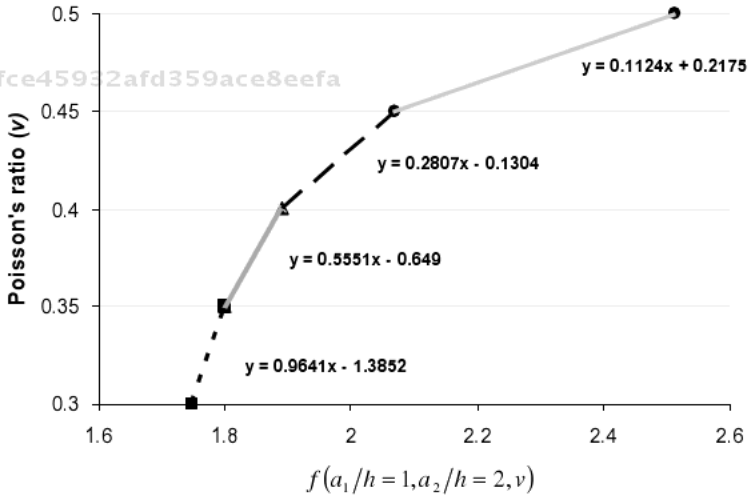


Fig. 1. The nonlinear relationship between the Poisson's ratio $(v)$ and the ratio of two $\kappa$ factors for infinitesimal indentation, i.e., $\kappa(a_1/h, v)/\kappa(a_2/h, v)$ with $a_1 = h = 4.5$ mm and $a_2 = 9$ mm. Linear interpolation can be used to calculate the corresponding Poisson's ratio.

The method of using two different sized indentors presented by Jin and Lewis[23] can be further improved by including the nonlinear effect of finite deformation. Equation (3) can be modified in association with the deformation-dependent scaling factor shown in Eq. (4). Then, the modified Eq. (3) yields,

$$\frac{P_1/w_1}{P_2/w_2} = \frac{a_1}{a_2}\frac{\kappa_n(a_1/h, v, w/h)}{\kappa_n(a_2/h, v, w/h)}. \tag{6}$$

This method provides a new approach for simultaneous estimation of the Young's modulus and the Poisson's ratio in two indentation tests with two different sized indentors. Equation (6) can be rewritten as

$$g(a_1/h, a_2/h, w/h, v) = \frac{P_1 w_2 a_2}{P_2 w_1 a_1}, \tag{7}$$



where $g(a_1/h, a_2/h, w/h, v)$ is similar to $f(a_1/h, a_2/h, v)$ except that it includes the finite deformation effect. For the given radii of indentors, tissue thickness and the deformation, $g$ is a function of the Poisson's ratio only. Figure 2 shows this function for different deformation ratio $(w/h)$, which was derived from Zhang *et al.*[19] It is obvious that different curves need to be used for different $w/h$ using Fig. 2 and Eq. (7). To calculate the Poisson's ratio using the two different sized indentors approach, $f$ and $g$ are estimated based on the simulated force-deformation data associated with Eq. (7). Using linear interpolation between two neighboring data points, an arbitrary Poisson's ratio can be predicted according to the conversion table for the Poisson's ratio and deformation ratio, as shown in Table 1. After obtaining the Poisson's ratio, the Young's modulus of the tissue can be calculated using Eq. (1) or (4) for the cases with and without considering the finite deformation effect of indentation, respectively.



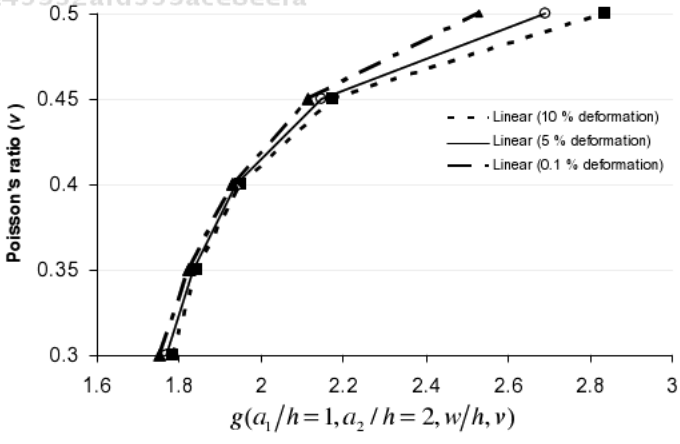


Fig. 2. The nonlinear relationship between Poisson's ratio $(v)$ and ratio of two $\kappa$ factors with different indentation deformations, which are calculated from Zhang's data.

Table 1. The conversion table of $f(a_1/h, a_2/h, v)$ and $g(a_1/h, a_2/h, w/h, v)$ between the Poisson's ratio and deformation ratio with $a_1 = h = 4.5\,\text{mm}$ and $a_2 = 9\,\text{mm}$.

| | Deformation ratios ($w/h$) | | | | |
|---|---|---|---|---|---|
| Poisson's ratios ($v$) | 0.1% | 2.5% | 5.0% | 7.5% | 10.0% |
| 0.30 | 1.754 | 1.762 | 1.770 | 1.779 | 1.787 |
| 0.35 | 1.824 | 1.829 | 1.834 | 1.839 | 1.844 |
| 0.40 | 1.930 | 1.935 | 1.940 | 1.945 | 1.949 |
| 0.45 | 2.114 | 2.130 | 2.146 | 2.161 | 2.175 |
| 0.50 | 2.529 | 2.611 | 2.692 | 2.767 | 2.837 |

### 2.2. *A single indentation*



Sometimes, the necessity of using two indentors may reduce the flexibility of two different sized indentors method. An alternative method for the simultaneous estimation of the Young's modulus and the Poisson's ratio using a single indentation test alone is developed. The proposed method uses to establish the relationship between the Poisson's ratio and the deformation dependent indentation stiffness. In this method, it is assumed that $\kappa_n$ can be written as

$$\kappa_n(a/h, v, w/h) = \kappa(a/h, v) \cdot (1 + \beta w/h)\,, \tag{8}$$

where $\beta$ is a factor that depends on the aspect ratio and Poisson's ratio, i.e., $\beta = \beta(a/h, \nu)$. We calculated $\beta$ for different $a/h$ ($0.2 \sim 2$) and $v$ ($0.1 \sim 0.5$) according to the table of $\kappa_n$. This $\beta$ table will be used to calculate the Poisson's ratio for a specific indentation test. By substituting Eq. (8) into Eq. (4), the deformation dependent indentation stiffness can be written as

$$P/w = c + c\beta \cdot w/h\,, \tag{9}$$



where

$$c = \frac{2 \cdot a \cdot E}{(1 - v^2)} \kappa(a/h, v) \tag{10}$$

is the $y$-intercept of the linear relationship between $P/w$ and $w/h$. Note that the slope of this linear relationship is $c\beta$.

Particularly, we can obtain pairs of $P$ and $w$, as well as the original tissue thickness ($h$), from an ultrasound indentation test. Therefore, the $y$-intercept ($c$) and slope ($c\beta$) in Eq. (9) can be easily calculated from the indentation data using a linear regression for $P/w$ and $w/h$, then $\beta$ can be obtained. Since the aspect ratio ($a/h$) is known for a specific indentation test, $v$ is the only unknown for finding out $\beta$ as $\beta$ is a function of $a/h$ and $v$ only. The Poisson's ratio can then be determined using the $\beta$ table. As a result, the Young's modulus ($E$) can be calculated with the known Poisson's ratio using Eq. (10).

## 3. Finite Element Analysis

Axisymmetric solid FE models were established using ABAQUS (Version 6.4, Hibbitt, Karlsson & Sorensen, Inc, US) to simulate the indentation with two different sized rigid cylindrical flat-ended indentors, which were 4.5 and 9 mm in radius. Note that the radius of the indentor was set to be 4.5 mm in the case of the single indentation test. The modeled tissue thickness and diameter was 4.5 and 90 mm, respectively. The tissue diameter was large enough in comparison with the indentation diameter so that the lateral boundary condition of the tissue could be neglected.[24] To ensure the accuracy of FE simulations, the grid density of the FE model was selected to be $0.5 \times 0.5\,\text{mm}^2$.[19] The rigid indentors with the radius of 4.5 and 9 mm were meshed with 81 and 162 four-node bilinear elements, respectively. The Young's modulus of 100 GPa and Poisson's ratio of 0.49 were assigned for the rigid indentor. The tested tissue was assumed to be linearly elastic and isotropic, with a typical Young's modulus of 60 kPa[25] and varying Poisson's ratio from 0.3 to 0.4999 (approximating the value of 0.5).[17] The tissue was meshed with 810 four-node bilinear elements. It was assumed that there was no friction between the surfaces of the indentor and the tissue, and the tissue was fixed on a rigid substrate. The calculation for the Poisson's ratio and Young's modulus were conducted when the deformation ratios are equal to 0.01, 0.025, 0.05, and 0.1. For the single indentation test, different FE models were built for the aspect ratio of 0.6, 0.8, 1, 1.5, and 2. To verify the accuracy of the proposed FE models, the values of $\kappa$ obtained from the simulated force-deformation data in the case of the infinitesimal deformation are compared with those reported from Jurvelin[18] and Hayes *et al.*[17]



## 4. Results and Discussion

Table 2 lists the values of $\kappa$ obtained from our FE models and the numerical analyses by Hayes *et al.*[17] and Jurvelin[18] for the case of the infinitesimal deformation. It is found that the percentage difference between the values of $\kappa$ reported for infinitesimal deformation in the present study for $0.1 \leq \nu \leq 0.5$ and those by Hayes and Jurvelin for $0.3 \leq \nu \leq 0.5$ and $0.1 \leq \nu \leq 0.2$, respectively, is within $\pm 3.5\%$. This comparison indicates that our FE models can represent the real indentation problem with a good accuracy.



### 4.1. *Two different sized indentors*

The comparison of Poisson's ratios calculated from the simulated force-deformation data with and without considering the finite deformation effect is illustrated in Table 3. Poisson's ratios calculated without consideration of the finite deformation effect are slightly larger than the real values with an overall mean estimation error of $2.77\% \pm 2.14\%$. It is observed that Poisson's ratios calculated without

Table 2. Comparison of the scaling factor ($\kappa$) values obtained using our FE model and the numerical analyses by Hayes *et al.*[17] and Jurvelin[18] for the case of an infinitesimal indentation depth (0.1%).

| | Poisson's ratio | | | | | | | | | | | | | | | | | | | |
|---|---|---|---|---|---|---|---|---|---|---|---|---|---|---|---|---|---|---|---|---|
| | 0.10 | | | 0.20 | | | 0.30 | | | 0.35 | | | 0.40 | | | 0.45 | | | 0.50 | | |
| $a/h$ | Jurvelin | Present | % error | Jurvelin | Present | % error | Hayes | Present | % error | Hayes | Present | % error | Hayes | Present | % error | Hayes | Present | % error | Hayes | Present | % error |
| 0.2 | 1.183 | 1.207 | 2.04 | 1.192 | 1.212 | 1.69 | 1.207 | 1.218 | 0.94 | 1.218 | 1.221 | 0.28 | 1.232 | 1.228 | −0.35 | 1.252 | 1.233 | −1.50 | 1.281 | 1.242 | −3.06 |
| 0.4 | 1.413 | 1.459 | 3.26 | 1.434 | 1.479 | 3.14 | 1.472 | 1.513 | 2.81 | 1.502 | 1.540 | 2.54 | 1.542 | 1.577 | 2.27 | 1.599 | 1.624 | 1.54 | 1.683 | 1.695 | 0.69 |
| 0.6 | 1.677 | 1.717 | 2.39 | 1.715 | 1.755 | 2.33 | 1.784 | 1.821 | 2.06 | 1.839 | 1.871 | 1.72 | 1.917 | 1.939 | 1.15 | 2.031 | 2.033 | 0.08 | 2.211 | 2.177 | −1.53 |
| 0.8 | 1.963 | 1.997 | 1.72 | 2.018 | 2.055 | 1.84 | 2.124 | 2.154 | 1.43 | 2.211 | 2.231 | 0.91 | 2.338 | 2.340 | 0.08 | 2.532 | 2.495 | −1.47 | 2.855 | 2.785 | −2.44 |
| 1.0 | 2.260 | 2.294 | 1.48 | 2.334 | 2.371 | 1.60 | 2.480 | 2.523 | 1.75 | 2.603 | 2.620 | 0.63 | 2.789 | 2.778 | −0.39 | 3.085 | 3.060 | −0.82 | 3.609 | 3.583 | −0.73 |
| 1.5 | 3.030 | 3.104 | 2.44 | 3.149 | 3.219 | 2.24 | 3.400 | 3.476 | 2.22 | 3.629 | 3.708 | 2.17 | 3.996 | 4.076 | 1.99 | 4.638 | 4.725 | 1.88 | 5.970 | 6.039 | 1.16 |
| 2.0 | 3.804 | 3.895 | 2.38 | 3.966 | 4.055 | 2.24 | 4.336 | 4.425 | 2.05 | 4.685 | 4.777 | 1.96 | 5.272 | 5.360 | 1.68 | 6.380 | 6.464 | 1.32 | 9.070 | 9.046 | −0.26 |

Table 3. Comparison of Poisson's ratios calculated with and without the consideration of the effects of finite deformation for $E = 60$ kPa.

| | | Calculated Poisson's ratios ($v$) | | | |
|---|---|---|---|---|---|
| True Poisson's ratios ($v$) | Deformation ratio ($w/h$) | Without finite deformation effect | Estimation errors (%) | With finite deformation effect | Estimation errors (%) |
| 0.30 | 0.001 | 0.305 | 1.76 | 0.299 | −0.36 |
| | 0.025 | 0.310 | 3.28 | 0.291 | −3.07 |
| | 0.05 | 0.318 | 5.96 | 0.290 | −3.23 |
| | 0.075 | 0.326 | 8.76 | 0.291 | −3.02 |
| | 0.1 | 0.335 | 11.73 | 0.293 | −2.20 |
| 0.35 | 0.001 | 0.353 | 0.96 | 0.337 | −3.69 |
| | 0.025 | 0.356 | 1.58 | 0.336 | −4.08 |
| | 0.05 | 0.360 | 2.82 | 0.337 | −3.69 |
| | 0.075 | 0.364 | 4.12 | 0.339 | −3.15 |
| | 0.1 | 0.369 | 5.53 | 0.342 | −2.35 |
| 0.40 | 0.001 | 0.402 | 0.53 | 0.385 | −3.82 |
| | 0.025 | 0.403 | 0.84 | 0.384 | −3.94 |
| | 0.05 | 0.406 | 1.40 | 0.386 | −3.55 |
| | 0.075 | 0.408 | 1.99 | 0.388 | −3.12 |
| | 0.1 | 0.411 | 2.64 | 0.390 | −2.60 |
| 0.45 | 0.001 | 0.451 | 0.28 | 0.441 | −2.03 |
| | 0.025 | 0.452 | 0.44 | 0.439 | −2.49 |
| | 0.05 | 0.453 | 0.75 | 0.439 | −2.53 |
| | 0.075 | 0.455 | 1.06 | 0.439 | −2.54 |
| | 0.1 | 0.456 | 1.38 | 0.439 | −2.53 |
| 0.50 | 0.001 | 0.501 | 0.30 | 0.500 | −0.03 |
| | 0.025 | 0.507 | 1.31 | 0.496 | −0.81 |
| | 0.05 | 0.512 | 2.38 | 0.493 | −1.35 |
| | 0.075 | 0.517 | 3.41 | 0.492 | −1.66 |
| | 0.1 | 0.520 | 4.08 | 0.489 | −2.17 |



considering the finite deformation effect of indentation increase with the increase of the deformation, with the estimation error ranged from 0.28% to 1.76% for 0.1% deformation and from 1.38% to 11.73% for 10% deformation. The results show that the estimation error of the Poisson's ratio with the consideration of the finite deformation is relatively stable, with an overall mean estimation error of $-1.20\% \pm 0.82\%$. It is revealed that the estimation error of the Poisson's ratio can be improved by considering the finite deformation effect.

According to Eqs. (1) and (4), the Young's modulus of the tissue can be calculated using the calculated Poisson's ratio and the force-deformation data obtained by either the bigger or the smaller indentor. Tables 4 and 5 show the comparisons of the Young's modulus calculated in the cases of using the indentors with the radius of 4.5 and 9 mm, respectively. For both cases, the calculated Young's modulus without the consideration of the finite deformation effect becomes larger and larger when the deformation or the Poisson's ratio increases. For the indentation with the smaller indentor (radius $a = 4.5$ mm), the overall estimation

Table 4. Comparison of Young's moduli calculated with and without the consideration of the effect of finite deformation for $E = 60$ kPa and $a/h = 1$.

| True Poisson's ratios ($v$) | Deformation ratio ($w/h$) | Calculated Young's modulus ($E$) (kPa) | | | |
|---|---|---|---|---|---|
| | | Without finite deformation effect | Estimation errors (%) | With finite deformation effect | Estimation errors (%) |
| 0.30 | 0.001 | 59.99 | −0.01 | 59.19 | −1.34 |
| | 0.025 | 60.21 | 0.35 | 59.52 | −0.80 |
| | 0.05 | 60.17 | 0.29 | 59.43 | −0.94 |
| | 0.075 | 60.10 | 0.16 | 59.30 | −1.17 |
| | 0.1 | 59.97 | −0.05 | 59.08 | −1.53 |
| 0.35 | 0.001 | 60.06 | 0.11 | 60.42 | 0.71 |
| | 0.025 | 60.58 | 0.97 | 60.42 | 0.70 |
| | 0.05 | 60.87 | 1.46 | 60.16 | 0.26 |
| | 0.075 | 61.14 | 1.89 | 59.86 | −0.24 |
| | 0.1 | 61.35 | 2.25 | 59.50 | −0.83 |
| 0.40 | 0.001 | 60.14 | 0.23 | 61.32 | 2.19 |
| | 0.025 | 61.00 | 1.66 | 61.22 | 2.03 |
| | 0.05 | 61.71 | 2.85 | 60.89 | 1.49 |
| | 0.075 | 62.39 | 3.98 | 60.55 | 0.92 |
| | 0.1 | 63.02 | 5.03 | 60.16 | 0.27 |
| 0.45 | 0.001 | 60.18 | 0.31 | 61.33 | 2.21 |
| | 0.025 | 61.65 | 2.76 | 61.54 | 2.57 |
| | 0.05 | 62.97 | 4.95 | 61.47 | 2.45 |
| | 0.075 | 64.28 | 7.13 | 61.38 | 2.31 |
| | 0.1 | 65.53 | 9.21 | 61.25 | 2.09 |
| 0.50 | 0.001 | 60.37 | 0.61 | 60.86 | 1.43 |
| | 0.025 | 62.35 | 3.91 | 61.43 | 2.39 |
| | 0.05 | 64.42 | 7.36 | 61.96 | 3.27 |
| | 0.075 | 66.52 | 10.9 | 62.43 | 4.05 |
| | 0.1 | 68.68 | 14.5 | 62.89 | 4.81 |



errors of the calculated Young's modulus with and without considering the finite deformation effect are $1.17\% \pm 1.73\%$ and $3.31\% \pm 2.90\%$, respectively. Similar results of Young's modulus were obtained from the indentation with the larger indentor (radius $a = 9.0$ mm). The overall estimation errors of the Young's modulus with and without considering the finite deformation effect are $-0.30\% \pm 0.72\%$ and $5.19\% \pm 4.25\%$, respectively. It is noticed that the finite deformation effect on calculating the Young's modulus becomes more serious when the aspects ratio $a/h$ are larger, particularly for a large deformation and a Poisson's ratio approaching to 0.5. After the compensation of the finite deformation effect, the Young's modulus could be precisely estimated with a very small estimation error, $0.15\% \pm 1.03\%$ for 0.1% deformation and $-0.93\% \pm 0.57\%$ for 10% deformation. The above results showed that the estimation of the Young's modulus could be dramatically improved with the compensation of the finite deformation effect. Moreover, such compensation could achieve better results when a large indentor or thinner specimen was used, i.e., larger aspect ratio.

Table 5. Comparison of Young's moduli calculated with and without consideration of the effect of finite deformation for $E = 60\,\text{kPa}$ and $a/h = 2$.

| | | Calculated Young's modulus ($E$) (kPa) | | | |
|---|---|---|---|---|---|
| True Poisson's ratios ($v$) | Deformation ratio ($w/h$) | Without finite deformation effect | Estimation errors (%) | With finite deformation effect | Estimation errors (%) |
| 0.30 | 0.001 | 60.16 | 0.27 | 59.18 | −1.37 |
| | 0.025 | 60.55 | 0.91 | 59.39 | −1.02 |
| | 0.05 | 60.79 | 1.32 | 59.30 | −1.16 |
| | 0.075 | 61.02 | 1.70 | 59.18 | −1.36 |
| | 0.1 | 61.20 | 2.01 | 59.00 | −1.66 |
| 0.35 | 0.001 | 60.26 | 0.43 | 59.83 | −0.29 |
| | 0.025 | 60.91 | 1.51 | 59.78 | −0.36 |
| | 0.05 | 61.47 | 2.45 | 59.61 | −0.65 |
| | 0.075 | 62.01 | 3.36 | 59.42 | −0.96 |
| | 0.1 | 62.53 | 4.22 | 59.20 | −1.34 |
| 0.40 | 0.001 | 60.36 | 0.59 | 60.28 | 0.47 |
| | 0.025 | 61.36 | 2.26 | 60.17 | 0.28 |
| | 0.05 | 62.34 | 3.89 | 59.95 | −0.09 |
| | 0.075 | 63.30 | 5.51 | 59.72 | −0.46 |
| | 0.1 | 64.25 | 7.08 | 59.48 | −0.87 |
| 0.45 | 0.001 | 60.52 | 0.87 | 60.35 | 0.58 |
| | 0.025 | 62.19 | 3.65 | 60.29 | 0.48 |
| | 0.05 | 63.90 | 6.50 | 60.12 | 0.20 |
| | 0.075 | 65.61 | 9.35 | 59.97 | −0.05 |
| | 0.1 | 67.30 | 12.2 | 59.81 | −0.32 |
| 0.50 | 0.001 | 60.69 | 1.15 | 60.81 | 1.35 |
| | 0.025 | 63.80 | 6.33 | 60.50 | 0.83 |
| | 0.05 | 67.13 | 11.9 | 60.28 | 0.47 |
| | 0.075 | 70.54 | 17.6 | 60.13 | 0.22 |
| | 0.1 | 73.65 | 22.8 | 59.73 | −0.45 |



From the above results, it was found that the estimation errors of the Poisson's ratio and Young's modulus could not be totally compensated with the data provided by Zhang. Unlike the data provided by Hayes for the infinitesimal deformation obtained from the analytical solutions, Zhang's data were obtained using FE simulation. Hence, the simulation error for those data could not be avoided. There was mean difference of $1.33\% \pm 0.85\%$ between the values of $\kappa$ reported by Hayes and those obtained by Zhang for the infinitesimal deformation. This can explain why the estimation error after the compensation is even slightly greater than that before the compensation for the cases with small Poisson's ratio and small aspect ratio in Tables 4 and 5. In those cases, the estimated errors are relatively small even without considering the finite deformation effect, and the small error of $\kappa$ calculated for different deformation may be dominant than the difference.

Compared with the method of using two different sized indentors without considering the finite deformation effect, our proposed method for the compensation of the finite deformation effect is more accurate for the estimation of the Young's

modulus and Poisson's ratio. This method can be very useful for the assessment of various tissues by applying the large deformation. The results of this study demonstrated that the finite deformation effect became serious when the aspect ratio, Poisson's ratio, and indentation deformation became larger. The finite

Table 6. The values of $\kappa$ and $\kappa_n$ for different aspect ratios, Poisson's ratios, and deformation ratios.

| | Poisson's ratio | | | | | | |
|---|---|---|---|---|---|---|---|
| $w/h$ | 0.10 | 0.20 | 0.30 | 0.35 | 0.40 | 0.45 | 0.50 |
| $a/h = 2$ | | | | | | | |
| 0.001 | 3.895 | 4.055 | 4.424 | 4.777 | 5.360 | 6.464 | 9.046 |
| 0.01 | 3.906 | 4.068 | 4.446 | 4.805 | 5.405 | 6.550 | 9.308 |
| 0.025 | 3.922 | 4.089 | 4.476 | 4.848 | 5.473 | 6.679 | 9.070 |
| 0.05 | 3.950 | 4.123 | 4.528 | 4.919 | 5.585 | 6.893 | 10.357 |
| 0.1 | 4.006 | 4.192 | 4.631 | 5.061 | 5.809 | 7.322 | 11.667 |
| $a/h = 1.5$ | | | | | | | |
| 0.001 | 3.104 | 3.219 | 3.476 | 3.708 | 4.076 | 4.725 | 6.039 |
| 0.01 | 3.111 | 3.229 | 3.490 | 3.728 | 4.109 | 4.781 | 6.193 |
| 0.025 | 3.121 | 3.242 | 3.512 | 3.759 | 4.158 | 4.875 | 6.424 |
| 0.05 | 3.138 | 3.265 | 3.549 | 3.811 | 4.241 | 5.025 | 6.809 |
| 0.1 | 3.173 | 3.311 | 3.622 | 3.915 | 4.406 | 5.326 | 7.579 |
| $a/h = 1$ | | | | | | | |
| 0.001 | 2.294 | 2.371 | 2.523 | 2.620 | 2.778 | 3.060 | 3.583 |
| 0.01 | 2.294 | 2.374 | 2.530 | 2.632 | 2.798 | 3.090 | 3.636 |
| 0.025 | 2.294 | 2.377 | 2.541 | 2.651 | 2.829 | 3.136 | 3.715 |
| 0.05 | 2.294 | 2.383 | 2.558 | 2.682 | 2.879 | 3.213 | 3.847 |
| 0.1 | 2.295 | 2.394 | 2.592 | 2.745 | 2.980 | 3.366 | 4.112 |
| $a/h = 0.8$ | | | | | | | |
| 0.001 | 1.997 | 2.055 | 2.154 | 2.231 | 2.340 | 2.495 | 2.785 |
| 0.01 | 1.997 | 2.056 | 2.159 | 2.239 | 2.354 | 2.520 | 2.828 |
| 0.025 | 1.997 | 2.057 | 2.166 | 2.252 | 2.375 | 2.558 | 2.893 |
| 0.05 | 1.998 | 2.059 | 2.177 | 2.273 | 2.410 | 2.621 | 3.001 |
| 0.1 | 2.000 | 2.062 | 2.199 | 2.314 | 2.479 | 2.747 | 3.217 |
| $a/h = 0.6$ | | | | | | | |
| 0.001 | 1.717 | 1.755 | 1.821 | 1.871 | 1.939 | 2.033 | 2.177 |
| 0.01 | 1.717 | 1.755 | 1.822 | 1.875 | 1.947 | 2.048 | 2.205 |
| 0.025 | 1.718 | 1.756 | 1.824 | 1.881 | 1.958 | 2.070 | 2.248 |
| 0.05 | 1.718 | 1.757 | 1.827 | 1.891 | 1.978 | 2.108 | 2.318 |
| 0.1 | 1.719 | 1.759 | 1.834 | 1.911 | 2.017 | 2.183 | 2.459 |
| $a/h = 0.4$ | | | | | | | |
| 0.001 | 1.459 | 1.479 | 1.513 | 1.540 | 1.577 | 1.624 | 1.695 |
| 0.01 | 1.459 | 1.479 | 1.514 | 1.542 | 1.581 | 1.632 | 1.710 |
| 0.025 | 1.460 | 1.480 | 1.515 | 1.546 | 1.587 | 1.645 | 1.734 |
| 0.05 | 1.460 | 1.480 | 1.516 | 1.551 | 1.598 | 1.666 | 1.773 |
| 0.1 | 1.461 | 1.481 | 1.519 | 1.562 | 1.619 | 1.708 | 1.850 |
| $a/h = 0.2$ | | | | | | | |
| 0.001 | 1.207 | 1.212 | 1.218 | 1.221 | 1.228 | 1.233 | 1.242 |
| 0.01 | 1.207 | 1.212 | 1.219 | 1.224 | 1.231 | 1.240 | 1.254 |
| 0.025 | 1.207 | 1.212 | 1.219 | 1.227 | 1.237 | 1.250 | 1.271 |
| 0.05 | 1.208 | 1.213 | 1.221 | 1.232 | 1.246 | 1.267 | 1.301 |
| 0.1 | 1.209 | 1.214 | 1.223 | 1.243 | 1.265 | 1.302 | 1.359 |

deformation effect on the estimation of Poisson's ratio was relatively smaller than that of Young's modulus.

### 4.2. *A single indentation*

Making use of the FE simulation, the values of $\kappa$ and $\kappa_n$ for different aspect ratios, Poisson's ratios, and deformation ratios were estimated, as shown in Table 6. From this table, it is found that $\kappa$ increases with the increase of aspect ratio and Poisson's ratio. Similarly, $\kappa_n$ also increases with these two parameters, as well as the deformation ratio. Moreover, a linear correlation of $\kappa_n$ and the deformation ratio is observed. Based on Table 6, the $\beta$ factor for different aspect ratios, Poisson's ratios, and deformation ratios can be calculated by using Eq. (6), as illustrated in Table 7. It is noticed that the $\beta$ factor monotonically increases with increasing Poisson's ratios in the cases of different aspect ratios. Figure 3 shows the nonlinear but monotonic relationships between the $\beta$ factor and the Poisson's ratio for different aspect ratios. Note that there is only one corresponding Poisson's ratio for a selected aspect ratio for a specific value of the $\beta$ factor. Figure 4 indicates that the corresponding relationship between the indentation stiffness $(P/w)$ and the deformation ratio $(w/h)$ could be well represented using linear regressions for different deformation ratios when the aspect ratio is equal to 2. According to Eq. (11), we can obtain $\beta$ and $c$ from the cases with different deformations for each aspect ratio $(a/h)$. The Poisson's ratio for each case can be obtained by looking up Table 7 or Fig. 3 and applying a linear interpolation.

In comparison with the actual value, the percentage errors of the calculated Poisson's ratio are between $-1.7\%$ and $-8.2\%$ when the aspect ratio is between 0.6 and 2, as listed in Table 8. The percentage error of the Poisson's ratio and the Young's modulus are limited nearly within 3.2% and 7.2%, respectively, when the aspect ratio is between 1 and 2. The errors are rather stable when different deformations (1% to 10%) are used for the estimation. The robustness of the estimation can be further improved by averaging the parameters calculated using

Table 7. The $\beta$ factor for different aspect ratios, Poisson's ratios, and deformation ratios.

| | Aspect ratio $(a/h)$ | | | | | | |
|---|---|---|---|---|---|---|---|
| Poisson's ratio $(v)$ | 0.2 | 0.4 | 0.6 | 0.8 | 1 | 1.5 | 2 |
| 0.10 | 0.012 | 0.014 | 0.012 | 0.016 | 0.004 | 0.222 | 0.286 |
| 0.20 | 0.012 | 0.014 | 0.023 | 0.034 | 0.098 | 0.284 | 0.338 |
| 0.30 | 0.035 | 0.037 | 0.073 | 0.208 | 0.271 | 0.421 | 0.466 |
| 0.35 | 0.179 | 0.141 | 0.215 | 0.373 | 0.478 | 0.559 | 0.595 |
| 0.40 | 0.301 | 0.265 | 0.401 | 0.597 | 0.728 | 0.810 | 0.838 |
| 0.45 | 0.554 | 0.519 | 0.740 | 1.012 | 1.002 | 1.271 | 1.327 |
| 0.50 | 0.946 | 0.920 | 1.295 | 1.551 | 1.478 | 2.550 | 2.897 |

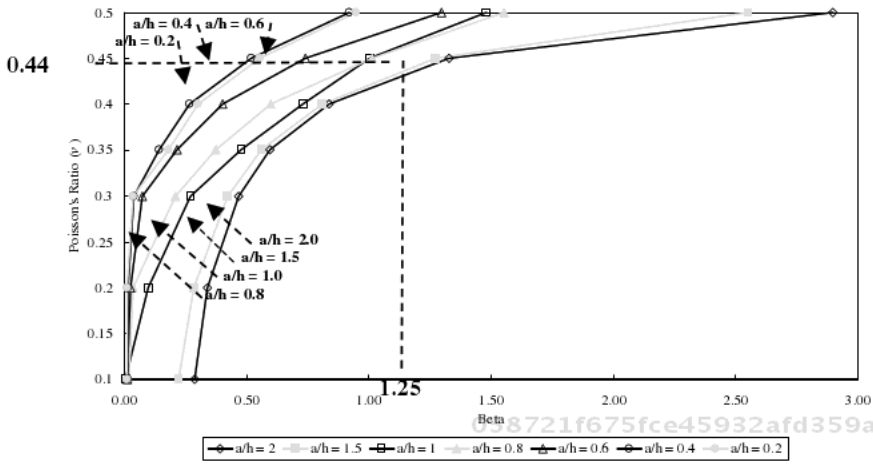


Fig. 3. The relationships between the Beta ($B$) factor and Poisson's ratio ($v$) for various aspect ratios ($a/h$). Poisson's ratio ($v$) can be determined by the interpolation of $B$ factor. For instance, when ($B$) = 1.25 and ($a/h$) = 2, the estimated ($v$) = 0.44 (the real Poisson's ratio was 0.45 for this case).

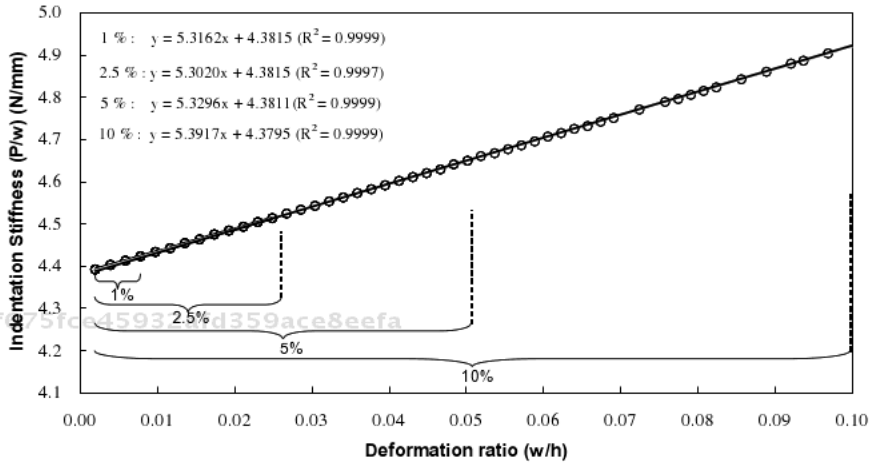


Fig. 4. The relationship between the indentation stiffness ($P/w$) and deformation ratio ($w/h$) extracted from simulated indentation data. The assigned parameters for the FE simulation were ($a/h$) = 2, ($E$) = 60 kPa, and ($v$) = 0.45. Linear regressions were performed for the data with different deformation ratios ($w/h$). We used the case with 10% deformation as an example, and the $y$-intercepts ($c$) and the slope ($cB$) were 4.35 and 5.46, respectively, so the factor ($B$) was 1.25, which was used as an example to estimate the Poisson's in Fig. 3.

different deformation levels (last 4 rows in Table 8). This averaging approach would be particularly useful when the proposed method is applied for the real indentation data, in which various noises may exist in the experimental force or deformation data.

that high concentrations of nanometer-sized metal wear particles are cytotoxic to human fibroblasts and macrophages *in vitro*,[110] there are also concerns about the release of metal ions from these small particles, and the potential effect that these ions may have on cells and tissues. Elevated ion concentrations have been reported in both the blood and urine of patients with metallic implant components.[111] Cobalt and chromium ions have high toxicity, and there are concerns about the effects of sub-lethal doses of metal ions, which have been shown to cause DNA damage.[112] It has been suggested that over long periods of exposure this damage will lead to the development of certain types of cancer, such as leukaemia and lymphoma. However, reports in the literature of malignancies developing after total hip or knee replacement surgery are exceedingly rare, and the relative risk of cancer after total joint replacement, has not been shown to be increased.[113]

Metal sensitivity may also be a problem. Metal ions, whether produced secondary to wear debris or via corrosion can initiate a hypersensitivity response.[114] A delayed cell-mediated response, or delayed-type hypersensitivity response can occur, in which cytokines are released by T-lymphocytes which in turn, recruit and activate macrophages, which may result in T-cell mediated periprosthetic osteolysis.[114] Many metals can initiate a hypersensitivity response, the most common is nickel followed by cobalt and chromium. Recently, an unusual immune pathology, exclusively associated with second-generation MOM hip prostheses, has been described.[115] Histomorphological changes suggest a type of hypersensitivity reaction to the all-metallic implants. The hypersensitivity hypothesis was further strengthened by the observation that these patients experienced early clinical failure at 11–60 months (mean 29 months), and the fact that patients who received a second MOM prosthesis did not experience any relief of symptoms. Conversely, patients who received either metal-on-polyethylene or ceramic-on-polyethylene couples reported that their symptoms completely disappeared. In a control group of patients with joint prostheses not containing cobalt, chromium, or nickel, these signs of an immunological reaction were absent. Reports of this type of reaction are becoming increasingly common; however, more research is needed in this area. It is not known whether these patients experienced prosthesis failure because of a pre-existing metal sensitivity, or whether metal sensitivity developed because of severe wear and the associated elevated metal ion levels. There is an increased probability of developing hypersensitivity to elevated metal ion levels, and hence, an increased risk of implant failure. Recently, Park *et al.*[116] reported a 6% incidence of early onset osteolysis which was associated with a delayed-type hypersensitivity response to metals in patients who received second-generation MOM hip prostheses. Interestingly, these authors reported that eight out of nine patients with early osteolysis were hypersensitive to cobalt, with only two patients eliciting a hypersensitive reaction to nickel. It has previously been reported that nickel is a potent sensitizer, with cross reactivity to cobalt being common.[117] This is the first report to link cobalt hypersensitivity with early failure of MOM hip prostheses.

These studies highlight the importance of coupled tribological studies of MOM bearings with biological studies of the resultant wear debris. The biological concerns

cannot be predicted from simple laboratory studies and rely on long-term clinical follow-up and laboratory analysis, which is currently ongoing in many centers around the world. It is important not only to monitor these long-term biological implications of the generation and release of metallic debris, but also to investigate the long-term performance of the current generation of MOM articulations, which may have a direct bearing on the former consideration. The current engineering approach is to minimize wear and wear debris generation, through optimizing the tribological performance of the MOM bearing, in order to limit the potential adverse biological consequences. The key engineering issues identified so far include high carbon cobalt chromium alloys, optimized clearance and head diameter, and improved manufacturing processes. Efforts will be made in future to understand better the tribological mechanisms of MOM bearings to achieve further wear reduction.



### 8.1. *New methodologies*

Further understanding of the tribology of MOM bearing surfaces is necessary to provide future design guidance and optimization. Integrated studies of friction, wear, and lubrication are clearly necessary to understand the complex tribological mechanisms involved in MOM bearings. It is important to develop experimental techniques that are capable of directly interrogating the bearing interfaces. These include, for example, the use of novel electrical, capacitance, and ultrasonic measurements of the separation between MOM bearing surfaces. The current understanding of the theoretical lubrication in MOM bearings is largely based on the classical elastohydrodynamic lubrication mechanism. The low viscosity of the pseudo-synovial fluid after joint replacement, coupled with the limitation of the clearance due to manufacturing capabilities and component deformation, result in the predicted lubricant film being equivalent to the roughness of the bearing surfaces and the thickness of the protein layers adsorped onto the metallic bearing surfaces.



Understanding the boundary lubrication mechanism and the mixed lubrication mechanism is essential for further theoretical developments. There is now increasing evidence that active and young patients receiving total hip joint replacements can walk up to 5 million steps per year.[102,103] Therefore, for a modest service life of 20–30 years, the equivalent walking steps can reach up to 100 million, as compared to 5–10 million currently adopted in simulator studies, and can easily become 200 million for those patients who are living longer. Consequently, long-term laboratory wear simulation will be required. Such a task is not trivial and requires considerable resources and time to conduct. Complimentary computational modeling may provide a valuable alternative.

### 8.2. *New developments*

The use of MOM hip implants, particularly in the resurfacing form, is increasing and it is estimated that about 10–20% of total hip replacements in the United

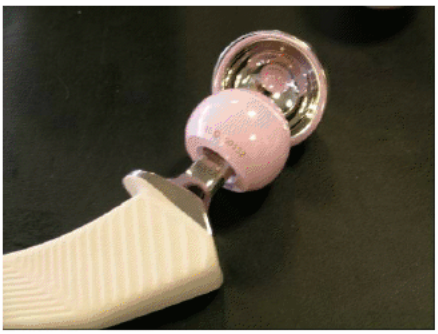

Fig. 10. A ceramic-on-metal hip implant developed at the Institute of Medical and Biological Engineering, University of Leeds[119].



Kingdom are of these types. Surface engineered ceramic-like coatings such as thick chromium nitride (CrN) and chromium carbonitride (CrCN, 8–12 $\mu$m) have been shown to reduce wear in MOM bearings considerably, at least 18-fold reduction after 2 million cycles and 36-fold lower after 5 million cycles in hip simulators[118] as well as reducing ion levels in the lubricants. The extremely low volume of wear debris and concentration of metal ions released by these surface engineered systems have considerable potential for the clinical application of this technology. Such a technology also has the potential to be used for large diameter hip resurfacing prostheses, which are not an option for ceramic-on-ceramic bearings. Alternative articulation of a ceramic head against a metal cup, as shown in Fig. 10, has been shown to reduce wear significantly.[119]

## References



1. D. Dowson and V. Wright (eds.), *Introduction to the Biomechanics of Joints and Joint Replacements* (Mechanical Engineering Publishing Ltd, London, 1981).
2. T. P. Schmalzried, M. Jasty and W. H. Harris, *J. Bone Jt. Surg.* **74A** (1992) 849.
3. L. D. Dorr, R. Bloebaum, J. Emmanuel and R. D. Meldrum, *Clin. Orthop. Relat. Res.* **261** (1990) 82.
4. J. A. Savio, L. M. Overcamp and L. Black, *Clin. Mater.* **12** (1994) 1.
5. U. E. Pazzaglia, C. Dell'Orbo and M. J. Wilkinson, *Arch. Orthop. Trauma Surg.* **106** (1985) 209.
6. P. Campbell, S. Ma, T. P Schmalzried and H. C. Amstutz, *J. Biomed. Mater. Res.* **28** (1994) 523.
7. P. Campbell, S. Ma, B. Yeom, H. McKellop, T. P. Schmalzried and H. C. Amstutz, *J. Biomed. Mater. Res.* **29** (1995) 127.
8. W. J. Maloney, R. L. Smith, D. Hvene, T. P. Schmalzried and H. Rubash, *J. Bone Jt. Surg.* **77A** (1994) 1301.
9. K. T. Margevicius, T. W. Bauer, J. T. McMahon, S. A. Brown and K. Merritt, *J. Bone Jt. Surg.* **76A** (1994) 1664.
10. A. A. Besong, J. T. Tipper, E. Ingham, M. H. Stone, B. M. Wroblewski and J. Fisher, *J. Bone Jt. Surg.* **80-B** (1998) 340.

11. J. L. Tipper, E. Ingham, J. L. Hailey, A. A. Besong, B. M. Wroblewski, M. H. Stone and J. Fisher, *J. Mater. Sci. Mater. Med.* **11** (2000) 117.
12. A. L. Galvin, L. Kang, J. L. Tipper, M. H. Stone, E. Ingham, Z. M. Jin and J. Fisher, *J. Mater. Sci. Mater. Med.* **17**(3) (2006) 235.
13. J. L. Tipper, A. L. Galvin, S. Williams, H. M. J. McEwen, M. H. Stone, E. Ingham and J. Fisher, *J. Biomed. Mater. Res. Part A* **78**(3) (2006) 473–480.
14. E. Ingham and J. Fisher, *Proc. Instn. Mech. Engrs.* **214H** (2000) 21.
15. M. Gowen, D. D. Wood, E. J. Ihrie, M. K. B. McGuire and R. G. G. Russell, *Nature* **306** (1983) 378.
16. D. R. Bertolini, G. E. Nedwin, T. S. Bringham, D. D. Smith and G. R. Mundy, *Nature* **319** (1986) 516.
17. J. A. Lorenzo, S. L. Sousa, J. M. Fonesca, J. M. Hock and E. S. Medlock, *J. Clin. Invest.* **80** (1987) 160.
18. T. R. Green, J. Fisher, M. H. Stone, B. M. Wroblewski and E. Ingham, *Biomaterials* **19** (1998) 2297.
19. J. B. Matthews, T. R. Green, M. H. Stone, B. M. Wroblewski, J. Fisher and E. Ingham, *Biomaterials* **21** (2000) 2033.
20. T. R. Green, J. Fisher, J. B. Matthews, M. H. Stone and E. Ingham, *J. Biomed. Mater. Res. Appl. Biomater.* **53** (2000) 490.
21. J. M. Cuckler, *Clin. Orthop. Relat. Res.* **441** (2005) 132.
22. M. T. Clarke, C. Darrah, T. Stewart, E. Ingham, J. Fisher and J. F. Nolan, *J. Arthroplasty* **20**(4) (2005) 542.
23. S. Jacobsson, K. Djerf and O. Wahstron, in *Metasul A Metal-on-Metal Bearing,* eds. C. Reiker, M. Windler and Hans H. Wyss (Huber, Bern, 1999), p. 61.
24. H. Dobbs, *J. Bone Jt. Surg.* **62B** (1980) 168.
25. A. August, C. Aldam and P. Pynsent, *J. Bone Jt. Surg.* **68B** (1986) 520.
26. T. Schmalzreid, V. Fowble, K. Ure and H. Amstutz, *Clin. Orthop. Relat. Res.* **329S** (1996) 106.
27. C. B. Rieker, R. Schon and P. Kottig, *J. Arthroplasty* **19**(8 Suppl 3) (2004) 5.
28. P. Grigoris, P. Roberts, K. Panousis and Z. Jin, *Proc. Inst. Mech. Eng. [H]* **220**(2) (2006) 95.
29. R. M. Hall and A. Unsworth, *Biomaterials* **18**(15) (1997) 1017.
30. M. T. Mai, T. P. Schmalzried, F. J. Dorey, P. A. Campbell and H. C. Amstutz, *J. Bone J. Surg. Am.* **78**(4) (1996) 505.
31. M. A. Wimmer, R. Nassutt, C. Sprecher, J. Loo, G. Tager and A. Fischer, *Proc. Inst. Mech. Eng. [H]* **220**(2) (2006) 219.
32. R. Buscher, G. Tager, W. Dudzinski, B. Gleising, M. A. Wimmer and A. Fischer, *J. Biomed. Mater. Res. B Appl. Biomater.* **72**(1) (2005) 206.
33. D. Dowson, *Proc. Inst. Mech. Eng. [H]* **220**(2) (2006) 161.
34. J. P. Paul, Lubrication and wear in living and artificial human joints, *Proc. Instn. Mech. Engrs.* **181**(3J) (1967) 8.
35. Z. M. Jin, J. B. Medley and D. Dowson, in *Proc. 29th Leeds-Lyon Symposium on Tribology*, eds. D. Dowson *et al.* (Elseviere, 2003), p. 237.
36. D. A. Dennis, R. D. Komistek, E. J. Northcut, J. A. Ochoa and A. Ritchie, *J. Biomech.* **34** (2001) 623.
37. H. Saarri, S. Santavirta, D. Nordstrom, P. Paavolainen and Y. T. Konttinen, *J. Rheumatol.* **20**(1) (1993) 87.
38. J. Delecrin, M. Oka, S. Takahashi, T. Yamamuro and T. Nakamura, *Clin. Orthop. Relat. Res.* **307** (1994) 240.
39. S. C. Scholes and A. Unsworth, *Proc. Inst. Mech. Eng. [H]* **220**(2) (2006) 183.

40. A. V. Cooke, D. Dowson and V. Wright, *Eng. Med.* **7** (1978) 66.
41. J. Q. Yao, M. P. Laurent, T. S. Johnson, C. R. Blanchard and R. D. Crowinshield, *Wear* **255** (2003) 780.
42. Z. M. Jin, D. Dowson and J. Fisher, *Proc. Inst. Mech. Eng. [H]* **211** (1997) 247.
43. A. Yew, Z. M. Jin, A. Donn, M. M. Morlock and G. Isaac, *Proc. Inst. Mech. Eng. [H]* **220**(2) (2006) 311.
44. A. A. Besong, R. Lee, R. Farrar and Z. M. Jin, *Proc. Inst. Mech. Eng. [H]* **215** (2001) 543.
45. O. Müller, W. J. Parak, M. G. Wiedemann and F. Martini, *J. Biomech.* **37**(10) (2004) 1623.
46. K. N. Bachus, A. L. DeMarco, K. T. Judd, D. S. Horwitz and D. S. Brodke, *Med. Eng. Phys.* **28**(5) (2006) 483.
47. N. Verdonschot, P. Vena, J. Stolk and R. Huiskes, *Clin. Orthop. Relat. Res.* **404** (2002) 353.
48. F. Liu, Z. M. Jin, P. Grigoris, F. Hirt and C. Rieker, *Proc. Inst. Mech. Eng. [H]* **217**(3) (2003) 207.
49. A. Yew, M. Jagatia, H. Ensaff and Z. M. Jin, *Proc. Inst. Mech. Eng. [H]* **217**(5) (2003) 333.
50. F. Liu, I. J. Udofia *et al.*, *Proc. Inst. Mech. Eng. [C]* **219**(7) (2005) 727.
51. M. Jagatia and Z. M. Jin, *Proc. Inst. Mech. Eng. [H]* **215**(6) (2001) 531.
52. S. C. Scholes and A. Unsworth, *Proc. Inst. Mech. Eng. [H]* **214**(1) (2000) 49.
53. K. Vassiliou, A. P. Elfick, S. C. Scholes and A. Unsworth, *Proc. Inst. Mech. Eng. [H]* **220**(2) (2006) 269.
54. D. McMinn, J. Daniel, A. Kamali, S. Sayad Saravi, M Youseffi, J. Daniel, T. Band and R. Ashton, in *Trans. Orthopaedic Research Society*, Chicago, IL, Vol. 31 (2006), p. 0500.
55. X. Hu, P. Twigg, J. Shelton, M. Tuke and A. Taylor, in *transactions of Orthopaedic Research Society*, Vol. 31, Chicago, IL (2006), p. 0502
56. F. C. Wang, C. Brockett, S. Williams, Z. M. Jin and J. Fisher, *Abstracts of the 5th World Congress of Biomechanics* (Munich, Germany, 2006), p. 5396.
57. K. L. Johnson, *Contact Mechanics* (Cambridge University Press, 1985).
58. C. Brockett, S. Williams, Z. M. Jin, G. Isaac and J. Fisher, *J. Biomed. Mater. Res. Part B: Appl. Biomater.* **81**(2) (2007) 508–515.
59. S. Williams, D. Jalali-Vahid, Z. M. Jin, M. Stone, E. Ingham and J. Fisher, *J. Biomech.* **39**(12) (2006) 2274–2278.
60. D. Dowson, C. M. McNie and A. A. J. Goldsmith, *Proc. Inst. Mech. Eng. [C]* **214** (2000) 75.
61. D. Dowson and G. R. Higginson, *Elasto-Hydrodynamic Lubrication* (Pergamon Press, 1977).
62. F. C. Wang and Z. M. Jin, *J. Tribol. Trans. ASME* **127** (2005) 729.
63. F. C. Wang and Z. M. Jin, *Proc. Inst. Mech. Eng. [J]* **218** (2004) 201
64. M. Jagatia and Z. M. Jin, *Proc. Inst. Mech. Eng. [H]* **216** (2002) 185.
65. F. Liu, F. C. Wang, Z. M. Jin, F. Hirt, C. Rieker and P. Grigoris, *Proc. Inst. Mech. Eng. [H]* **218** (2004) 261.
66. A. Yew, I. J. Udofia, M. Jagatia and Z. M. Jin, *Proc. Inst. Mech. Eng. [H]* **218**(1) (2004) 27.
67. I. J. Udofia and Z. M. Jin, *J. Biomech.* **36**(4) (2003) 537.
68. F. Liu, Z. M. Jin, P. Roberts and P. Grigoris, *Proc. Inst. Mech. Eng. [H]* in press (2006).

69. J. L. Tipper, P. J. Firkins, E. Ingham, J. Fisher, M. H. Stone and R. Farrar, *J. Mater. Sci. Mater. Med.* **10**(6) (1999) 353.
70. S. C. Scholes and A. Unsworth, *J. Mater. Sci. Mater. Med.* **12**(4) (2001) 299.
71. L. Kang, Z. M. Jin, G. Isaac and F. Fisher, *Trans. Orthopaedic Research Society*, Chicago, IL, Vol. 31 (2006), p. 0501.
72. H. McKellop, S. H. Park, R. Chiesa, P. Doorn, B. Lu, P. Normand, P. Grigoris and H. Amstutz, *Clin. Orthop. Relat. Res.* **329**(Suppl) (1996) S128.
73. G. Reinisch, K. P. Judmann, C. Lhotka, F. Lintner and K. A. Zweymuller, *Biomaterials* **24**(6) (2003) 1081.
74. A. G. Cobb and T. P. Schmalzreid, *Proc. Inst. Mech. Eng. [H]* **220**(2) (2006) 385.
75. C. B. Rieker, R. Schon, R. Konrad, G. Liebentritt, P. Gnepf, M. Shen, P. Roberts and P. Grigoris, *Orthop. Clin. North. Am.* **36**(2) (2005) 135.
76. F. W. Chan, J. D. Bobyn, J. B. Medley, J. J. Krygier and M. Tanzer, *Clin. Orthop. Relat. Res.* **369** (1999) 10.
77. D. Dowson, C. Hardaker *et al.*, *J. Arthroplasty* **19**(8, Supplement 1) (2004) 118.
78. J. G. Bowsher, J. Nevelos, P. A. Williams and J. C. Shelton, *Proc. Inst. Mech. Eng. [H]* **220**(2) (2006) 135.
79. M. F. Dörig, M. Schueler and E. Odstrcilik, in *Proc. of European Hip Society* (Domestic Meeting — Antalya (Turkey) — June 21–24, 2006), pp. 003.
80. I. Milosev, R. Trebse, S. Kovac, A. Cor and V. Pisot, *J. Bone J. Surg. Am.* **88**(6) (2006) 1173.
81. S. L. Smith, D. Dowson and A. A. J. Goldsmith, *Proc. Inst. Mech. Eng. [J]* **215**(5) (2001) 483.
82. S. L. Smith, D. Dowson and A. A. J. Goldsmith, *Proc. Inst. Mech. Eng. [H]* **215**(2) (2001) 161.
83. Z. M. Jin, *Proc. Inst. Mech. Eng. [H]* **216** (2002) 85.
84. D. Dowson, C. Hardaker *et al.*, *J. Arthroplasty* **19**(8, Supplement 3) (2004) 124.
85. J. Fisher, Z. M. Jin, J. L. Tipper, M. Stone and E. Ingham, *Clin. Orthop. Relat. Res.* **453** (2006) 25–34.
86. I. Leslie, S. Williams, C. Brown, J. Thompson, G. Isaac, E. Ingham and J. Fisher, *Abstracts of the 5th World Congress of Biomechanics*, Munich, Germany (2006), p. 5965.
87. M. T. Clarke, P. T. Lee, A. Arora and R. N. Villar, *J. Bone J. Surg. Br.* **85**(6) (2003) 913.
88. A. K. Skipor, P. A. Campbell, S. Gitelis, R. A. Berger, H. C. Amstutz and J. J. Jacobs, in *Trans. Orthopaedic Research Society*, Chicago, IL, Vol. 29 (2004), p. 0124.
89. A. Moroni, L. Savarino, M. Cadossi, M. Greco, N. Baldini and S. Giannini, in *Trans. Orthopaedic Research Society*, San Francisco, California, Vol. 31 (2006), p. 0514.
90. F. W. Chan, J. D. Bobyn, J. B. Medley, J. J. Krygier, S. Yue and M. Tanzer, *Clin. Orthop. Relat. Res.* **333** (1996) 96.
91. R. Farrar, *Simulation and Analysis of the Wear of Metal on Metal Articulations in Artificial Hip Joints*, PhD thesis (University of Leeds, 2001).
92. R. Farrar and M. B., in *Trans. Orthopaedic Research Society*, 43rd ed., Vol. 22, San Francesco, CA (1997), p. 71.
93. Y. S. Liao and M. Hanes, in *Trans. Orthopaedic Research Society*, Chicago, IL, Vol. 31 (2006), p. 0503.
94. M. E. Muller, *Clin. Orthop. Relat. Res.* **311** (1995) 54.
95. F. Liu, Z. M. Jin, F. Hirt, C. Rieker, P. Roberts and P. Grigoris, *Proc. Inst. Mech. Eng. [H]* **219** (2005) 319.